

UNIVERSIDADE DE SÃO PAULO
INSTITUTO DE GEOCIÊNCIAS

**GEOQUÍMICA E GEOCRONOLOGIA DO PLUTONISMO DE ARCO
MESO-CENOZOICO NA CORDILHEIRA CENTRAL DA COLÔMBIA E
OS PROCESSOS DE ACRESÇÃO CRUSTAL NOS ANDES DO NORTE**

Camilo Bustamante Londoño

Orientador: Prof. Dr. Carlos José Archanjo

TESE DE DOUTORAMENTO

Programa de Pós-Graduação em Mineralogia e Petrologia

SÃO PAULO

2016

UNIVERSIDADE DE SÃO PAULO
INSTITUTO DE GEOCIÊNCIAS

**GEOQUÍMICA E GEOCRONOLOGIA DO PLUTONISMO DE ARCO
MESO-CENOZOICO NA CORDILHEIRA CENTRAL DA COLÔMBIA E
OS PROCESSOS DE ACRESÇÃO CRUSTAL NOS ANDES DO NORTE**

Camilo Bustamante Londoño

Orientador: Prof. Dr. Carlos José Archanjo

TESE DE DOUTORAMENTO

Programa de Pós-Graduação em Mineralogia e Petrologia

SÃO PAULO

2016

Autorizo a reprodução e divulgação total ou parcial deste trabalho, por qualquer meio convencional ou eletrônico, para fins de estudo e pesquisa, desde que citada a fonte.

Ficha catalográfica preparada pelo Serviço de Biblioteca e Documentação
do Instituto de Geociências da Universidade de São Paulo

Bustamante Londoño, Camilo

Geoquímica e geocronologia do plutonismo de arco
meso-cenozoico na Cordilheira Central da Colômbia e
os processos de acresção crustal nos Andes do Norte
/ Camilo Bustamante Londoño. - São Paulo, 2016.

184 p. + anexos

Tese (Doutorado) : IGC/USP
Orient.: Archanjo, Carlos José

1. Rochas graníticas 2. Geoquímica 3.
Geocronologia I. Título

in memoriam
Fernando, Bernardo e Marta

AGRADECIMENTOS

Agradeço ao Instituto de Geociências da Universidade de São Paulo pela oportunidade que me deu para o desenvolvimento de um projeto de doutorado nos Andes do Norte, e com isso contribuir ao conhecimento de uma das áreas mais complexas e desconhecidas da cadeia Andina. Este projeto não poderia ter sido realizado sem o apoio da Fundação de Amparo a Pesquisa do Estado de São Paulo (**FAPESP**; **proc. 2010/19068-6**), da *Fundación para la Promoción de la Ciencia y la Investigación del Banco de la República de Colombia (Proyecto 3171)* e do *Fondo Corrigan-ACGGP-ARES*, a quem agradeço imensamente.

Ao Prof. Dr. Carlos José Archanjo que aceitou o desafio de me orientar na modalidade de doutorado direto, agradeço a confiança e liberdade que me deu para encaminhar a minha pesquisa, bem como sua disposição para aprender sobre a geologia Colombiana e discutir, sem preconceitos científicos, os diversos temas da tectônica dos Andes do Norte. Sua orientação foi fundamental para entender a importância de publicar os resultados de uma pesquisa científica.

Ao Prof. Dr. Agustín Cardona Molina que me encaminhou na pesquisa científica desde que orientou meu trabalho de formatura na *Universidade EAFIT*. Ele é o responsável pela estruturação inicial do atual projeto de doutorado e a motivação para enfrentar este estágio da minha vida acadêmica. Suas constantes discussões foram fundamentais para esclarecer diversos aspectos da complexa tectônica Andina.

Ao Dr. Victor Valencia que foi o responsável pela qualidade dos dados analíticos disponíveis nessa tese. Agradeço o tempo que ele dedicou para que eu pudesse fazer com segurança as análises em zircão, bem como as interessantes discussões sobre a interpretação dos resultados.

Ao Prof. Dr. Jeff Vervoort que me abriu a portas do *GeoAnalytical Lab* da *Washington State University*. Deixo o meu reconhecimento a ele e sua equipe, Diane Wilford, Charles Knaak e Chris Fisher, que facilitaram a aquisição de dados isotópicos de Sr, Nd, Pb e Hf de qualidade. A ajuda e assessoria do Dr. Rick Conrey e a Dra. Laureen Wagoner foi ainda muito importante na confecção do banco de dados geoquímicos disponíveis nessa tese. O estágio na *Washington State University*, financiado pelo programa BEPE da FAPESP (**proc. 2012/14396-0**), foi um período decisivo tanto na consolidação dos dados analíticos como no amadurecimento de minha formação acadêmica.

Ao Prof. Dr. Antonio García Casco, que conheci no final da minha graduação na Colômbia, e com quem depois tive interessantes discussões em São Paulo sobre petrologia e

tectônica, iluminou o meu trabalho no momento no qual eu precisava de ideias alternativas para encaminhar as interpretações tectônicas.

Ao Prof. Dr. Andres Bustamante Londoño pelo apoio que foi de fundamental importância durante todo o período na pós-graduação. A ele agradeço a orientação em todos os aspectos, notadamente em como viver na cidade de São Paulo e sobre a vida universitária na USP. Além disso, sou reconhecido pelas discussões e esclarecimentos relacionados ao metamorfismo da Cordilheira Central da Colômbia.

Interessantes e frutíferas discussões sobre diferentes aspectos da vida pessoal e acadêmica foram mantidas constantemente com os meus colegas da pós-graduação, os quais sem dúvida contribuíram para minha formação pessoal e profissional. Por isso quero agradecer a Giovanna de Souza Pereira, Luiz Gustavo Viegas, Diego Gómez, María Isabel Giraldo, Santiago León e Astrid Siachoque. Ao geólogo Mario Lara agradeço sua disposição e apoio nas etapas de campo nas bonitas regiões de Caldas e Tolima. Aos colegas da minha sala Alice, Cláudio, Cassandra, Aniceto e Letícia, agradeço o respeito e companheirismo que propiciou um ambiente tranquilo para estudar.

Quero reconhecer o apoio do pessoal técnico e administrativo do Instituto de Geociências da USP durante o período de pós-graduação, em particular o Vasco, Angélica, Paulo, Luiz, Henrique, Katherine, Magali e Leonardo.

Aos meus sobrinhos brasileiros Emilio e Rebeca pela sua inspiradora e agradável presença no começo da minha estada em São Paulo.

Aos meus pais Emilio e Judith por seu infinito apoio, fortaleza e exemplo.

A minha esposa Sofía que me acompanhou desde o começo desta jornada e sempre me alentou a continuar.

RESUMO

Os Andes do Norte evoluíram a partir dos episódios sucessivos de subducção e colisão de terrenos após a separação de Pangea no Triássico Inferior. Em contraste com a parte central e sul dos Andes, a margem continental do Equador, Colômbia e Venezuela registram a influência do *plateau* do Caribe que colidiu com a placa Sul Americana no Cretáceo Superior. Nossa estudo concentra-se nas rochas magmáticas do Jurássico e Paleógeno hospedadas em sua maioria na Cordilheira Central da Colômbia. Os modelos tectônicos tradicionais tem definido um embasamento Permo-Triássico para a Cordilheira Central, também conhecido como Terreno Tahamí, enquanto rochas mais antigas de idade Paleozoica e núcleos restritos Grenvillianos (ca. 1 Ga) ocorrem na Cordilheira Oriental, sendo reunidos no Terreno Chibcha. A falha Otú-Pericos limitaria os terrenos Tahamí e Chibcha. Contudo, os resultados aqui obtidos indicam que: (i) as rochas Permo-Triássicas intrudidas por batólitos Jurássicos mostram composições similares nos dois lados da falha, e (ii) sequências metassedimentares Jurássicas, até então desconhecidas na Cordilheira Central, ocorrem intercaladas com o embasamento metamórfico. Estes resultados mostram que a falha Otú-Pericos não deve representar um limite de terrenos tectonoestratigráficos, e que a distribuição espacial das sequências Permo-Triássicas na Cordilheira Central tem sido superestimada. Além disso, idades U-Pb associadas a composições de Lu-Hf dos zircões detriticos sugere uma origem para-autóctone para rochas permo-triássicas. Um volumoso magmatismo que se estende do Jurássico ao Cretáceo intrude o embasamento do flanco oriental da Cordilheira Central. Embora sua colocação num arco magmático continental seja incontestável, a gênese desses magmas ainda é debatida. Nossos resultados indicam que o magmatismo Jurássico evoluiu num arco estacionário ativo em torno de 200 Ma. O volume de magma diminuiu em ca. 165 Ma para cessar em 130 Ma. Além disso, dados geoquímicos e isotópicos indicam que esses magmas foram diferenciados em níveis crustais rasos e tornaram-se mais juvenis nos pulsos magmáticos finais. Isto implica que a fonte do magma mudou no ambiente de subducção, provavelmente em resposta à diminuição do aporte de sedimentos na cunha mantélica associado a um regime tectônico onde a convergência foi francamente oblíqua. O magmatismo reiniciou em ca. 90 Ma com a subducção da placa do Caribe sob a margem NW da placa Sul-Americana, o que ocasionou a acreção de vários fragmentos oceânicos e, consequentemente, espessamento da margem continental. Uma fonte profunda dos plútuns do Cretáceo Superior e Eoceno aparentemente está registrada na elevada razão Sr/Y desses magmas, que se formariam e seriam diferenciados em alta pressão onde granada é estável. Zircons detriticos eocênicos são encontrados nas bacias sedimentares do leste da Colômbia, os

quais relacionamos à fontes ígneas distais e/ou mais proximais, provavelmente localizadas na Cordilheira Central conforme indicam as composições isotópicas de Hf nos zircões. Alguns batólitos eocênicos, como o tonalito de Santa Marta, estão alojados perto da sutura que reune os complexos de acresção de origem oceânica à margem continental pré-cretácica da Sierra Nevada de Santa Marta. Estudos da trama magnética do tonalito de Santa Marta indicam que sua colocação explorou estruturas extensionais formadas numa zona de cisalhamento destral formada pelo deslocamento da placa do Caribe no Eoceno. O magmatismo continental do segmento dos Andes do Norte terminou no Eoceno Meio, provavelmente pela dificuldade em subductar a espessa litosfera do *plateau* do Caribe.

ABSTRACT

The Northern Andean mountain belt, which includes the western margin of Ecuador, Colombia and Venezuela evolved by successive episodes of subduction and terrane collision after the break-up of Pangea in the Lower Triassic. In contrast with the Central and Southern Andean Cordillera, the northern chain records the influence of the Caribbean plateau that collided with the South American plate in the Late Cretaceous. Our study focuses on the Jurassic and Paleogene magmatic rocks hosted mostly in the Central Cordillera of Colombia. The traditional tectonic models have been defining a Permo-Triassic basement for the Central Cordillera, named Tahamí Terrane, and Paleozoic sequences including vestiges of the Grenville orogeny (ca. 1 Ga) hosted in the Eastern Cordillera and grouped in the Chibcha Terrane. The Otú-Pericos fault has been considered as the limit between both terranes. Nevertheless, the results obtained here indicate that: (i) the Permo-Triassic rocks intruded by Jurassic batholiths show similar compositions on both sides of the fault, and (ii) until now unnoticed Jurassic metasedimentary sequences occur interleaved with the Permo-Triassic metamorphic basement. These findings imply that the Otú-Pericos fault is not a limit of tectonostratigraphic terranes and that the spatial distribution of the Permo-Triassic sequences in the Central Cordillera has been overestimated. A para-autochthonous origin for rocks recording contrasting Permian to Jurassic histories is proposed for the units at both sides of the Otú-Pericos fault. A voluminous Late Jurassic to Early Cretaceous magmatism intrudes the basement of eastern flank of the Central Cordillera. Although their emplacement in a continental arc setting is indisputable, the magma genesis is still debated. Our results indicate that the Jurassic magmatism evolved in a stationary arc at ca. 200 Ma. The magma volumes decreased at ca. 165 Ma to cease at ca. 130 Ma. Furthermore, geochemical and isotopic data indicates that these magmas differentiated at shallow crustal levels and became more juvenile towards the latest magmatic pulses. This implies that the magma source changed in a subduction setting probably recording the decreasing of the sedimentary input to the mantle wedge in a tectonic setting dominated by oblique convergence. The magmatism resumed at ca. 90 Ma with the subduction of the proto-Caribbean under NW South America which, in addition, accreted to the continent several oceanic fragments that thickened the continental margin. A deep source of the Late Cretaceous to Eocene plutons would be recorded in the adakite-like signature (high Sr/Y ratios) of the magmas that would have been differentiated at a high pressure where garnet is stable. Detrital Eocene zircons are also recorded in basins from eastern Colombia, which could be related to both distal igneous sources and/or more proximal sources that according the Hf isotopic compositions would be located in the Central

Cordillera. Some Eocene batholiths, like the Santa Marta tonalite, are emplaced close to the suture that juxtaposes the Cretaceous oceanic terranes to the continent. Fabric studies of the Santa Marta tonalite indicated that its emplacement exploited extensional structures formed in bulk dextral shear component formed by the lateral displacement of the Caribbean plate in the Eocene. The continental magmatism of the northern Andean margin stops in the Middle Eocene probably related to the difficulty of the thick Caribbean plateau to subduct.

SUMÁRIO

	Página
Capítulo 1. Introdução	1
1.1. ORGANIZAÇÃO DA TESE	1
1.2. CONTEXTO GEOLÓGICO REGIONAL	2
1.2.1. Arcabouço tectônico da Colômbia	3
1.2.2. Magmatismo Meso-Cenozóico na Cordilheira Central	7
1.3. JUSTIFICATIVA E OBJETIVOS	10
1.4. MATERIAIS E MÉTODOS	11
1.4.1. Geoquímica em rocha total	11
1.4.2. Geocronologia U-Pb LA-ICP-MS em zircão	12
1.4.3. Isótopos de Nd, Hf, Pb e Sr	12
1.4.4. Anisotropia de Suscetibilidade Magnética	14
Capítulo 2. U-Pb ages and Hf isotopes in zircons from Para-Autochthonous Mesozoic terranes in the western margin of Gondwana: implications for the terrane configurations in the Northern Andes	17
ABSTRACT	17
2.1. INTRODUCTION	18
2.2. GEOLOGICAL SETTING	21
2.3. ANALITICAL METHODS	23
2.3.1. LA-ICP-MS U-Pb Geochronology in zircon	23
2.3.2. Hf isotopes in zircon	23
2.4. RESULTS	24
2.4.1. Tierradentro unit	24
2.4.2. Detrital zircons of the Tahamí terrane	27
2.5. Hf ISOTOPE GEOCHEMISTRY	29
2.5.1. Tierradentro unit	29
2.5.2. Graphite-quartz-muscovite schist	30
2.6. DISCUSSION	30
2.7. CONCLUSIONS	33
Capítulo 3. Late Jurassic to Early Cretaceous plutonism in the Colombian Andes: a record of long-term arc maturity	34
ABSTRACT	34
3.1. INTRODUCTION	35
3.2. GEOLOGICAL SETTING	37
3.2.1. Mesozoic plutonism in the southern Central Cordillera and the Upper Magdalena valley	37
3.3. SAMPLING AND ANALYTICAL METHODS	38
3.3.1. U-Pb Geochronology in zircon	39
3.3.2. Hf isotopes in zircon	39
3.3.3. Whole rock XRF and ICP-MS geochemistry	40
3.3.4. Nd, Hf and Pb radiogenic isotopes	40
3.4. RESULTS	41

3.4.1. Zircon U-Pb geochronology	41
3.4.2. Whole-rock elemental and isotope geochemistry, and Hf isotopes in zircon	44
3.4.2.1. <i>Payandé stock</i>	47
3.4.2.2. <i>Ibagué batholith</i>	48
3.4.2.3. <i>Mariquita stock</i>	49
3.5. DISCUSSION	50
3.5.1. Age distribution of the Jurassic-Early Cretaceous magmatic activity	50
3.5.2. Genesis of the Mesozoic magmatic arc of the Central Cordillera	52
3.5.3. Jurassic tectonomagmatic evolution of the Northern Andes	59
3.6. CONCLUSIONS	60

Capítulo 4. Geochemistry and isotopic signatures of Paleogene plutonic and detrital rocks of the Northern Andes of Colombia: a record of post-collisional arc magmatism 62

ABSTRACT	62
4.1. INTRODUCTION	63
4.2. GEOLOGICAL SETTING	63
4.2.1. Paleogene magmatism in the Colombian Andes	65
4.3. SAMPLING AND METHODS	66
4.3.1. Whole rock geochemistry	67
4.3.2. Whole rock Sr, Nd and Pb isotopes	67
4.3.3. U-Pb Geochronology in zircon	68
4.3.4. Hf isotopes in zircon	68
4.4. RESULTS	69
4.4.1. Petrography, whole rock geochemistry and Sr-Nd-Pb isotopes of the Hatillo stock and el Bosque batholith	69
4.4.2. Zircon U-Pb ages and Hf isotopes	71
4.4.3. Volcanoclastic rocks	74
4.4.3.1. <i>Pre-Paleogene zircons</i>	74
4.4.3.2. <i>Early Paleogene zircons</i>	75
4.5. DISCUSSION	75
4.5.1. Origin of the Paleogene plutonism	75
4.5.2. Detrital zircon signatures	80
4.6. CONCLUSIONS	81

Capítulo 5. Magnetic fabric (AMS, AAR) of the Santa Marta batholith (northern Colombia) and the shear deformation along the Caribbean plate margin 82

ABSTRACT	82
5.1. INTRODUCTION	83
5.2. GEOLOGICAL SETTING	84
5.2.1. Early Paleogene magmatism in the Sierra Nevada de Santa Marta	86
5.3. U-Pb ZIRCON (SHRIMP) GEOCHRONOLOGY	88
5.3.1. Sampling and methods	88
5.3.2. Results	89
5.4. ANISOTROPY OF SUSCEPTIBILITY AND ANHYSTERETIC REMANENCE	90

5.4.1. Background	90
5.4.2. Sampling and Methods	91
5.4.3. Magnetic susceptibility and mineralogy	92
5.4.4. Anisotropy of magnetic susceptibility	94
5.4.5. Anisotropy of anhysteretic Remanence	95
5.5. DISCUSSION	98
5.5.1. Significance of magnetic fabrics	98
5.5.2. Emplacement structures and tectonic implications	100
5.6. CONCLUSIONS	102
Capítulo 6. Discussão	103
Capítulo 7. Conclusões	108
Referências	110
ANEXOS. Tabelas de dados	131
Tabela 2.1. U-Pb zircon ages from the Tierradentro unit.	132
Tabela 2.2. U-Pb detrital zircon ages from the Cajamarca Complex.	137
Tabela 2.3. Zircon Hf isotope data from the Tierradentro gneisses and amphibolites and micaschist from the Cajamarca Complex.	140
Tabela 3.1. U-Pb zircon ages from the Payandé, Ibagué and Mariquita plutons.	142
Tabela 3.2. Hf isotopic data from the Payandé, Ibagué and Mariquita plutons.	159
Tabela 3.3. Geochemistry of major, trace and rare earth elements of the Payandé, Ibagué and Mariquita plutons.	162
Tabela 3.4. Whole rock Nd, Pb and Hf isotopic analyses of the Payandé, Ibagué and Mariquita plutons.	163
Tabela 4.1. Whole rock geochemistry and Sr, Nd and Pb isotopes from the Hatillo and El Bosque plutons.	164
Tabela 4.2. Zircon U-Pb geochronology results.	166
Tabela 4.3. Zircon Hf isotope results.	175
Tabela 5.1. SHRIMP U-Pb zircon data of a tonalite from the Santa Marta batholith.	181
Tabela 5.2. AMS parameters of the Santa Marta batholith.	183

LISTA DE FIGURAS

	Página
Figura 1.1. Arcabouço geológico da Colômbia (encarte) com destaque para as principais feições geológicas da Cordilheira Central (CC). WC, Cordilheira Ocidental; EC, Cordilheira Oriental; SNMS, Sierra Nevada de Santa Marta; RFS, sistema de falha de Romeral.	4
Figura 1.2. Reconstrução esquemática do desmembramento borda ocidental da Pangea no Triássico. Fragmentos do arco permiano estão preservados do México ao Peru, com a Cordilheira Central (Colômbia) – Real (Equador) contendo rochas do arco permiano e do estágio rifte triássico (in Spikings <i>et al.</i> , 2015).	5
Figura 1.3. Migração da placa do Caribe entre o Cretáceo e o Paleoceno. O plateau oceânico do Caribe-Colômbia (CCOP) colide com o continente Sulamericano em trono de 75 Ma favorecendo a acresção de terrenos oceânicos na borda noroeste da Placa Sul-americana. Dioritos, tonalitos e granodioritos (triângulo vermelho) formados por subducção foram originados tanto em arco oceânico como continental (modificado de Weber <i>et al.</i> , 2015).	7
Figura 2.1. Geology of the Central Cordillera (CC) in Colombia and Cordillera Real in Ecuador, showing the distribution of Cretaceous metamorphic and volcanic rocks, Jurassic continental arc intrusions: Abitagua (AB), Ibagué (IB), Mocoa (MB) and Segóvia (SB) batholiths and Permo-Triassic rocks. Inset – Main geological domains of Colombia highlighting the location of the Western (WC) and Eastern (EC) Cordilleras.	19
Figura 2.2. Detailed geological map of the study area, showing the samples distribution (squares) and the relations between the studied units.	21
Figura 2.3. U-Pb ages and Concordia diagram obtained from zircon rims representing the crystallization age of the CI12 sample (Quartz-feldspathic-gneiss). Scale bar on CL image is 100 µm.	25
Figura 2.4. U-Pb ages and Concordia diagram obtained zircon rims representing the metamorphic age of the CAT1A sample (amphibolite). Scale bar on CL image is 100 µm.	26
Figura 2.5. U-Pb zircon ages and Concordia diagram obtained from sample GCC8 (augen granodiorite) whose age is in the same range of sample CAT1A.	26
Figura 2.6. U-Pb detrital zircon results from the quartz-muscovite schist (CH21C), showing less than 30% discordance and less than 10% discordance for comparison.	28
Figura 2.7. Upper: Distribution of the whole $\epsilon_{\text{Hf(i)}}$ obtained for the Cajamarca Complex. Lower: Initial ϵ_{Hf} vs. $^{206}\text{Pb}/^{238}\text{U}$ age diagram. Squares	

represents zircons from sample CAT1A (amphibolite) with a strong juvenile signature as opposite to the zircons from the sample CI12 (hornblende gneiss) represented by triangles, which reflects the involvement of crustal sources for this rock. Circles are from detrital zircons of the Tahamí terrane. See the comparison with published data from other Middle Jurassic plutons of the Central and Northern Andes [Ilo batholith: Boekhout et al. (2012). Payandé and Ibagué plutons: Bustamante et al. (2016); Cochrane et al. (2014b)].

29

Figura 3.1. A: Distribution of the Jurassic plutonic belt in the Northern Andes. B: Detailed map of the occurrences of Lower Jurassic to Lower Cretaceous plutonic rocks in the Central Cordillera of Colombia and isolated massifs with associated volcanic rocks.

36

Figura 3.2. Representative Scanning Electron Microscope Cathodoluminescence (SEM-CL) images from zircon grains of each pluton studied. Upper: Payandé stock, middle: Ibagué batholith, bottom: Mariquita stock.

41

Figura 3.3. U-Pb zircon ages with 1σ box heights and Tera-Wasserburg diagrams with 68.3% confidence error ellipses from the Payandé stock.

42

Figura 3.4. U-Pb zircon ages with 1σ box heights and Tera-Wasserburg diagrams with 68.3% confidence error ellipses from the Ibagué Batholith.

43

Figura 3.5. U-Pb zircon ages with 1σ box heights and Tera-Wasserburg diagrams with 68.3% confidence error ellipses from the Mariquita stock.

44

Figura 3.6. Harker diagrams of the three studied plutons, showing how fractional crystallization is a common process among them.

45

Figura 3.7. Geochemical classification and discrimination diagrams of samples from the three studied plutons. A: Classification of plutonic rocks based on the TAS diagram of Cox et al. (1979). B: Alkalinity index diagram of Pecerillo and Taylor (1976). C: Alumina saturation index diagram of Shand (1943).

46

Figura 3.8. Multi-element plot normalized to primitive mantle according to Sun and McDonough (1989).

47

Figura 3.9. Chondrite normalized REE patterns according to Nakamura (1974).

48

Figura 3.10. Map from Colombia showing the distribution of the Jurassic-Cretaceous magmatic belt. U-Pb zircon ages from this study and other works are plotted in rectangles. 1: Leal-Mejía (2011); 2: Bustamante et al. (2010); 3: Villagómez et al. (2011); 4: Álvarez-Galíndez (2013). Lower to mid-Cretaceous mafic magmatism is represented by white (Yavi Fm.: Toro-Toro et al., 2011) and black (Eastern Cordillera: Vásquez and Altenberger, 2005) squares.

51

- Figura 3.11.** Detrital U-Pb zircon ages from boreholes showing that the density of ages is higher for the Lower to Middle Jurassic and decreases towards the Upper Jurassic to Lower Cretaceous, which is consistent with a decreasing volume of magma. Data are compiled from Nie et al. (2010), Horton et al. (2010), Saylor et al. (2011), Bayona et al. (2013), Caballero et al. (2013) and Silva et al. (2013). 52
- Figura 3.12.** LREE/HREE ratios and alkalis content (K₂O and Na₂O) over time. 53
- Figura 3.13.** Discrimination diagram of granites ($\text{Hf-Rb}/30 \cdot \text{Ta}^*30$) according to Harris et al. (1986). 53
- Figura 3.14.** Lead isotopic evolution curve according to the plumbotectonics model of Zartman and Doe (1981). 54
- Figura 3.15.** Variation of initial Σ_{Hf} and $^{176}\text{Hf}/^{177}\text{Hf}$ in zircon and whole rock with $^{206}\text{Pb}/^{238}\text{U}$ crystallization age. **Triangles and rotated crosses:** Mariquita stock zircon and whole-rock data, respectively; **Diamonds and crosses:** Ibagué Batholith zircon and whole-rock data, respectively; **Squares and star:** Payandé stock zircon and whole-rock data, respectively; **Dark grey rectangles:** data from Colombian granites; **Light grey rectangles:** data from Ecuadorian granites (Cochrane et al., 2014b). 55
- Figura 3.16.** Initial Σ_{Hf} vs. Σ_{Nd} diagram. Symbols same as in fig. 13. Hf-Nd mantle array from Vervoort and Blichert-Toft (1999). 56
- Figura 3.17.** Model proposed (not to scale) for the generation of the Early Jurassic to Early Cretaceous magmatic arc in the Northern Andes of Colombia. The figure shows the relationship between oblique convergence, clastic input, and basalt+sediment melting of the crust to form granodioritic batholiths (modified from Castro, 2014). 58
- Figura 4.1. A.** Location of Paleogene igneous bodies sampled in Western and Central Cordillera and Paleogene detrital zircons sampled in Eastern Cordillera of Colombia; **B.** Regional cross section of Central Colombia with Paleogene samples; **C.** Sedimentary section with detrital samples analyzed. Figure modified from Bayona et al. (2012). 65
- Figura 4.2.** Prismatic epidote crystal in the Hatillo stock. Vertical length is 2.7 mm for each photograph. 69
- Figura 4.3.** Geochemical classification and discrimination diagrams of samples from the studied plutons. **A:** Alkalinity index diagram of Pecerillo and Taylor (1976). **B:** Alumina saturation index diagram of Shand (1943). **C:** Multi-element plot normalized to primitive mantle according to Sun and McDonough (1989). **D:** $\text{Hf-Rb}/30 \cdot \text{Ta}^*3$ geotectonic discrimination diagram of Harris et al. (1986). **E:** Chondrite normalized REE patterns according to Nakamura (1974). 71

Figura 4.4. CL images from representative zircons from the Hatillo (upper) and El Bosque (lower) plutons.	72
Figura 4.5. U-Pb Concordia ages obtained from plutons of the Central Cordillera: Hatillo stock and El Bosque batholith.	73
Figura 4.6. Initial Σ_{Hf} vs $^{206}\text{Pb}/^{238}\text{U}$ age. Data from Paleogene igneous and detrital zircons from Central and Eastern Cordilleras of Colombia.	74
Figura 4.7. Hf isotope data from pre-Paleogene (>66 Ma) detrital zircons of the Bogotá Formation.	75
Figura 4.8. Sr/Y vs Y diagram after Defant and Drummond (1990) for adakite rocks discrimination.	76
Figura 4.9. Variation of crustal depth with age in the western margin of the Colombian Andes during the Meso-Cenozoic. Blue points represent the whole data used to show the variations after applying the filters suggested by Profeta et al. (2015). Green line is an average every ~10 Ma. Relations between Sr/Y ratio and depth are according to Profeta et al. (2015).	78
Figura 4.10. A. $\Sigma_{\text{Nd(i)}}$ vs $^{87}\text{Sr}/^{86}\text{Sr}$. B. Lead isotopic evolution curve according to the plumbotectonics model of Zartman and Doe (1981). Both diagrams show a comparing between the Eocene plutons analyzed with other Paleogene plutons from the Central Cordillera and the Colombian Caribbean.	79
Figura 5.1. Caribbean oceanic plateau bounded by the subduction zones of Antilles and Panamá, and strike-slip (transform) faults. Accreted oceanic terranes related to the oblique subduction of the Caribbean plate beneath South America are shown to the Ecuador, Colombia and Panama to the west of the Romeral fault system. 1. Cretaceous oceanic rocks; 2, thrust; 3, subduction zone (modified from Kerr, 2014).	84
Figura 5.2. Simplified physiographic map of the northern Andes showing the Cretaceous oceanic rocks of the West Cordillera (WC) in contact with the Central Cordillera along the Romeral fault system. The Eastern Cordillera (EC) is separated from the Sierra Nevada de Santa Marta (SNSM) block and Central Cordillera by sedimentary deposits of the César-Rancheria and Magdalena basins. Plutonic rocks corresponding to the Paleocene-Eocene magmatic arc are shown in red (modified from Bayona et al., 2012).	86
Figura 5.3. Geological map of the eastern part of the Sierra Nevada de Santa Marta.	87
Figura 5.4. AMS sampling sites with the domain with the granitoid with foliated and/or gneissic microstructure (modified from Tschanz et al. (1969)). The location of the sites with geochronological determinations after Duque (2009) and Cardona et al. (2011a).	88
Figura 5.5. Cathodoluminescence images of representative zircons of a	

horblende-biotite tonalite (sample SM54). Some grains show dark (U-rich) cores (left) enclosed by more luminescent (and low U) rims. Oscillatory zoning typical of magmatic zircons are visible in cores and rims.	89
Figura 5.6. Concordia diagram of the hornblende-biotite tonalite, with the zircon age determined by average of the concordant data. Analyses corresponding to the grey ellipses were discarded from the age calculation (see text).	90
Figura 5.7. Relation between the mean-site magnetic susceptibility (Km), degree of anisotropy (P) and shape (T) of the AMS ellipsoid.	93
Figura 5.8. Dependence of the magnetic susceptibility with temperature for representative samples of the Santa Marta batholith.	94
Figura 5.9. Magnetic fabric (foliation and lineation) and domains where the rock microstructure is foliated and/or gneissic (grey area). Dashed line corresponds to the corridors where the foliation trend is nearly E-W. Stereonets of the magnetic lineation (right) and pole of the magnetic foliation (Schmidt diagrams, lower hemisphere; contours of 2%, 4%, 1% area). Black; xenolith. ND and SD; northern and southern domain.	95
Figura 5.10. Coercivity spectra for samples with different susceptibility magnitudes (k, 10 ⁻³ SI). Grey areas indicate the windows chosen to determination of partial anisotropy of anhysteretic remanence. H, induced field, ARM; normalized anhysteretic remanent magnetization.	96
Figura 5.11. Stereograms (lower hemisphere) of the principal directions of AMS and partial AAR for sites with moderate to strong magnetic susceptibility magnitudes.	97
Figura 5.12. Stereograms (lower hemisphere) of the principal directions of AMS and partial AAR for sites with low magnetic susceptibility magnitudes (symbols as in Fig. 5.11).	98
Figura 5.13. Tectonic model of the Santa Marta batholith (upper left) combining the trend of magnetic foliation (red lines) and the metamorphic fabric of the host-rocks (after Tschanz <i>et al.</i> , 1969). Dashed lines correspond to the synthetic shear bands originated by the regional strain field dominated by dextral shear. The shear component is transmitted to the magmatic arc (lower right) by the oblique subduction of the Caribbean plate.	100

Capítulo 1

Introdução

1.1. ORGANIZAÇÃO DA TESE

Após a apresentação do contexto geológico no qual a tese se desenvolve, introduzimos os conceitos e ideias fundamentais da evolução tectônica dos Andes do Norte sob a perspectiva da evolução magmática, e com foco na Cordilheira Central da Colômbia. Nessa introdução estão ainda descritos os objetivos que justificaram a realização deste trabalho bem como os métodos analíticos utilizados para alcançar os objetivos propostos.

A apresentação dos resultados se dá sob a forma de artigos científicos submetidos a periódicos internacionais. Embora conectados pelo tema geral que fundamenta a pesquisa, cada artigo pode ser lido de forma independente em cada capítulo da tese.

O capítulo 2 compreende o artigo intitulado “*U-Pb ages and Hf isotopes in zircons from Para-Autochthonous Mesozoic terranes in the western margin of Gondwana: implications for the terrane configurations in the Northern Andes*”, submetido ao periódico *The Journal of Geology*. O manuscrito trata da conformação do embasamento Permo-Triássico da Cordilheira Central e sua relação com o cinturão metamórfico Jurassico, explorando suas implicações na definição dos terrenos tectonoestratigráficos da Colômbia.

O capítulo 3 está submetido ao periódico *Geological Society of America Bulletin* sendo intitulado “*Late Jurassic to Early Cretaceous plutonism in the Central Cordillera of the Colombian Andes: a record of long-term arc maturity*”. Ele aborda a origem, distribuição e evolução do cinturão plutônico Jurássico-Cretáceo da Cordilheira Central e discute os mecanismos de “*slab roll-back*” relacionados à subducção da placa do Pacífico.

O capítulo 4 refere-se ao artigo “*Geochemistry and isotopic signatures of Paleogene plutonic and detrital rocks of the Northern Andes of Colombia: a record of post-collisional arc magmatism*”, submetido ao periódico *Lithos*. Esse artigo discute a gênese do plutonismo Paleógeno da Cordilheira Central, o registro do magmatismo na proveniência dos zircões detriticos das bacias a leste da Colômbia, e a relação entre o arco magmático Paleógeno na Cordilheira Central com a tectônica do Caribe.

O capítulo 5 trata da colocação do batólito Santa Marta no arco magmático Paleógeno formado pela interação da placa do Caribe com o continente Sul-Americano. Utilizamos a

técnica da anisotropia de susceptibilidade magnética (ASM) para caracterizar as estruturas do batólito e entender o alojamento de magmas em uma margem ativa. O artigo denominado "*Magnetic fabric (AMS, AAR) of the Santa Marta batholith (northern Colombia) and the shear deformation along the Caribbean plate margin*" foi submetido ao *Journal of South American Earth Science* e encontra-se em fase de revisão

O capítulo final procura consolidar os resultados descritos nos capítulos anteriores para apresentar um quadro geral da história tectônica da Cordilheira Central da Colômbia entre o Jurássico e o Eoceno. São discutidos os modelos atuais da evolução da parte norte da cadeia andina e suas implicações para a acreção continental ao longo da margem colombiana. Finalmente, as conclusões abrangem os principais resultados obtidos no presente trabalho.

1.2. CONTEXTO GEOLÓGICO REGIONAL

A margem noroeste de América do Sul durante o Meso-Cenozóico é o resultado de uma sucessão de ambientes tectônicos distintos, que incluem subducção e acreção/colisão de terrenos. A convergência entre a placa Sul-Americana e placas oceânicas de origem diversa (*e.g.*, Pacífico, Caribe, Nazca) moldaram a estrutura atual do orógeno Andino (Toussaint, 1995; Jaillard *et al.*, 2000; Ramos & Aleman, 2000; Ramos, 2009; Pindell & Keenan, 2010). Os modelos tectônicos regionais consideram que a subducção da litosfera oceânica ao longo da margem noroeste da América do Sul foi acompanhada de mudanças drásticas quanto à origem da placa e o seu modo de convergência no tempo. Durante o Meso-Cenozóico a convergência consumiu essencialmente uma placa de afinidade pacífica, enquanto no Paleoceno-Eoceno toda a margem norte do continente foi afetada pela convergência oblíqua da *plateau* do Caribe (Kerr *et al.*, 1997; Pinell & Kennan, 2009; Kerr, 2014). A partir do Mioceno foi restabelecido no Pacífico a subducção da Placa Farallones (atual Placa Nazca; Ramos, 2009). A placa do Caribe, por sua vez, está atualmente separada do Pacífico e Atlântico pelos arcos vulcânicos da América Central e Antilhas, respectivamente. A migração para nordeste e leste da placa caribenha define ainda as zonas transformantes de Hispaniola-Porto Rico a norte (Calais *et al.*, 2016) e, na Venezuela a sul, a de Oca-Cordilheira da Costa (Escalona and Mann, 2011).

1.2.1. Arcabouço tectônico da Colômbia

A geologia colombiana pode ser compreendida em termos de três grandes cordilheiras, a oriental, central e ocidental (Figura 1.1) separadas a leste por bacias pós-paleozoicas e pela vasta planície amazônica. Na extremidade oriental do país afloram núcleos precambrianos correlacionados ao Cráton Amazônico.

As rochas mais antigas das cordilheiras estão expostas na Cordilheira Oriental e na região de Sierra Nevada de Santa Marta (SNSM, Figura 1.1), que ocorrem como blocos isolados e dispersos de idade Grenviliana (Restrepo-Pace *et al.*, 1997). A Cordilheira Oriental contém, portanto um embasamento Precambriano sucedido por rochas metasedimentares de afinidade oceânica depositados no Paleozóico Inferior. Estudos recentes baseados em geoquímica isotópica e geocronologia U-Pb em zircão indicam um embasamento autóctone de afinidade Gondwanica para a Cordilheira Oriental, com a subducção no Ordoviciano do oceano *Iapetus-Rheic* promovendo a intrusão de rochas magmáticas, metamorfismo e deformação no embasamento da Cordilheira Oriental (Van der Lelij *et al.*, 2016). A bacia dos Llanos limita a borda leste da Cordilheira Oriental enquanto exposições locais do cráton Amazônico ocorrem perto da fronteira com o Brasil.

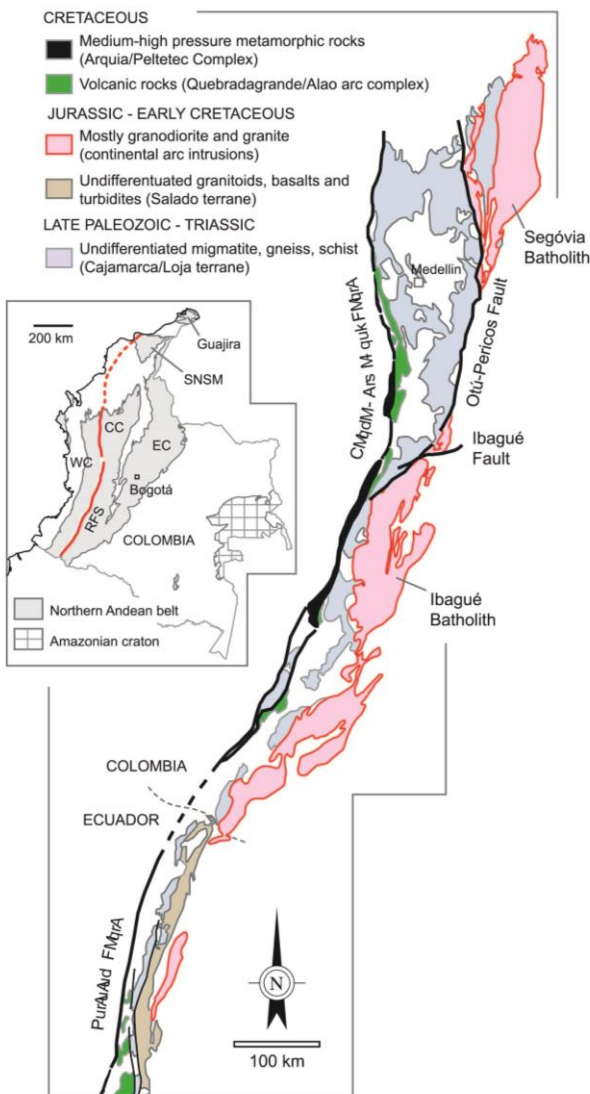


Figura 1.1. Arcabouço geológico da Colômbia (encarte) com destaque para as principais feições geológicas da Cordilheira Central (CC). WC, Cordilheira Ocidental; EC, Cordilheira Oriental; SNMS, Sierra Nevada de Santa Marta; RFS, sistema de falha de Romeral.

A Cordilheira Central da Colômbia, objeto de estudo desta tese, consiste de um embasamento Permo-Triássico de afinidade predominantemente continental que evoluiu a partir da fragmentação da Pangea no Triássico Inferior (c. 240 Ma) com o desmembramento da América do Sul e da América Central. A borda noroeste da América do Sul permaneceu como uma margem passiva até o final do Triássico quando começa a subducção da placa do Pacífico (Spikings *et al.*, 2015). A Cordilheira Central é limitada a oeste por rochas maficas cretácicas de afinidade oceânica reunidas no Complexo Quebradagrande. O contato entre as cordilheiras Ocidental e Central é feita pelas falhas de Cauca-Almaguer (Colômbia) e Peltetec

(Equador), e que inclui sequências metamórficas de média-alta pressão do Complexo Arquia (Bustamante *et al.*, 2012). As cordilheiras ocidental e central se prolongam para sul em direção ao Equador e Peru onde estão agrupadas na "Cordilheira Real".

Os processos que levaram a formação de granitoides tipo-S, migmatitos e anfibolitos que constituem as unidades de embasamento da Cordilheira Central foram formados entre 240 e 216 Ma (Cochrane *et al.*, 2014a). Na Colômbia essas unidades estão reunidas no Complexo Cajamarca enquanto no Equador ao terreno Loja (Figura 1.1; Spikings *et al.*, 2015). As reconstruções geodinâmicas sugerem a existência de um arco Parmiano que se estendeu do México ao Peru consumindo a placa do Pacífico até pelo menos o final do Jurássico. O arco foi submetido à extensão e desenvolvimento de bacias retro-arco no Permo-Triássico (Figura 1.2) antecendo à colocação no Jurássico de extenso e volumoso magmatismo. Na Cordilheira Central esse magmatismo está representado principalmente pelos batólitos de Segóvia e Ibagué, e na Cordilheira Real pelo batólito de Azafrán (Figura 1.1).

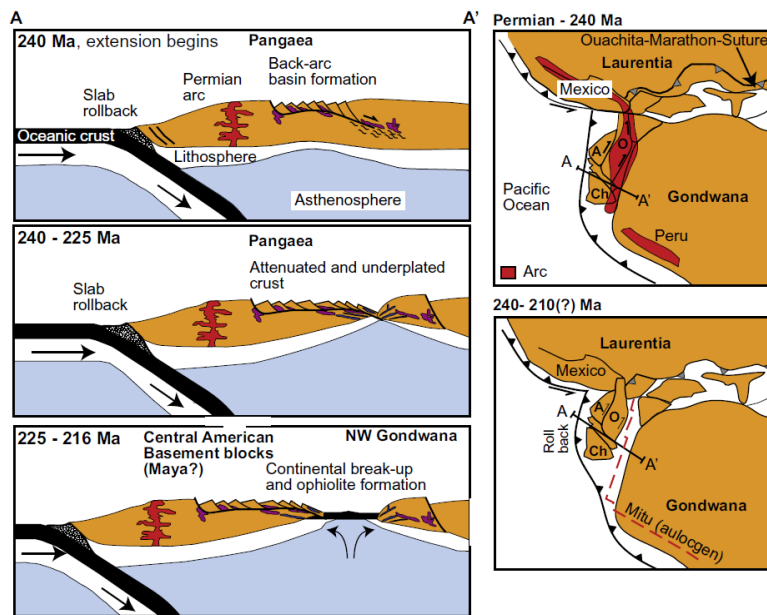


Figura 1.2. Reconstrução esquemática do desmembramento borda ocidental da Pangea no Triássico. Fragmentos do arco permiano estão preservados do México ao Peru, com a Cordilheira Central (Colômbia) – Real (Equador) contendo rochas do arco permiano e do estágio rifte triássico (*in* Spikings *et al.*, 2015).

Restrepo e Toussaint (1988) sugeriram que a margem da Colômbia poderia se entendida em termos de “terrenos alóctones” e definiram os terrenos Tahamí e Chibcha para as Cordilheiras Central e Oriental, respectivamente. A falha de Otú-Pericos (Figura 1) separaria os terrenos Tahami e Chibcha, sendo que este último conteria os fragmentos do embasamento Grenviliano e estariam registrados os eventos tectono-metamórficos pré-

ordovicianos. O modelo de “terrenos” aplicado a Cordilheira Oriental foi recentemente contestado por Van der Lelij *et al.* (2016) e, nessa tese (Capítulo 2), apresentamos evidências geoquímicas e geocronológicas de que a falha de Otú-Pericos não representa um limite onde a evolução geológica seria distinta nos lados opostos da falha. Rochas permo-triássicas foram ainda reconhecidas a sul na Cordilheira Real no Equador, e a norte na Sierra Nevada de Santa Marta e na península de Guajira.

A Cordilheira Central é separada da Cordilheira Ocidental pelas falhas de Calca-Almaguer-Peltetec, que reunidas definem o Sistema de Falhas de Romeral (RFS, Figura 1). A RFS é delineada por unidades litológicas diferenciadas de idade diversa tais como: (i) rochas vulcâno-sedimentares do Cretáceo Inferior (Complexo Quebradagrande/Alao; Villagomez *et al.*, 2011), (iii) metapelitos, intrusivas máficas e serpentinitos do Permo-Triássico, e (iii) intrusivas máficas e ultramáficas, metapelitos e quartzitos de média-alta pressão (Complexo Arquia/Peltetec) que incluem ocorrências de xistos com glaucofana cujas idades $^{40}\text{Ar}/^{39}\text{Ar}$ situam-se em torno de 120 Ma (Bustamante *et al.*, 2012). Essa unidades estiradas e segmentadas na RFS definem, portanto uma *mélange* ou uma zona de sutura entre as cordilheiras Central e Ocidental.

A Cordilheira Ocidental compreende rochas de afinidade oceânica (vulcânicas máficas e ultramáficas com química de MORB e arco oceânico, sedimentos de água profunda) formadas no Cretáceo. Essas unidades foram reunidas por Restrepo e Toussaint (1988) no Terreno Calima. A acresção do terreno Calima ao continente começou no Campaniano com a convergência obliqua da placa do Caribe (Figura 1.3). As reconstituições palinspáticas de Pindell and Kennan (2009) indicam que desde o Cretáceo pelo menos 1.600 km da litosfera caribenha subductou sob a Colômbia e Venezuela, e que entre 85 e 45 Ma o continente acomodou pelo menos 1.000 km de deslocamento lateral com movimento para nordeste do *plateau* do Caribe. A subducção originou um plutonismo de arco oceânico e continental com a intrusão, entre o Cretáceo Superior e Paleoceno, de dioritos, tonalitos e granodioritos (Weber *et al.*, 2015). A magmatismo cessa em torno de 45 Ma provavelmente pela dificuldade da espessa litofera oceânica subductar sob a América do Sul.

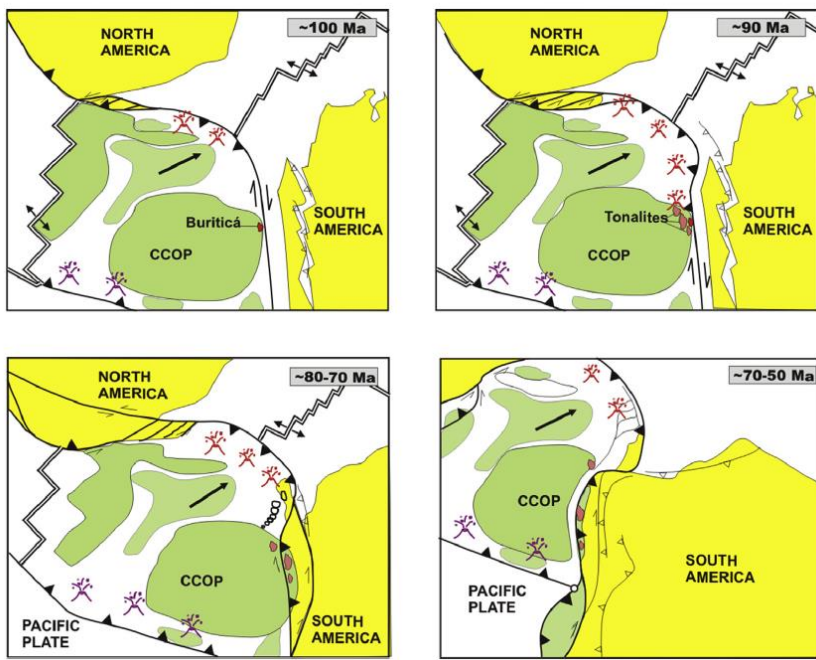


Figura 1.3. Migração da placa do Caribe entre o Cretáceo e o Paleoceno. O plateau oceânico do Caribe-Colômbia (CCOP) colide com o continente Sulamericano em trono de 75 Ma favorecendo a acresção de terrenos oceânicos na borda noroeste da Placa Sul-americana. Dioritos, tonalitos e granodioritos (triângulo vermelho) formados por subducção foram originados tanto em arco oceânico como continental (modificado de Weber *et al.*, 2015).

1.2.2. Magmatismo Meso-Cenozóico na Cordilheira Central

O magmatismo resultante da complexa evolução tectônica acima mencionada tem sido relativamente pouco explorado, particularmente na Colômbia. Uma compilação e síntese das idades radiométricas do magmatismo cálcio-alcalino Meso-Cenozóico foi apresentado por Aspden *et al.* (1987). A cronologia do magmatismo, entretanto, está fundamentada no método K-Ar que, além da imprecisão inherente ao sistema isotópico, foi aplicado em corpos que aparecam ter sofrido sucessivos eventos de reaquecimento, o que limita, portanto a interpretação dos dados. Trabalhos mais sistemáticos com base em modelos da evolução magmática que reunem dados petrológicos, geoquímicos, geocronológicos e tectônicos foram desenvolvidos em áreas do Equador e Colômbia (Villagómez *et al.*, 2011; Cochrane *et al.*, 2014b) embora poucos corpos magmáticos dos Andes da Colômbia tenham sido estudados em detalhe. As únicas exceções são os plútões eocênicos de Santa Marta e Parashi situados no Caribe Colombiano: (Tschanz *et al.*, 1974; Duque, 2009; Cardona *et al.*, 2011a). Outro batólito bem estudado é o Antioqueño, notadamente sua petrografia (Feininger & Botero, 1982), e ainda sobre o qual estão localmente disponíveis dados radiométricos e geoquímicos (Ordóñez & Pimentel, 2001; Ibañez-Mejia *et al.* 2007; Restrepo-Moreno *et al.* 2007; Ordóñez-Carmona *et al.* 2007; Leal-Mejia, 2011). Os dados do batólito Antioqueño, porém

foram disponibilizados apenas em apresentações de congressos e ainda não foram discutidos e integrados dentro de um modelo coerente. Estudos regionais que também trazem novos dados isotópicos e geoquímicos de diferentes plút ons Meso-Cenoz óicos podem ser encontrados nos trabalhos de Villag ómez *et al.* (2011), Bayona *et al.* (2012), Cochrane *et al.* (2014b) e Spikings *et al.* (2015). Destaca-se ainda o trabalho de Leal-Mejia (2011), que propôs um modelo para a evolução metalogenética na Colômbia durante o Fanerozoico.

Os dados geoquímicos disponíveis sugerem para a Cordilheira Central um ambiente tectônico de subducção em regime de extensão no back-arc e intra-ar do Jurássico Inferior até o Cretáceo Inferior (Aspden *et al.*, 1987; Bayona *et al.*, 2006; Bustamante *et al.*, 2010; Villag ómez *et al.*, 2011). A evolução do magmatismo neste período tem sido relacionado a migração de arco para o oceano devido ao mecanismo de slab-roll back da placa descendente (Cochrane *et al.*, 2014b). Contudo, este modelo vem sendo questionado pela possível translação de terrenos situados em latitudes mais ao sul, o que poderia ter justaposto diferentes domínios jurássicos na mesma latitude (Bayona *et al.*, 2006). Além disso, evidências para uma fase compressiva associada a metamorfismo regional no Jurássico Superior têm sido documentadas na encaixante ocidental do batólito de Ibagué (Blanco-Quintero *et al.*, 2014). As idades U-Pb em zircão de rochas plutônicas forneceram para o magmatismo uma idade entre ~190 e 145 Ma (Bustamante *et al.*, 2010; Villag ómez *et al.*, 2011; Leal-Mejia, 2011; Álvarez-Galindez, 2013; Cochrane *et al.*, 2014b).

Diferentes autores reconheceram a ausência do registro plutônico (na Cordilheira Central) ao final do Jurássico e início do Cretáceo. Aspden *et al.* (1987) reportam um hiato no magmatismo entre 142 e 124 Ma, o qual relacionaram a um ângulo baixo entre a subducção da placa oceânica sob a continental. Além disso, os dados mais recentes de Villag ómez *et al.* (2011) não registram a presença de rochas magmáticas com idades em torno de 145 Ma, o que foi relacionado à acresção de *seamounts* atualmente preservados no embasamento da Cordilheira Central (*i.e.*, Complexo Quebradagrande). Outra possibilidade seria a de um regime de convergência extremamente oblíquo ao final do Jurássico, o que impediria a geração do magmatismo de arco (Kennan e Pindell, 2009). Uma situação similar é reportada nos Andes do Equador com a ausência de registro de magmático no Cretáceo Inferior (Chiaradia *et al.*, 2009). O ressurgimento do magmatismo de arco continental na margem NW da Colômbia é marcada pelo Batólito Antioqueño em torno de 90 Ma, o qual tem sido relacionado à subducção do proto-Caribe (Iba ñez-Mejia *et al.*, 2007; Ordóñez-Carmona *et al.*, 2007; Leal-Mejia *et al.*, 2010; Villag ómez *et al.*, 2011). Esse magmatismo continuou durante

o Paleogeno, mas como produto da subducção do *plateau* do Caribe sob a margem NW da placa Sul-Americana. Os corpos magmáticos intrudem uma zona relativamente estreita na Cordilheira Central e Ocidental (Montes *et al.*, 2012; Bayona *et al.*, 2012), com algumas manifestações restritas no oeste da Colômbia (Bayona *et al.*, 2012). Também no Caribe Colombiano, especialmente nas regiões de Santa Marta e Guajira, afloram plútuns eocênicos que resultaram da subducção da Placa do Caribe (Cardona *et al.*, 2011; Cardona *et al.*, 2014). Segundo o registro de idades U-Pb em zircão, o magmatismo cessa no Eoceno Meio possivelmente devido a dificuldade de subductar a espessa litosfera do *plateau* do Caribe. O "bloqueio" da subducção favoreceria a convergência oblíqua da placa do Caribe bem como a mudança no regime de deformação ao longo do arco para francamente transpressivo (Bayona *et al.*, 2012; Kennan e Pindell, 2009).

Nesta tese propõe-se um modelo alternativo para a evolução tectono-magmática dos Andes Colombianos entre o Jurássico e o Eoceno. Incluímos uma discussão sobre embasamento do arco magnético da Cordilheira Central cujas implicações tectônicas se estendem até o Equador. São apresentados novos dados isotópicos U-Pb e Hf em zircão, geoquímica em rocha total e isótopos de Sr, Nd, Pb e Hf em rocha total de diferentes plútuns localizados na Cordilheira Central da Colômbia. O estudo do embasamento permitiu rediscutir a validade do modelo de "terrenos alóctones" para os Andes Colombianos proposto por Toussaint e Restrepo, (1988) e Restrepo *et al.*, (2011). Os resultados mostram que a Falha Otú-Pericos separa o embasamento Permo-Triássico (anteriormente considerado de idade Grenvilliana) de um cinturão metamórfico Jurássico até e tão desconhecido na Cordilheira Central (Capítulo 2).

Este embasamento Permo-Triássico a leste da Falha Otú Pericos encontra-se intrudido pelo magmatismo Jurássico. Embora o arco continental esteja relacionado à subducção da placa Farallón (Aspden *et al.*, 1987), o mecanismo tectônico que originou os magmas é ainda controverso. Cochrane *et al.* (2014b) propuseram que o arco magnético migrou para o oceano através do *slab roll-back* da litosfera oceânica, com plutonismo terminando em ~145 Ma. Nossos dados sugerem que o mecanismo de *slab roll-back* pode ter contribuído com o magmatismo apenas no início do processo com a subducção da mistura de sedimentos e basaltos favorecendo a fusão da cunha mantélica. O regime de subducção evoluiria sob uma componente progressivamente oblíqua entre 145 e 129 Ma, após o que o registro magnético é bruscamente interrompido (Capítulo 3).

O magmatismo de arco retorna na Cordilheira Central em torno de 90 Ma com a interação entre as placas do Caribe e Sul-América. São apresentados aqui novos dados geoquímicos e isotópicos dos plútões eocênicos da Cordilheira Central. O modelo geodinâmico proposto considera uma diferenciação de magmas em regime de alta pressão em coerência com o espessamento da crosta após a colisão de arco oceânico e continente no Paleógeno (Capítulo 4). Zircões detriticos de bacias situadas no leste da Colômbia mostram idades U-Pb eocênicas com composições de Hf comparáveis aos da Cordilheira Central (Bayona *et al.*, 2012). Finalmente, investigamos o mecanismo de colocação do batólito Santa Marta situado no Caribe Colombiano (Capítulo 5). As estruturas magnáticas do batólito são consistentes com o deslocamento para norte-nordeste (relativo à América do Sul) da placa do Caribe. Nesse contexto, o arco se deformou localmente em um regime cisalhante extensional favorecendo a ascenção de magmas. O *flat slab* que caracterizou este período foi determinante para que o desaparecimento do magmatismo no Eoceno Superior.

1.3. JUSTIFICATIVA E OBJETIVOS

As incertezas quanto à duração do magmatismo Meso-Cenozóico da Colômbia, a natureza da fonte, os processos geoquímicos e petrologicos dos magmas e as características de suas rochas encaixantes, devem ser mais bem exploradas com o estudo sistemático de plútões representativos no tempo geológico. Com isso, procuramos refinar os modelos de subducção e suas possíveis variações que marcaram a margem oeste da Colômbia.

Diante do exposto os objetivos desta tese são:

- Determinar a idade de cristalização e duração do magmatismo granítico através do estudo geocronológico utilizando o método U-Pb (LA-ICP-MS) em zircão;
- Definir o ambiente de formação e fonte dos diferentes magmas mediante análises geoquímicas de rocha total e análises isotópicas de Hf em zircão e de Sr, Nd, Hf e Pb;
- Precisar a natureza do embasamento do plutonismo Jurássico e suas correlações regionais, particularmente investigando as características geológicas dos cinturões Grenvilliano e Permo-Triássico da Cordilheira Central;
- Reconstruir a evolução tectônica da margem convergente entre o Jurássico e o Eoceno na perspectiva o plutonismo de arco.

1.4. MATERIAIS E MÉTODOS

Para atingir os objetivos propostos nesta tese de doutorado foram utilizados dados geoquímicos (elementos maiores e traços), isótopos de Sr, Nd, Pb e Hf em rocha total, e geocronologia U-Pb combinado a isótopos de Hf em zircão. Uma descrição geral destes métodos é apresentada a seguir. Informações adicionais podem ainda ser encontradas nos artigos que formam os Capítulos 2 a 5. Os dados geoquímicos e geocronológicos apresentados nesta tese foram obtidos nos laboratórios da Washington State University.

1.4.1. Geoquímica em rocha total

As características compostionais das rochas ígneas plutônicas são controladas pela natureza das fontes (crosta e/ou manto), proporção ou o grau da fusão e possível participação dos fluidos, e os processos de diferenciação e contaminação posteriores. As fontes, por sua vez, apresentam variações compostionais relacionadas com o reservatório mantélico, o tipo de rocha e a profundidade onde ocorre a fusão (Faure & Mensing, 2005). Esta complexidade pode se analisada mediante a integração da modelagem geoquímica (elementos maiores e traços) e isotópica, com uma apropriada temporalização do magmatismo e os elementos geológicos regionais.

Análises de elementos maiores, menores e traço em amostras de rocha total foram realizados mediante as técnicas e XRF (*X-Ray Fluorescence*) e ICP-MS (*Inductively Coupled Plasma Mass Spectrometry*). A informação geoquímica foi utilizada para classificação, discriminação e comparação das rochas através da construção de diagramas discriminatórios (Rollinson, 1993), que por sua vez fornecem informações sobre a evolução do magmatismo de arco.

As amostras selecionadas foram trituradas com um britador de mandíbula e pulverizadas utilizando um moinho de carboneto de tungstênio. Os elementos maiores e traços foram analisados com um espectrômetro *Rigaku 3370 XRF*. Detalhes da preparação de amostras, diluição e dos procedimentos analíticos para a obtenção dos elementos maiores e traços mediante fluorescência de raios X são descritos em Johnson *et al.* (1999). Para os elementos terras raras foram usados 2 g de amostra num cadiño de grafita misturados com 2g de LiBO₂, os quais foram fundidos a 1000 °C por 30 minutos. A pérola resultante foi moída num moino de aço e 0,25 mg e foi dissolvida usando HNO₃ (2 ml), HF (6 ml) e HClO₄ (2 ml) a 110 °C. As soluções da amostra foram aspiradas num ICP-MS (*Perkins-Elmer Elan 6000*) para determinação dos elementos traços, especialmente os elementos terras raras.

1.4.2. Geocronologia U-Pb LA-ICP-MS em zircão

A geocronologia pelo método U-Pb em monocrystalis de zircão foi utilizada com o intuito de estabelecer a idade de cristalização magmática. Este método baseia-se na capacidade do Urânio (U) de substituir ao zircônio (Zr) na estrutura cristalina do zircão (cf. Dickin, 1995) via decaimento radioativo. A transformação dos isótopos de U em Pb combinado à determinação das razões isotópicas do sistema pai-filho no espectrômetro de massa permite a definição da idade do mineral portados desses elementos.

O método do LA-ICP-MS (*Laser Ablation Inductively Coupled Plasma Mass Spectrometry*) permite realizar análises *in-situ* em monocrystalis de zircão em segmentos entre 20-30 µm (Gehrels *et al.*, 2008). O princípio do método consiste no ataque ao monocrystal por um laser a gás que gera partículas por abrasão e as transporta a um espectrômetro de massa acoplado a um plasma, onde é possível realizar a quantificação isotópica. Em rochas plutônicas normalmente são analisados cerca de 20 cristais, dos quais se obtêm idades concordantes que podem representar a idade de cristalização da rocha. Porém, em alguns casos, estas idades podem corresponder à herança isotópica relacionadas com as fontes.

A totalidade das análises realizadas para obter as idades de cristalização foram obtidas com um feixe de 30 µm diâmetro e uma razão de repetição de 10 Hz num laser *New Wave Nd-YAG UV 213-nm* acoplado a um coletor *ThermoFinnigan Element 2*. Cada dado consistiu em uma análise em branco seguida de 300 varreduras por meio de massas 204, 206, 207, 208, 232, 235 e 238, num tempo de aproximadamente de 35 segundos. O padrão usado foi o Plešovice com uma idade $^{206}\text{U}/^{238}\text{Pb}$ de 337.13 ± 0.37 Ma. (Sláma *et al.*, 2008), e as correções de Pb foram feitas segundo o método ^{207}Pb (Williams, 1998). Finalmente, os dados de U-Pb foram reduzidos segundo Chang *et al.* (2006) e as idades calculadas com *Isoplot 4.15* (Ludwig, 2003).

1.4.3. Isótopos de Nd, Hf, Pb e Sr

A aplicação dos isótopos de Sr, Nd, Pb e Hf na determinação da composição isotópica inicial das rochas ígneas permite reconstruir a evolução dos magmas desde a fonte até os processos que os modificaram (mistura e/ou contaminação) (Dickin, 1995; Faure & Mensing, 2005). Com esta análise integrada, é possível reconhecer a participação do manto, da crosta superior e inferior e sua evolução magmática, além da composição da crosta subjacente (Faure & Mensing, 2005).

O sistema Sm-Nd deve-se principalmente à habilidade dos elementos terra raras (no caso Sm e Nd) de residirem em vários minerais formadores de rochas, como o plagioclásio, os minerais máficos, allanita, zircão e apatita. O método é baseado na variação da composição isotópica do Nd pelo decaimento do ^{143}Nd e pelo fracionamento de Sm e Nd no processo de diferenciação magmática (De Paolo, 1988). A comparação entre a razão $^{143}\text{Nd}/^{144}\text{Nd}$ com o reservatório *CHUR* representativo da Terra primitiva, permite definir um indicador petrogenético denominado ε_{Nd} , o qual, ao ser determinado para a idade de cristalização de uma rocha ígnea, permite definir a contribuição das fontes mantélicas ou crustais na gênese do magma.

Paralelamente, os isótopos de Hf tem um significado similar aos isótopos de Nd visto que o sistema Sm-Nd é análogo ao sistema Lu-Hf durante a fusão. Neste caso, a determinação do ε_{Hf} baseia-se na comparação entre a razão $^{176}\text{Hf}/^{177}\text{Hf}$ com o reservatório *CHUR*. Os isótopos de Hf são determinados em rocha total ou em zircão, o que tem a vantagem de permitir conhecer a composição isotópica do mesmo ponto onde foi datado o grão. O zircão que pode ser datado pelo método U-Pb, igualmente permite incorporar Hf em sua estrutura cristalina, rejeitando o Lu. Desta forma o Hf inicial que se encontra nestes zircões reflete a composição do magma original antes da cristalização do zircão e, portanto, poderia refletir características específicas do manto do qual o Hf derivou-se ou a contribuição de crosta continental (Kinny & Maas, 2003; Dickin, 2005).

O Pb tem três isótopos radiogênicos que se formam pela desintegração radioativa do U e Th. As razões isotópicas do Pb registram os diferentes ambientes onde residiu esse elemento. Os reservatórios de Pb que podem ser reconhecidos incluem a crosta inferior, o manto e a crosta superior. Esses reservatórios podem misturar-se durante uma orogênese, originando um sinal particular que reflete a idade e os processos de evolução tectônica, o qual pode ser característico de um domínio crustal não exposto (Aitcheson *et al.*, 1995).

A sistemática isotópica do Sr deve-se a desintegração radioativa do ^{87}Rb em ^{87}Sr . A relação isotópica inicial de $^{87}\text{Sr}/^{86}\text{Sr}$, determinada para a idade de cristalização, constitui um indicador petrogenético que permite distinguir nas rochas magmáticas a presença de materiais do manto ou da crosta superior durante a gênese da rocha (fonte) ou adquiridos em processos posteriores (contaminação).

As análises desses isótopos foram realizadas num *Multicoletor Thermo-Finnigan Neptune*. Os isótopos de Sr, Nd e Hf em rocha total foram obtidos dissolvendo 250 mg de rocha pulverizada com uma mistura 10:1 de HF e HNO₃ a 150 °C em bombas de Teflon

seladas durante 7 dias. Depois desse processo foi usada uma mistura dos traçadores ^{149}Sm – ^{150}Nd e ^{176}Lu – ^{180}Hf . Lu-Yb e LREE foram separados em colunas de troca catiônica (*AG 50W-X8 resin*). A purificação de Hf foi realizada segundo os procedimentos de Münker *et al.* (2001), Lu foi separado de Yb segundo (Vervoort *et al.*, 2004) e Sm e Nd foram preparados com os procedimentos de Vervoort & Blichert-Toft (1999).

O Nd foi corrigido por fracionamento de massas usando $^{146}\text{Nd}/^{144}\text{Nd}=0,7219$ e normalizado usando um padrão Ames Nd, enquanto o Sm foi corrigido usando $^{147}\text{Sm}/^{152}\text{Sm}=0,56081$. Sr foi corrigido usando $^{86}\text{Sr}/^{88}\text{Sr} = 0,1194$ e normalizado usando o padrão *NBS-987*. As medições de Lu foram obtidas segundo o método de Vervoort *et al.* (2004). A reprodutibilidade media com dois desvios padrão é de $\pm 0,000020$ para o padrão Ames Nd e de $\pm 0,000014$ para o padrão *JMC-475*, e para o $^{87}\text{Sr}/^{86}\text{Sr}$ é de $\pm 0,00005$. Os valores de ϵ_{Nd} foram calculados usando valores presentes de $^{143}\text{Nd}/^{144}\text{Nd} = 0,512630$ e $^{147}\text{Sm}/^{144}\text{Nd} = 0,160$ para o *CHUR* (Bouvier *et al.*, 2008), e para o ϵ_{Hf} usando valores presentes de $^{176}\text{Hf}/^{177}\text{Hf} = 0,282785$ e $^{176}\text{Lu}/^{177}\text{Hf} = 0,0336$ para o *CHUR* (Bouvier *et al.*, 2008). Valores isotópicos iniciais foram calculados usando concentrações de Rb e Sr do *XRF* para os isótopos de Sr.

Isótopos de Pb foram obtidos dissolvendo 250 mg de rocha pulverizada em bêquer de 15 ml selados com uma mistura 10:1 de HF e HNO_3 a 120 °C por 24 horas. O Pb foi separado usando uma resina Bio Rad AG1-X8 e medido segundo o método de White *et al.* (2000). O padrão usado foi *NBS-981* com uma concentração de 150 ppb de Pb e 30 ppb de Tl (Galer e Abouchami, 1998).

Para as análises de isótopos de Hf em zircão foi usado um diâmetro de feixe de 40 μm . O sinal de Hf esteve entre 2 e 6 V, e para melhorar sua sensibilidade, foi usado o gás He com pequenas quantidades de N_2 para minimizar a formação de óxidos. Os dados foram obtidos com integrações de 60 segundos. Para obter as idades modelo do manto empobrecido para o Hf, foram usadas as razões $^{176}\text{Hf}/^{177}\text{Hf}$ e $^{176}\text{Lu}/^{177}\text{Hf}$ para grãos individuais de zircão, e assim determinar as razões $^{176}\text{Hf}/^{177}\text{Hf}$ iniciais para sua idade de cristalização. A curva de evolução de Hf para o manto empobrecido foi calculada com valores presentes de $^{176}\text{Hf}/^{177}\text{Hf}$ $\text{DM}_{(0)}=0,283240$ e $^{176}\text{Lu}/^{177}\text{Hf}$ $\text{DM}_{(0)}=0,03979$ (Vervoort *et al.*, 2015).

1.4.4. Anisotropia de Suscetibilidade Magnética

A estrutura de rochas ígneas, e consequentemente os processos de deformação sin-magmática, podem ser investigados através da Anisotropia de Susceptibilidade Magnética

(ASM; eg. Hrouda, 1982; Borradaile e Henry, 1998). A suscetibilidade magnética é uma propriedade física que relaciona o campo magnético indutor (H) e a magnetização resultante (M). A suscetibilidade magnética (k) é o parâmetro que relaciona M e H , de maneira que $M = k \cdot H$. A susceptibilidade magnética pode ser entendida com a medida do quanto facilmente o material adquire uma magnetização. A anisotropia de susceptibilidade nos materiais rochosos, por sua vez, refere-se à variação direcional da susceptibilidade magnética (e de M). Por outro lado se a susceptibilidade magnética é constante em qualquer ponto da rocha, o material é considerado magneticamente isotrópico.

As rochas ígneas são essencialmente formadas por silicatos, podendo ainda conter óxidos e, mais raramente, sulfetos. Esses minerais apresentam propriedades magnéticas que os distinguem em diamagnéticos, paramagnéticos e ferromagnéticos (*s.l.*). Os minerais diamagnéticos, como o quartzo e o feldspato, exibem uma suscetibilidade muito fraca e negativa (c. -10^{-5} SI). Os paramagnéticos, representados pela mica, anfibólio e piroxênio, possuem suscetibilidade positiva da ordem de 10^{-4} a 10^{-3} SI. Magnetita, hematita e ilmenita são os principais óxidos das rochas ígneas félsicas (Ishihara, 1977). A magnetita possui suscetibilidade da ordem de 10^{-1} a 2 SI e, como a pirrotita, apresenta magnetização espontânea. A hematita é antiferromagnética (sem magnetização espontânea) com suscetibilidade da ordem de 10^{-3} SI. A magnetita e a hematita apresentam o fenômeno da remanência, propriedade que é explorada nas investigações paleomagnéticas. Os sulfetos em geral ocorrem como traço nas ígneas intermediárias e félsicas, de forma que contribuição deles à suscetibilidade total é irrelevante.

Em plátanos graníticos a magnetita é o principal mineral magnético. Embora presente como mineral acessório, sua forte suscetibilidade faz com que mesmo pequenas quantidades (1 a 3 % da massa nos granitoides) sejam suficientes para que as propriedades magnéticas da rocha (suscetibilidade, remanência, anisotropia) sejam controladas pela magnetita. Na ausência de magnetita a suscetibilidade magnética vai depender principalmente dos minerais paramagnéticos que, geralmente, estão em volume suficiente para suplantar a contribuição da ilmenita e dos eventuais sulfetos. A ASM nos granitoides com magnetita depende, portanto, da orientação preferencial dos grãos de magnetita. A direção de maior suscetibilidade é denominada de lineação magnética enquanto o plano normal à direção de menor suscetibilidade denominada foliação magnética (eg. Bouchez, 1997). Na ausência de magnetita a anisotropia de suscetibilidade é geralmente fornecida pela orientação preferencial dos minerais paramagnéticos. A distribuição planar da mica normalmente define a foliação

magnética, enquanto a lineação magnética depende da trama plano-linear de mica e do anfibólio. A magnetita, no entanto, nunca está totalmente ausente do agregado mineral. Muitas vezes ela forma finas inclusões no interior dos silicatos decorrente dos processos de exsolução e/ou alteração hidrotermal que ocorrem nos estágios finais da cristalização magmática. A determinação da orientação preferencial desses grãos pode ser feita através de técnicas que exploram a anisotropia de remanência da magnetita (Jackson, 1991).

Diferentes métodos de investigação vêm demonstrando a boa correlação entre as direções principais de ASM e a trama magmática. Os resultados confirmam o uso da ASM como marcador da direção da foliação e lineação de rochas ígneas intermediárias e félsicas. Essas informações são essenciais na investigação dos processos de alojamento e deformação dos corpos magmáticos e de suas relações com a tectônica regional.

Capítulo 2

U-Pb ages and Hf isotopes in zircons from Para-Autochthonous Mesozoic terranes in the western margin of Gondwana: implications for the terrane configurations in the Northern Andes¹

ABSTRACT

U-Pb LA-ICP-MS ages and Hf isotopes in zircons were used to constrain the nature of the basement of the Central Cordillera of Colombia. Graphite-quartz-muscovite schists show detrital zircons supplied mostly from Late Jurassic (c. 167 Ma), Ediacaran (c. 638 Ma) and Tonian ('Grenvillian'; c. 1.000 Ma) sources. These marine volcanosedimentary deposits form a N-trending metamorphic belt in fault contact to the east with orthogneisses and amphibolites of the Tierradentro unit. Zircon U-Pb determinations of the Tierradentro rocks, previously interpreted as Grenvillian basement slices, provided crystallization ages between 268 and 240 Ma. Initial Hf data reveal that the Tierradentro unit share isotopic characteristics similar to others Permo-Triassic rocks of the Central Cordillera. In contrast, detrital zircons from the Jurassic metasedimentary rocks suggest that their sources are distinct from the Central Cordillera and nearby Jurassic magmatic rocks. Large xenoliths of the Tierradentro unit within the Ibagué batholith indicate that the granodioritic magma intruded mostly a Permo-Triassic basement possibly by exploring the Otú-Pericos fault. The Jurassic metasedimentary belt is correlated further south with a similar sequence in the Ecuadorian Andes.

¹ Bustamante, C., Archanjo, C., Cardona, A., Bustamante, A., Valencia, V., Vervoort, J. U-Pb ages and Hf isotopes in zircons from Para-Autochthonous Mesozoic terranes in the western margin of Gondwana: implications for the terrane configurations in the Northern Andes. *The Journal of Geology* (Under review).

2.1. INTRODUCTION

Continental margins are modified by the accretion of oceanic and continental terranes during subduction. While the allochthonous origin of oceanic terranes can be recognized by their particular tectonostratigraphic record, identifying continental terranes as transferred from another continental margin (allochthonous) or formed at the same continental margin and transferred by along-strike translation (i.e. para-autochthonous) may be more complicated (Howell, 1995).

The Northern Andean Belt evolved by incorporating continental and oceanic crustal fragments accreted to the margin of South America by strike-slip faults and subduction zones, with the main periods of accretion occurring mostly in the Permo-Triassic, Jurassic and Late Cretaceous (Ramos, 2009). The Permo-Triassic events have been recently characterized as related to continental rifting and anatexis associated to the break-up of Western Pangea (Cochrane et al., 2014a). In the Jurassic the former rifted margin was intruded by continental arc batholiths characterized in their earlier phases by a significant extensional signature (Sarmiento-Rojas et al., 2006; Cochrane et al., 2014b), while the interactions of the Caribbean, Pacific and South American plates in the Cretaceous lead to the bulk compression of the continental margin, accretion of oceanic rocks and lateral migration of crustal blocks along strike-slip faults (Bayona et al., 2006; Pindell and Kennan, 2009; Spikings et al., 2015).

Restrepo and Toussaint (1988) and Restrepo et al. (2011) adopted the tectonostratigraphic terrane model of Howell et al. (1983) to divide the accretionary sequences of the Colombian Andes in four major terranes. They comprise an allochthonous Eastern Andean or Chibcha terrane adjacent to the Precambrian Guiana and Amazonian shields separated by other allochthonous units grouped in the Central and Western Cordilleras (Fig. 2.1). In the Central Cordillera they recognized a Late Paleozoic to Triassic Tahamí terrane bounded to the east by the Otú-Pericos fault. Further west and south, the Tahamí and Chibcha terranes are in contact with Cretaceous oceanic terranes (Calima, Cuna) that form the Western Cordillera. The Central and Western Cordilleras are in contact along the Cauca-Romeral fault system that includes slices of medium- to high-pressure metasedimentary and metavolcanic rocks grouped, respectively, in the Arquia and Quebradagrande complexes (Fig. 2.1; Maya and González, 1995; Villagómez et al., 2011). This suture zone has been connected further south with the Peltetec fault zone that forms the western limit of the Permian to Jurassic rocks of the Cordillera Real in Ecuador (Ramos, 2009; Spikings et al., 2015).

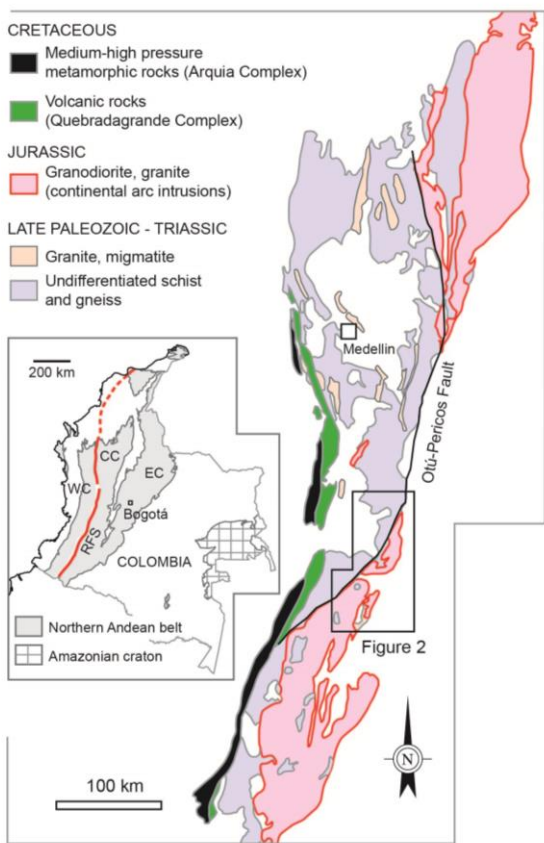


Figure 2.1. Geology of the Central Cordillera (CC) in Colombia and Cordillera Real in Ecuador, showing the distribution of Cretaceous metamorphic and volcanic rocks, Jurassic continental arc intrusions: Abitagua (AB), Ibagué (IB), Mocoa (MB) and Segóvia (SB) batholiths and Permo-Triassic rocks. Inset – Main geological domains of Colombia highlighting the location of the Western (WC) and Eastern (EC) Cordilleras.

The origin of these terranes, and particularly the age of tectono-magmatic events of the Tahami and Chibcha terranes have been intensely debated (Vinasco et al., 2006; Cardona-Molina et al., 2006; Restrepo et al., 2011; Martens et al., 2014; Blanco-Quintero et al., 2014; Spikings et al., 2015). According to Restrepo and Toussaint (1988) and Toussaint and Restrepo (1989), one of the major distinctions between Tahami and Chibcha terranes account for Permian metamorphic events just recorded in the former, and the Jurassic magmatism and sedimentation that would be found only in the Chibcha terrane (Restrepo et al., 2011). Jurassic metasedimentary rocks, however, have been identified in the Cordillera Real of Ecuador (Salado terrane) next to the Peltetec fault (Litherland et al., 1994; Spikings et al., 2015), although no Jurassic metasedimentary sequences have been recognized until now in the Central Cordillera of Colombia. Furthermore, Permo-Triassic gneisses have been recently identified to the east of the Otú-Pericos fault (Villagómez et al., 2011; Cochrane et al., 2014a), and a Jurassic metamorphism on rocks attributed to the Permian Cajamarca Complex

has been identified to the west of the Ibagué batholith (Blanco-Quintero et al., 2014). These recent results therefore challenge the identification of the Otú-Pericos fault as a terrane-related boundary and consequently the definition of Tahamí and Chibcha as allochthonous terranes based on the criteria outlined by Restrepo and Toussaint (1988).

Our study examines the geological evolution of units on both sides of the Otú-Pericos fault near the northern termination of the Ibagué batholith (Tolima Department). We present new zircon U-Pb LA-ICP-MS and Hf isotope data for orthogneisses and amphibolites from a geological unit known as Tierradentro sequence, and detrital zircons of pelitic schist from the Tahamí terrane. The Tierradentro sequence has been mapped as slices of Grenvillian rocks (ca. 1 Ga) that bound the Chibcha Terrane (Fig. 2.2). According to the geological map of Colombia (Gómez-Tapias et al., 2015), such gneisses and amphibolites also form kilometre-size enclaves interpreted as roof-pendants within the Ibagué batholith. In contrast, the pelitic schists have been correlated to the Cajamarca Complex. Our data show that the Tierradentro gneisses and amphibolites are not ‘Grenvillian rocks’ while the metapelites record a peak detrital zircon population at ca. 167 Ma. These results suggest that the Otú-Pericos fault may represent a more complicated structure, which seems to limit distinct sequences that were separated from the continental margin by major extensional faults. The new results also evidence the existence of Jurassic metasedimentary deposits in the Central Cordillera undocumented until now and the use of Hf isotopic signatures to discriminate the origin of contemporaneous magmatic rocks.

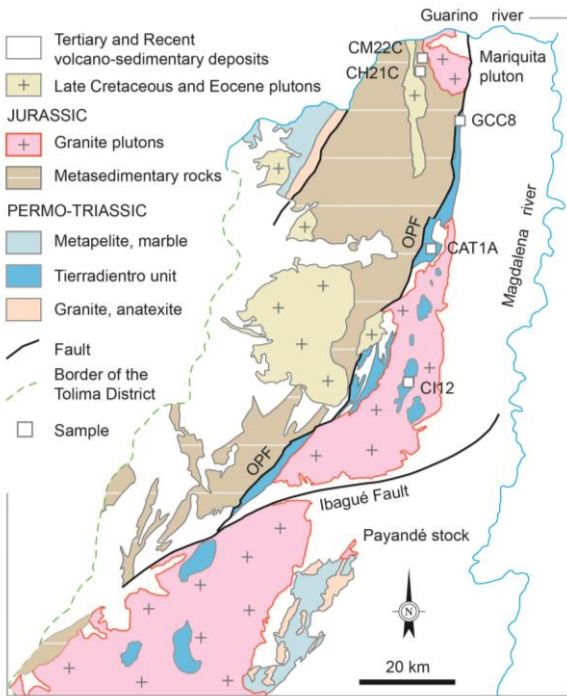


Figure 2.2. Detailed geological map of the study area, showing the samples distribution (squares) and the relations between the studied units.

2.2. GEOLOGICAL SETTING

The Andean Chain in Colombia is composed by three mountain ranges – the Western, Central and Eastern Cordilleras – separated from Amazonia craton by an extensive foreland basin (Fig. 2.1, inset). The Western Cordillera comprises allochthonous oceanic rocks that accreted to the continental margin since the Late Cretaceous (Kerr et al., 1997; Villagómez et al., 2011). These sequences were separated in the Calima and Cuna terranes, the later accreted to the continent in the Miocene (Restrepo et al., 2011). The Eastern Cordillera comprises a basement composed by Precambrian gneisses, granulites and amphibolites, Ordovician to Silurian granitoids that are covered by transitional siliciclastic and carbonate Paleozoic deposits (Kroonenberg, 1982; Restrepo-Pace et al., 1997; Cordani et al., 2005; Ordóñez-Carmona et al., 2006; Cardona-Molina et al., 2006; Van der Lelij et al., 2015). A major Late Carboniferous tectonic event has been discriminated based on a major Pennsylvanian hiatus and the existence of some angular discordance with the Permian (Toussaint, 1995).

They form the Chibcha terrane which is limited to the east by the Guaicáramo fault. Isolated Proterozoic inliers to the southeast of the Guaicáramo fault define the Andaquí terrane which is also considered as a prolongation of the continental margin (Ibañez-Mejia et al., 2011). In turn, the Central Cordillera consists of Permian to Triassic I-type magmatic

rocks, migmatites and amphibolites (Vinasco et al., 2006; Cochrane et al., 2014a; Spikings et al., 2015) grouped in the Cajamarca Complex, with an Ordovician protolith (Martens et al., 2104). The Permo-Triassic units of the Central Cordillera have been correlated in Central America with the Mexican terranes which were formed in a continental arc (Torres et al., 1999; Dickinson and Lawton, 2001). Further south in Ecuador, they were correlated with Triassic S-type granitoids and metamorphic rocks of the Loja Terrane in the Cordillera Real (Noble et al., 1997; Riel et al., 2013; Spikings et al., 2015).

The high- to medium grade rocks of the Cajamarca Complex intruded by Triassic S-type granitoids form the basement sequence of the Central Cordillera, with the age of its metamorphism varying from Mid- to Late Triassic (ca. 240-230 Ma; Vinasco et al., 2006; Restrepo et al., 2011; Cochrane et al., 2014a).

In the Ibagué area to the south of the Central Cordillera (Fig. 2.2) the metasedimentary rocks included in the Cajamarca complex are intruded by Jurassic to Cretaceous plutons (i.e. Ibagué batholith and Mariquita stock) and Eocene magmatic rocks. According to Blanco-Quintero et al. (2014), the peak metamorphic conditions determined in garnet-biotite schists reached 550-580 °C and 8 kbar while $^{40}\text{Ar}/^{39}\text{Ar}$ determinations in amphibole and phengite between 146 and 158 Ma defined the age of the peak metamorphic conditions. These Late Jurassic ages contrasted with previous Triassic metamorphism of the Cajamarca Complex, which lead Blanco-Quintero et al. (2014) to propose a distinct Late Jurassic collision-accretion event in the Central Cordillera.

The Tierradentro gneisses and amphibolites are exposed in the limit between the Tahami and Chibcha terranes and define the trace of the Otú-Pericos fault (Restrepo et al., 2011). These poorly studied rocks have been correlated with the Proterozoic basement of the eastern flank of the Central Cordillera (Kroonenberg, 1982; Restrepo-Pace et al., 1997) due to lithological similarities (Marquinez and Núñez, 1998; Núñez, 2001) and a K-Ar age of 1360 ± 270 Ma (Vesga and Barrero, 1978), and therefore have been included as part of the Chibcha Terrane. The Tierradentro unit is composed by discontinuous lenses of ortho- and paragneisses, amphibolites, minor granulites and marbles that form both the host-rocks and enclaves of the northern part of the Ibagué batholith (Fig. 2.2). The batholith shows zircon U-Pb ages ranging from 142 to 170 Ma (Villagómez et al., 2011; Leal-Mejía, 2011; Bustamante et al., 2016). The wall-rocks to the east of the batholith include Triassic limestones intruded by the Payandé stock (ca. 165 Ma, Bustamante et al., 2016). Anatexites close to the Payandé

stock provided zircon U-Pb ages of ca. 230 Ma, which is the first Triassic ages reported to the east of the Otú-Pericos fault (Cochrane et al., 2014a).

2.3. ANALITICAL METHODS

2.3.1. LA-ICP-MS U-Pb Geochronology in zircon

LA-ICP-MS U-Pb analyses were acquired in a New Wave Nd: YAG UV 213-nm laser coupled to a ThermoFinnigan Element 2 single collector, double-focusing, magnetic sector ICP-MS at the Washington State University. Laser spot size was 30 μm and repetition rate 10 Hz. He and Ar carrier gases delivered the sample aerosol to the plasma. Each analysis consisted of a short blank analysis followed by 300 sweeps in approximately 35 seconds, through masses 204, 206, 207, 208, 232, 235, and 238. A compilation of ages obtained in this study is presented in Tables 2.1 and 2.2.

Time-independent fractionation was corrected by normalizing U-Pb and Pb/Pb ratios of the unknowns to the zircon standards (Chang et al., 2006). For this study we used the zircon standard Plešovice, with a $^{206}\text{U}/^{238}\text{Pb}$ age of 337.13 ± 0.37 Ma (Sláma et al., 2008) with the common Pb corrections using the ^{207}Pb method (Williams, 1998). Uranium-lead data were reduced following Chang et al. (2006) and ages were calculated and plotted using Isoplot v. 4.15 of Ludwig (2003). The final crystallization ages that we report are Tuff Zircon ages.

2.3.2. Hf isotopes in zircon

Hf isotope geochemistry was investigated in 3 samples (Table 2.3) at the Geoanalytical Lab at Washington State University, in a ThermoFinnigan NeptuneTM MC-ICP-MS with 9 faraday collectors interfaced with a New WaveTM 213 nm UP Nd-YAG laser. Pulse rate of the laser was 10 Hz, fluence was of 10–12 J/cm² and laser spot size was 40 μm . Purified He plus small quantities of N₂ gases were used as carrier gases to minimize oxide formation and increase Hf sensitivity.

Analytical procedures and data treatment are detailed in Vervoort et al. (2004) and DuFrane et al. (2007). $^{176}\text{Hf}/^{177}\text{Hf}$ and $^{176}\text{Lu}/^{177}\text{Hf}$ were used to calculate Hf-depleted mantle model ages (Hf_{TDM}) for the individual zircon samples, in order to determine their initial $^{176}\text{Hf}/^{177}\text{Hf}$ ratios at their crystallization ages. Projection back from zircon crystallization was calculated using a present value of 0.0150 for the estimated $^{176}\text{Lu}/^{177}\text{Hf}$ of continental crust (Vervoort and Patchett, 1996; Goode and Vervoort, 2006). Present-day depleted mantle

values of $^{176}\text{Hf}/^{177}\text{Hf}$ DM₍₀₎=0.283240 and $^{176}\text{Lu}/^{177}\text{Hf}$ DM₍₀₎=0.03979 (Vervoort et al., 2015) were used to calculate the depleted mantle Hf evolution curve.

2.4. RESULTS

2.4.1. Tierradentro unit

The samples (see location in Fig. 2.1) of the Tierradentro unit comprise an orthogneiss (GCC8) and an amphibolite (CAT1A) exposed in faulted contact with micaschists, and an hornblende gneiss (CI12) that crops out as a roof pendant within the Ibagué batholith.

The hornblende gneiss (CI12) that forms a roof pendant within the Ibagué batholith is composed by plagioclase An₁₂ (39%), orthoclase (28%), quartz (22%), and hornblende (11%). The secondary phases are included as products of saussuritization and sericitization processes at the core and rims respectively in plagioclase grains. Prenhite occurs in veins cutting the sample and chlorite as a pseudomorphic phase after biotite. Accessory phases include zircon, apatite, titanite and opaque minerals. The gneiss shows a foliation defined by recrystallized quartz ribbons surrounded by hornblende and plagioclase. Quartz has sutured boundaries and undulatory extinction. The amphibole also appears as porphyroblasts with minor portions replaced by chlorite and calcite, mainly at the cleavage planes. Using mineralogical data it is possible to suggest that the sample reached the amphibolite facies and the protolith correspond to a quartz-feldspatic rock.

Zircons of the hornblende gneiss range from 70 to 300 μm in length. They are mainly subhedral normally with subrounded to rounded terminations. CL images record a faint oscillatory zoning close to the margin as well as in the center of some zircons (Fig. 2.3). Th/U ratios of the grain population vary from 0.21 to 1.04 (Table 2.1) suggesting they are magmatic zircons (Rubatto, 2002).

U-Pb analyses were performed in 79 zircons. After removing from the calculations two younger ages (c. 188 Ma) apparently with no geological significance and two older ages (280 and 287 Ma) possibly corresponding the inheritance, the analysis provided a $^{206}\text{Pb}/^{238}\text{U}$ mean age of 268.2 +1.9/-0.5 Ma (Fig. 2.4). There is no significant age difference between the U-Pb ages in cores and their respective rims in the zircons of the hornblende gneiss (see analytical results in Table 2.1). These results indicate that the zircons record the age of the igneous protolith and that they were not affected by late metamorphic events as suggested by the absence of overgrowths observed on CL images.

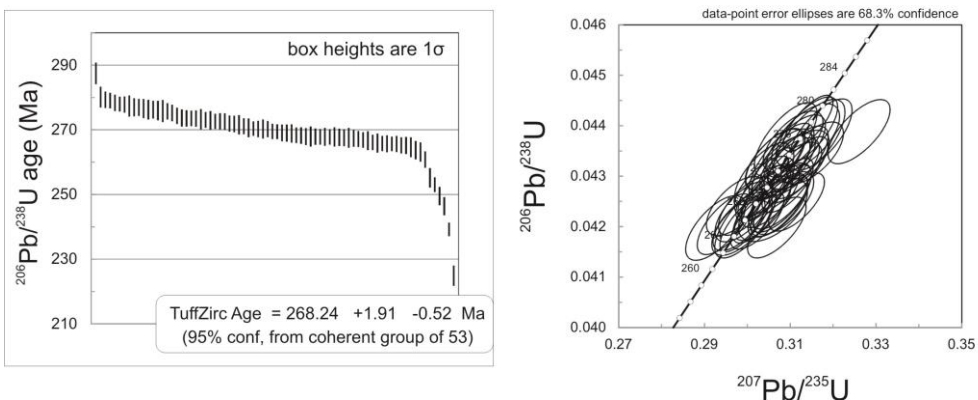


Figure 2.3. U-Pb ages and Concordia diagram obtained from zircon rims representing the crystallization age of the CI12 sample (Quartz-feldspathic-gneiss). Scale bar on CL image is 100 μm .

The amphibolite (CAT1A) is made up of hornblende (61%), plagioclase An₃₆ (27%) and quartz (12%). Secondary minerals include mainly muscovite as product of retrograde metamorphism of plagioclase and chlorite replacing hornblende. Normal zoning of plagioclase is detected by the saussuritization at the core and sericitization in the rims. Texturally the sample exhibit a nematoblastic texture defined by the hornblende crystals orientation, but several mylonitic textures are observed in recrystallized and mortar quartz and deformed plagioclase twins systems. Through the mineralogical analyses is determined the amphibolite facies and an intermediate protolith for the sample.

Zircons of this amphibolite sample are anhedral to subhedral, usually with rounded terminations but a few prismatic grains. Their sizes range from 60 to 250 μm in length (Fig. 2.4). CL images shows zircons usually with dark, U-rich cores rimmed by lighter rims (Fig. 2.3). A few grains, however, display light U-poor cores surrounded by darker rims. However, no significant differences were found in Th/U ratios and ages after analyzing cores and rims of the zircons.

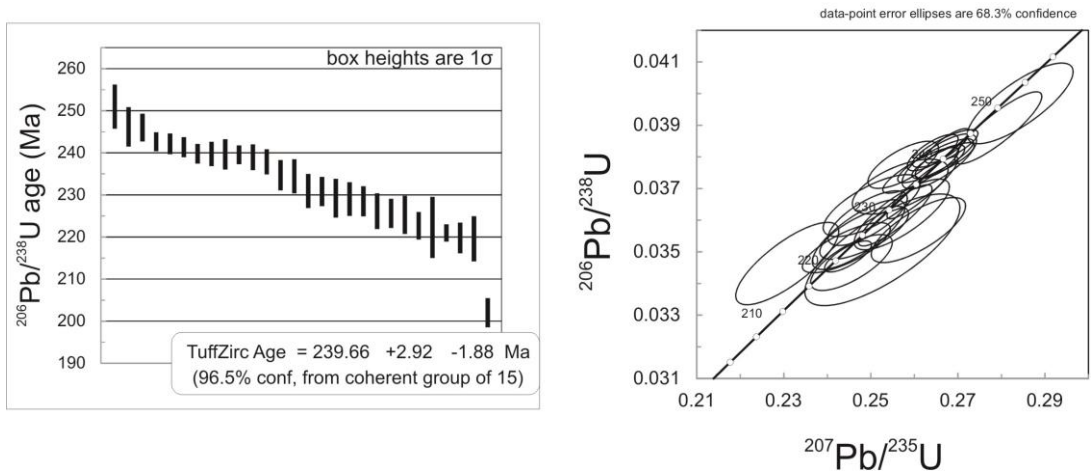


Figure 2.4. U-Pb ages and Concordia diagram obtained zircon rims representing the metamorphic age of the CAT1A sample (amphibolite). Scale bar on CL image is 100 μm .

Thirty zircons of the amphibolite (CAT1A) provided a $^{206}\text{Pb}/^{238}\text{U}$ mean age of 239.7 ± 2.9 -1.9 Ma (Fig. 2.5). The age calculation was obtained after discarding two zircons with older ages (ca. 330 Ma), possibly corresponding to inheritance, and one zircon with a younger age attributed to Pb loss. Th/U ratios are relatively low, ranging from 0.1 to 0.44 with a few grains with even lower values. The mean age is interpreted as the magmatic crystallization of the zircon which show Th/U ratios which are systematically higher than 0.1 (Rubatto, 2002).

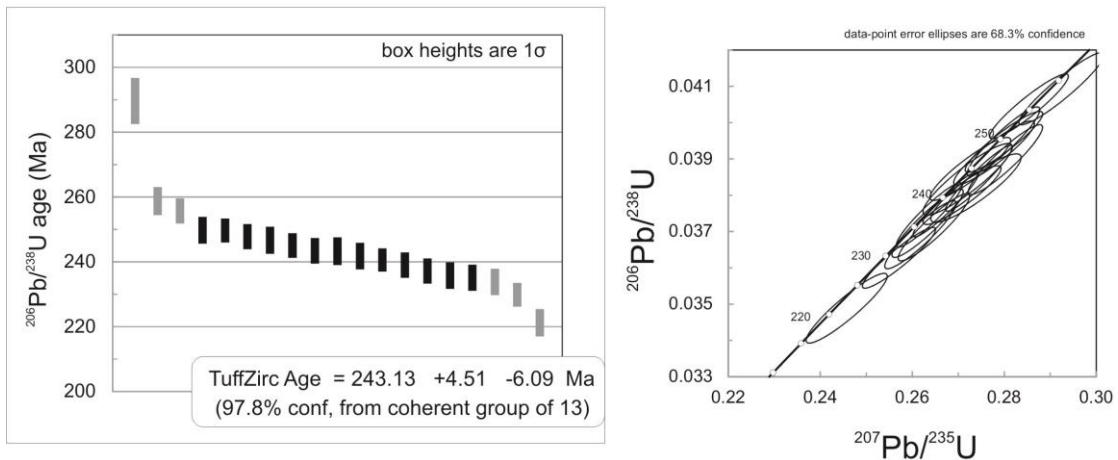


Figure 2.5. U-Pb zircon ages and Concordia diagram obtained from sample GCC8 (augen granodiorite) whose age is in the same range of sample CAT1A.

A mylonitized augen granodiorite (GCC8) was described in hand sample. It is composed by plagioclase (50%), quartz (20%), K-feldspar (15%), biotite (10%) and muscovite (5%). The latter associated to the main deformational fabric, whereas the K-feldspar is found as the augen phenocryst.

Nineteen zircons of the ortho-gneiss (GCC8) yielded a $^{206}\text{Pb}/^{238}\text{U}$ mean crystallization age of $243.1 \pm 2.5/-6.1$ Ma (Fig. 2.5). Two zircons with younger ages (221 and 230 Ma) and one zircon possibly corresponding to a xenocryst (c. 290 Ma) were removed from the mean age calculation.

2.4.2. Detrital zircons of the Tahamí terrane

Two schist samples were obtained from the Tahamí Terrane (see locations on Fig. 2.2). They possess intrusive relationships with the early cretaceous Mariquita Stock (CM22C) and the Eocene Hatillo Stock (CH21C). However, zircons were only obtained from sample CH21C and sample CM22C is described for reference.

Sample CH21C is graphite-quartz-muscovite schists. It is composed by muscovite (44%), quartz (34%), graphite (15%), biotite (3%), plagioclase (2%), and andalusite (2%). Accessories include apatite, zircon and opaque minerals. Tourmaline is found as a trace mineral. Schistosity is defined by oriented micas with recrystallized quartz, which form a granolepidoblastic texture. Decussate texture defined by biotite indicates a possible superimposed contact metamorphism event. Epidote and muscovite appears locally as an alteration product. With the mineral association of this sample it is possible to propose the greenschist facies and pelite sediment as the protolith for the analyzed sample.

Eighty seven zircons were extracted from the micaschist (Table 2.2) since the amphibole schist did not provide any zircon. The grains exhibit oscillatory zoning and have mainly subrounded to rounded terminations. Sizes range from 40 to 100 μm although a few crystals can reach $\sim 170 \mu\text{m}$ in length (Fig. 2.3). The analysis come from the sectors with oscillatory zoning usually next to the zircon margin; some analysis, however, were obtained in the cores to check the possible multistage evolution of the zircons.

Th/U ratios of the grain population range from 0.13 to 2.07, which are typical of magmatic zircons (Rubatto, 2002). Three zircons with Proterozoic ages have Th/U ratios of ~ 0.04 which suggest a metamorphic origin. The major zircon population, however, shows Middle Jurassic (~ 167 Ma) and Ediacaran (~ 638 Ma) ages with the youngest detrital zircon set at 162.5 ± 1.8 Ma. A few zircons display Paleozoic (Ordovician and Carboniferous),

Mesoproterozoic (Grenvillian) and Paleoproterozoic (Siderian and Statherian) ages (Fig. 2.6). Permo-Triassic zircons are represented, by one grain showing Triassic (~245 Ma) and other one grain with Permian (~281 Ma) concordant ages.

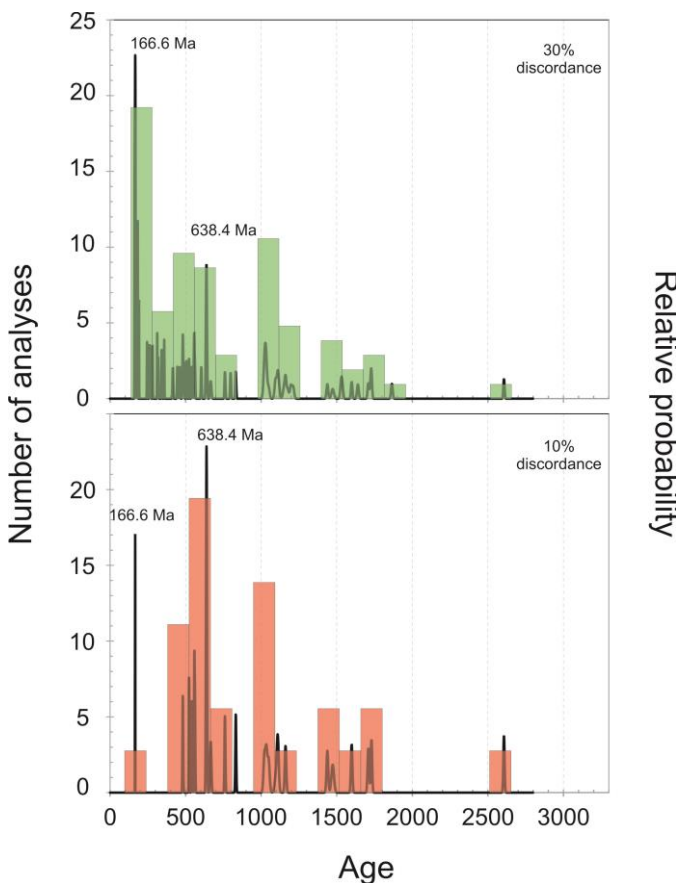


Figure 2.6. U-Pb detrital zircon results from the quartz-muscovite schist (CH21C), showing less than 30% discordance and less than 10% discordance for comparison.

Sample CM22C is a plagioclase-hornblende schists composed by hornblende (63%), plagioclase An₃₂ (25%), and quartz (10%). Clinzoisite veins crosscut the foliation, which is defined by alternating bands of recrystallized plagioclase-quartz and oriented hornblende. Several clinzoisite grains are also accompanying the foliation of the rock. Opaque minerals (2%) as ilmenite and magnetite are observed as disseminated phases in the sample. Fine-grain muscovite is also observed as a replacement product of plagioclase. These alternating bands, in turn, define a granonematoblastic texture in the rock. The mineralogical composition suggests that the sample was submitted to amphibolite facies and the protolith was an intermediate rock.

2.5. Hf ISOTOPE GEOCHEMISTRY

2.5.1. Tierradentro unit

Hf isotopes were measured in the rims of eight zircons from samples CI12 (hornblende gneiss) and CAT1A (amphibolite). Contrasting values were obtained on these samples. Initial ϵ_{Hf} values range from -0.1 to -2.5 for the ortho-gneiss, which suggest a crustal source for the protolith (Fig. 2.7). The amphibolite yielded initial ϵ_{Hf} values ranging from +9.2 to +10.9 indicating a mantle source for the protolith with values close to the depleted mantle curve (Fig. 2.7). Similar values were obtained by Cochrane et al. (2014a) in other Permo-Triassic localities of the Central Cordillera (Fig. 2.7).

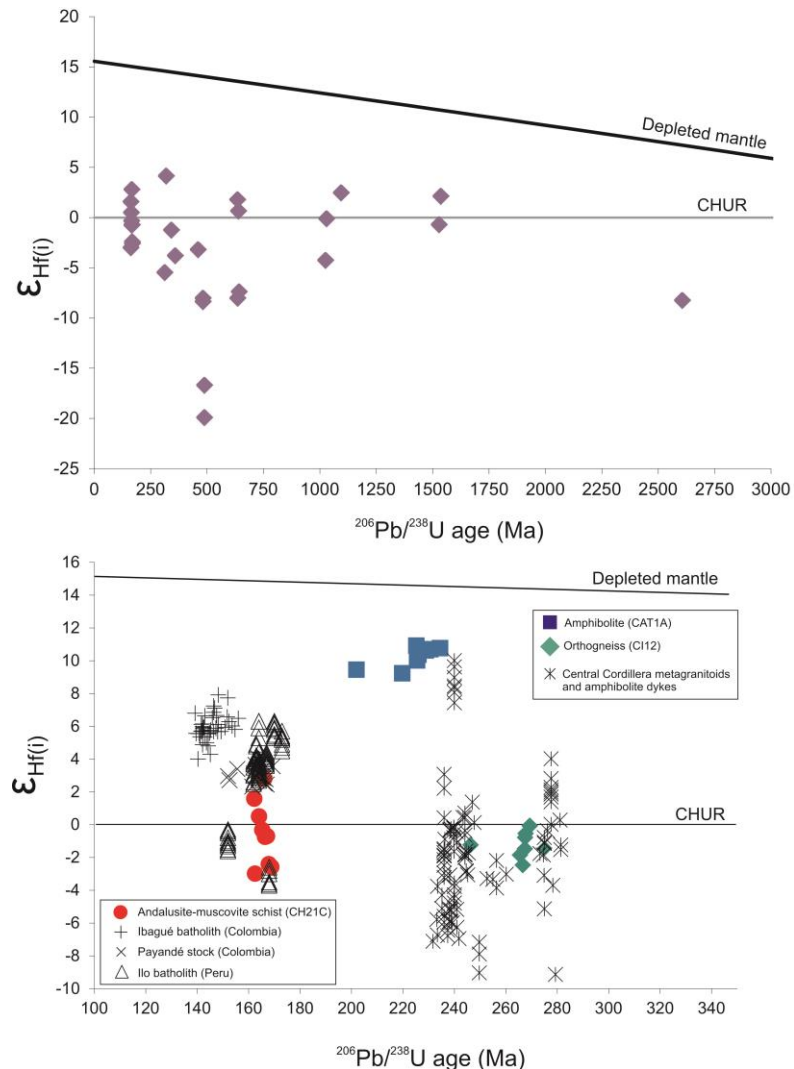


Figure 2.7. Upper: Distribution of the whole $\epsilon_{\text{Hf}(i)}$ obtained for the Cajamarca Complex. **Lower:** Initial ϵ_{Hf} vs. $^{206}\text{Pb}/^{238}\text{U}$ age diagram. Squares represents zircons from sample CAT1A (amphibolite) with a strong juvenile signature as opposite to the zircons from the sample CI12 (hornblende gneiss) represented by triangles, which reflects the involvement of crustal sources for this rock. Circles are from detrital zircons of the Tahamí terrane. See the comparison with published data from other Middle Jurassic plutons of the Central and Northern Andes [Illo batholith: Boekhout et al. (2012). Payandé and Ibagué plutons: Bustamante et al. (2016); Cochrane et al. (2014b)].

2.5.2. Graphite-quartz-muscovite schist

We analyzed twenty-eight zircons covering the U-Pb age spectra of the micaschist, but with a special emphasis on the Jurassic zircons. Hf isotopes from the older zircons usually show a strong involvement of an old crustal component (Fig. 2.7). $\Sigma_{\text{Hf(i)}}$ for the oldest zircons is -8.2 and -0.7 (Siderian and Statherian respectively). For the Grenvillian zircons, $\Sigma_{\text{Hf(i)}}$ is -0.3 and -4.3 with a crystals showing a juvenile value of +2.5. Two Ediacaran zircons have $\Sigma_{\text{Hf(i)}}$ of -7.4 and -8.0, and other two yielded slightly juvenile values of +0.7 and +1.8. Paleozoic (Ordovician and Carboniferous) zircons show values from -19.9 to -1.2. $\Sigma_{\text{Hf(i)}}$ values of nine Jurassic zircons (Fig. 2.7) provided three zircons with positive values ranging from +0.5 to +2.8, and six zircon yielded values between -0.3 and -3.0 (Table 2.3; Fig. 2.7).

2.6. DISCUSSION

U-Pb zircon ages indicate that the Tierradentro orthogneiss and amphibolite were formed in the Permo-Triassic (ca. 268-239 Ma). The orthogneiss exposed as a roof pendant within the Ibagué batholith provided initial Σ_{Hf} from -0.1 to -2.5 and show a component that is more characteristic of an older radiogenic continental crust input. The amphibolite, in contrast, provided initial Σ_{Hf} from +9.2 to +10.9 to indicate a juvenile mantle derived source. These data are similar to those obtained in different regions of the basement rocks of the Central Cordillera and Ecuador that are attributed to a geodynamic setting that includes Permo-Triassic rifting with associated bimodal magmatism related to continental break-up succeeded by subduction of the proto-Pacific (Cardona et al., 2010; Villagómez et al., 2011; Cochrane et al., 2014a). Our results therefore show that not all the Tierradentro rocks are Grenvillian in age as previously considered, and that accordingly the walls of the Jurassic Ibagué batholith were formed in the Permo-Triassic. The distribution of Precambrian rocks in the Central Cordillera therefore also appears to be overstated (Kroonenberg, 1982; Restrepo-Pace et al., 1997). Although, Mesoproterozoic sequences close to the northern border of the Jurassic Segovia batholith has been documented in the San Lucas Range and the Las Minas Serranía in the Upper Magdalena Valley (Restrepo-Pace et al., 1997; Cuadros et al., 2014).

Permo-Triassic gneisses, migmatites, amphibolites and metasedimentary rocks have been considered as a major element of the Cajamarca Complex and the Tahamí Terrane (Restrepo and Toussaint, 1988; Vinasco et al., 2006; Restrepo et al., 2011; Martens et al., 2014). Zircon crystallization age of S-type granitoids and $^{40}\text{Ar}/^{39}\text{Ar}$ amphibole cooling ages indicate that the high grade metamorphism of the northern part of the Cajamarca Complex

occurred in the Mid- to Late Triassic (Vinasco et al., 2006; Cochrane et al., 2014a). Their continuity to the south of the Central Cordillera, however, has been previously inferred based on few geochronological constraints and lithological correlations.

In the Tolima Department, the Otú-Pericos fault marks the contact of the Tierradientro gneisses and amphibolites with pelitic schists deposited in the Jurassic. Further south the Tierradientro unit pinches out and the Otú-Pericos fault defines the western contact of the Ibagué batholith. We can envisage that the Ibagué batholith intruded mostly Permo-Triassic orthogneisses and amphibolites. The granitic magma would have moved upward to incorporate, during the ascent, xenoliths of variable sizes of the Tierradientro unit. Smaller Jurassic-Early Cretaceous plutons, such as the Payandé stock and the Mariquita pluton, intruded respectively the Late Triassic calcareous rocks located east of the Otú-Pericos fault and amphibole schists (sample CH21C) (Fig. 2.2). Permo-Triassic rocks found on both sides of the Otú-Pericos fault agree with recent data reported in the Central Cordillera that put into question the reliability of the terrane discrimination analysis that used contrasting Mesozoic basement history as the major criteria for the terrane model (Villagómez et al., 2011; Cochrane et al., 2014a; Blanco-Quintero et al., 2014; Spikings et al., 2015). However, Blanco-Quintero et al. (2014) have identified a Jurassic (158-147 Ma) metamorphism based on $^{40}\text{Ar}/^{39}\text{Ar}$ plateau ages in mica and amphiboles from schists and amphibolites, and which contrast with the Triassic metamorphism of the Cajamarca Complex defined in the northern part of the Central Cordillera.

Our results confirm the presence of Mesozoic record in the metamorphic rocks of the Central Cordillera formerly considered as the Cajamarca Complex. The new data suggest the existence of a Jurassic depositional basin floored by Permo-Triassic rocks that was feed by detrital zircons supplied in part by the erosion of Jurassic sources, highlighting the importance of the Jurassic events in the assembly of the Central Cordillera. The Jurassic metavolcanosedimentary belt in the Tolima Department including the area defined by Blanco-Quintero et al. (2014) forms an N-trending elongated sequence in fault-contact with Permo-Triassic rocks (Fig. 2.2). This fault system corresponds to the Otú-Pericos that was used to define the eastern limit of the Tahami terrane.

A critical aspect of the detrital zircon results from the Jurassic detrital zircons found in the metasedimentary rocks of the Cajamarca Complex is their source area. Although Middle to Late Jurassic magmatic rocks are common along the Ecuadorian and Colombian Andean margins (Cochrane et al., 2014b; Spikings et al., 2015; Bustamante et al., 2016), initial Hf

isotopic signatures in zircons from the mica schist are more radiogenic and differed from those recognized in the Jurassic magmatic belts that characterized the Northern Andes east of the Cajamarca Complex (Fig. 2.7). Their higher radiogenic values show some resemblance with magmatic rocks farther south such as the Ilo batholith in Peru which is emplaced in Precambrian crust (Boekhout et al., 2012). Both the presence of Triassic and Jurassic magmatic record questioned the simple separation of the Tahamí and Chibcha terranes with an age criteria. However the radiogenic Hf isotopic signature found in the schist sample from the Cajamarca Complex suggest that the Jurassic source areas for the studied schist differed from the eastern Jurassic magmatic rocks associated to the Chibcha Terrane.

When the Jurassic tectonostratigraphic record is compared, a major difference also arises between the Chibcha and Tahamí terranes. Whereas the former records the growth of an arc setting (Bustamante et al., 2016), the later experienced a metamorphic event associated with a collisional setting (Blanco-Quintero et al., 2014) in a geothermal gradient which do not match with the high heat flux expected in an arc setting. Such contrasting tectonic scenarios separated by the Otú-Pericos fault suggest that their tectonic history cannot be explained by lateral variation of tectonic style (Howell, 1995), and suggest a contrasting tectonic evolution. After such tectonostratigraphic constraints we therefore suggest a series of different tectonic scenarios for the Triassic to Jurassic tectonic evolution of both terranes.

Triassic rocks from the Chibcha and Tahamí terranes are similar in character and age, and therefore suggest that they experience a common sin-tectonic extensional evolution associated to the early Pangea break-up and the subduction of the Pacific plate (Cochrane et al., 2014a; this contribution). Several continental blocks may have been detached from the margin during this extensional event. During the Jurassic several arcs were formed along different segment of the Northern Andean margin and the detached fragments. As suggested by Blanco-Quintero et al. (2014), during the Jurassic some segments of the Northern Andes experienced a collisional event, whereas others were experiencing continuous subduction with the growth of magmatic arcs.

The Tahami terrane in the Colombian Andes and the Salado terrane of the Cordillera Real in Ecuador represent remnants of such Jurassic segments that experienced collision (Fig. 2.1). The Salado terrane in Ecuador consists of interbedded Late Jurassic turbiditic metasedimentary rocks and mafic lavas with associated deformed granitoids (Litherland et al., 1994) sandwiched between the Jurassic Abitagua batholith and the Permo-Triassic Loja terrane (Spikings et al., 2015). Detrital zircons from a metasandstone provided zircon ages

similar to the mica schists from Colombia, with peak ages in the Mesoproterozoic, Neoproterozoic and Jurassic (Cochrane et al., 2014a). This terrane has been interpreted as formed as an extensional arc setting limited to the east by the Cosanga fault that separate them from undeformed Jurassic granitoids and the Amazon foreland. During the Late Jurassic to Early Cretaceous this terrane also experienced a relatively higher pressure collisional event (Massone and Toulkeridis, 2010). Such along strike variation in the tectonic evolution of the margin reflects both the aforementioned Triassic extension and the oblique convergence experienced by the South American continental margin during the Jurassic. In such scenario the Otú-Pericos marks the site of oblique subduction and collision of the Tahamí terrane with the Gondwana margin. Following such events the Otú-Pericos fault change to a strike slip suture that allow the final juxtaposition of the Tahamí and Chibcha terrane (Pindell and Kennan, 2009; Bayona et al., 2006; 2010). This tectonic evolution suggests that the Chibcha and Tahamí are para-autochthonous terranes to the western margin of South America.

2.7. CONCLUSIONS

New U-Pb zircon ages combined with Hf isotopes reveals that the Tierradientro gneisses and amphibolites, traditionally considered as part of the Grenville event of the Colombian Andes, are actually the record of Permo-Triassic extension and subduction processes that affected western Pangea. The Tierradientro unit is limited by the Otú-Pericos fault that forms the eastern border of a Jurassic sequence that includes mica schists in which their younger detrital zircons were dated at c. 162 Ma. Such Jurassic rocks, until now undetected in the Central Cordillera of Colombia, can be correlate to the south with the Salado belt in Ecuador. Initial Hf signatures of the Jurassic detrital zircons are distinct of the nearby magmatic rocks of the same age, which suggest sources far from that located at the western margin Colombia and Ecuador.

Capítulo 3

Late Jurassic to Early Cretaceous plutonism in the Colombian Andes: a record of long-term arc maturity²

ABSTRACT

Integrated geochemical, isotopic and geochronological constraints from Jurassic plutonic rocks of the Central Cordillera in Colombia were used to determine the tectonic setting and long-term tectonomagmatic evolution of the northern Andes. We examined three plutonic units with compositions that vary from diorite to granite with U-Pb zircon crystallization ages from 165 Ma to 129 Ma. These units are interpreted as subduction-related magmas as indicated by their K₂O, Na₂O contents, LREE/HREE ratios and Pb isotope signatures. The Nd and Hf isotope compositions of these magmatic events become more juvenile with time. This compositional record suggests an arc maturity trend in which partial melting of basaltic sources becomes more significant than radiogenic subducted sediments or the ancient continental crust. These processes are associated with the oblique convergence of the Farallon oceanic lithosphere against the Andean continental margin during the Mesozoic, which, in combination with the reduction of more fusible components transported by the subduction into the mantle, resulted in decreasing magmatic activity that ceased in the Early Cretaceous. These same characteristics have also been described in the southern Andes and other subduction regimes, suggesting that the evolution of stationary continental arc magmatism involves a progressive juvenile character with time, where the obliqueness in the convergence reduces the amount of sediments to be melted with basalt, rendering the source more refractory and decreasing the volumes of magma through time.

² Bustamante, C., Archanjo, C., Cardona, A., Valencia, V., Vervoort, J., 2016. Late Jurassic to Early Cretaceous plutonism in the Colombian Andes: a record of long-term arc maturity. *Geological Society of America Bulletin*.

3.1. INTRODUCTION

The Middle Mesozoic convergence of the Farallon oceanic plate beneath the northwestern margin of South America was responsible for the growth of several magmatic arcs and the development of deep sedimentary basins and a major Cretaceous marine transgression (Jaillard et al., 1990, 2000; Toussaint, 1995; Sarmiento-Rojas et al., 2006; Ramos and Aleman, 2000; Ramos, 2009; Pindell and Keenan, 2009). Geological and geochronological data from the Andes of Colombia and Ecuador indicate the existence of a Late Triassic to Late Jurassic magmatism between 203 and 145 Ma (Fig. 3.1; Aspden et al., 1987; Noble et al., 1997; Gendall et al., 2000; Chiaradia et al., 2009; Bustamante et al., 2010; Villagómez et al., 2011; Leal-Mejía, 2011; Álvarez-Galindez, 2013; Mantilla et al., 2013; Cochrane et al., 2014a). This magmatism includes large NNE-trending elongated batholiths commonly associated with volcanic rocks distributed along the eastern margin of the Central Cordillera and the middle and upper Magdalena valley of Colombia (Fig. 3.1; Aspden et al., 1987; Toussaint, 1995).

Two different tectonic models have been proposed for the Jurassic and Early Cretaceous evolution of the Northern Andes. The first model, based on a succession of sedimentary strata and regional paleogeography, proposed that the Jurassic igneous rocks evolved in an intracontinental rift setting (review in Cediel et al., 2003; Pindell and Keenan, 2009). The second model, based on geochemical data of magmatic rocks, proposed a subduction extensional setting characterized by the development of a back-arc and intra-arc tectonic setting (Aspden et al., 1987; Bayona et al., 2006; Bustamante et al., 2010; Villagómez et al., 2011; Cochrane et al., 2014a; Zapata et al., 2016). In the subduction-related model, the long-term evolution of the active margin would be characterized by ocean-ward arc migration due to slab roll-back (Cochrane et al., 2014a). Alternative scenarios include the translation of terranes from southern latitudes in an oblique convergence setting that would juxtapose Jurassic metamorphic terranes with a magmatic arc (Bayona et al., 2006; Blanco-Quintero et al., 2014).

Our study examines the Mesozoic evolution of the paleomargin of the Northern Andes from the Jurassic to the Early Cretaceous. In particular, we explore the slab roll-back model to show that there is no connection between the proposed migration of the arc and the age distribution of the continental plutonic rocks. We have analyzed how the long-term increase in the juvenile character of the magmatic record in arcs is controlled by the evolution of a single hybrid sedimentary and mantle source formed in the subduction mélange (Castro et al.,

2010; 2013) and show that this does not necessarily reflect of an extensional setting that allow continuous exposure of mantle material. This apparently counter-intuitive character of the maturation of continental arc magmas has been described in other magmatic belts such as in the Southern Andes (Bellos et al., 2015; Hervé et al., 2007), the Iberia magmatic arc (Pereira et al., 2015), and the Central Asian orogenic belt (Li et al., 2014), and therefore can be seen as a major pattern of magmatic arcs.

In this contribution we present new zircon U-Pb ages combined with Hf isotopes, as well as whole-rock Hf, Nd and Pb isotope data and also major and trace element data, from selected plutons of the Colombian Andes (Fig. 3.1). The new results, combined with previous studies, are used to constrain the tectonomagmatic evolution of the Central Cordillera between 165 and 129 Ma. These results are consistent with the existence of a more stationary arc that resulted from diminishing magmatic fertility as a consequence of the long-term evolution of the magma sources and the plate convergence obliquity. A similar evolutionary history can be found in the Jurassic record of the Ecuadorian Andes (Chiaradia et al., 2009) and suggests that regional stationary arc maturation reflects source and regional tectonic controls.

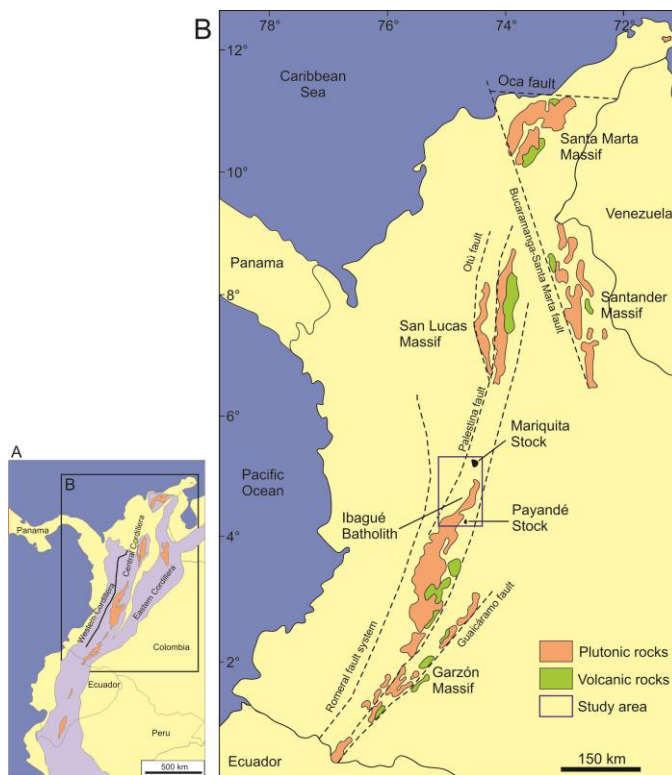


Figure 3.1. A: Distribution of the Jurassic plutonic belt in the Northern Andes. **B:** Detailed map of the occurrences of Lower Jurassic to Lower Cretaceous plutonic rocks in the Central Cordillera of Colombia and isolated massifs with associated volcanic rocks.

3.2. GEOLOGICAL SETTING

The Northern Andes of Colombia are characterized by three mountain ranges separated by major rivers that drain to the Caribbean Sea (Fig. 3.1). The Central Cordillera has an extensive Meso-Cenozoic magmatic record characterized by a series of plutonic bodies considered to be Late Jurassic to Late Cretaceous in age (Aspden et al., 1987; Villagómez et al., 2011). These rocks intrude the Permo-Triassic and older metamorphic basement (Vinasco et al., 2006; Restrepo et al., 2011; Villagómez et al., 2011; Martens et al., 2014). The Mesozoic magmatic record is related to a volcanic arc formed by the subduction of the Farallon Plate beneath NW South America (Aspden et al., 1987; Villagómez et al., 2011; Cochrane et al., 2014a). Jurassic arc-related magmatism extends towards the Middle and Upper Magdalena valley as a series of volcanic rocks included in the Saldaña Formation (Fig. 3.1) (Bayona et al., 1994). Older Early Triassic red sandstones and conglomerates overlain by carbonates (Luisa and Payandé Formations) lie below these volcanic rocks and are related to an extensional rift-related setting associated with the break-up of Pangea or the opening of the Proto-Caribbean Ocean (Cediel et la., 2003; Pindell and Keenan, 2009).

The western Cordillera is characterized by a series of allochthonous Cretaceous oceanic terranes that have accreted to the continental margin since the Late Cretaceous (Restrepo and Toussaint, 1988; Kerr et al., 1997; Villagómez et al., 2011; Villagómez and Spikings, 2013). The Eastern Cordillera also includes a more limited Late Triassic to Early Jurassic siliciclastic series covered by an extensive Early Cretaceous transgressive sequence, with well-defined extensional structures (Sarmiento-Rojas et al., 2006) and limited small gabbroic plutons of Early to Late Cretaceous in age (Vásquez and Altenberger, 2005, Vásquez et al., 2009).

3.2.1. Mesozoic plutonism in the southern Central Cordillera and the Upper Magdalena valley

The Ibagué Batholith (Fig. 3.1) is one of the largest Jurassic plutons of the Central Cordillera, located at its central to southern segment. It covers an area of approximately 11,700 km², and includes several intrusions with compositions ranging from tonalite to granodiorite. This batholith intrudes a pre-Jurassic metamorphic basement and is in faulted contact with Jurassic and Tertiary sedimentary rocks (Vesga and Barrero, 1978). Available U-Pb and K-Ar geochronological data show that the batholith ranges in age from 189 Ma in the southernmost segment (Bustamante et al., 2010; Leal-Mejía., 2011), to 177 and 145 Ma in the

north (Vesga and Barrero, 1978; Sillitoe et al., 1982; Brook, 1984; Aspden et al., 1987; Altenberger and Concha, 2005; Villagómez et al., 2011; Leal-Mejía, 2011). To the east, the Ibagué Batholith is probably in tectonic contact with metamorphosed volcano-sedimentary rocks included in the Cajamarca Complex (Blanco-Quintero et al., 2014). The metamorphism of part of these metamorphic complexes apparently took place in the Jurassic between 158 Ma and 147 Ma, which is when magmatism was active to the east; therefore, the metamorphism probably took place in an allochthonous position and was subsequently juxtaposed to its current position (Blanco-Quintero et al., 2014). The Payandé stock (Fig. 3.1), which intrudes Late Triassic carbonate rocks, is exposed east of the Ibagué Batholith. Other Jurassic plutons to the south of the Ibagué Batholith include the Altamira, Las Minas and Garzón granites (Bustamante et al., 2010) and the southernmost Mocoa Batholith (Aspden et al., 1987; Zapata et al., 2016).

Early Cretaceous plutons are limited and may include the Mariquita stock (Fig. 3.1), with an approximate area of 65 km² and compositions ranging from granodiorite to tonalite (Barrero and Vesga, 1976). These plutons intrude metamorphic rocks of the Cajamarca Complex. These have been covered by Tertiary sedimentary rocks. K-Ar dates in biotite of 113 ± 4 Ma (Barrero and Vesga, 1976; Vesga and Barrero, 1978), are considered minimum dates and are related to cooling.

Late Cretaceous 90-65 Ma calc-alkaline magmatism is represented by the ca. 8,000 km² areal exposure of the Antioquian batholith and other smaller intrusive bodies that are widely exposed in the northern segment of the Central Cordillera (Ibáñez-Mejía et al., 2007; Restrepo-Moreno et al., 2007; Ordóñez and Pimentel, 2001; Ordóñez-Carmona et al., 2007; Leal-Mejía et al., 2011; Villagómez et al., 2011).

3.3. SAMPLING AND ANALYTICAL METHODS

We have focused our work on the plutonic record exposed in the central segment of the Central Cordillera, north of the Ibagué fault and east of the Romeral fault system, including the Ibagué batholith and the Payandé and Mariquita stocks (Fig. 3.1). The Ibagué batholith and Mariquita stock intrude greenschist-facies metamorphic rocks of the Cajamarca Complex, whereas the Payandé stock intrudes Triassic limestones of the Payandé formation forming Cu-skarn deposits (Barrero, 1969; Alvarán et al., 2011).

A total of 50 samples were taken from the Ibagué batholith (18), Mariquita stock (30) and Payandé stock (2). Petrography was performed on thin sections from all 50 samples to

identify mineralogy and textural features, and also as a guide to select representative samples for geochemical analyses and for U-Pb geochronology.

3.3.1. U-Pb Geochronology in zircon

Heavy mineral concentrates of the <350 µm fraction were separated using traditional techniques. Zircons from the non-magnetic fraction were handpicked under the microscope and mounted in a 1-inch diameter epoxy puck and slightly ground and polished to expose the surface and keep as much material as possible for laser ablation analyses. After CL imaging, the LA-ICP-MS U-Pb analyses were conducted using a New Wave Nd:YAG UV 213-nm laser coupled to a ThermoFinnigan Element 2 single collector, double-focusing, magnetic sector ICP-MS at Washington State University. Operating procedures and parameters are similar to those of Chang et al. (2006). Laser spot size and repetition rate were 30 microns and 10 Hz, respectively. He and Ar carrier gases delivered the sample aerosol to the plasma. Each analysis consists of a short blank analysis followed by 250 sweeps through masses 202, 204, 206, 207, 208, 232, 235, and 238, taking approximately 30 seconds. Fractionation was corrected by normalizing U/Pb and Pb/Pb ratios of the unknowns to the zircon standards (Chang et al., 2006). U and Th concentration were monitored by comparing to NIST 610 trace element glass. Zircon standard Plesovice was used, with an age of 337.13 ± 0.37 Ma (Sláma et al., 2008). Uranium-lead ages (Table 3.1) were calculated using Isoplot 4.15 (Ludwig, 2003).

3.3.2. Hf isotopes in zircon

Hf isotope geochemistry analysis was performed on 12 samples (Table 3.2) at the Geoanalytical Lab at Washington State University, using a ThermoFinnigan Neptune™ MC-ICP-MS equipped with 9 faraday collectors interfaced with a New Wave™ 213 nm UP Nd-YAG laser. Laser spot size was 40 µm and the data were acquired in static mode with 60 second integrations. Details of analytical procedures and data treatment follow those of Vervoort et al. (2004) and DuFrane et al. (2007). For the Hf-depleted mantle model ages (Hf_{TDM}), we used $^{176}\text{Hf}/^{177}\text{Hf}$ and $^{176}\text{Lu}/^{177}\text{Hf}$ for the individual zircon samples to determine their initial $^{176}\text{Hf}/^{177}\text{Hf}$ ratios at their crystallization ages. Projection back from zircon crystallization was calculated using a present value of 0.0150 for the estimated $^{176}\text{Lu}/^{177}\text{Hf}$ of continental crust (Vervoort and Patchett, 1996; Goodge and Vervoort, 2006). The depleted

mantle Hf evolution curve was calculated from present-day depleted mantle values of $^{176}\text{Hf}/^{177}\text{Hf}$ DM₍₀₎=0.283240 and $^{176}\text{Lu}/^{177}\text{Hf}$ DM₍₀₎=0.03979 (Vervoort et al., 2015).

3.3.3. Whole rock XRF and ICP-MS geochemistry

Bulk whole rock chemical analyses of 23 samples were determined, avoiding veins and weathered surfaces. The samples were crushed using a jaw crusher and powdered using a tungsten carbide ring mill. Major and trace elements were analyzed using a Rigaku 3370 XRF spectrometer at Washington State University. Details of sample preparation, dilution and analytical procedures are described in Johnson et al. (1999). Major, trace and rare earth element results are reported in Table 3.3.

REE were determined by inductively coupled plasma-mass spectrometry (ICP-MS) at Washington State University. A 2 g aliquot is weighed into a graphite crucible and mixed with 2 g of LiBO₂ flux. The crucibles are placed in an oven and fused at 1000° C in a muffle furnace for 30 minutes. The resultant bead is ground in a steel ring mill, and a 0.25 mg portion is dissolved using HNO₃ (2 ml), HF (6 ml) and HClO₄ (2 ml) at 110° C. Calibration standards and reagent blanks are added to the sample sequence. Sample solutions are aspirated into an ICP emission spectrograph (Jarrel Ash Atom Comb 975) for determining major oxides and certain trace elements (Ba, Nb, Ni, Sr, Sc, Y and Zr), while the sample solutions are aspirated into an ICP-MS (Perkins-Elmer Elan 6000) for determination of the trace elements, including rare earth elements.

3.3.4. Nd, Hf and Pb radiogenic isotopes

Analyses were acquired using a Thermo-Finnigan Neptune multicollector system at Washington State University and results are presented in Table 3.4. Procedures for sample preparation and dilution details for Nd, Hf and Pb isotopes are those as in Gaschnig et al. (2011). A final Hf purification was performed following Münker et al. (2001); Lu was separated from Yb according to (Vervoort et al., 2004) and for Sm and Nd were prepared by following the procedures described in Vervoort and Blachert-Toft (1999). Pb was separated using the Tl doping method of White et al. (2000). After correcting for the mass bias using the Tl, samples were normalized to the triple-spike values for NBS-981 from Galer and Abouchami (1998).

Nd analyses were corrected for mass fractionation using $^{146}\text{Nd}/^{144}\text{Nd}$ =0.7219 and normalized using the Ames Nd standard (± 0.000020 2σ average reproducibility), and Hf

analyses were corrected using $^{179}\text{Hf}/^{177}\text{Hf}=0.7325$ and the JMC-475 standard (± 0.000014 2σ average reproducibility). Sm was corrected using $^{147}\text{Sm}/^{152}\text{Sm}=0.56081$. Lu measurements are according to the methods of Vervoort et al. (2004). ε_{Nd} values were calculated using present day values of $^{143}\text{Nd}/^{144}\text{Nd} = 0.512630$ and $^{147}\text{Sm}/^{144}\text{Nd} = 0.160$ for CHUR (Bouvier et al., 2008), and ε_{Hf} using present-day values of $^{176}\text{Hf}/^{177}\text{Hf} = 0.282785$ and $^{176}\text{Lu}/^{177}\text{Hf} = 0.0336$ for CHUR (Bouvier et al., 2008).

3.4. RESULTS

3.4.1. Zircon U-Pb geochronology

Scanning Electron Microscope Cathodoluminescence (SEM-CL) images are shown in Figure 2, and crystallization ages from representative zircon grains analyzed are shown in Figure 3 to 5. Approximately 30 zircon tips were analyzed per sample. Th/U ratios for these analyses are less than 12, which is typical of magmatic zircon (Rubatto, 2002).

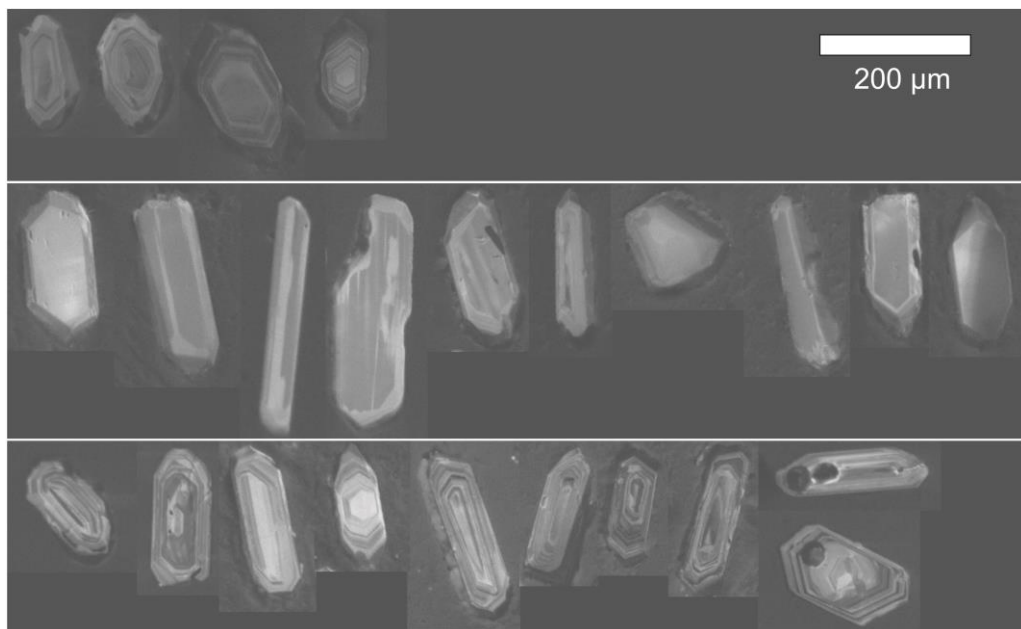


Figure 3.2. Representative Scanning Electron Microscope Cathodoluminescence (SEM-CL) images from zircon grains of each pluton studied. **Upper:** Payandé stock, **middle:** Ibagué batholith, **bottom:** Mariquita stock.

Two samples from the Payandé stock are characterized by short prismatic to rounded zircon grains with typical lengths of 100 to 250 μm and well-defined oscillatory zoning and lack of overgrowths. Inherited cores were not observed in the CL images (Fig. 3.2). The ages obtained for this granitoid are ca. 165-164 Ma (Middle Jurassic) (Fig. 3.3).

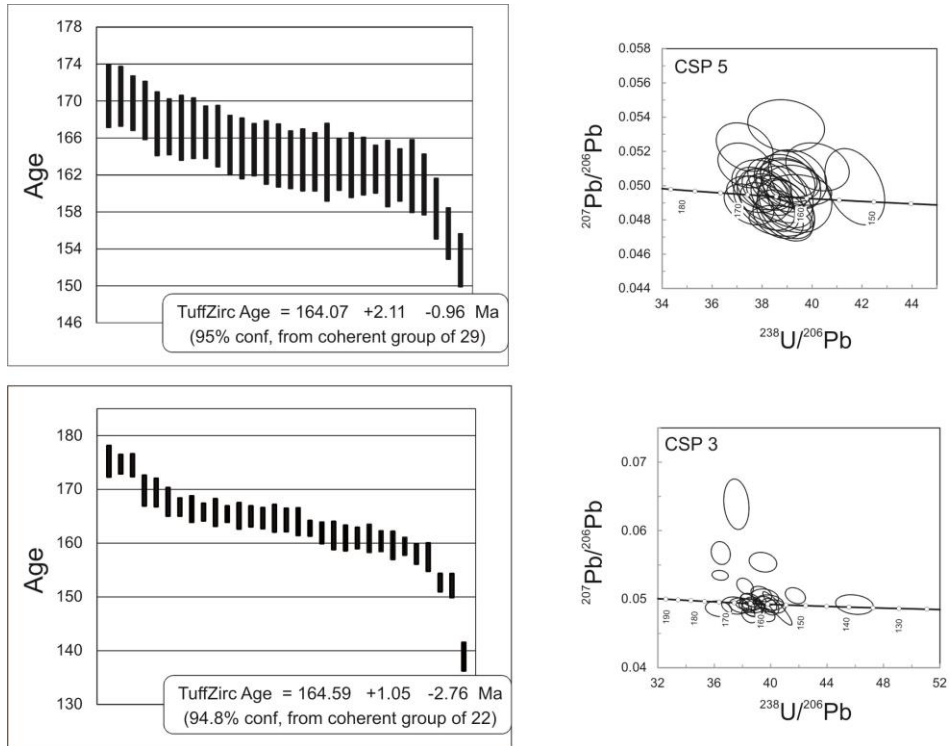


Figure 3.3. U-Pb zircon ages with 1σ box heights and Tera-Wasserburg diagrams with 68.3% confidence error ellipses from the Payandé stock.

The six samples from the Ibagué Batholith have elongated prismatic zircon with sizes between 100 to 300 μm (Fig. 3.2). Zoning is nearly absent, although it can be present in short-prismatic crystals from dioritic samples. Ages were obtained from tips and range from Lower Cretaceous (granodiorite: 141.9 +1.1/-0.8 Ma) to Upper Jurassic (diorite: 158.2 +1.2/-0.4 Ma) (Fig. 3.4).

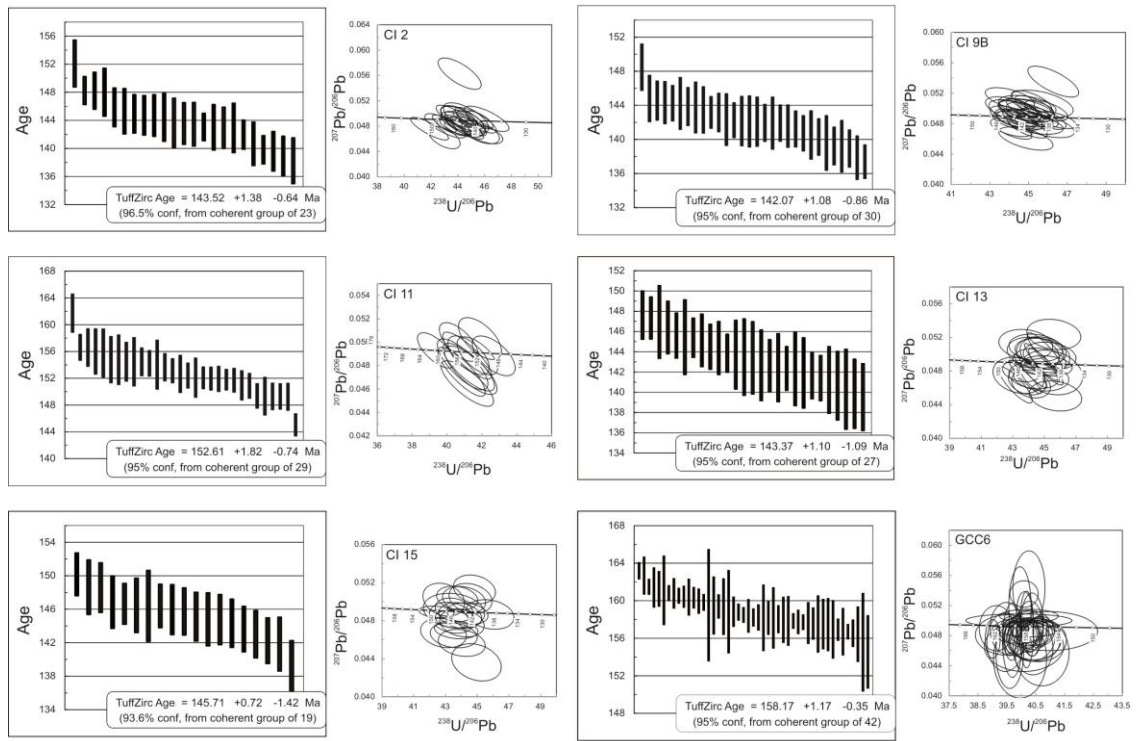


Figure 3.4. U-Pb zircon ages with 1σ box heights and Tera-Wasserburg diagrams with 68.3% confidence error ellipses from the Ibagué Batholith.

Lower Cretaceous ages were obtained from seven samples of the Marquita stock. Short, prismatic zircon show clear oscillatory concentric zoning patterns and a larger range of sizes from ~ 75 to $350 \mu\text{m}$, although short crystals are more common (Fig. 3.2). A trend of older ages in the south to younger in the north is evident from the results, with ages ranging from $143.4 +0.6/-0.7$ Ma in the south to $129.2 +1.1/-1.0$ Ma in the north (Fig. 3.5).

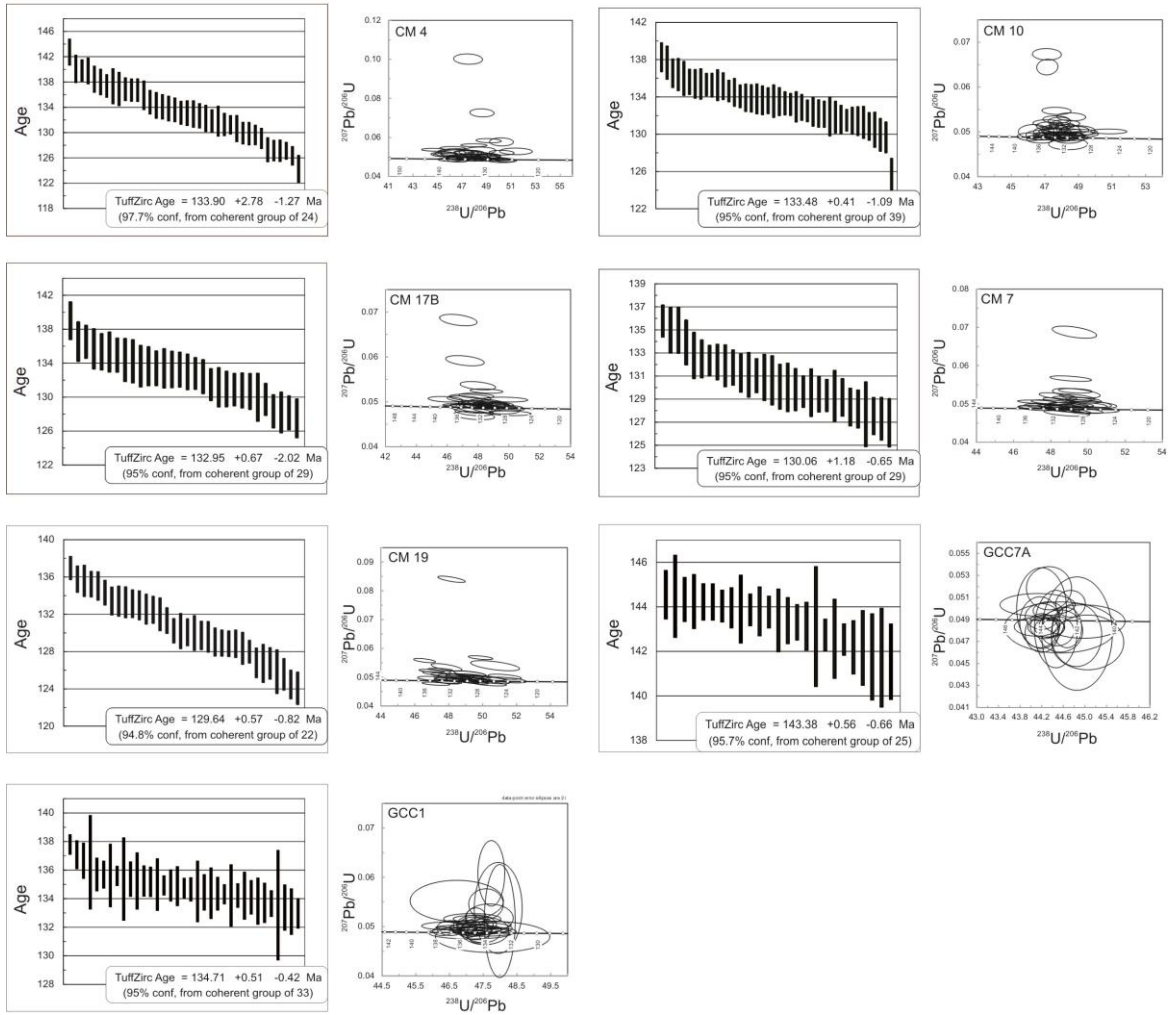


Figure 3.5. U-Pb zircon ages with 1σ box heights and Tera-Wasserburg diagrams with 68.3% confidence error ellipses from the Mariquita stock.

3.4.2. Whole-rock elemental and isotope geochemistry, and Hf isotopes in zircon

A total of 23 samples were analyzed from the Ibagué, Payandé, and Mariquita plutonic bodies, whereas seven samples were chosen for whole-rock Nd, Pb and Hf isotopes, and Hf isotopic analyses were obtained for the twelve dated samples. Isotopic ratios were calculated using U-Pb ages in zircon and are reported in Table 3.4.

Harker diagrams (Fig. 3.6) are characterized by decreases in Al_2O_3 , MgO , TiO_2 , CaO , FeO_t and an increase in K_2O relative to SiO_2 . Na_2O is scattered for all of the samples in the different plutons and is probably associated with plagioclase alteration. The element distribution patterns suggest fractional crystallization of mafic phases that is a common process in the studied plutons.

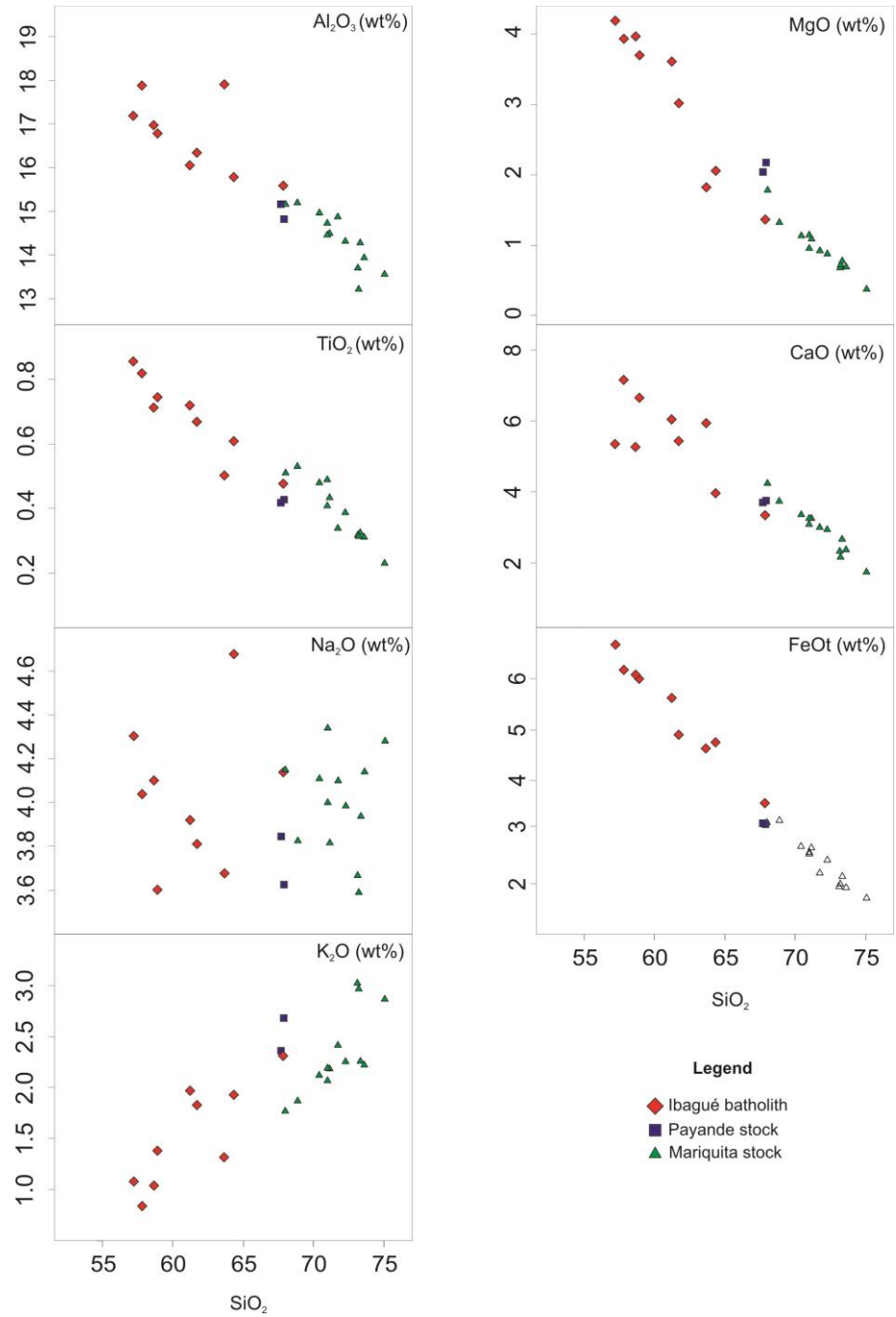


Figure 3.6. Harker diagrams of the three studied plutons, showing how fractional crystallization is a common process among them.

The loss on ignition for the majority of the analyzed samples is less than 1.5 wt%, with three samples achieving values of ca. 2.3 wt% that reflect an intermediate degree of alteration (also seen in thin section). All samples have an intermediate to felsic composition (Fig. 3.7A) and are calc-alkaline according to the alkalinity index (Fig. 3.7B) of Pecerillo and Taylor (1976). They are also predominantly metaluminous to slightly peraluminous in some

Mariquita samples, as shown in the diagram of Shand (1943) (Fig. 3.7C). The latter probably reflects higher amounts of biotite. Multi-element diagrams normalized with respect to the primitive mantle (Sun and McDonough, 1989) show that all samples exhibit characteristics of a subduction-related environment, which are reflected in the enrichments of K, Rb and Ba and in the negative anomalies in Nb and Ti (Fig. 3.8). Details from each pluton will be described in the following sections.

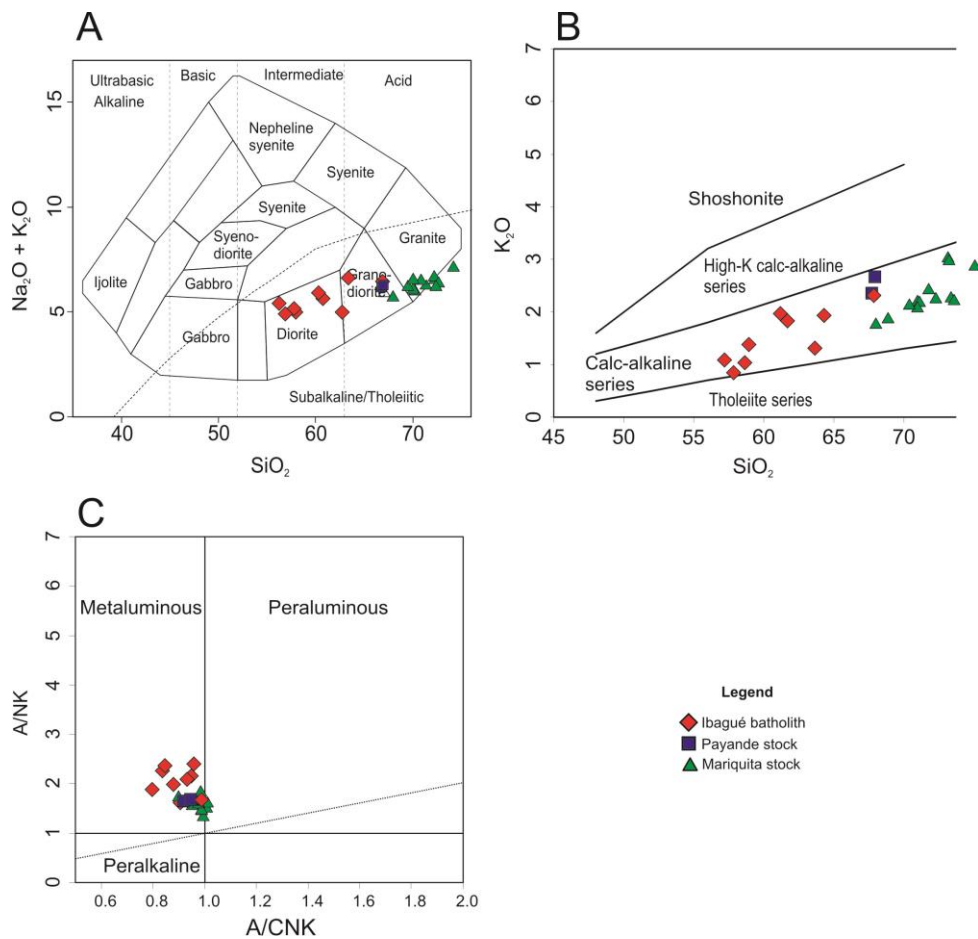


Figure 3.7. Geochemical classification and discrimination diagrams of samples from the three studied plutons. **A:** Classification of plutonic rocks based on the TAS diagram of Cox et al. (1979). **B:** Alkalinity index diagram of Pecerillo and Taylor (1976). **C:** Alumina saturation index diagram of Shand (1943).

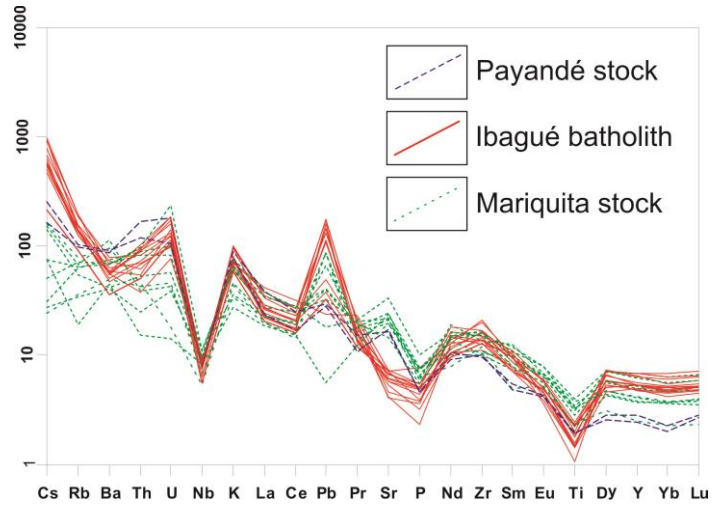


Figure 3.8. Multi-element plot normalized to primitive mantle according to Sun and McDonough (1989).

3.4.2.1. Payandé stock

Samples from the Payandé stock are composed of plagioclase, quartz, orthoclase, Ca-amphibole and biotite. Zircon, apatite and tourmaline are common accessories. The samples plot in the granodiorite field of the TAS diagram (Cox et al., 1979) and have relatively high average SiO₂ (~68 wt%), low K₂O (2.5 wt%), similar values of CaO and Na₂O (3.8 and 3.7 wt%, respectively), and a MgO content of 2.1 wt%. Both samples analyzed have relatively high Sr/Y ratios (28.2 and 31.7). REE patterns (Fig. 3.9) normalized to chondrite after Nakamura (1974) show moderate enrichment in light rare earth elements (LREE) when compared with heavy rare earth elements (HREE), and they exhibit a steeper pattern compared with the other plutons ([La/Yb]_N≈ 13.6). Eu anomalies are absent (Eu/Eu*≈1), and an almost flat-shaped pattern for the MREE-HREE is common for the studied granites ([Dy/Yb]_N ≈ 1.2). The whole-rock $\Sigma_{Nd(i)}$ and $\Sigma_{Hf(i)}$ values of the analyzed samples are lower than in the other plutons (+2.2 and +3.9, respectively). This finding is consistent with the Hf isotopes in zircon, where the $\Sigma_{Hf(i)}$ values range from +2.3 to +4.1. The $^{206}\text{Pb}/^{204}\text{Pb}$ ratio is 18.80, $^{208}\text{Pb}/^{204}\text{Pb}$ is 38.55 and $^{207}\text{Pb}/^{204}\text{Pb}$ is 15.62.

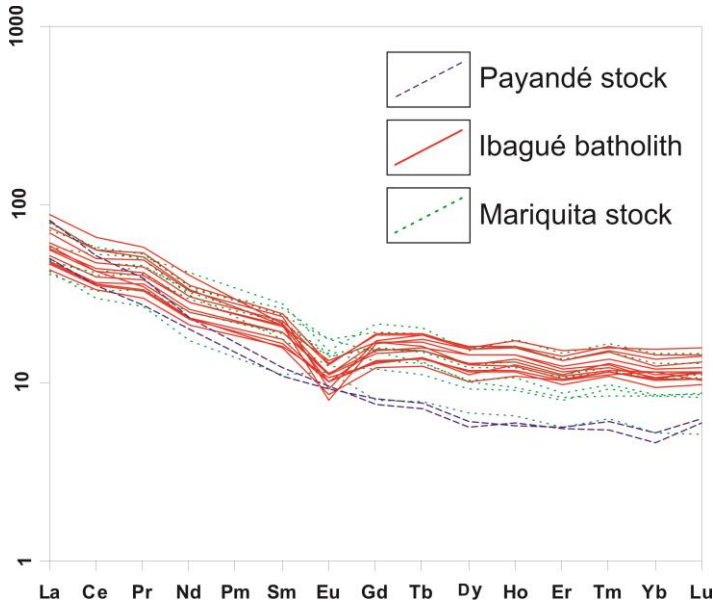


Figure 3.9. Chondrite normalized REE patterns according to Nakamura (1974).

3.4.2.2. Ibagué Batholith

The Ibagué Batholith (Fig. 3.1) was sampled north of the Ibagué fault. In terms of petrography, this batholith shows marked differences in texture and mineral content from the north to the south. The main compositions of the northern half of the batholith are tonalite to granodiorite with Ca-amphibole and biotite. The Fe-Mg silicates in these rocks are usually replaced by chlorite. Plagioclase is generally altered to saussurite. Accessory phases are zircon, apatite and ilmenite. Diorites with roughly oriented fabrics defined by the preferred orientation of amphibole are exposed in the middle-southern part of the batholith. Diopside is locally rimmed by Ca-amphibole. In most mafic rocks in this segment, enstatite-ferrosilite, which is also rimmed by Ca-amphibole, is present in the same proportion as diopside. Most Ca-amphiboles have a skeletal appearance caused by multiple quartz inclusions. Some tourmaline and sphene are common as accessory minerals, and xenotime sometimes occurs as inclusions in Ca-amphibole and occurs exclusively in the most mafic rocks. Interstitial orthoclase is identified in some samples, as well as prehnite filling and bent biotite cleavages.

An intermediate composition is reflected in the TAS diagram (Fig. 3.7a) of Cox et al. (1979), and the samples are classified as diorites and granodiorites. SiO_2 contents are intermediate (57.2 – 67.8 wt%), and K_2O is low (0.8 – 2.3 wt%). CaO exhibits a relatively wide range of values, which reflects the felsic and mafic facies (3.4 – 7.2 wt%), whereas Na_2O has steady values (~ 4.1 wt%). MgO values are variable (1.4 – 4.2 wt%). The rocks

have intermediate to high Sr/Y ratios (14.6 – 37.9 wt%) and the Ibagué Batholith has fairly steep REE patterns ($[La/Yb]_N = 3.8 - 9.4$) (Fig. 3.9). Multi-element diagrams normalized to chondrite (Nakamura, 1974) show moderate enrichment in LREE compared with HREE. Eu anomalies are absent to slightly negative, and only sample CI7 has a positive anomaly ($Eu/Eu^* = 0.6 - 1.2$). The MREE-HREE pattern is flat-shaped ($[Dy/Yb]_N = 1.04 - 1.29$).

Whole-rock isotopes and Hf isotopes in zircon from the Ibagué Batholith have intermediate values compared with the Payandé and Mariquita stocks. $\varepsilon_{Nd(i)}$ ranges from +0.8 to +4.2, and whole-rock $\varepsilon_{Hf(i)}$ ranges from +4.4 to +7.6. Hf isotope analyses in zircon yielded $\varepsilon_{Hf(i)}$ values from +4.0 to +7.9. $^{206}Pb/^{204}Pb$ ratios are from 18.50 to 18.71, and $^{208}Pb/^{204}Pb$ ranges from 38.28 to 39.10. The $^{207}Pb/^{204}Pb$ values range from 15.59 to 15.62.

3.4.2.3. Mariquita stock

The Cretaceous Mariquita stock is composed of quartz, plagioclase, orthoclase, Ca-amphibole and biotite. It differs from the Jurassic plutons by the higher amount of orthoclase and sometimes by a poikilitic texture defined by chadacrysts of plagioclase and biotite. Euhedral zoned biotite crystals and allanite are present to the south of the stock, whereas rutile inclusions in biotite are identified in the north.

An acidic composition is reflected in the TAS diagram (Fig. 3.7a) of Cox et al. (1979), and the rocks are classified as granites. The Mariquita stock has high SiO_2 (68.0 - 75.1 wt%), low K_2O (1.8 - 3.0 wt%), low CaO (1.3 - 1.7 wt%) and Na_2O values similar to those of the other plutons (3.6 - 4.3 wt%). MgO values are low (0.4 - 1.8 wt%), and Sr/Y ratios are very low (3.0 – 6.9). As in the Ibagué Batholith, REE patterns of all analyzed samples (Fig. 3.9) are coherent having LREE enrichment ($[La/Yb]_N = 3.7 - 8.2$, distinctive negative Eu-anomalies ($Eu/Eu^* = 0.46 - 0.75$), and flat-shaped MREE-HREE ($[Dy/Yb]_N = 0.9 - 1.4$).

Whole-rock isotopes and Hf isotopes in zircon exhibit a more juvenile character compared with the others plutons. $\varepsilon_{Nd(i)}$ ranges from +2.4 to +4.6, and $\varepsilon_{Hf(i)}$ ranges from +7.3 to +10.6. Hf isotopes in zircon yield $\varepsilon_{Hf(i)}$ values from +5.9 to +12.2. $^{206}Pb/^{204}Pb$ ratios range from 18.70 to 18.84, $^{208}Pb/^{204}Pb$ ratios range from 38.37 to 38.56, and the $^{207}Pb/^{204}Pb$ ratio is ~15.61.

3.5. DISCUSSION

3.5.1. Age distribution of the Jurassic-Early Cretaceous magmatic activity

Our new U-Pb crystallization ages span from 165 to 129 Ma with no latitudinal or longitudinal trends in age distribution, which suggests a stationary arc that was active for ca. 40 Ma. Although the ages obtained in the Ibagué Batholith are within the 152 to 142 Ma interval, older U-Pb zircon crystallization ages ranging from 190 to 160 Ma have been documented south of the Ibagué fault (Bustamante et al., 2010; Villagómez et al., 2011). Other Jurassic plutons with crystallization ages between 187 and 154 Ma are exposed in the Sierra Nevada de Santa Marta (Tschanz et al., 1974; Leal-Mejía, 2011), the Santander massif (Mantilla-Figueroa et al., 2013; Van der Lelij et al., 2015), the San Lucas range (Leal-Mejía, 2011; Álvarez-Galindez, 2013; Cochrane, 2014a), and the Mocoa Batholith (Aspden et al., 1987), as well as minor plutons and stocks such as the Altamira, Garzón and Las Minas in southern Colombia (Bustamante et al., 2010). Thus, the available geochronological data, including our results, suggests that the Jurassic magmatism in the Colombian Andes extends from 200 to 129 Ma (Fig. 3.10), which is at least 20 Ma longer than the previous age compilations of Aspden et al. (1987) and Villagómez et al. (2011). In the Central Cordillera, the age distribution suggests that the magmatic activity was continuous for almost 60 Ma. The Jurassic magmatism can be followed further south to Ecuador, where zircon U-Pb ages ranging from 190 to 145 Ma have been documented in the Abitagua, Azafran, Zamora and Rosa Florida Batholiths (Noble et al., 1997; Chiaradia et al., 2009; Villagómez et al., 2011; Cochrane et al., 2014a; Spikings et al., 2015).

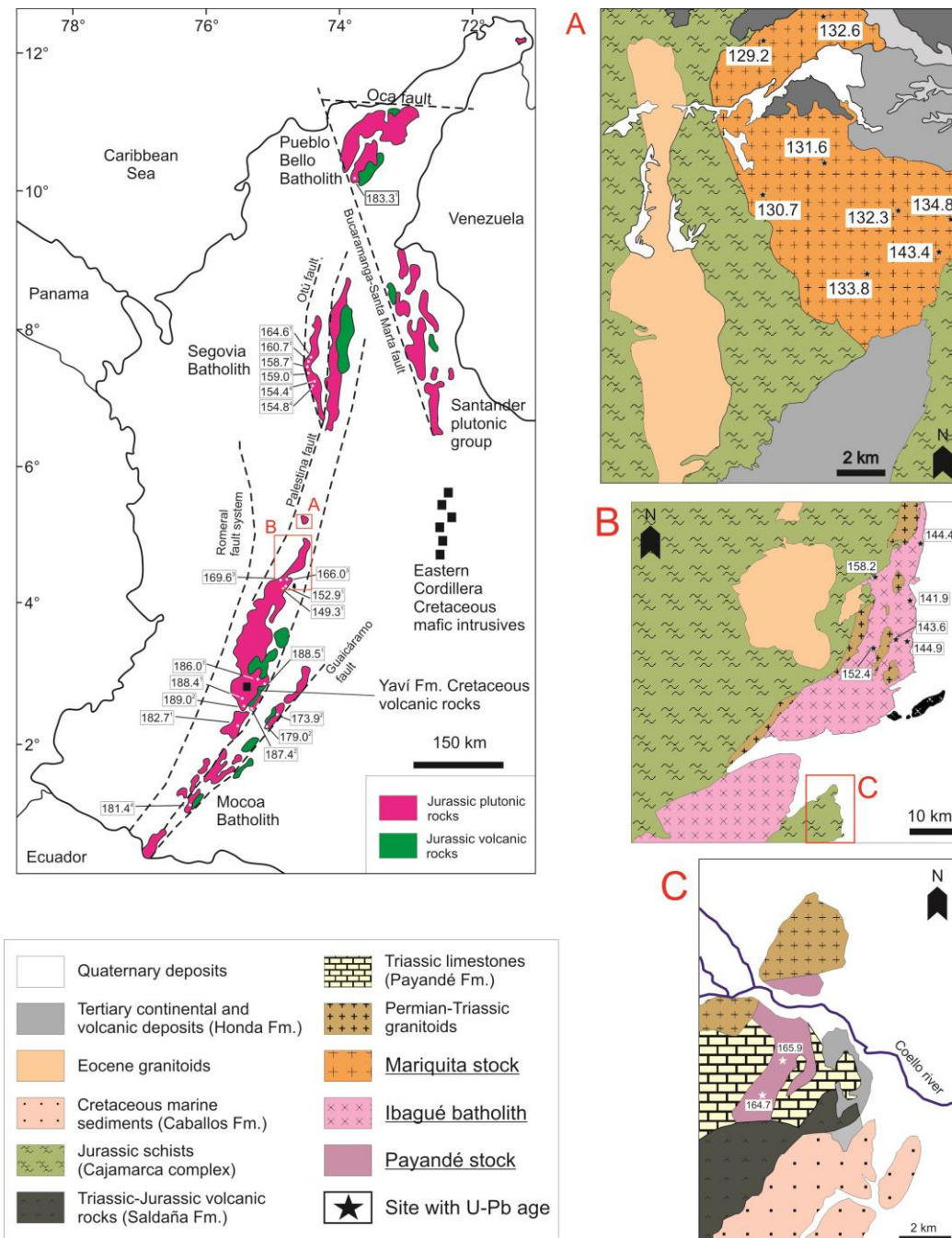


Figure 3.10. Map from Colombia showing the distribution of the Jurassic-Cretaceous magmatic belt. U-Pb zircon ages from this study and other works are plotted in rectangles. **1:** Leal-Mejía (2011); **2:** Bustamante et al. (2010); **3:** Villagómez et al. (2011); **4:** Álvarez-Galíndez (2013). Lower to mid-Cretaceous mafic magmatism is represented by white (Yavi Fm.: Toro-Toro et al., 2011) and black (Eastern Cordillera: Vásquez and Altenberger, 2005) squares.

This stationary arc model supported by the distribution of crystallization ages of the Jurassic plutonic rocks, also present several lines of evidence that suggest that the magmatic activity apparently decreased in volume between 200 Ma and 129 Ma. This is indicated by the areal expression of the Jurassic to Early Cretaceous magmatic rocks, with a major reduction of the plutonic activity occurring after 170 Ma. The younger plutonic rocks have smaller

areas, such as in the northern part of the Ibagué Batholith and in the Payandé and Mariquita stocks. Geochronology from volcanic rocks also suggest a similar trend, such as the larger Early Jurassic volcanism of the Saldaña Formation (Bayona et al., 1994; Zapata et al., 2016) compared with the limited Late Jurassic to Early Cretaceous volcanic products of the Yaví Formation (Toro-Toro et al., 2011). Likewise, detrital zircon from post-Jurassic sedimentary strata in the Magdalena and eastern Colombian Basins also show a significant decrease in the supply of Early Cretaceous zircon grains compared with Late Jurassic zircon, which may indicate reduced Cretaceous source areas available for erosion (Fig. 3.11; Nie et al., 2010; Horton et al., 2010; Saylor et al., 2011; Bayona et al., 2013; Caballero et al., 2013; Silva et al., 2013).

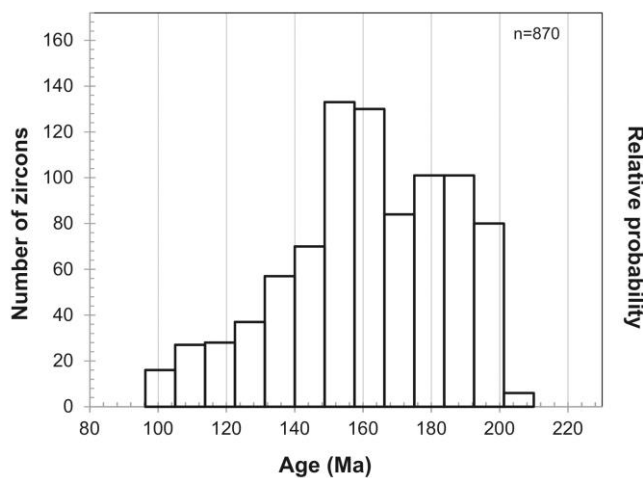


Figure 3.11. Detrital U-Pb zircon ages from boreholes showing that the density of ages is higher for the Lower to Middle Jurassic and decreases towards the Upper Jurassic to Lower Cretaceous, which is consistent with a decreasing volume of magma. Data are compiled from Nie et al. (2010), Horton et al. (2010), Saylor et al. (2011), Bayona et al. (2013), Caballero et al. (2013) and Silva et al. (2013).

3.5.2. Genesis of the Mesozoic magmatic arc of the Central Cordillera

Geochemical results of the Middle Jurassic (Payandé stock, c. 165 Ma), the northern segment of the Ibagué Batholith (c. 158-142 Ma), and the Lower Cretaceous (Mariquita stock, ca. 143-129 Ma) plutonic rocks, indicate a limited variation in the LREE/HREE ratios (Fig. 3.12) and in the alkalis content (K_2O and Na_2O) over time. Trace-element patterns, combined with the negative Nb and Ti anomalies, suggest a volcanic-arc setting, which is also confirmed by the tectonic discrimination diagrams (Fig. 3.13; Harris et al., 1986). The distinctive depletion in HFSE and LILE enrichment, along with the widespread presence of Ca-amphibole and sphene in Jurassic and Cretaceous rocks, suggests a significant input of volatile aqueous contents in the melt, as expected in a subduction setting (Best, 2003).

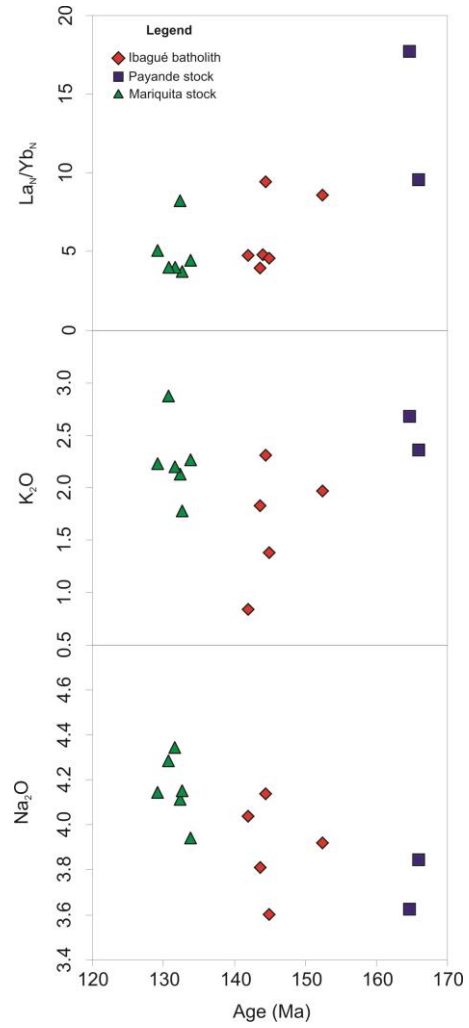


Figure 3.12. LREE/HREE ratios and alkalis content (K_2O and Na_2O) over time.

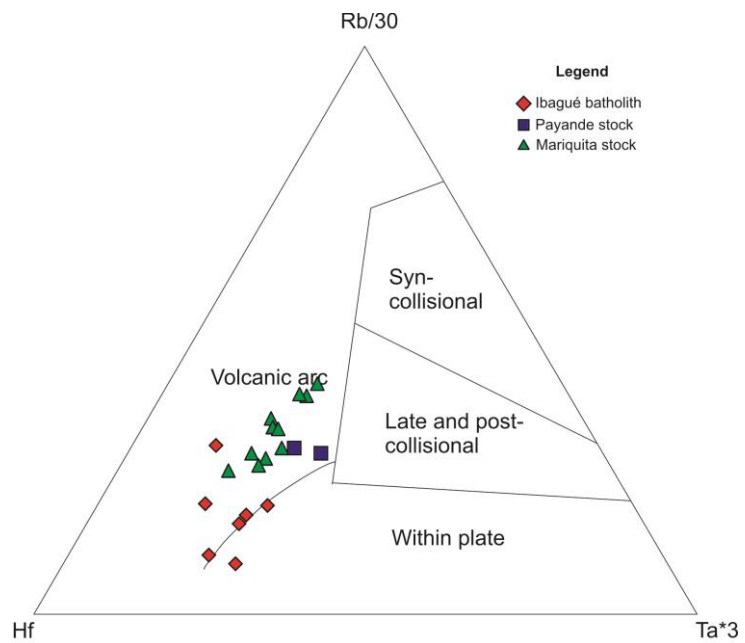


Figure 3.13. Discrimination diagram of granites (Hf-Rb/30-Ta*30) according to Harris et al. (1986).

Lead isotopes show a linear array in $^{207}\text{Pb}/^{204}\text{Pb}$ vs $^{206}\text{Pb}/^{204}\text{Pb}$ (Fig. 3.14), in agreement with similar lead isotope studies documented in other plutons of the Central Cordillera (Leal-Mejía, 2011). $^{207}\text{Pb}/^{204}\text{Pb}$ values ranging from 15.59 to 15.62 are almost constant for the Payandé and Mariquita stocks, as well in the northern part of the Ibagué Batholith. These values fall along the orogenic curve of the plumbotectonic model (Fig. 3.14) of Zartman and Doe (1981), which suggests mixed lead sources. $^{208}\text{Pb}/^{204}\text{Pb}$ ratios have more scattered values ranging between 38.28 and 39.10, but they still form a linear array that matches both the upper crust and orogenic curves in the plumbotectonic model (Zartman and Doe, 1981). A remarkable feature of lead isotope data is that there is limited variation in the Pb isotope ratios, which suggests that the Pb from the three plutons comes from the same crustal source.

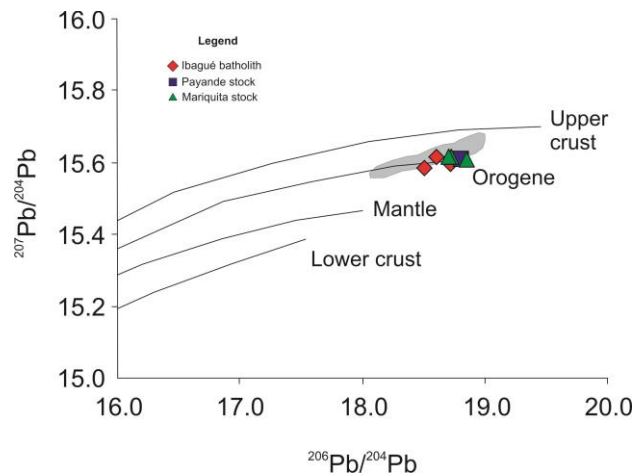


Figure 3.14. Lead isotopic evolution curve according to the plumbotectonics model of Zartman and Doe (1981).

Hf and Nd isotope data indicate an increasing juvenile character from the older to the younger plutons. This is observed in the negative correlation between initial ϵ_{Hf} and $^{176}\text{Hf}/^{177}\text{Hf}$ in the zircon and whole-rock geochemical data compared with $^{206}\text{Pb}/^{238}\text{U}$ crystallization ages (Fig. 3.15). Similar results were obtained by Cochrane et al. (2014a) in their study of magmatic rocks of Colombia and Ecuador. Despite this increasing juvenile trend with time, the comparison of initial ϵ_{Hf} vs. ϵ_{Nd} reveals differences between zircon and whole-rock data, with whole-rock data plotting at slightly more radiogenic values than the corresponding zircon with a few exceptions from the Mariquita stock (Fig. 3.16). This suggests that the Hf isotope ratios of zircon record an important sedimentary input that is not detected in the $^{206}\text{Pb}/^{238}\text{U}$ ages (Figs. 3-5) or in other whole-rock isotopic values (Fig. 3.15 and 16). Clearly, the sample of the Payandé stock (CSP5), which shows both whole-rock and

zircon data below the terrestrial array, has a sedimentary contamination of its source. The Ibagué Batholith samples also show that some clastic material is entraining by subduction and thus contaminating its mantle source. This behavior is similar to a sample of the Mariquita stock (CM19) in that whole-rock Hf and Nd values plot above the mantle array and the ϵ_{Hf} in zircon plot below it. This probably indicates a clastic source of contamination similar to that for the Ibagué Batholith. In Sample CM4, in contrast, the majority of Hf values in zircon and whole-rock data are situated above the mantle array (Fig. 3.16), indicating minor clastic sediment contamination. Although no zircon grains were analyzed in samples CI7 (Ibagué Batholith) and CM8 (Mariquita stock), their whole-rock ϵ_{Hf} and ϵ_{Nd} values, which plot above the mantle array, possibly indicate that the magmas were derived from a pelitic source.

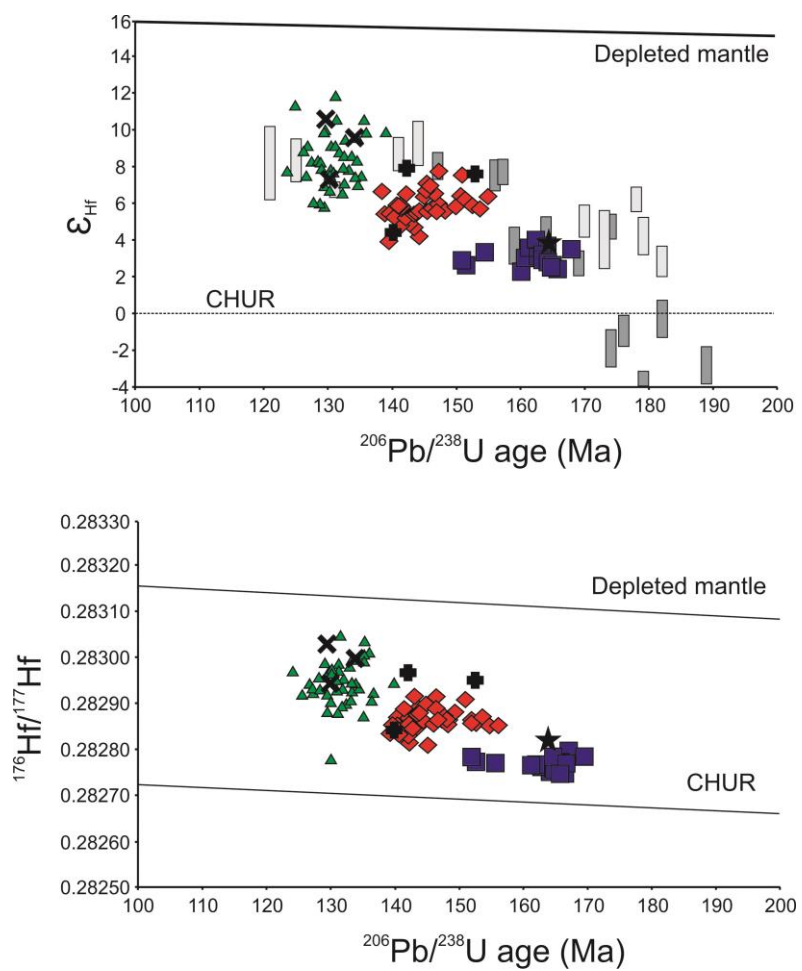


Figure 3.15. Variation of initial ϵ_{Hf} and $^{176}\text{Hf}/^{177}\text{Hf}$ in zircon and whole rock with $^{206}\text{Pb}/^{238}\text{U}$ crystallization age. **Triangles and rotated crosses:** Mariquita stock zircon and whole-rock data, respectively; **Diamonds and crosses:** Ibagué Batholith zircon and whole-rock data, respectively; **Squares and star:** Payandé stock zircon and whole-rock data, respectively; **Dark grey rectangles:** data from Colombian granites (Cochrane et al., 2014a); **Light grey rectangles:** data from Ecuadorian granites (Cochrane et al., 2014a).

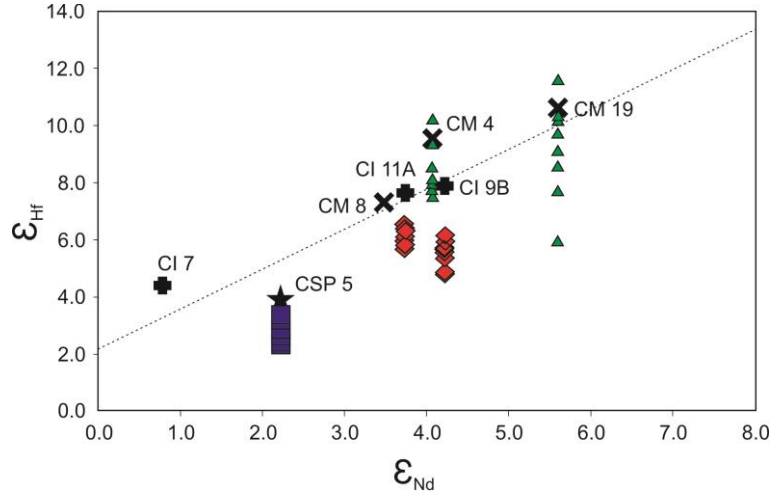


Figure 3.16. Initial ϵ_{Hf} vs. ϵ_{Nd} diagram. Symbols same as in fig. 13. Hf-Nd mantle array from Vervoort and Blöcher-Toft (1999).

The temporal trend observed in the isotopic fingerprints of the Jurassic magmatism is related to the behavior of the subduction setting through time. Slab roll-back has been considered as a potential mechanism that also controls the extensional tectonic on the margin (Leal-Mejía, 2011; Cochrane et al., 2014a; Spikings et al., 2015). This mechanism can also provide a progressive addition of juvenile material to the crust (Kemp et al., 2009) that, combined with a rapid upward migration of the magma, may prevent significant contamination of the magma with the continental crust, resulting in the Hf and Nd isotopic evolution previously described.

However, the roll-back model is faced with some issues, such as (1) the unreliability of the westward migration of magmatism (Leal-Mejía, 2011; Cochrane et al., 2014a; Spikings et al., 2015) and (2) the decreasing magmatic activity after c. 165 until the Early Cretaceous. Regarding the age distribution of the magmatic rocks, we note that the Payandé stock is located to the east of the older granitoids of the southern part of the Ibagué Batholith. Furthermore, when all published geochronologic results are taken into account (e.g., Bustamante et al. 2010), we see no clear east or west age migration in the time interval between 190 Ma and 129 Ma.

We suggest the following alternative models to explain the compositional (juvenile trend) and spatial features such as the reduction of the magmatic products in the study area:

1. A two-stage melting model, where early mantle-derived basaltic magmas are emplaced in the lower crust and are re-melted by mantle heat input to yield intermediate to felsic magmas (Annen and Sparks, 2002; Annen et al., 2006).

2. Continuous melting of subducted mélange, consisting of basalt and sediments, and subsequent transport of molten material as silicic diapirs into the mantle wedge. Further fractionation will form granodioritic melts, leaving a granulite residue in the source (Vogt et al., 2013; Castro et al., 2013).

The former process implies a long-term evolution of the arc system in that the recurrent mafic underplating of the lower crust would provide melts less contaminated by crustal rocks through time (and consequently more juvenile). Although this scenario has been suggested for the evolution of other magmatic arcs (Pankhurst et al., 1999; Hervé et al., 2007), it does not consider the continental radiogenic input transferred by subducted sediments that was identified in the isotopic analysis.

Recent numerical and experimental models predict the melting of subducted mélange (basalt + sediments) and subsequent transport of molten material as silicic diapirs into the mantle wedge (Vogt et al., 2013; Castro et al., 2013). The emplacement of these diapirs at crustal levels is caused by relamination when melt extraction from the diapir weakens the lithosphere assisting its ascent (Hacker et al., 2011; Behn et al., 2011; Castro, 2014). Further partial melting of the diapirs produces granodiorite liquids and mafic granulite residues. Geochemical and isotopic characteristics of the liquid will depend on the rates of basalt and sediment melting (source) and will not reflect any changes in major element compositions, whereas the isotopic signature will evolve towards a more primitive composition (Vogt et al., 2013).

Within the scenario where the Na₂O, K₂O and La_N/Yb_N composition is preserved (Fig. 3.12), the rocks became isotopically more juvenile through time (Vogt et al., 2013). This isotope evolution is associated with a hybrid source composed by melting of basalt and sediment, where an increase in the basaltic component and a decrease in sediment will move the isotopic ratios to more radiogenic isotope compositions (more positive epsilon Nd and Hf values). As a consequence, the major element composition will remain unaffected since it is dependent on the temperature of melting rather than the source composition, as demonstrated by the experimental work of Castro et al. (2010). The melting of the sedimentary components will yield magmas that consequently end up in a diapir, which will be more refractory, and magma volumes will also decrease as a result (Fig. 3.17).

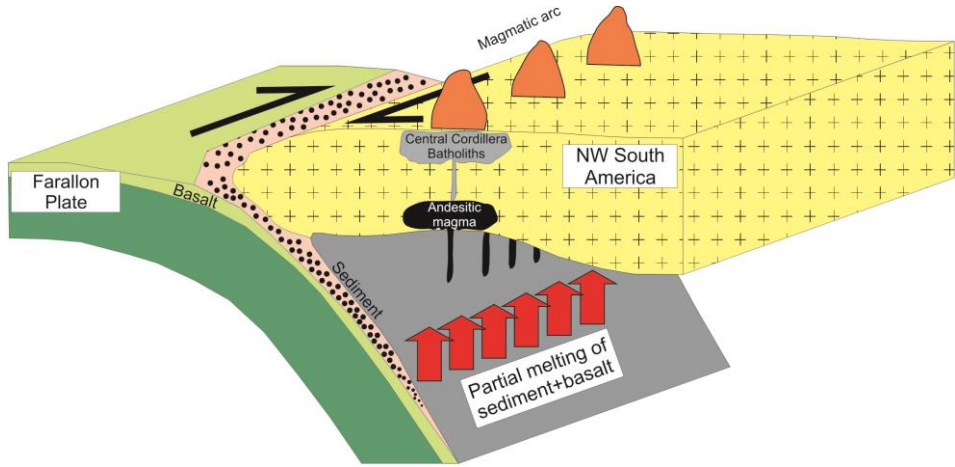


Figure 3.17. Model proposed (not to scale) for the generation of the Early Jurassic to Early Cretaceous magmatic arc in the Northern Andes of Colombia. The figure shows the relationship between oblique convergence, clastic input, and basalt+sediment melting of the crust to form granodioritic batholiths (modified from Castro, 2014).

We therefore suggest that the model of melting of a subducted mélange seems more plausible than the lower crustal emplacement of basaltic magmas because the latter does not fit with the juvenile trend recorded in the isotopic values of the studied rocks.

The decrease in magmatic activity after ca. 145 Ma is significant in Colombia (Villagómez et al., 2011; Cochrane et al., 2014a) and Ecuador (Chiariadía et al., 2009). Several mechanism have been proposed to explain the absence of magmatic activity in convergent margins, including shallowing of the subduction angle, changes in convergence rate or removal of the fusible components of the magmatic source (Jarrard, 1986; Glazner, 1991; Ducea, 2001; Sagong et al., 2005; Gorczyk et al., 2007; Hervé et al., 2007). Shallowing of the slab is not considered to be a viable mechanism in this case because it is accompanied by broadening of the arc and compressional tectonic events (Ramos, 2009). Such a process is not observed in the margin, which is instead characterized by extensional deformation (Sarmiento-Rojas et al., 2006). Slow convergence is commonly associated with an increase in magma production in a subduction margin. Paleotectonic reconstructions for the Andes have shown that the convergence rate between 140 and 130 Ma slowed down (Maloney et al., 2013). However, as already discussed, igneous productivity also seems to have decreased over this interval.

Stratigraphic and paleomagnetic constraints suggest that the continental margin of the northern Andes is characterized by prominent extensional tectonics and lateral displacement of terranes (Bayona et al., 2006, 2010; Sarmiento-Rojas et al., 2006). Moreover, tectonic reconstructions have shown that the plate margin may have had a significant south to north convergence vector in the Late Jurassic (Seton et al., 2012). This change in the upper plate

configuration is related to a major change in the convergence obliquity (Fig. 3.17), resulting in a magmatic arc controlled by transtensional strains. In this scenario, the amount of sediment entering the subduction channel becomes minor because they are preferentially transported along a trench (Malatesta et al., 2013); consequently reducing the water content that reaches the mantle wedge. This model, together with the aforementioned refractory behavior of the source mélange, which probably has already removed the most fusible components, represents the major controls of arc evolution in the northern Andes.

3.5.3. Jurassic tectonomagmatic evolution of the Northern Andes

We now integrate the characteristics of the aforementioned magmatic interval with the older Jurassic record, which includes the southern segment of the Ibagué Batholith along with the plutonic rocks from the Garzón Massif and the Mocoa Batholith further south.

During the Permo-Triassic, the Central Cordillera and the Cordillera Real of Colombia and Ecuador experienced the last phases of the agglomeration of Pangea and the beginning of its break-up, which is reflected in a bimodal S-type and gabbroic syn-tectonic magmatism (Vinasco et al., 2006; Restrepo et al., 2011; Cochrane et al., 2014b; Martens et al., 2014). Following this event, there is an apparent magmatic and tectonic quiescence, reflected in the formation of significant carbonate platforms until the Late Triassic to Early Jurassic (Cediel et al., 2003; Ramos, 2009), until subduction resumes in the Early Jurassic (Ramos, 2009; Vásquez et al., 2009).

During the earlier phases of subduction, voluminous I-type magmatism took place, as suggested by the presence of large 200 Ma to 170 Ma plutons in the Northern Andes. These magmatic bodies are characterized by a more radiogenic signature compared with the younger rocks (Leal-Mejía, 2011; Cochrane et al., 2014a). Major extensional basins were also formed within the margin during this time interval (Sarmiento-Rojas et al., 2006). These events may reflect the presence of a steeper subduction (Gorczyk et al., 2007) and probably the existence of a slab roll-back mechanism (Cochrane et al., 2014a). This earlier magmatic phase was replaced by changes in magmatic volumes and the formation of an oblique margin with a strong decrease in magma production until ca. 110 Ma (Villagómez et al., 2011). A Jurassic collision-related metamorphic event between 158 Ma and 147 Ma immediately to the west of the northern segment of the Ibagué Batholith took place (Blanco-Quintero et al., 2014). This event overlaps in time with the formation of the studied plutonic rocks that do not show signs of syn-tectonic intrusion. Therefore, following Blanco-Quintero et al. (2014), this event may

have taken place in an allochthonous position and may reflect along-strike segmentation of the Jurassic margin in an oblique regime where transpression and transtension behavior are distributed along the margin. As oblique convergence continues and the subducted hybrid mélange (Castro et al., 2013) is melted losing the sedimentary input and increasing the basaltic and serpentinite signature, arc magmatism become isotopically more juvenile and refractory. As convergence become more oblique the formation of new mélanges and fluid flow in the mantle wedge is also reduced (Hoernle et al., 2008; Malatesta et al., 2013; Rooney et al., 2015) contributing to the reduction in the magmatic products seen in the Late Jurassic to Early Cretaceous arc.

The discussed tectonomagmatic model involves Jurassic magmatic units that are spatially related along the Central Cordillera and Upper Magdalena Valley, and represent a long termed evolution of a stationary arc. Nevertheless, we are aware that the correlation with other Jurassic segments of the Northern Andes must be viewed with caution because several Mesozoic domains appear to have paleomagnetic signatures of south to north terrane transfer (Bayona et al., 2006; 2010), which might have translated different blocks, masking their original tectonic relations and leading to misinterpretations. However, even if an allochthonous or autochthonous view is followed (Bayona et al., 2006; Spikings et al., 2015), the discussed tectonomagmatic controls seem to be a characteristic of the Northern Andes of Colombia and Ecuador.

3.6. CONCLUSIONS

The integration of new petrographic, geochronological, geochemical, and isotopic results from magmatic rocks of the Central Cordillera and Upper Magdalena valley indicate magmatism in a stationary arc between 165 Ma and 129 Ma. This magmatism is characterized by an increase in the isotopic $\epsilon_{\text{Nd(i)}}$ and $\epsilon_{\text{Hf(i)}}$ values that can be related to the evolution of the source area over time. Possible scenarios for the long-term evolution of the magmas include: (1) compositional changes in the lower crust, in which the older crust is replaced by basaltic magmas that are subsequently melted; and (2) a cold plume basalt+sediment diapir that involves the replacement of radiogenic sedimentary inputs towards more juvenile basaltic and mantle sources. However, the second model, when combined with changes in convergence obliquity, is able to explain the progressive reduction in magmatic activity until it eventually ceases between 129 Ma and 110 Ma. The integrated results indicates that the Northern Andes experienced very high magmatic productivity between 200 Ma and 170 Ma but that ceased

completely in the Early Cretaceous probably with the reduction of fusible components transported by the subduction zone into the mantle.

It is therefore suggested that the long-term evolution of stationary continental arcs is characterized by an increase in its juvenile character and decrease in the volume as its source become more depleted and refractory trough time, which is also expected to be a cyclic process. More regional scale tectonic controls such as steepening of the subduction angle with associated roll-back or changes in convergence obliquity may also influence the compositional, spatial distribution and volumes of the magmatic productivity of arcs, and therefore suggest that the reconstruction of feasible magmatic arc models requires a detailed field, compositional and geochronological approach.

Capítulo 4

Geochemistry and isotopic signatures of Paleogene plutonic and detrital rocks of the Northern Andes of Colombia: a record of post-collisional arc magmatism³

ABSTRACT

The northern Andes have experienced overimposed processes of subduction and collision associated with the convergence against the Caribbean Plate. Since the end of the Mesozoic, these processes have been recorded in the formation of Late Cretaceous to Eocene plutonic rocks in the Central Cordillera of the Colombian Andes. In this contribution the magmatic evolution and tectonic relation of selected Paleogene plutons is analyzed by means of integrated geochronological, geochemical and isotopical constraints. U-Pb zircon crystallization ages from representative Paleocene-Lower Eocene plutonic rocks (tonalites and granodiorites) shows that this magmatism is characterized by crystallization ages between 60 Ma and 53 Ma, whereas $\epsilon_{\text{Hf(i)}}$ values range between -4 and +7, Nb and Ti negative anomalies, a high LREE/HREE and Sr/Y >28 ratios are consistent with a continental magmatic arc setting. Sr, Nd and Pb relatively low radiogenic isotopes from selected samples account for an heterogeneous crustal source.

It is proposed that this Paleocene to Eocene arc rocks of relatively limited areal expression when compared with older Mesozoic arc rocks, were affected by high pressure differentiation at the garnet stability field as indicated in the high Sr/Y ratios. When evaluated through time the continental crust shows evidences of crustal thickening as a consequence of the former Mesozoic subduction and arc-continent collisional history. Ages and Hf isotopes from detrital zircon extracted from volcanoclastic rocks of eastern Colombia re-enforced the possibility of a distal magmatic focus. It would have formed due to mantle flow in the inherited Mesozoic extensional structures, as the subduction of the Caribbean oceanic slab was active during the Paleogene after the arc-continent collisional event.

³ Bustamante, C., Cardona, A., Archanjo, C., Bayona, G., Lara, M., Valencia, V. 2016. Geochemistry and isotopic signatures of Paleogene plutonic and detrital rocks of the Northern Andes of Colombia: a record of post-collisional arc magmatism. *Lithos*.

4.1. INTRODUCTION

The Late Cretaceous to Paleogene tectonic evolution of the northern Andes has been related to the initial collision and subsequent subduction of the buoyant Caribbean oceanic plate under the northwestern South American margin (Kerr et al., 1997; Pindell and Kennan, 2009; Spikings et al., 2001, 2005, 2015; Luzieux et al., 2006; Vallejo et al., 2006; Villagómez et al., 2011; Bayona et al., 2011; Cardona et al., 2011a). Vestiges of such settings are found in a series of intrusive rocks in both the Central and Western Cordilleras of the Colombian Andes (Aspden et al., 1987; Villagómez et al., 2011; Bayona et al., 2012), together with immature volcanoclastic sandstones and tuffs in the Eastern Cordillera and Llanos basin as far as ca. 400 km inland (Fig. 4.1A; Bayona et al., 2012).

The Paleocene to Eocene plutonic rocks of the Central Cordillera were formed after an island arc and plateau-continent collision. Also, they have been related to the new subduction of the Caribbean plate under the South American margin (Pindell et al., 2005; Cardona et al., 2011b; Villagómez et al., 2011; Bayona et al., 2012). However, their precise origin and its role as a record of collisional to subduction tectonics have not been fully explored. This is because geochemical data is still limited and the age constraints are based only on K-Ar data which represent cooling instead of crystallization ages (see Aspden et al., 1987 for a review) or limited U-Pb zircon ages (Leal-Mejía, 2011; Bayona et al., 2012).

In this contribution, we present new U-Pb magmatic zircon crystallization ages, whole rock geochemistry and Sr-Nd-Pb and Hf isotopes on magmatic and detrital rocks to investigate the origin of Paleogene magmatism of the Colombian Andes. We propose a tectonic setting in which melting and differentiation of mafic and sialic crust occurred at high pressures in a lower continental crust (Chiaradia, 2015; Chapman et al., 2015). That crust was underplated tectonically and magmatically during Late Cretaceous and Paleocene arc-continent collisional event (Cardona et al., 2011b; Villagómez et al., 2011; Bayona et al., 2012; Spikings et al., 2015). The inherited tectonic evolution of a margin, in turn, can influence the composition and spatial distribution of the overimposed magmatic rocks.

4.2. GEOLOGICAL SETTING

The Andean range in Colombia is divided into three different Cordilleras separated by major river valleys (Fig. 4.1 A, B): (i) the *Western Cordillera*, which includes Cretaceous oceanic rocks, was accreted during the Late Cretaceous to Early Paleogene migration and collision of the Caribbean plate against the northwestern South American margin (Nivia,

1996; Spaeda and Espinosa, 1996; Kerr et al., 1997; Pindell and Kennan, 2009; Villagomez et al., 2011; Villagómez and Spikings, 2013; Spikings et al., 2015). (ii) The *Central Cordillera* is built over an extensive Paleozoic to Triassic metamorphic basement with associated S-type granitoids (Vinasco et al., 2006; Martens et al., 2014; Cochrane et al., 2014a). Late Cretaceous plutonic rocks formed between ca. 90 and 65 Ma (Aspden et al., 1987; Ibañez-Mejia, 2007; Ordóñez-Carmona et al., 2008; Vinasco et al., 2006; Villagómez et al., 2011; Leal-Mejia et al., 2010) intrudes Jurassic metamorphic rocks (Blanco-Quintero et al., 2014; Bustamante et al., 2016). Its eastern flank includes an extensive series of arc-related Jurassic to Cretaceous plutonic and volcanic rocks (ca. 190 and 129 Ma) (Brook, 1984; Aspden et al., 1987; Sillitoe et al., 1982; Bayona et al., 1994; Cediel and Cáceres, 2000; Cediel et al., 2003; Vinasco, 2006; Villagómez et al., 2011; Leal-Mejia, 2011; Bustamante et al., 2010; 2016; Cochrane et al., 2014b). (iii) The *Eastern Cordillera* is formed by discontinuously exposed Proterozoic and Paleozoic metamorphic and sedimentary rocks. These are covered by thick deformed Mesozoic and Cenozoic sedimentary rocks of marine, transitional and continental environments. These deposits document the transition from extensional to compressional tectonics, and the subsequent Cenozoic deformation and uplift of the Eastern Cordillera (Villamil, 1999; Horton et al., 2010; Sarmiento-Rojas et al., 2006; Parra et al., 2012; Bayona et al., 2013).

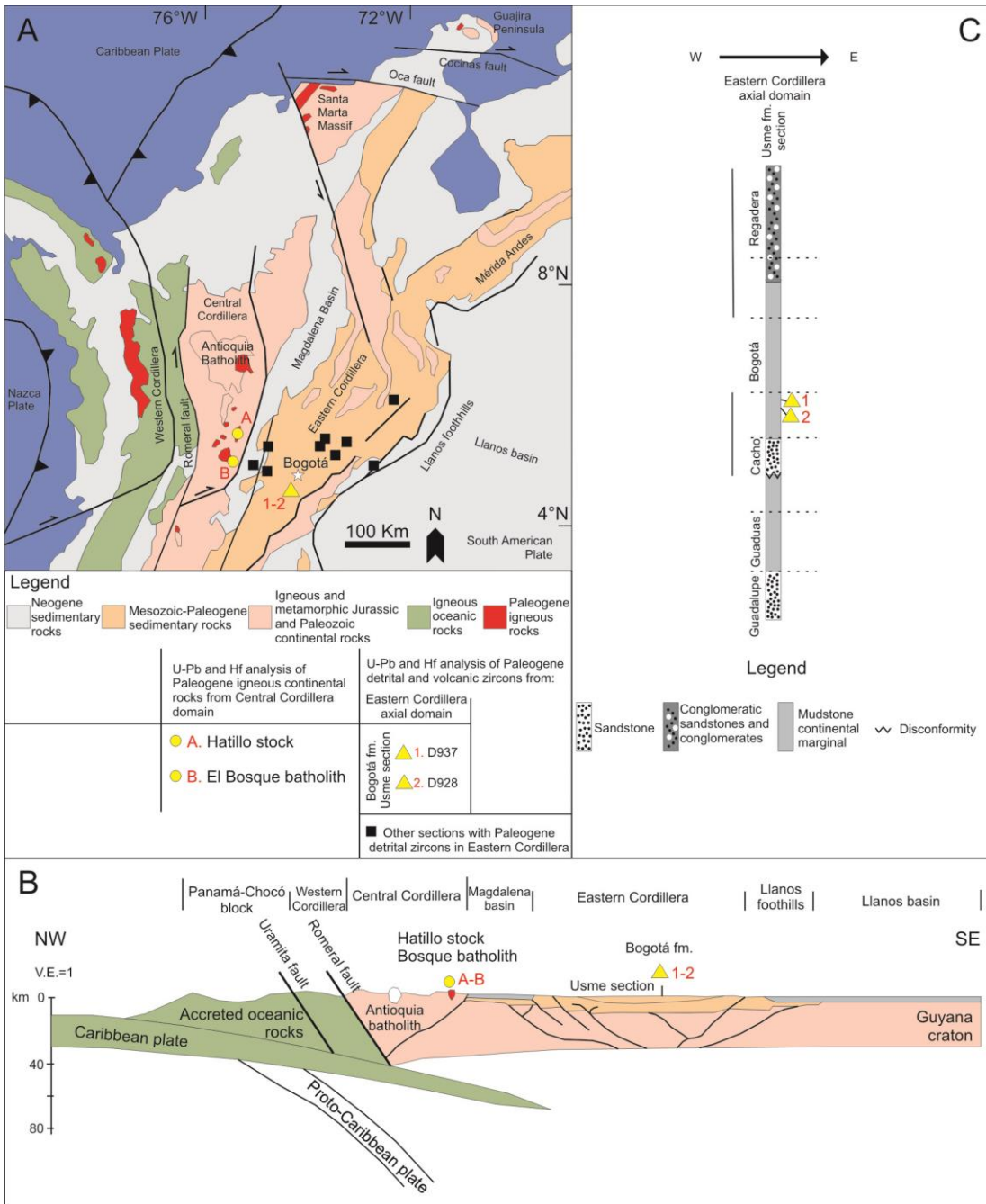


Figure 4.1. A. Location of Paleogene igneous bodies sampled in Western and Central Cordillera and Paleogene detrital zircons sampled in Eastern Cordillera of Colombia; **B.** Regional cross section of Central Colombia with Paleogene samples; **C.** Sedimentary section with detrital samples analyzed. Figure modified from Bayona et al. (2012).

4.2.1. Paleogene magmatism in the Colombian Andes

Paleogene arc-related magmatic bodies with crystallization ages between ca. 60 - 40 Ma are exposed in the Western Cordillera as bodies of batholithic (eg. Mandé and Acandí) to stock dimension intruding Upper Cretaceous oceanic volcano-sedimentary sequences (Aspden et al., 1987; Montes et al., 2015). Such rocks are considered as intra-oceanic arc related

sequences accreted to the continental Panamá-Chocó block since the Miocene (Duque-Caro, 1990; Montes et al., 2015).

Within the Central Cordillera, outcrops several bodies of stock and batholithic sizes and mainly granodiorite to tonalite compositions, include Hatillo, Manizales, Norcasia, El Bosque, Sonsón and Santa Barbara plutons (Fig. 4.1), and some of the eastern facies of the Antioquia Batholith (Aspden et al., 1987; Leal-Mejía, 2011; Bayona et al., 2012). All of them intrude the Triassic and Jurassic metamorphic rocks of the Central Cordillera and are characterized by their smaller sizes when compared with the Jurassic and Cretaceous magmatic belt of the Central Cordillera, reaching mostly stock dimensions (Aspden et al., 1987). Plutonic rocks of the same age are also found in the Sierra Nevada de Santa Marta (Tschanz et al., 1969; Cardona et al., 2011a; 2011b) and the Jarara range of the Guajira Península (Fig. 4.1A). They include the Santa Marta batholith and the Parashi stock and intrude metamorphosed Cretaceous volcano-sedimentary sequences (Cardona et al., 2014).

Provenance studies including detrital zircon geochronology of siliciclastic deposits from Cesar-Rancheria basin in northern Colombia (Ayala-Calvo et al., 2009; Cardona et al., 2011a; Bayona et al., 2012), and the Eastern Cordillera basins (Bayona et al., 2012) show the presence of zircons with U-Pb ages ranging between 65 and 45 Ma. They are interpreted as derived from the erosion of both distal and proximal magmatic centers. According to Bayona et al. (2012), the wide distribution of Paleogene detrital zircons and sedimentological characteristics of several tuffaceous levels indicate that their detritus would be supplied by nearby volcanic centers. Provenance analysis on sedimentary basins and available geochronological results from magmatic rocks have suggested that after 50-45 Ma magmatic activity ceased in the Northern Colombian Andes, until it resumed as a well-defined magmatic arc that started to growth at ca. 25 Ma (Bayona et al., 2012; Echeverry et al., 2015; Montes et al., 2015).

4.3. SAMPLING AND METHODS

To understand the timing and processes that characterized the Paleogene magmatism of the Northern Andes, we sampled two Paleogene plutons, the Hatillo stock and the Bosque batholith (see location on Fig. 4.1), to investigate their whole rock geochemistry, Sr, Nd and Pb isotope compositions and Hf isotopes in zircons dated by U-Pb method. Besides plutonic rocks, two samples from volcanoclastic sedimentary rocks of the Bogotá formation (Fig. 4.1) were investigated to determine the provenance of their zircons. These samples are the same as

those studied by Bayona et al. (2012), in which Paleogene zircons were found. We combine the detrital zircon geochronology with Hf isotopes to check the origin of these crystals by comparing their signatures with zircons from plutonic rocks of the same age. U-Pb ages from the detrital samples are those presented by Bayona et al (2012). Although our analysis will be concentrated in a local segment of the margin, we will integrate the new results with published geochemical constraints from other Paleogene and Cretaceous magmatic rocks of the Colombian Andes, in order to gain a regional perspective of the Early Paleogene evolution of the Northern Andean margin.

4.3.1. Whole rock geochemistry

Bulk whole rock chemical analysis of 14 samples (Table 4.1) were determined for the Hatillo stock (12 samples) and Bosque batholith (2 samples). The samples were crushed using jaw crusher and powdered using tungsten carbide ring mill. Major and trace elements were analyzed using a Rigaku 3370 XRF spectrometer at the Washington State University. Details of sample preparation, dilution and analytical procedure are described in Johnson et al. (1999). REE were determined by inductively coupled plasma-mass spectrometry (ICP-MS) at the Washington State University. A 2 g aliquot is weighed into a graphite crucible and mixed with 2 g of LiBO₂ flux. The crucibles are placed in an oven and fused at 1000° C in a muffle furnace for 30 minutes. The resultant bead is ground in a steel ring mill and a 0.25 mg portion is dissolved using HNO₃ (2 ml), HF (6 ml) and HClO₄ (2 ml) at 110° C.

4.3.2. Whole rock Sr, Nd and Pb isotopes

Analyses were acquired using a Thermo-Finnigan Neptune multicollector system at Washington State University and results are presented in Table 4.1. Procedures for sample preparation and dilution details for Sr, Nd, and Pb isotopes are those as in Gaschnig et al. (2011). Sr analyses were corrected for mass fractionation using ⁸⁶Sr/⁸⁸Sr = 0.1194 and normalized using NBS-987. Average reproducibility with 2 standard deviations of ⁸⁷Sr/⁸⁶Sr was ±0.00005. Initial isotopic values were calculated using Rb and Sr concentrations from XRF for Sr isotopes. Sm and Nd were prepared by following the procedures described in Vervoort and Blichert-Toft (1999). Sm was corrected using ¹⁴⁷Sm/¹⁵²Sm=0.56081 and Nd was corrected for mass fractionation using ¹⁴⁶Nd/¹⁴⁴Nd=0.7219 and normalized using the Ames Nd standard (±0.000020 2σ average reproducibility). Pb was separated using the Tl doping method of White et al. (2000). After correcting for the mass bias using the Tl, samples were

normalized to the triple-spike values for NBS-981 from Galer and Abouchami (1998). ϵ_{Nd} values were calculated using present day values of $^{143}\text{Nd}/^{144}\text{Nd} = 0.512630$ and $^{147}\text{Sm}/^{144}\text{Nd} = 0.160$ for CHUR (Bouvier et al., 2008).

4.3.3. U-Pb Geochronology in zircon

Traditional techniques for separating zircon concentrates were used, including crushing, fragmentation, pulverization, sieving. Water table and Frantz isodynamic were used for an initial density and magnetic separation respectively. Zircon concentrates were obtained after using methylene iodide (3.30-3.33 g/cm³) to separate by density the non-magnetic fraction. Zircons were handpicked under the microscope and mounted in a 1-inch diameter epoxy puck and slightly ground and polished to expose the surface and keep as much material as possible for laser ablation analyses. Cathodoluminescence (CL) images were obtained for zircons and then LA-ICP-MS U-Pb analyses were conducted using a New Wave Nd:YAG UV 213-nm laser coupled to a ThermoFinnigan Element 2 single collector, double-focusing, magnetic sector ICP-MS at Washington State University. Operating procedures, parameters and fractionation correction are described in Chang et al. (2006). Laser spot size was 30 µm and repetition rate was 10 Hz. He and Ar carrier gases delivered the sample aerosol to the plasma. Each analysis consists of a short blank analysis followed by 300 sweeps through masses 202, 204, 206, 207, 208, 232, 235, and 238, taking approximately 30 seconds. NIST 610 trace element glass was used to monitor U and Th concentrations. Zircon standard Plesovice with an age of 337.13 ±0.37 Ma (Sláma et al., 2008) was used. Uranium-lead ages were calculated using Isoplot 4.15 (Ludwig, 2003).

4.3.4. Hf isotopes in zircon

Hf isotope geochemistry analysis was performed on nine samples (Table 4.3) at the Geoanalytical Lab at Washington State University, using a ThermoFinnigan Neptune™ MC-ICP-MS equipped with 9 faraday collectors interfaced with a New Wave™ 213 nm UP Nd-YAG laser. Laser spot size was 40 µm and the data were acquired in static mode with 60 second integrations. Details of analytical procedures and data treatment follow those of Vervoort et al. (2004) and DuFrane et al. (2007). For the Hf-depleted mantle model ages (Hf_{TDM}), we used $^{176}\text{Hf}/^{177}\text{Hf}$ and $^{176}\text{Lu}/^{177}\text{Hf}$ for the individual zircon samples to determine their initial $^{176}\text{Hf}/^{177}\text{Hf}$ ratios at their crystallization ages. Projection back from zircon crystallization was calculated using a present value of 0.0150 for the estimated $^{176}\text{Lu}/^{177}\text{Hf}$ of

continental crust (Vervoort and Patchett, 1996; Goodge and Vervoort, 2006). The depleted mantle Hf evolution curve was calculated from present-day depleted mantle values of $^{176}\text{Hf}/^{177}\text{Hf}$ DM₍₀₎=0.283240 and $^{176}\text{Lu}/^{177}\text{Hf}$ DM₍₀₎=0.03979 (Vervoort et al., 2015).

4.4. RESULTS

4.4.1. Petrography, whole rock geochemistry and Sr-Nd-Pb isotopes of the Hatillo stock and el Bosque batholith

The Hatillo stock intrudes pelitic schists of Mesozoic age that formed mottled schists with biotite accumulations close to the intrusion site, probably formed by contact metamorphism. It is mainly granodioritic in composition with plagioclase An₂₅₋₃₅ (55-65 %), quartz (15-25 %), K-feldspar (5-15 %) and biotite (5-15 %). Hornblende is less than 2% modal and accessory minerals include epidote, zircon, apatite and ilmenite. Tourmaline is present as a product of hydrothermal alteration. Myrmekites are observed when alkali-feldspar is in contact with plagioclase. Epidote forms locally euhedral prismatic crystals with apatite inclusions (Fig. 4.2). Biotite crystals can reach 1.5 cm length and some grains display poikilitic textures with chadacrysts of zoned plagioclase and hornblende. El Bosque batholith has a granodioritic composition with plagioclase An₃₀₋₄₀ (50-60%), quartz (20-30 %), K-feldspar (10-20%) and biotite (10-15%); zircon and apatite are the main accessory minerals. Deformation twinning in plagioclase is common and along with quartz is recrystallized.

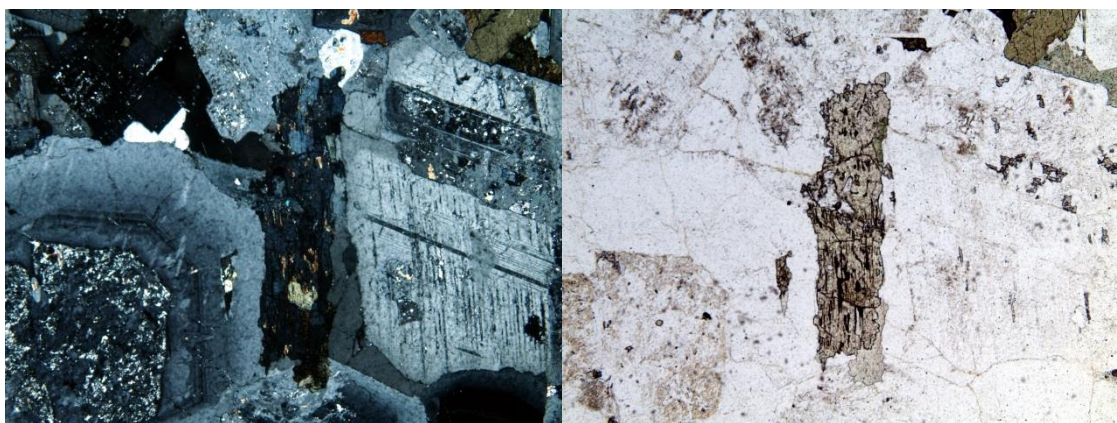


Figure 4.2. Prismatic epidote crystal in the Hatillo stock. Vertical length is 2.7 mm for each photograph.

In the SiO₂ vs K₂O diagram (Pecerillo and Taylor, 1976) the Hatillo stock and El Bosque batholith plot in the calc-alkaline field (Fig. 4.3A). Differences appear in the Alumina Saturation Index (ASI; Shand, 1943) where the Hatillo samples are metaluminous with a

subtle trend to the peraluminous field, whereas the two samples of the El Bosque batholith are clearly peraluminous (Fig. 4.3B). Such a divergence occurs possibly due to the higher content of biotite in the El Bosque samples.

Mg# ($\text{Mg}/[\text{Mg}+\text{Fe}^{2+}]$) for the Hatillo stock range from 49.7 to 54.4 and Sr/Y ratios from 34 to 55, El Bosque batholith has Mg# of 43.2 in average and Sr/Y ratios from 28 to 34. Multi-element plots (Fig. 4.3C) normalized to the primitive mantle (Sun and McDonough, 1989), shows that both the Hatillo and El Bosque plutons have deep negative Nb and Ti anomalies, relative depletion of HFSE, and enrichments in Ba and K which are characteristic of a subduction related setting. A volcanic arc affinity is defined according to the Hf-Rb/30-Ta*3 diagram (Harris et al., 1986; Fig. 4.3D). REE patterns (Fig. 4.3E) are characterized by the strong enrichment in light rare earth elements (LREE) and a strong depletion in heavy rare earth elements (HREE), with a high LREE/HREE ratio in both the Hatillo ($\text{La}/\text{Yb}_N=8.4-19.6$) and El Bosque ($\text{La}/\text{Yb}_N\sim27.3$) plutons. These rocks are usually characterized by an absence of Eu anomalies, but in a few samples it can be barely detected ($\text{Eu}/\text{Eu}^*=0.8 - 1.0$).

The Hatillo stock has an initial $^{87}\text{Sr}/^{86}\text{Sr}$ average value of 0.7047, whereas sample (CH21B) show a lower value of 0.7031. Initial $^{143}\text{Nd}/^{144}\text{Nd}$ isotopes ranges from 0.512604 to 0.512648 ($\epsilon_{\text{Nd(i)}}$ from +0.84 to +1.06). $^{206}\text{Pb}/^{204}\text{Pb}$ ratios are from 18.814 to 18.978, $^{207}\text{Pb}/^{204}\text{Pb}$ values range from 15.625 to 15.633 and $^{208}\text{Pb}/^{204}\text{Pb}$ ranges from 38.762 to 38.815. The Bosque batholith has higher initial $^{87}\text{Sr}/^{86}\text{Sr}$ (0.7062) and lower initial $^{143}\text{Nd}/^{144}\text{Nd}$ (0.512455 with an $\epsilon_{\text{Nd(i)}}$ of -1.98) than the Hatillo stock. $^{206}\text{Pb}/^{204}\text{Pb}$ ratios are of 18.764, $^{207}\text{Pb}/^{204}\text{Pb}$ of 15.575 and $^{208}\text{Pb}/^{204}\text{Pb}$ of 38.655.

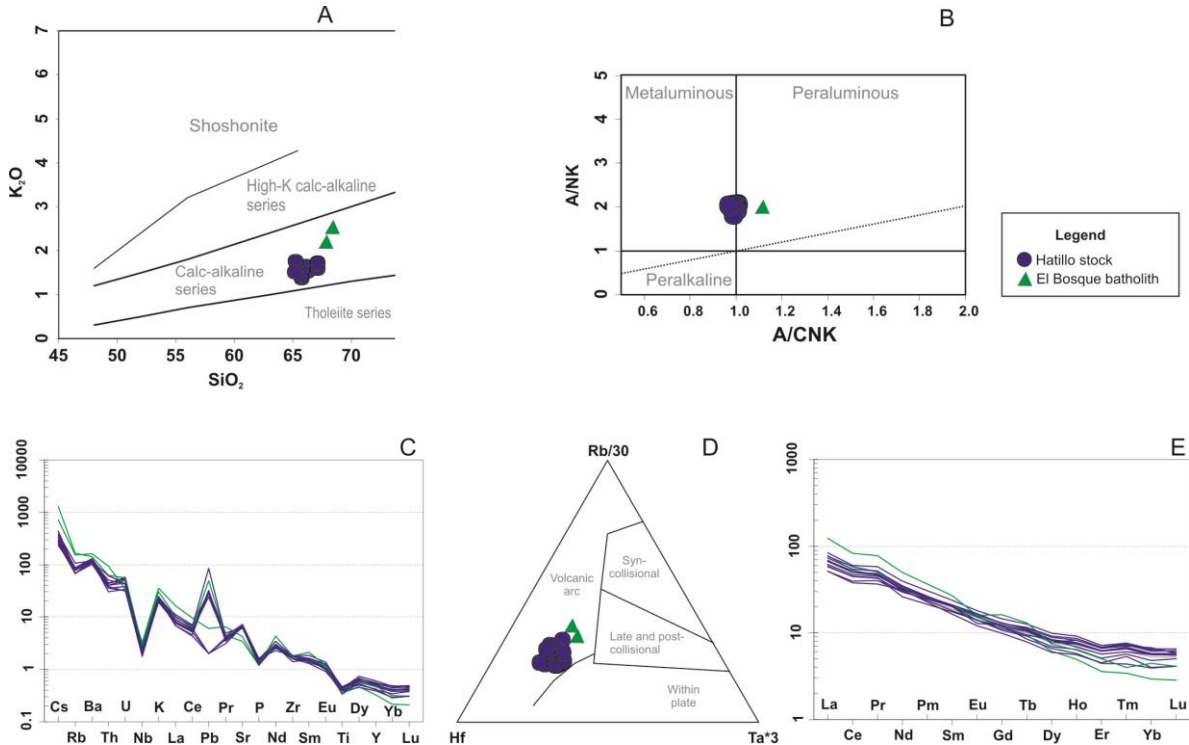


Figure 4.3. Geochemical classification and discrimination diagrams of samples from the studied plutons. A: Alkalinity index diagram of Pecerillo and Taylor (1976). B: Alumina saturation index diagram of Shand (1943). C: Multi-element plot normalized to primitive mantle according to Sun and McDonough (1989). D: Hf-Rb/30-Ta*3 geotectonic discrimination diagram of Harris et al. (1986). E: Chondrite normalized REE patterns according to Nakamura (1974).

4.4.2. Zircon U-Pb ages and Hf isotopes

Zircon CL images (Fig. 4.4), Concordia ages and Hf isotopes were obtained from a total of nine samples of the Hatillo (8) and El Bosque (1) plutons. 30 to 40 zircon rims were analyzed per sample, whereas Hf isotopes were obtained from eight dated zircons from each sample at the same spot where the ages were obtained. Ages from each pluton are presented in Figure 4.5.

Zircons in the CL images (Fig. 4.4) are euhedral with sizes varying between 120 and 400 µm. They normally are prismatic with a well-defined oscillatory zoning in agreement with their magmatic origin. Overgrowths were not observed.

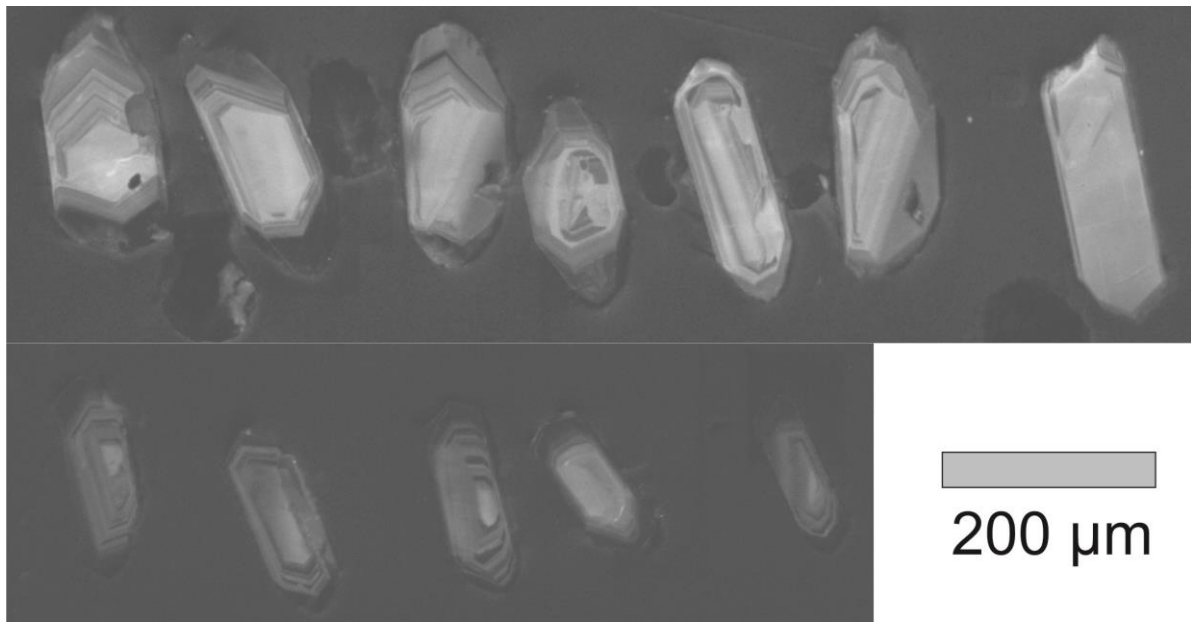


Figure 4.4. CL images from representative zircons from the Hatillo (upper) and El Bosque (lower) plutons.

The Hatillo stock show crystallization ages in the range of 55.0 ± 0.7 Ma and 53.2 ± 1.3 Ma (Fig. 4.5), which are similar to U-Pb ages reported by Bayona et al. (2012) obtained on the same stock. Initial ϵ_{Hf} isotope values in zircon ranges from -0.6 to +6.1 (Fig. 4.6). A core U-Pb age of 1000 Ma was found and with initial ϵ_{Hf} of +4.4.

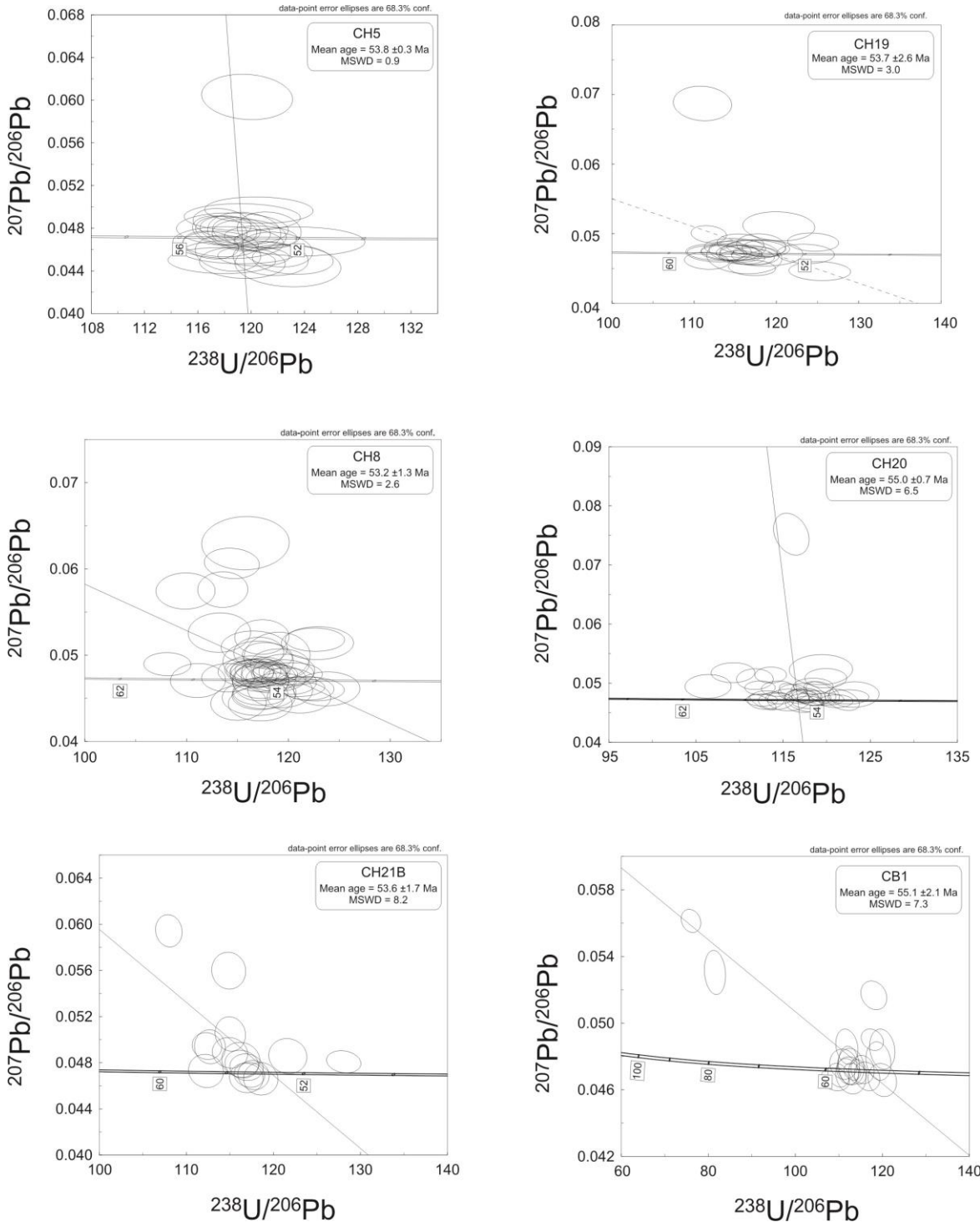


Figure 4.5. U-Pb Concordia ages obtained from plutons of the Central Cordillera: Hatillo stock and El Bosque batholith.

El Bosque batholith yielded a crystallization age of 55.1 ± 2.1 Ma (Fig. 4.5). Two crystals provided older ages (c. 238 Ma) which we attribute to inheritance. Initial ϵ_{Hf} values ranging from -4.5 to +1.3 are more radiogenic when compared with the others granitoids (Fig. 4.6).

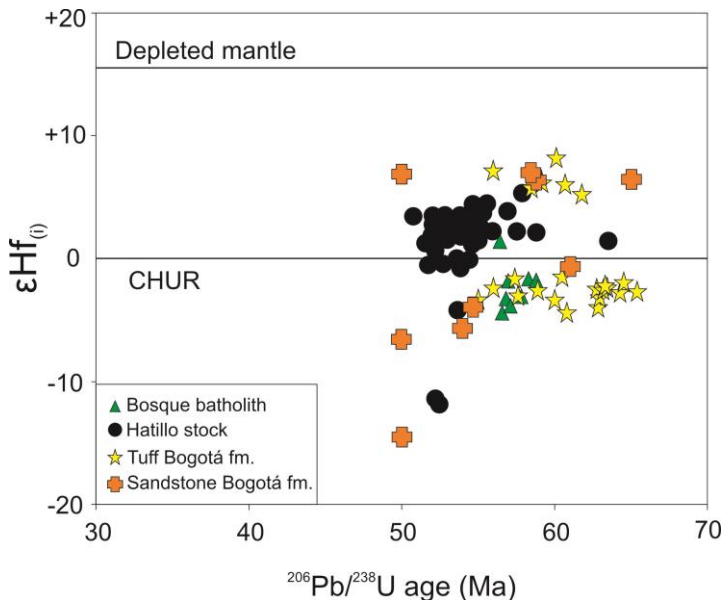


Figure 4.6. Initial ϵ_{Hf} vs $^{206}\text{Pb}/^{238}\text{U}$ age. Data from Paleogene igneous and detrital zircons from Central and Eastern Cordilleras of Colombia.

4.4.3. Volcanoclastic rocks

Samples from the Eastern Cordillera are Late Paleocene to Early Eocene levels from the Bogotá Formation (Usme section) including a sandstone (litharenite) and a tuffaceous level with 50-65 Ma detrital zircons. In these same samples Bayona et al. (2012) first identified the Paleogene magmatic zircons, we decided to get insight into their possible sources and test with Hf isotopes their relation with Central Cordillera sources or the existence of unexposed magmatic centers. We have analyzed 105 detrital zircons from two samples of the Bogotá Formation, both samples have yield late Paleocene to early Eocene zircons (39 zircon crystals; 37%), as well as Mesozoic to Precambrian zircons population in the litharenite (D937).

4.4.3.1. Pre-Paleogene zircons

The older detrital zircon grains are characterized by Mesoproterozoic to early Neoproterozoic (1701 - 778 Ma; 10 grains) and Paleozoic (525 - 264 Ma; 7 grains) ages. The Proterozoic zircons have a wide range of initial ϵ_{Hf} values ranging from -8.7 to +7.4 whereas Paleozoic zircons range from -11.3 to -1.0 (Fig. 4.7).

Triassic (244 - 210 Ma; 4 grains) and Jurassic (195 - 146 Ma; 10 grains) detrital zircons show initial ϵ_{Hf} values, respectively, from -3.5 to +8.8 and from -10.2 to +9.9 (Fig. 4.4). A population of thirty-one Cretaceous zircons (144 - 65 Ma) has initial ϵ_{Hf} values between -7.7 and +7.8 (Fig. 4.7).

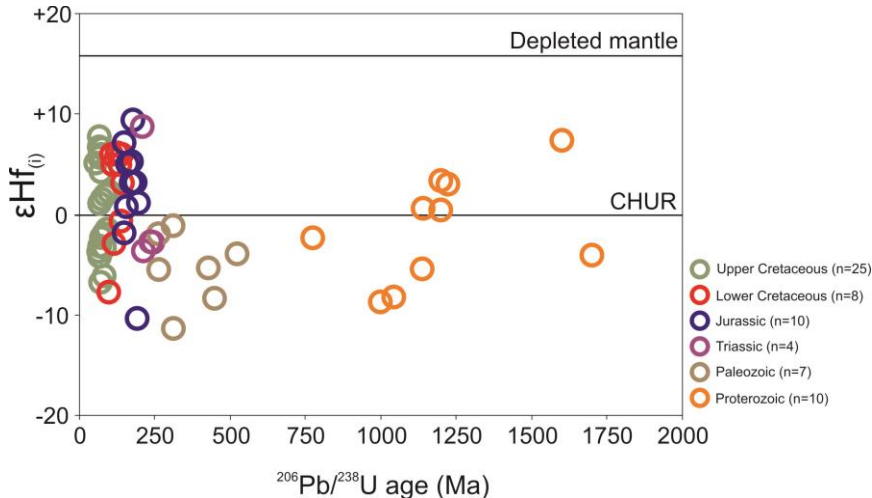


Figure 4.7. Hf isotope data from pre-Paleogene (>66 Ma) detrital zircons of the Bogotá Formation.

4.4.3.2. Early Paleogene zircons

Late Paleocene to Early Eocene detrital zircons with ages ranging from 65 to 50 Ma have initial ϵHf values from -14.4 to +8.1 (Fig. 4.7). Eighteen zircons have positive values ranging from +4.5 to +8.1 and twenty-two are negative ranging from -14.4 to -0.6, but predominantly between -7.2 to -0.6 (see it detailed in Fig. 4.6). When compared with zircons from Central Cordillera plutons, the more radiogenic cluster of this detrital record shows a close resemblance with El Bosque batholith (Fig. 4.6). Most of the Hf data of this pluton overlaps with those of the tuffaceous level of the Bogotá formation, whereas the Hatillo stock defines an isolated cluster, not related with any of the detrital data.

4.5. DISCUSSION

4.5.1. Origin of the Paleogene plutonism

The geochemical results of the Eocene magmatism, represented in our study by the Hatillo and El Bosque plutons, are characteristic of a convergent margin setting. They include Nb and Ti anomalies and relatively high LILE values recorded in K/Rb ratios about 250. A similar tectonic setting has been defined for other Eocene bodies such as the Parashi stock (Cardona et al., 2014) and the Santa Marta batholith (Cardona et al., 2011a) in the Colombian Caribbean region, as well as in the Manizales stock and the Antioquia and Sonson batholiths (Ordoñez et al., 2001; Leal-Mejía, 2011).

In the Colombian Andes, the 60 to 50 Ma arc-related magmatism within the Central Cordillera (Bayona et al., 2012), followed a former extensional Late Cretaceous magmatism

(Ibáñez-Mejía et al., 2007; Restrepo-Moreno et al., 2009; Ordóñez and Pimentel, 2002; Ordóñez-Carmona et al., 2008; Leal-Mejía, 2011; Villagómez et al., 2011), and a major arc-continent collisional event (Cardona et al., 2011b; Villagómez et al., 2011; Bayona et al., 2012; Spikings et al., 2015). In such geodynamic scenarios, the lower continental crust might have experienced crustal thickening associated to magmatic and tectonic underplating during continuous subduction and the oceanic-continent collision.

High Sr/Y ratios (Fig. 4.8), Al₂O₃ and Na₂O compositions were recognized in the El Bosque and Hatillo granitoids, as well as in the Paleocene to Eocene pulses of the Antioquian batholith in the Central Cordillera (Leal-Mejía, 2011), and in the Santa Marta and Parashi plutons in the Caribbean domain (Cardona et al., 2011b; 2014). Additionally, for the Eocene Manizales stock high Sr (580-685 ppm) and Rb (27-51 ppm) values have been reported (González and Londoño, 2002). This geochemical feature have been used to differentiate normal arc from adakite-like magmatic rocks, which are originated from the melting of a basaltic crust, and were initially considered as slab derived melts (Defant and Drummond, 1990). However, under normal subduction conditions the oceanic lithosphere in a subduction zone is subjected mostly to dehydration and do not extensively melt (Peacock et al., 1994; Poli and Schmidt, 2002). Therefore, alternative mechanism have been proposed to explain such a geochemical pattern commonly seen in different tectonic scenarios, and a caution on the use of adakite as a slab melting signature has been widely discussed (Richards and Kerrich, 2007; Moyen, 2009; Castillo, 2012).

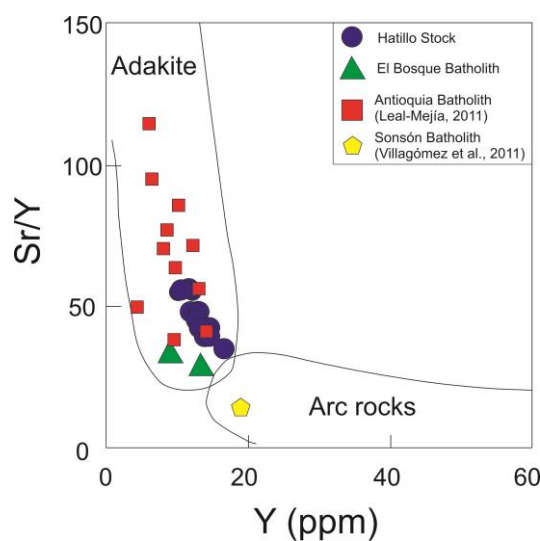


Figure 4.8. Sr/Y vs Y diagram after Defant and Drummond (1990) for adakite rocks discrimination.

The alternative models for the presence of high Sr/Y ratio in arc-related rocks include high pressure differentiation of arc magmas in the stability field of garnet (Macpherson et al., 2006), in which crustal thickness allows the stabilization of garnet and amphibole, that may or may not be related to delamination of the lower crust (Kay and Kay, 1993). Müntener et al. (2001) and Alonso-Perez et al. (2009) have pointed out that garnet stability is closely related with the H₂O content in a silicate liquid and that at pressures between 0.8 to 1.2 GPa (~25-40 km depth) in convergent settings, it becomes an essential fractionating phase that affects major and trace elements contents in calc-alkaline liquids. According to Lee et al. (2007), Y partitions into garnet and amphibole at high pressures (>12 kbar) and plagioclase is unstable, whereas is incompatible at low pressures. Kay and Mpodozis (2001) proposed that the Sr/Y ratio is a suitable guide to discriminate the presence of garnet versus amphibole or pyroxene in the source of magmas and has been used as an indicator of pressure differentiation (Bachmann et al., 2005). Recently, Chiaradia (2015) identified a direct relationship between crustal depth and Sr/Y ratios at intermediate to low MgO values (1-6 wt. %) based on compiled data from arc rocks around the world. Such results indicated that Sr/Y values higher than ~20 can be related to thick crusts and consequently the magma differentiation at the arc roots would have occurred at elevated pressures. The variations in the Sr/Y ratios has been used as major tracer of Meso-Cenozoic changes in crustal thickness on the North American Cordillera and the Central Andes (Chapman et al., 2015; Profeta et al., 2015).

Using the same approach is possible to document an increase in the Sr/Y ratio since Late Cretaceous to Eocene (Fig. 4.9), when evaluating the Jurassic to Eocene magmatic record of the Colombian Andes. This suggest that the crustal thickness was certainly taking place in the Northern Andes, due both to arc growth and collisional tectonics (Cardona et al., 2011a; Villagómez et al., 2011; Bayona et al., 2012; Spikings et al., 2015). Leal-Mejia (2011) have suggested that the adakite-like signature identified in the Paleogene facies of the Antioquia batholith can be related with lithosphere delamination after the Late Cretaceous to Paleocene collision. Therefore, this model may be precluded by the discrete sized plutons of the Central Cordillera and a lack of associated basic magmatism as seen in Cenozoic delamination zones such as the Central Andes (Coldwell et al., 2011) and Western United States (Ducea, 2001). It is therefore proposed that the adakite-like signatures of the Hatillo and El Bosque plutons (this work), the Manizales stock (González and Londoño, 2002) and the Antioquia batholith are akin to magmatic differentiation at a pressure of 1 – 1.2 GPa that allow garnet stabilization (Müntener et al., 2001; Alonso-Perez et al., 2009; Chiaradia, 2009;

Rooney et al., 2011). Although the Sr/Y and La/Yb ratios of the Caribbean plutons such as Santa Marta and Parashi (Cardona et al., 2011b; 2014) are lower than those of the Central Cordillera, they suggest that melting took place in the amphibole stability (Cardona et al., 2014), indicating some significant crustal thickness. A similar petrogenetical model in which an inherited thick lower crust influences arc magmatism has been documented by Schwartz et al. (2011) in the Late Jurassic of the NW United States. The presence of magmatic epidote in the Hatillo stock and also reported in the Paleocene Manizales stock (Plazas et al., 2013), is also compatible with high pressure crystallization conditions of these magmas (Schmidt and Poli, 2004; Matsumoto et al., 2014; Evans and Vance, 1987).

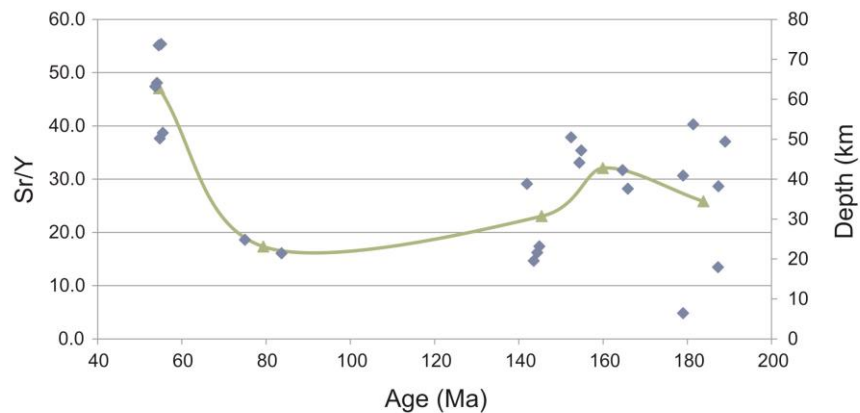


Figure 4.9. Variation of crustal depth with age in the western margin of the Colombian Andes during the Meso-Cenozoic. Blue points represent the whole data used to show the variations after applying the filters suggested by Profeta et al. (2015). Green line is an average every ~10 Ma. Relations between Sr/Y ratio and depth are according to Profeta et al. (2015).

The lower Mg# (43.2 – 54.4) and isotopic compositions with initial ϵ_{Hf} from -11.8 to +6.9, $^{87}\text{Sr}/^{86}\text{Sr}$ from 0.7031 to 0.7062 and $^{143}\text{Nd}/^{144}\text{Nd}$ from 0.512455 to 0.512648 ($\epsilon_{\text{Nd}}(i) = -1.98 - +1.76$) (Fig. 4.10A), suggest mixing of continental and juvenile basaltic sources (Chiaradia, 2015; Tarney and Jones, 1994). Thus, a slab-melting scenario that is characterized by remarkable non-radiogenic and high Mg# associated to the mix between the slab melts and the overlying mantle (Defant and Drummond, 1990; Moyen, 2009) is discarded. Whole rock lead isotopes also account for heterogeneous, mixed sources as they plot along the orogen curve (Fig. 4.10B) in the $^{208}\text{Pb}/^{204}\text{Pb}$ vs $^{206}\text{Pb}/^{204}\text{Pb}$ diagram of Zartman and Doe (1981), and are also characterized by moderate to radiogenic values of $^{207}\text{Pb}/^{204}\text{Pb}$ in the Hatillo and Bosque stock (15.625 to 15.575 and 15.633).

After evaluating the feasibility of the high-pressure differentiation as the most appropriate mechanism to reach the high Sr/Y signature, a remaining question is the origin of the melts. A plausible source for this would be the melting of diapirs composed of sediment, altered oceanic crust and peridotites transferred from the subduction zone towards the lithosphere, which are then emplaced at the lower crust (Castro, 2014). This model has been supported by experimental work (Gerya and Yuen, 2003; Vogt et al., 2013; Castro, 2014) and discussed as an alternative origin for the tonalite-granodiorite magmas in arc settings (Castro et al., 2010; Castro, 2014). Melting temperatures for this process are higher than 1,000 °C, which favors water-undersaturated magma generation and hence the late formation of amphibole (Castro et al., 2010; Castro, 2014). This is a feature present in our samples and reported in other Eocene plutons of the Central Cordillera (González and Londoño, 2002; Plazas et al., 2013; Leal-Mejía, 2011) where this mineral is less than 5 % modal.

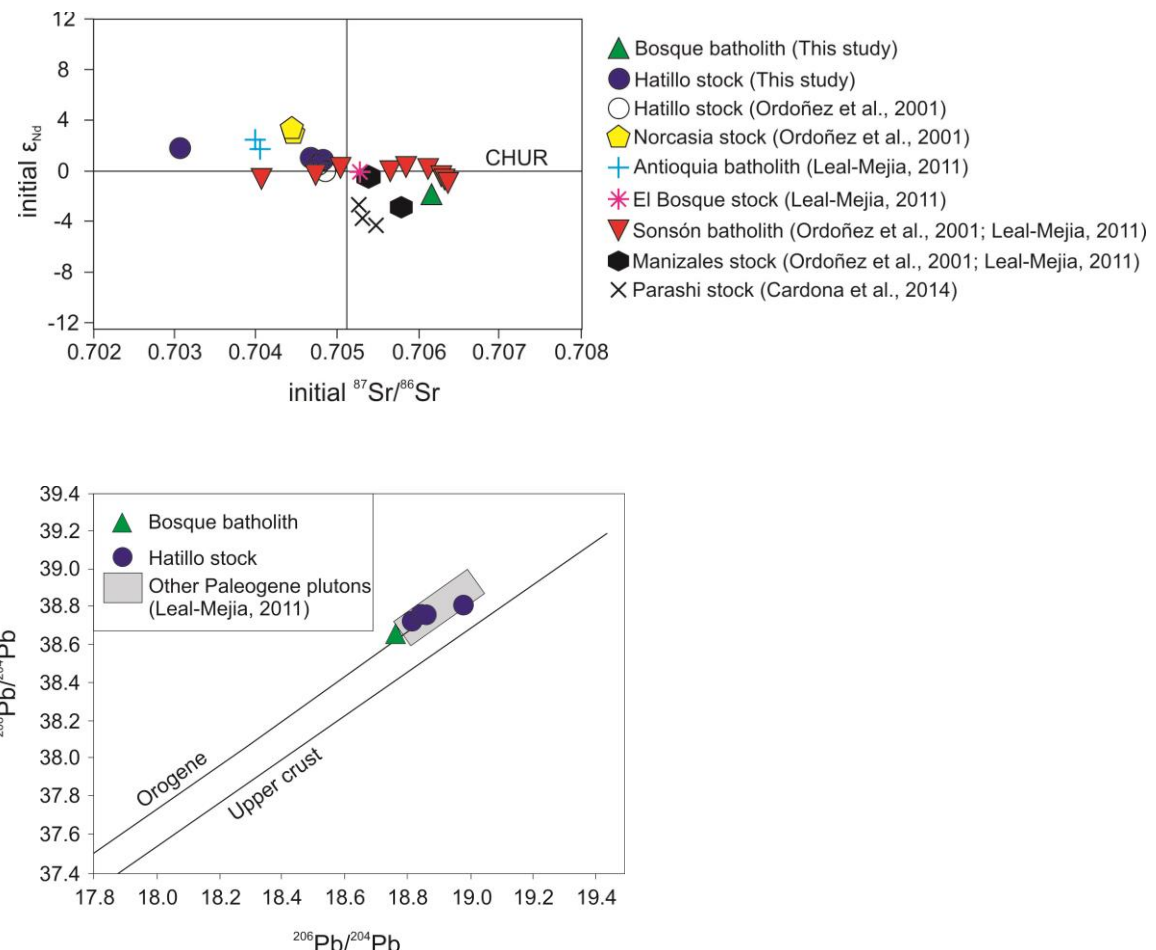


Figure 4.10. A. $\epsilon_{\text{Nd(i)}}$ vs $^{87}\text{Sr}/^{86}\text{Sr}$. **B.** Lead isotopic evolution curve according to the plumbotectonics model of Zartman and Doe (1981). Both diagrams show a comparing between the Eocene plutons analyzed with other Paleogene plutons from the Central Cordillera and the Colombian Caribbean.

Due to the deep origin of these melts, the stock dimensions that characterize the plutonic rocks of the Paleogene arc, might be the result of the difficulty of magmas to be emplaced at the upper crust due to its thickness. Although an exception seems to be the Paleogene Sonsón batholith with Sr/Y ratio of ~ 14 (Fig. 4.8) (60 to 55 Ma: Ordóñez et al., 2001; Leal-Mejía, 2011; Villagómez et al., 2011). It may suggest that garnet was not a phase present during the differentiation that gave rise to this pluton. However, a more systematic study of this batholith is needed to fully understand its origin.

4.5.2. Detrital zircon signatures

Provenance and sedimentological analysis in Eastern Colombian basins have suggested the existence of Paleogene detritus of volcanic origin and tuffaceous material more than 400 km from the Paleogene arc in the Central Cordillera (Fig. 4.9). The Hf isotope signatures of the Early Paleogene zircons measured in detrital samples of the Eastern Cordillera suggest that some of these zircons may be sourced from the Central Cordillera arcs. Although this Cordilleran source is a simple connection, sedimentological characteristic from some of these volcanic horizons, including their apparent proximal character, do not rule out the existence of some volcanic focus in eastern Colombia that have been covered or eroded (Bayona et al., 2012; 2015). If this is the case, such volcanism temporally overlie with a major phase of local basin inversion in a compressive setting (Bayona et al., 2012; 2013), and therefore the volcanism may be explained by some kind of distal process, probably associated to mantle flow that allow melting of the crust or the mantle.

Shear-driven cavity flow of the asthenosphere on inherited extensional structures (Conrad et al., 2010; 2011), such as those documented on Eastern Colombia (Sarmiento-Rojas et al., 2006; Mora et al. 2009) is commonly considered as a process that may trigger melting. Thus, mantle flow and inland melting associated with basin inversion and exhumation recorded east of the Central Cordillera, may be prompted by the transition of the normal subduction setting to a flat slab configuration. This seems to affect the Colombian margin because of the subduction of a thick Caribbean plate under South America (Cardona et al., 2011a; Bayona et al., 2012). Moreover, the apparent magmatic hiatus in the Late Eocene may be also related to such a scenario, although oblique convergence during the Paleogene has also influenced magmatic fluxes in the margin (Bayona et al., 2012).

4.6. CONCLUSIONS

U-Pb ages and Hf isotopes in zircons together with petrography and whole rock geochemistry in plutonic rocks from the Central Cordillera, allow us to understand the mechanisms that lead to the magmatism in Colombia between 60 and 50 Ma. The processes involved in the origin of such magmatism account for a high-pressure differentiation of the Central Cordillera granitoids that give rise to adakite-like signature in the plutonic rocks. This compositional feature is related to magmatic differentiation of the melts in a thick lower crust, that experienced both tectonic and magmatic underplating during the former Cretaceous to Early Paleocene arc and collisional events that experienced the NW margin of South America. Melt source include the tectonic mélange composed by sediments and basalts transported by subduction. Emplacement of the plutonic rocks to the upper crust might be difficult by the already thickened crust, resulting in small sized plutons. Hf isotopic signatures of Paleogene detrital zircons from Eastern Colombia suggest a Central Cordillera source of zircons. However, a proximal eastern volcanic focus is not discarded, since it may be associated to basin inversion and mantle flow formed during slab flattening.

Capítulo 5

Magnetic fabric (AMS, AAR) of the Santa Marta batholith (northern Colombia) and the shear deformation along the Caribbean plate margin⁴

ABSTRACT

Anisotropy of low-field magnetic susceptibility (AMS) and anhysteretic remanence (AAR) were measured in the Santa Marta Batholith formed by subduction of the Caribbean Plate beneath the northern South America. The batholith, elongated in the N-S direction, records multiple pulses of quartzdiorite to tonalite and granodiorite magmas between 58 and 49 Ma. The high mean magnetic susceptibility (4×10^{-3} SI) combined with thermomagnetic and partial magnetic remanence measurements indicate that the magnetic susceptibility depends on Ti-poor magnetite. AMS is defined by ellipsoids that are dominantly oblate. The foliation was used to distinguish a narrow band of E-trending magnetic structures that separate the batholith in two lobes. The southern lobe is characterized by foliations that are broadly parallel to the contact with the wall rocks, while the northern lobe by foliations oblique to the batholith elongation. Late tonalitic magmas dated at c. 50 Ma record, in turn, a fabric apparently controlled by E-trending tectonic events. Partial AAR indicates that the subfabrics of magnetite with different grain sizes are nearly parallel to AMS, therefore discarding the possibility of superposed fabrics with different orientations. The magnetic fabric pattern is consistent with a magma emplaced in an arc setting deformed by a dextral shear. Synthetic extensional shear bands localize the magmatic deformation along East-trending corridors that probably were exploited to emplace the late magmatic pulses. Accretion of the Eocene batholith and the Late Cretaceous metasedimentary host-rocks to the South American continent defines a major strike-slip shear suture that resulted from the oblique convergence of the Caribbean Plate.

⁴ Salazar, C.A., Bustamante, C., Archanjo, C.J., 2016. Magnetic fabric (AMS, AAR) of the Santa Marta batholith (northern Colombia) and the shear deformation along the Caribbean plate margin. *Journal of South American Earth Sciences*.

5.1. INTRODUCTION

Anisotropy of magnetic susceptibility (AMS) in granitic rocks is a reliable recorder of the kinematics of regions in which plutons are emplaced (Archanjo et al., 1994; Neves et al., 1996; Wilson and Grocott, 1999; Moyen et al., 2003; Stevenson et al., 2007; Wei et al., 2014, among many others), being used for plate tectonic analysis of orogenic belts (Benn et al. 2001). AMS studies of granite plutons from magmatic arc settings, such as in Chilean Central Andes or in western North America Cordillera, have shown that magnetic fabrics are either strongly coupled with the arc deformation (Tikoff and Saint-Blanquat, 1997; Wilson, 1998; Fawcett et al., 2003; Titus et al., 2005) or record structures formed by body (ascent, convection) forces and tectonic-related fabrics (Saint-Blanquat et al., 2001; Parada et al., 2005). Magnetic fabrics orientations controlled by the deformation in magmatic arcs have been documented in Jurassic to Middle Cretaceous plutons emplaced in the Central Andean Belt (Wilson, 1998) when the arc was submitted to extension (Ramos, 2009). According to Grocott and Taylor (2002), the granitic complexes were accommodated in the crust by a mechanism of floor-depression and/or roof uplift that allowed a vertical transfer of magma without important horizontal displacement of the wall rocks. In contrast AMS of the Mid-Cretaceous Las Tazas batholith evidence finite strains when the arc was deforming by transtension (Wilson and Grocott, 1999). AMS, therefore, was interpreted as recording a tectonic overprint in the final stages of the magmatic crystallization due to the lateral movement of the Atacama Fault (Grocott and Taylor, 2002).

Between Late Cretaceous and Eocene the Central and Northern Andes were submitted to contraction (Ramos, 2009). While in the Central Andes the contraction would be linked to the shallowing of the subduction zone, convergence between the oceanic Caribbean Plate and the Northern South America Plate would account for the accretion of terranes and magmatic activity along the margin of Ecuador and Colombia (Pindell and Kennan, 2009; Cardona et al., 2011a; Boschman, et al. 2014). Likewise, the northward migration of the triple junction between the Farallon and Caribbean plates relative to the South American Plate would indicate that the collage of terranes was accompanied by large dextral shearing (Kennan and Pindell, 2009). The Caribbean Plate is, in present day, bordered by the magmatic arcs of the Panama and Antilles (Fig. 5.1). A considerable proportion of the plate consists of a thick (up to 20 km) oceanic crust referred to as Caribbean-Colombian Oceanic Plateau (Kerr, 2014). The plateau would have been formed over the Galapagos hot-spot and gradually moved to its present position over the past 90 Ma (Duncan and Hargraves, 1984; Kerr and Tarney, 2005;

Pindell and Kennan, 2009). Subduction of the Caribbean Plate between 60-40 Ma resulted in the emplacement of calc-alkaline tonalites, granodiorites and quartz diorites in the Central Cordillera, Sierra Nevada de Santa Marta and Guajira Peninsula in Colombia (Fig. 5.2) (Bayona et al., 2012; Cardona et al. 2014). The relatively short period (< 15 Ma), wide areal distribution of the igneous bodies and the abrupt interruption of the magmatism in Middle Eocene are attributed to the difficulty of the thick oceanic crust to subduct (Bayona et al., 2012).

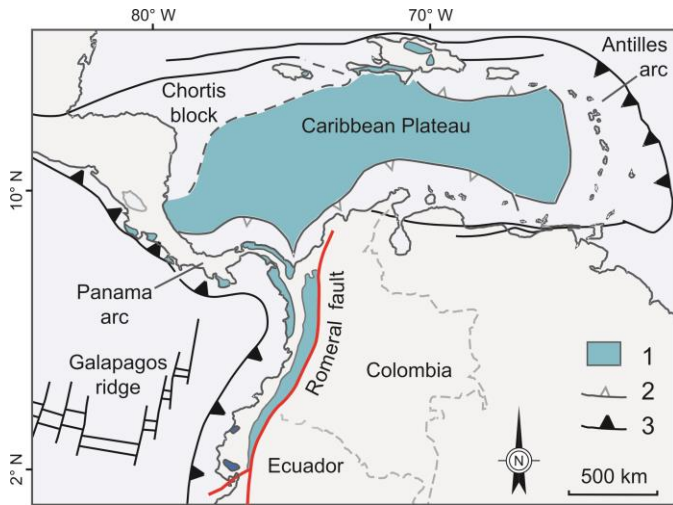


Figure 5.1. Caribbean oceanic plateau bounded by the subduction zones of Antilles and Panamá, and strike-slip (transform) faults. Accreted oceanic terranes related to the oblique subduction of the Caribbean plate beneath South America are shown to the Ecuador, Colombia and Panama to the west of the Romeral fault system. 1. Cretaceous oceanic rocks; 2, thrust; 3, subduction zone (modified from Kerr, 2014).

Our study is focused on the Santa Marta batholith, one of the largest Eocene pluton of Colombia that intruded subduction complexes of the leading-edge of the Caribbean plate accreted to the northern margin of the South America (Cardona et al 2011a; Escalona and Mann, 2011). We use anisotropy of magnetic susceptibility to define the batholith magmatic fabric and anisotropy of anhysteretic remanence to investigate the possible contribution of superposed fabrics (Trindade et al., 1999; Usui et al., 2006) in an actively deforming arc setting. This study also documents the tectonic record in the pluton emplacement fabrics when the subducted plate contains thick oceanic crust.

5.2. GEOLOGICAL SETTING

The Andean Belt in Colombia can be divided in three major “cordilleras”. The Western Cordillera (WC, Fig. 5.2) consists of slivers of oceanic plateau basalt, island arcs and volcano-sedimentary rocks accreted to South America at c. 75 Ma (Kerr and Tarney, 2005; Vallejo et al., 2006). The central Cordillera (CC) comprises mostly Late Paleozoic to Triassic

foliated granitoid, amphibolite and migmatite interpreted to record crustal melts formed during extension and break-up of the western Pangea (Vinasco et al., 2006; Martens et al., 2014). These rocks were intruded by I-type Jurassic batholiths evolved in a continental arc setting due to east dipping subduction of the Farallon Plate (Aspden et al., 1987; Cochrane et al., 2014b). Paleozoic rocks including dispersed inliers of Grenvillian-aged basement characterize the Eastern Cordillera (EC), the Sierra Nevada de Santa Marta (SNSM) block and part of the Guajira Peninsula (Fig. 5.2; Cordani et al., 2005; Cardona et al., 2010). A suture zone would juxtapose the Eastern and the Central Cordilleras to characterize, respectively the Chibcha and Tahami Terranes (Restrepo and Toussaint, 1988), while the Sierra Nevada de Santa Marta would be a rotated block detached from the Central Cordillera in the Eocene (Montes, et al., 2010). In turn, slices of ultramafic-mafic rocks metamorphosed at medium- to high pressure and emplaced along the Cauca-Almaguer-San Jerónimo faults (hereafter named Romeral fault system; Fig. 5.1) define the suture zone between the Central and Western Cordilleras. Although covered by Cenozoic to recent sediments, the Romeral fault system has been traced to northern Colombia following the contact between Late Cretaceous and Paleozoic sequences (Fig. 5.2; Kennan and Pindell, 2009; Ramos, 2009).

The SNSM block consists of Paleozoic rocks intruded by Jurassic granitoids including remnants of high-grade metamorphic rocks of Grenvillian age. The Paleozoic metamorphic sequence (Sevilla belt of Tschanz et al., 1974) is juxtaposed to a narrow belt of Late Cretaceous pelitic to psamitic schists and amphibolites intruded by the Santa Marta batholith (Fig. 5.3). The host rocks of the batholith have been associated to forearc deposits related to the east-dipping subduction of the Caribbean plate and that were accreted to the South America margin by arc-continent collision (Cardona et al., 2011a).

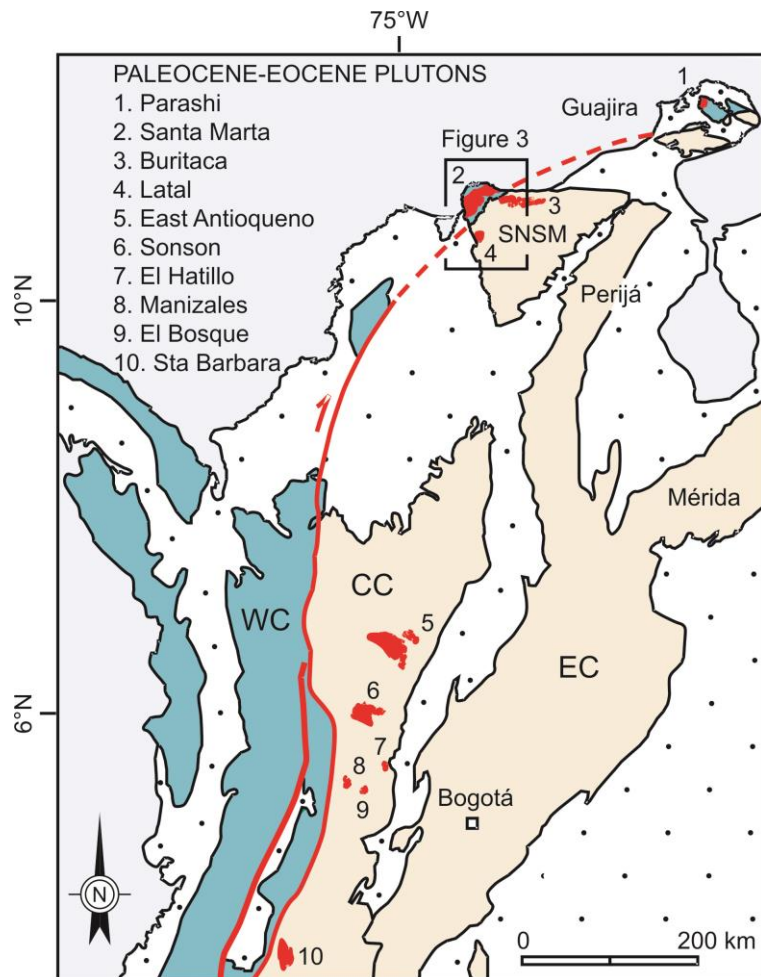


Figure 5.2. Simplified physiographic map of the northern Andes showing the Cretaceous oceanic rocks of the West Cordillera (WC) in contact with the Central Cordillera along the Romeral fault system. The Eastern Cordillera (EC) is separated from the Sierra Nevada de Santa Marta (SNSM) block and Central Cordillera by sedimentary deposits of the César-Rancheria and Magdalena basins. Plutonic rocks corresponding to the Paleocene-Eocene magmatic arc are shown in red (modified from Bayona et al., 2012).

5.2.1. Early Paleogene magmatism in the Sierra Nevada de Santa Marta

Two distinct magmatic events are recognized in the eastern part of the SNSM block. The older 65-63 Ma magmatism consists of leucogranite stocks with garnet, muscovite and biotite intruding Late Cretaceous metapelites and Paleozoic metamorphic rocks (Fig. 5.3). According to Cardona et al. (2011a), the Paleocene magmatism records the collision of Caribbean arc with the northern South American Plate. Tonalite, quartz diorite and granodiorite with crystallization ages between 58-50 Ma constitute the younger magmatic event (Bayona et al., 2012; Cardona et al. 2014), with the Santa Marta batholith representing the largest Eocene pluton (c. 600 km²) of the SNSM block. The batholith consists mostly of a tonalite with hornblende and biotite. Titanite, magnetite, ilmenite, apatite and zircon occur as accessory minerals. The microstructure is holocrystalline equigranular, medium- to coarse-

grained, locally porphyritic and pegmatoid. Medium to fine-grained mafic enclaves with amphibole and biotite are relatively abundant. Tschanz et al. (1969) recognized a foliated to gneissic granitoid including a mafic gneiss xenolith situated along the eastern margin of the batholith (Fig. 5.4). Zircon U/Pb ages (LA-ICP-MS) yielded crystallization ages of tonalites and granodiorites between 58 and 55 Ma (see location of samples in Fig. 5.4). A mafic enclave from the northwestern margin provided a zircon U/Pb age of 57 Ma and late porphyritic to equigranular dikes that cut the batholith and its wall-rocks yielded ages in the range of 56 and 52 Ma (Duque 2009; Cardona et al. 2011a).

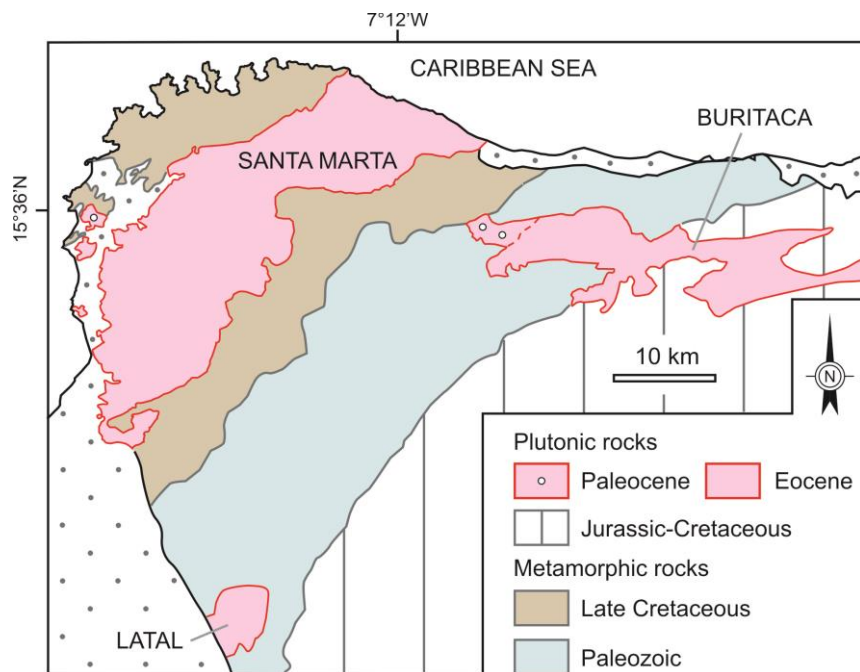


Figure 5.3. Geological map of the eastern part of the Sierra Nevada de Santa Marta

Late, coarse-grained tonalite and quartzdiorite with andesine, calcic amphibole and biotite are found in the northern part of the batholith. Duque (2009) distinguished the coarse tonalitic facies from the main plutonic unit based on the occurrence of abundant amphibolite xenoliths in the former and by field relations that show intrusive contacts of the coarse tonalite in the main plutonic unit. A late magmatic pulse corresponding to the coarse tonalite is supported by zircon U/Pb analysis that provided ages in the range of 52-49 Ma (Fig. 5.4). Uncertainties in the error analysis between the main plutonic unit dated at 58-54 Ma and the late magmatic pulse at 52-49 Ma suggest they are distinct events (Duque, 2009). We present a new U-Pb (SHRIMP) analysis by dating zircon cores and their zoned rims that support multiple magmatic stages during batholith construction.

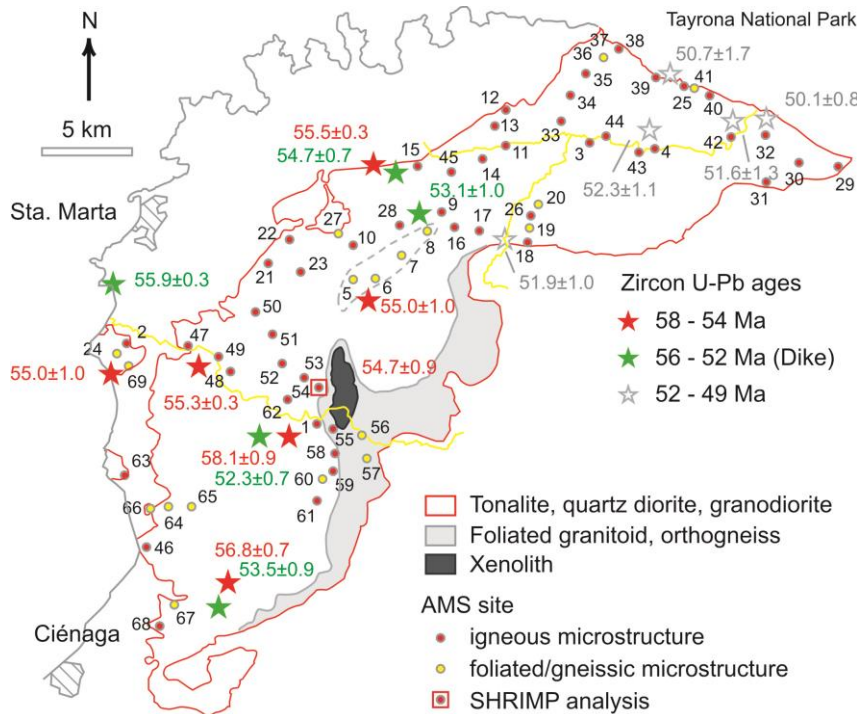


Figure 5.4. AMS sampling sites with the domain with the granitoid with foliated and/or gneissic microstructure (modified from Tschanz et al. (1969). The location of the sites with geochronological determinations after Duque (2009) and Cardona et al. (2011a).

The Buritaca pluton and Latal stock intrude the Paleozoic Sevilla belt and Jurassic-Cretaceous rocks of the central part SNSM block (Fig. 5.3). The Buritaca forms a pluton of 40 km in width elongated in the E-W direction, while the Latal stock crops out close to the southern margin of the SNSM. Buritaca and Latal plutons consist of tonalites and quartzdiorites with amphibole and biotite. The Buritaca pluton showed zircon U/Pb crystallization ages of 55 Ma and 51 Ma (Duque 2009). No geochronological data is available for the Latal stock and its connection with the Santa Marta and Buritaca plutons is inferred by their similar compositions.

5.3. U-Pb ZIRCON (SHRIMP) GEOCHRONOLOGY

5.3.1. Sampling and methods

The sample (SM54, see localization on Fig. 5.4) consists of coarse-grained equigranular tonalite with sodic andesine, quartz, hornblende, biotite and K-feldspar (< 5%). The zircon grains were handpicked after standard crushing and separation procedures. We selected clear euhedral to subhedral grains that were mounted in epoxy together with chips of TEMORA 1 reference zircon (Black et al. 2003). The mount was polished and cathodoluminescence (CL) SEM images were taken for all grains. The analysis of the U-Th-

Pb of the zircons was conducted at the Beijing SHRIMP Center (China). The isotopic data were collected in sets of five scans through the masses, and the TEMORA standard was measured after four unknown analysis. The abundances of U, Th and Pb, and the Pb isotopic ratios were normalized using the SL13 zircon standard. The data reduction was performed using the SQUID Excel macro (Ludwig, 2000), and the statistical assessments were calculated using the ISOPLOT/Excel 3.0 (Ludwig, 2003). The results are reported in Table 5.1 with uncertainties in the isotopic ratios and the ages in data reported at the 1σ level and the weighted mean ages as 95% confidence limits.

5.3.2. Results

The zircon grain sizes range between 50 and 300 μm in length and show axial ratios (long/short dimensions) mostly from 1.2:1 to 3.5:1. The zircons have distinct oscillatory zoned dark cores enveloped by light grey phase also displaying concentric oscillatory zone patterns (Fig. 5.5). The overgrowths sometimes cut the oscillatory zoned cores suggesting multiple events of zircon growth. From a total of 19 analyses three are from the zircon cores (spots #8.1; #14.1 and #16.1) and sixteen analyses are from the overgrowths. There is no difference between the $^{204}\text{Pb}/^{238}\text{U}$ ages of the cores and overgrowths, except in one analysis (spot #14) in that the core is slightly older (see Table 5.1). By removing three analyses with reverse ages (#6.1, #13.1 and #14.2) and one analysis with an older age (#9.1) the remaining fifteen analyses form a cluster on the Concordia curve to define a mean $^{206}\text{Pb}/^{238}\text{U}$ age of 54.7 ± 0.9 Ma (Fig. 5.6). This result is consistent with zircon U-Pb ages reported in the literature for the Santa Marta batholith and corresponds to the main episode of the batholith construction (Cardona et al. 2010).

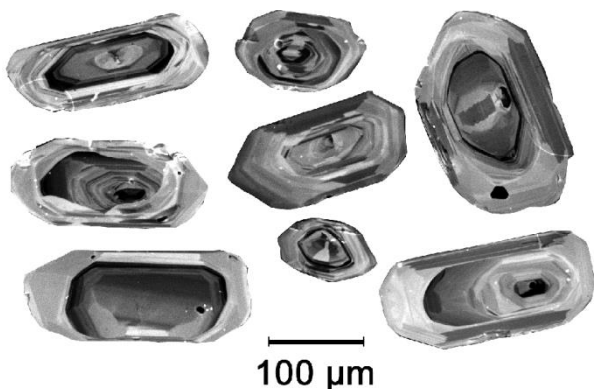


Figure 5.5. Cathodoluminescence images of representative zircons of a horblende-biotite tonalite (sample SM54). Some grains show dark (U-rich) cores (left) enclosed by more luminescent (and low U) rims. Oscillatory zoning typical of magmatic zircons are visible in cores and rims.

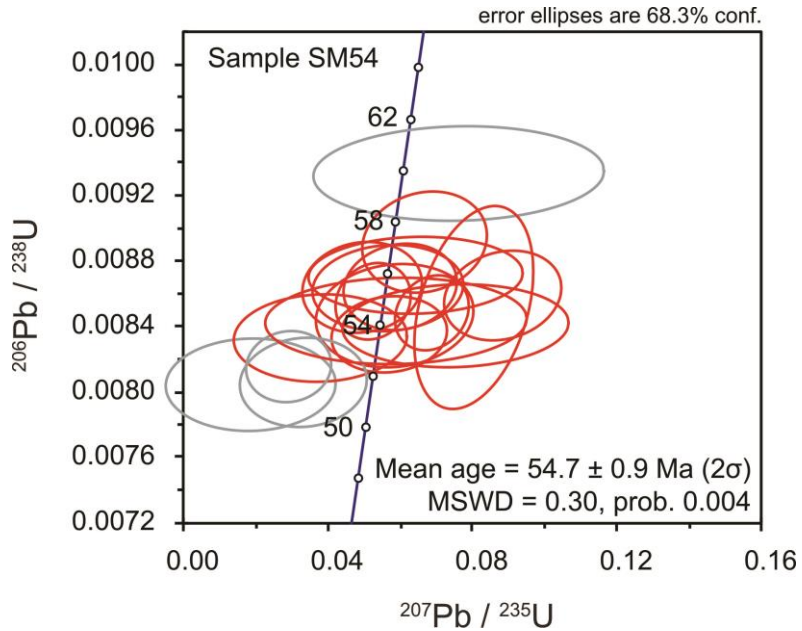


Figure 5.6. Concordia diagram of the hornblende-biotite tonalite, with the zircon age determined by average of the concordant data. Analyses corresponding to the grey ellipses were discarded from the age calculation (see text).

5.4. ANISOTROPY OF MAGNETIC SUSCEPTIBILITY AND ANISOTROPY OF ANHYSTERETIC REMANENCE

5.4.1. Background

The low-field ($\sim 10^{-4}$ T) anisotropy of magnetic susceptibility (AMS) refers to a material property whereby an external field (H) applied in different directions produces different magnitudes of the induced magnetization (M). The magnetization is related to the applied field by a susceptibility (k) parameter so that $k = M/H$. AMS is defined in terms of a susceptibility ellipsoid which has principal axes along the directions of maximum (k_1), intermediate (k_2) and minimum (k_3) susceptibility (see details in Hrouda, 1982; Borradaile and Henry, 1997). AMS is an intrinsic property of the rock that represents the contribution of the susceptibility anisotropies of all the mineral components and that depends on the shape and degree of alignment (fabric) of their grains.

The anisotropy of anhysteretic remanence (AAR) isolates the contribution of the remanence-bearing minerals, usually magnetite, from that of the whole-rock matrix. An anhysteretic remanence is imparted to a ferromagnetic grain when it is subjected simultaneously to alternating field (AF) and small bias direct magnetic field. Such as AMS, AAR can be described by an ellipsoid of anhysteretic remanence susceptibility (k_A) with

maximum (k_{1A}), intermediate (k_{2A}) and minimum (k_{3A}) principal directions (Jackson, 1991). AAR also permits the isolation of sub-fabrics within the magnetite fabric. Since there is a correlation between the coercivity spectra and the magnetite grain-size (Jackson et al., 1988), it is possible to measure the AAR associated with a particular grain-size using the partial AAR (pAAR). Fine particles, for instance, reach maximum coercivities for high-AF windows while coarser grains are more sensitive to weaker AFs. As magnetite in igneous rocks may crystallize at different times with different orientations, the determination of pAAR allows the investigation of possible overprinted fabrics (eg. Trindade et al., 1999; Usui et al., 2006).

5.4.2. Sampling and Methods

Oriented samples were extracted from 69 sites separated from each other by 1-2 km apart (Fig. 5.4). The sites are relatively well distributed on the whole batholith but some areas, mostly to the east and southeast, that were not accessible. Between three and five cores of approximately 8 cm in length and 2.5 cm in diameter were collected at each site using a portable gasoline powered drill. The cores were oriented in place with a magnetic compass. In the laboratory each core was cut in standard specimens that were 2.2 cm in length providing a total of 759 specimens.

The magnetic properties of the samples were studied in the *Laboratório de Paleomagnetismo* of the São Paulo University. Low-field AMS was determined in a KLY-4 Kappabridge susceptometer that provides the bulk volumetric magnetic susceptibility of the specimen and the principal directions of anisotropy. The intensity of AMS was indicated by the degree of anisotropy $P = k_1/k_3$ and the symmetry of the ellipsoid by the shape parameter $T = [2\ln(k_1/k_2)/\ln(k_2/k_3)]-1$, where $0 < T \leq 1$ correspond to the oblate and $-1 \leq T < 0$ to the prolate ellipsoids. The directions of the susceptibility ellipsoid are k_1 , quoted as the magnetic lineation, and k_3 quoted as the pole of magnetic foliation. The data were statistically evaluated by ANISOFT v.3.2 software that calculates the mean-site AMS parameters (all caps, $K_1 \geq K_2 \geq K_3$) after averaging the data of 6 to 18 specimens by site. The mean-site AMS magnitudes and directions indicated in Table 5.2.

Partial anhysteretic remanent magnetizations of specimens with different low-field magnetic susceptibilities were investigated following the procedures described in Jackson et al. (1988). The specimen is initially demagnetized by tumbling at peak alternating field (AF) of 100 mT using a LDA-3-AMU demagnetizer (AGICO ltd). The partial anhysteretic remanent magnetization (pARM) acquisition consists of applying a steady direct field (DC) of

between two chosen values of a decaying AF peak (see details in Jackson et al. 1988). pARM was determined by exposing the specimen in an AF peak of 100 mT and a DC field of 0.1 mT with an AF window of 10 mT, and the anhysteretic remanence measured in JR6-A spinner magnetometer (AGICO Ltd).

The anisotropy of anhysteretic remanence (AAR) was investigated using the procedures described in McCabe et al. (1985). The specimen is demagnetized by tumbling in a peak AF of 100 mT and the base level magnetization measured in the JR-6A. Then an ARM is induced along a specific specimen axis by applying a decaying AF combined with a DC field and the remanence measured in the magnetometer. The specimen is demagnetized by tumbling and a new anhysteretic magnetization imparted along a different axis. Cycles of demagnetization and anhysteretic magnetization are induced along six different positions and the respective remanence measured in the JR6-A. The magnitude and directions of the remanence can be described by an anisotropy tensor calculated by least squares method using the REMASOFT-W software.

The magnetic mineralogy was investigated through the temperature dependence of the magnetic susceptibility ($k-T$). Representative samples of the batholith were crushed to a fine sand-size, and a small volume fraction measured from -200 °C to 700 °C using a CS-3 furnace/CSL cryostat attached to the KLY-4 Kappabridge. At low temperatures, the magnetic susceptibility was recorded by warming the sample from approximately -200 °C to room temperature. From room temperature up to 700 °C (heating cycle) and back (cooling cycle), $k-T$ was measured in an argon environment to prevent oxidation of the sample by atmospheric oxygen in the heating/cooling cycle.

5.4.3. Magnetic susceptibility and mineralogy

AMS parameters of the Santa Marta batholith are indicated by the mean arithmetic values (all caps) of the all specimens collected in each site. The bulk magnetic susceptibility ($K = 1/3[K_1 + K_2 + K_3]$) ranges from 0.024 to 15.7×10^{-3} SI (mSI) and the anisotropy degree ($P = K_1 / K_3$) from 1.034 to 1.51 (Fig. 5.7A). Susceptibility magnitude is low ($K < 1$ mSI) in 29 sites with the respective degree of anisotropy ranging from 1.03 to 1.12 (average of 1.07). Moderate ($1 < K$ (mSI) < 10) and strong ($K > 10$ mSI) magnetic susceptibility magnitudes are recorded in 40 sites. These sites have P values higher (average of 1.25) and more variable ($1.085 < P < 1.513$) compared to those with low susceptibility. The shape of the AMS ellipsoids is dominantly neutral to oblate ($T \geq 0$) with a few prolate ellipsoids ($T < 0$) found

principally in the specimens with low susceptibility (Fig. 5.7). There is no relation between the P parameter and a particular sector of the pluton, although ellipsoids with neutral to oblate shapes are recorded mostly the northern part of the intrusion.

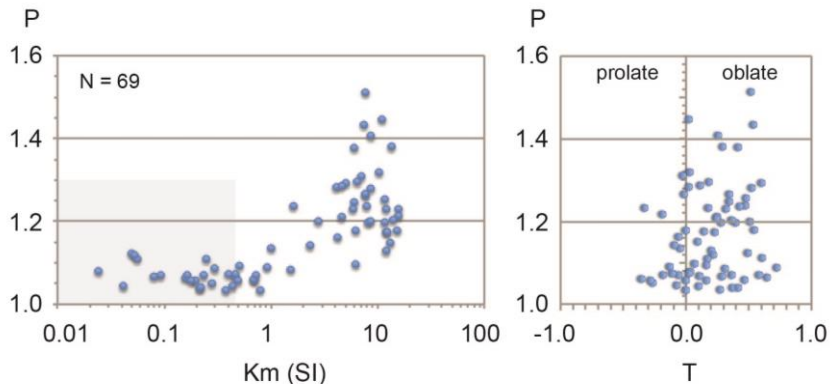


Figure 5.7. Relation between the mean-site magnetic susceptibility (K_m), degree of anisotropy (P) and shape (T) of the AMS ellipsoid.

$k - T$ curves for specimens with moderate and high susceptibilities show similar and very simple shapes. They display a net Verwey transition at c. -160°C and a strong drop of susceptibility close to 580°C (Fig. 5.8A, B). The susceptibility at the end of cooling cycle is a rather higher than in the heating cycle at room temperature indicating that new magnetic phases were produced on heating. Similar results are typical of coarse (Ti-poor) magnetite and have been documented in granitoid rocks of different ages and tectonic settings (Salazar et al., 2008; Henry et al., 2009; Ferré et al., 2012).

The Verwey transition becomes poorly defined (Fig. 5.8C) or disappears at low temperature (Fig. 5.8D) while the susceptibility decreases progressively as temperature increases in specimens with low susceptibility. The poorly defined, smooth Verwey transition suggests small amounts and/or an oxidized magnetite (Ozdemir et al., 1993) while the decrease of magnetic susceptibility with temperature indicates the strong contribution to the bulk magnetic susceptibility of the paramagnetic phases. The curves are irreversible at room indicating that some new magnetic phases were formed in the heating and cooling cycle.

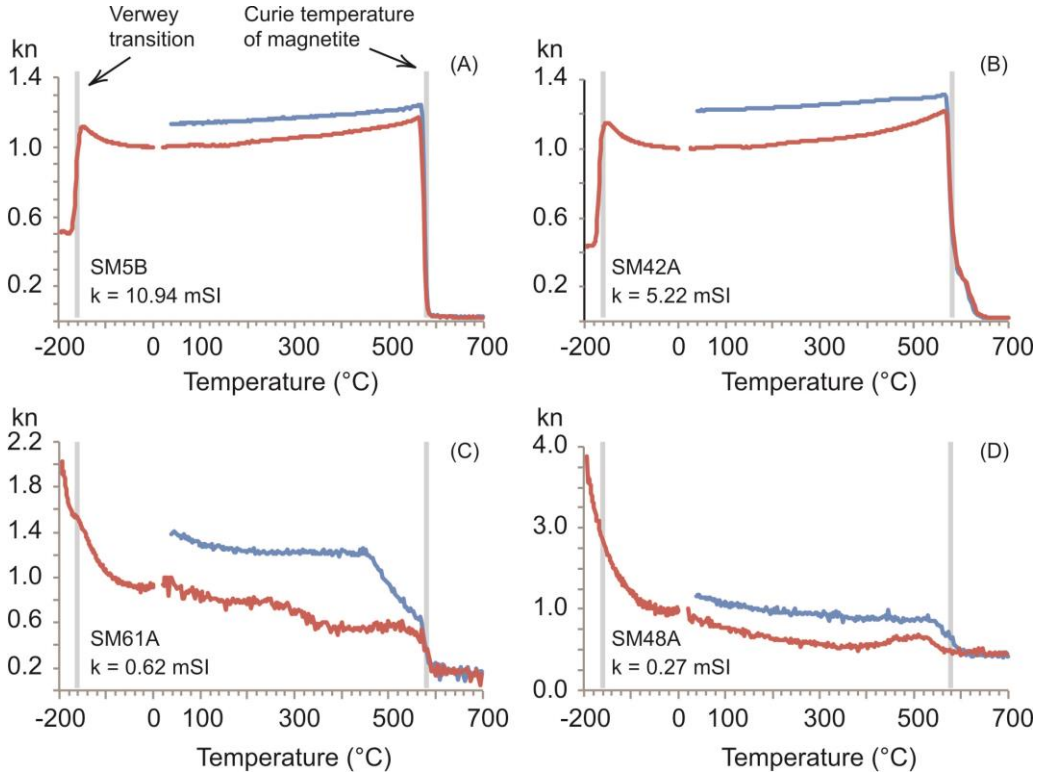


Figure 5.8. Dependence of the magnetic susceptibility with temperature for representative samples of the Santa Marta batholith.

5.4.4. Anisotropy of magnetic susceptibility

The dominant oblate AMS ellipsoids indicate that the foliation is the best-defined magnetic fabric element of the Santa Marta batholith. Their dips vary mostly to the northwest, southeast and south, and locally to the north and northeast (Fig. 5.9). Based on the foliation trend we define two major structural domains; (i) a northern domain in that foliation strikes mainly in the N-S direction, and (ii) a southern domain in that foliation strikes to NW or NE directions. These domains, or lobes, are divided by a set of E-trending foliations (dashed line in Fig. 5.9) that are also found in the northeastern margin of the batholith.

The northern lobe is characterized by neutral to oblate AMS ellipsoids ($0.0 \leq T \leq 0.5$) and degree of anisotropy between 1.04 and 1.51 ($P_{\text{mean}} = 1.23$). The foliation shows variable dips to the southeast or to the northwest and is usually associated with a NE-trending gentle plunge lineation. In contrast, the northeast margin shows mostly E- to NW-trending foliations. The lineations vary from subhorizontal to down-dip in agreement with the dominant oblate ($K_1 \sim K_2 > K_3$) ellipsoid.

AMS of the southern lobe differs from the northern lobe by ellipsoids that vary from prolate to oblate ($-0.35 < T < 0.72$) and a weaker anisotropy ($P_{\text{mean}} = 1.12$). The foliation

shows moderate to gentle dips in the center of the lobe (Fig. 5.9) and strikes that tend to be parallel to the lobe elongation. The lineation aligns mostly in the E-W and N-S directions.

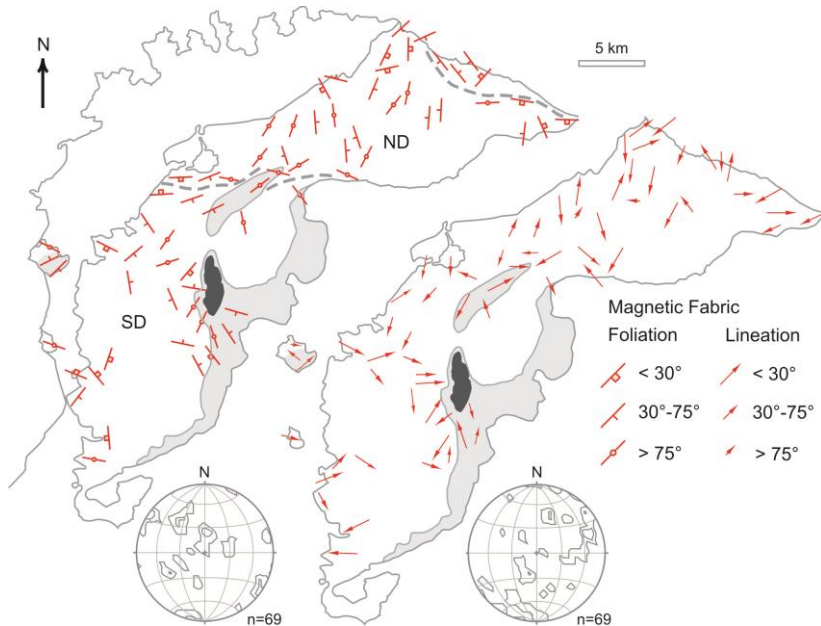


Figure 5.9. Magnetic fabric (foliation and lineation) and domains where the rock microstructure is foliated and/or gneissic (grey area). Dashed line corresponds to the corridors where the foliation trend is nearly E-W. Stereonets of the magnetic lineation (right) and pole of the magnetic foliation (Schmidt diagrams, lower hemisphere; contours of 2%, 4% / 1% area). Black; xenolith. ND and SD; northern and southern domain.

5.4.5. Anisotropy of Anhysteretic Remanence

The coercivity spectra of selected specimens with different magnitudes of magnetic susceptibility are presented in figure 10. Specimens with strong susceptibility show typically a unimodal distribution with a simple peak by 10 mT, with the coercivity practically vanishing after 30 mT. This indicate that the low coercivity, coarse magnetite grains dominate the remanence of specimens with strong magnetic susceptibility (Jackson et al., 1988). In contrast the specimens with very low magnetic susceptibility ($k \leq 0.5$ mSI) show a noisy spectra but with a distinct peak of coercivity in the range of 40-80 mT. The remanence of specimens with very low magnetic susceptibility is therefore dominated by fine-grained, highly coercive magnetite (Jackson et al., 1988). Coercivity curves of specimens with moderate susceptibility displays a grain size bimodality, with a peak about 10 mT and another between 40 mT and 70 mT. Specimens with moderate susceptibility show therefore two population of magnetite, a low coercive coarse fraction and a subordinate more coercive formed by finer grains.

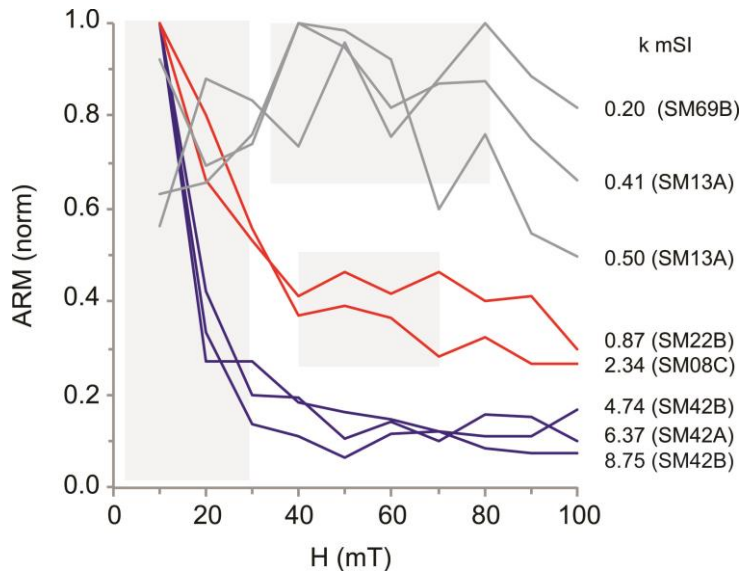


Figure 5.10. Coercivity spectra for samples with different susceptibility magnitudes (k , 10^{-3} SI). Grey areas indicate the windows chosen to determination of partial anisotropy of anhysteretic remanence. H , induced field, ARM; normalized anhysteretic remanent magnetization.

The pAAR₍₀₋₃₀₎ ellipsoid of the specimens with moderate and strong susceptibility is similar to AMS both in shape and orientation of their principal directions (Fig. 5.11). The AMS and AAR₍₀₋₃₀₎ ellipsoids are oblate (SM42, SM8) or prolate (SM59) and their principal directions groups to define a lineation and a foliation. A weak obliquity between the K₂ and K₃ directions is observed in the sample SM59, which is attribute to the prolate shape ($T = -0.19$) of the AAR₍₀₋₃₀₎ ellipsoid. These results indicate that the coarse magnetite grains control the anisotropy of magnetic susceptibility of the specimens with moderate and strong susceptibility. Anisotropy of remanence for the more coercive fractions remain similar to AMS (Fig. 5.11; SM8) or shows principal directions that tend to scatter (SM59) although the lineation defined by AAR₍₅₀₋₇₀₎ tends to group in a direction parallel to the lineation provided by AMS and AAR₍₀₋₃₀₎.

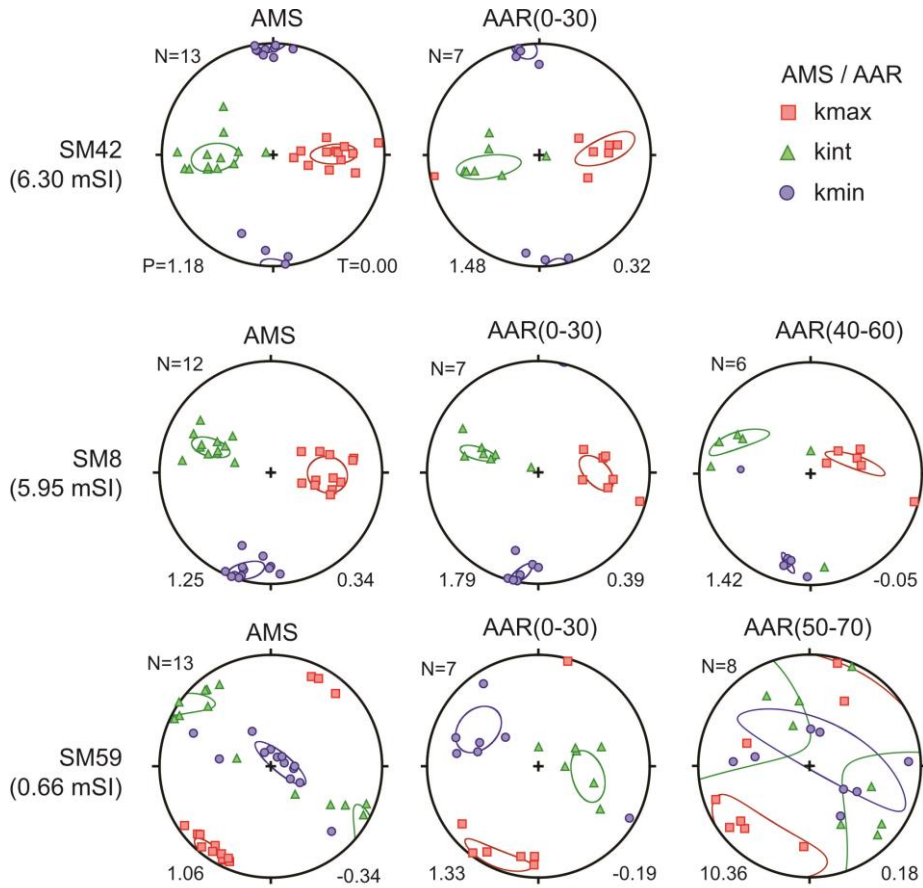


Figure 5.11. Stereograms (lower hemisphere) of the principal directions of AMS and partial AAR for sites with moderate to strong magnetic susceptibility magnitudes.

Different ellipsoid shapes and/or distribution of principal directions are recorded in the sites with very low susceptibility (Fig. 5.12). Although slightly oblique, only the foliation defined by AMS and AAR keeps a good correspondence. A switch between the maximum and intermediate principal directions of AMS and AAR (SM36) probably originates from the oblate distribution of AMS principal directions coupled with different carriers of the magnetic fabric, mostly the paramagnetic silicates for AMS and fine magnetite for AAR.

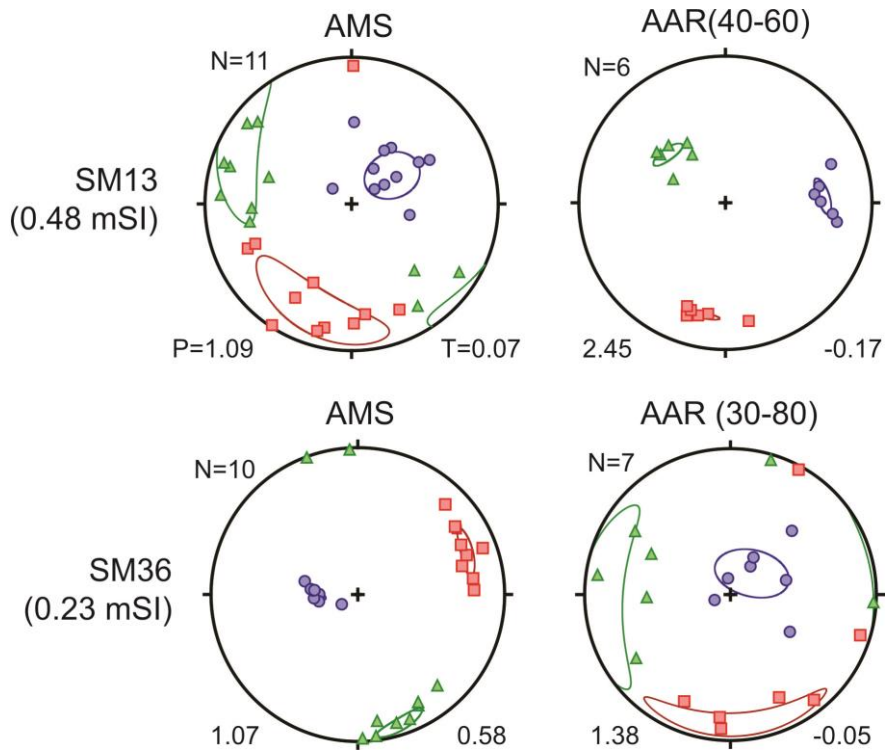


Figure 5.12. Stereograms (lower hemisphere) of the principal directions of AMS and partial AAR for sites with low magnetic susceptibility magnitudes (symbols as Fig. 11).

5.5. DISCUSSION

5.5.1. Significance of magnetic fabrics

The dependence of susceptibility with temperature ($k-T$) combined with the coercivity spectra indicate the mineral that control the susceptibility signal in the Santa Marta batholith is Ti-poor magnetite. For specimens with $k > 0.55$ mSI (65 % of the stations) the Curie temperature at c. 580 °C, well-defined Verwey transition at c. -160 °C and rapid acquisition of remanence in applied fields below 30 mT indicate a coarse, multidomain magnetite (Muxworthy and McClelland, 2000). Petrographic examination shows that magnetite grain size normally ranges between 50 µm and 500 µm and occur associate with titanite, amphibole and biotite. For specimens with $k < 0.5$ mSI the Verwey transition becomes poorly defined or disappears for $k < 0.35$ mSI. Moreover, between -150 °C and approximately 350 °C the susceptibility magnitude decreases progressively as the temperature increases, indicating an important contribution to the paramagnetic minerals to the magnetic susceptibility (Rochette et al., 1987). However, even in the specimens in that the Verwey transition is not detected and $k-T$ is governed by the paramagnetic fraction, the ARM experiments find the presence of magnetite. These highly coercive grains are not observed in

thin-sections, which suggest they must occur as inclusions within the silicates. Moreover, the directional correspondence between principal directions AMS and AAR indicates that the size of the ferrimagnetic inclusions is above the single domain threshold of magnetite, discarding therefore the effect of inverse fabrics in AMS results (Rochette et al., 1992).

Shape and orientations of the AMS and $AAR_{(0-30)}$ ellipsoids are similar to show that AMS depends on the magnetostatic anisotropy of coarse, low coercive magnetite grains. However, between approximately $0.5 < k \text{ (mSI)} < 2$ a subordinate high coercivity fraction can be detected along with the low coercive grains. The orientations of the principal directions of AMS, $AAR_{(0-30)}$ and $AAR_{(40-70)}$ agree to each other to indicate that the fractions with different coercivities, i.e., different magnetite grain sizes, are coaxial. Recent experimental evidence (Arbaret et al., 2013) and X-ray tomography (Schopa et al., 2015) have been confirming the remarkable consistency between the AMS signal defined by magnetite preferred orientation and the rock fabric elements, notably the lineation and foliation. We conclude, therefore, that the magnetic foliation recorded in the Santa Marta batholith tracks fairly well the planar magmatic fabric acquired when the magma was crystallizing.

For specimens with very low magnetic susceptibility the contribution of magnetocrystalline anisotropy of paramagnetic silicates to the bulk susceptibility becomes important. The agreement between the minimum principal directions of AMS and AAR indicates that the crystallographic directions of the host silicates would control the distribution of magnetite inclusions. Indeed fine magnetite inclusions in plagioclase (Usui et al., 2015) and micas (Borradaile and Werner, 1994; Martin-Hernandez and Hirt, 2003) appear to be a common feature in many intermediate to felsic plutonic rocks due to exsolution in silicate minerals upon cooling of magma (Trindade et al., 1999; Usui et al. 2006; Salazar et al., 2013). Furthermore, late-magmatic fluids interacting with the silicate mush may also form fine oxides (e.g. Raposo and Gastal, 2009; Nedelec et al., 2015), which in some cases can be able to disorganize the magnetic fabric (Just et al., 2004; Archanjo et al., 2009). Despite of the potential problems that exsolution and/or hydrothermalism can carry to the AMS interpretations, fine ferrimagnetic particles may also be a proxy for the preferred orientation of the silicates if the inclusions are aligned due to the host lattice. We therefore consider that equivalence between AMS and AAR for the most coercive fractions combine with the $k-T$ results indicates that: (i) the magnetic fabric of the very low susceptibility sites records the preferred orientation of the paramagnetic silicates, and (ii) the absence of superposed sub-fabrics with different orientations in the Santa Marta batholith.

5.5.2. Emplacement structures and tectonic implications

Figure 13 integrates the trend of magnetic foliations defined by AMS, the domains in that the rock texture varies from foliated to gneissic, the metamorphic foliation of the wall-rocks (Tschanz et al., 1969) and the sectors of the batholith corresponding to the late magmatic pulses indicated by zircon U-Pb ages (Duque, 2009; Cardona et al., 2011a). This information allows proposing an emplacement model in which magma crystallized when the magmatic arc was deforming by dextral shear. P-T data from the metapelitic wall rocks and Al-in horblende from the tonalite suggest a depth of emplacement of c. 16 km (Cardona et al. 2011b; Zuluaga and Stowell, 2012). The batholith is divided approximately in a half by East-trending magnetic foliations and lineations which we interpret as recording an synthetic shear band (C'-surface; dashed line in Fig. 5.13) related to an NE-trending shear C-plane. These extensional structures have been reproduced in analogue models simulating the deformation of partially molten aggregates, with the melt channeled into the shear band during their propagation (Rosenberg and Handy, 2000).

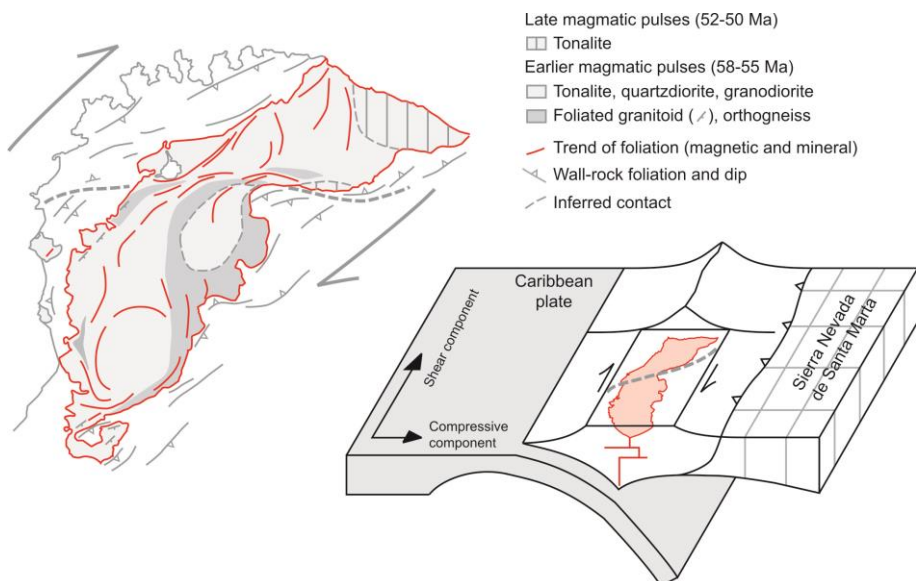


Figure 5.13. Tectonic model of the Santa Marta batholith (upper left) combining the trend of magnetic foliation (red lines) and the metamorphic fabric of the host-rocks (after Tschanz et al., 1969). Dashed lines correspond to the synthetic shear bands originated by the regional strain field dominated by dextral shear. The shear component is transmitted to the magmatic arc (lower right) by the oblique subduction of the Caribbean plate.

The orientation of magnetic foliations in the northern lobe of the batholith tend to be N-S parallel to the maximum flattening plane (S-surface) of the shear deformation, except on its northeastern margin in that foliations tend to be aligned in the NW-SE direction. Magnetic lineations show two contrasting directions, parallel to the N-trending foliations or

perpendicular plunging moderately to the east or to the west. The different directions of the lineations are attributed to the dominant oblate AMS ellipsoid that characterizes the northern lobe of the batholith. The southern lobe shows foliations nearly parallel to the contact with the wall-rocks where the tonalite is foliated or display a gneissic texture. A semi-concentric foliation pattern can be traced to the south of the batholith that could indicate a possible magmatic feeder zone or, alternatively, be originated by the shearing deformation along the wall-rock contact.

Five U-Pb zircons ages in the range of 58-54 Ma (Cardona et al., 2011a; Duque, 2009; this study) come from the southern lobe and one from the northern lobe. This magmatic event must correspond to the main phase of the batholith construction. Late porphyritic to equigranular felsic dikes provided U-Pb ages in the range of 56 and 52 Ma, and are attributed to brittle deformation of still molten igneous body submitted to shear stress. Four samples collected in the north domain close to the Tayrona Park yielded zircon U-Pb ages between 52 and 50 Ma. One sample situated to the east of the E-trending corridor in the middle part of the batholith also provided a zircon U-Pb age of 52 Ma. Uncertainties in the error analysis show that the earlier magmatic pulses and the late pulse are distinct, which indicates that the Santa Marta is a composite batholith formed over a relatively long-lived magmatic source above a subducting slab (Coleman et al., 2004; Matzel et al., 2006; Schaltegger et al., 2009). Although the younger magmatic pulse can be locally recognized penetrating an older plutonic unit, such as described by Duque (2009), their similar composition, color and grain sizes make very difficult to individualize these units on the batholith scale. We inferred the contacts of these magmatic units by the location of the U-Pb analysis combined with the trend of the magnetic foliations. The late tonalite shows the same East-trending elongation of the Buritaca pluton that also provided a zircon U-Pb age in the range of 51 Ma (Duque, 2009). By considering the similar age and compositions between Santa Marta and Buritaca plutons, we propose that late reactivations C'-planes would have assisted the nucleation and emplacement of the late magmatic pulses.

Palinspatic reconstructions suggest that at least 1.000 km dextral offset between the southern Caribbean and northern South America plates between 84 and 46 Ma, as well estimate that c. 1500 km of the Caribbean lithosphere has been subducting beneath Colombia and Venezuela since late Cretaceous (Kennan and Pindell, 2009). Part of the continental deformation related to the interactions between the two plates has been accommodated along the Romeral fault system. The shear movement parallel to the magmatic arc would have

assisted the ascension and emplacement of the Santa Marta and Buritaca batholiths probably exploiting the host-rock extensional structures. Evidence for ascent fabrics and/or body structures (feeder zones, internal convection) were not positively identified, which indicated that arc-parallel shear deformation outlasted the crystallization of the magmas and controlled the shape and orientation of the magnetic fabrics.

5.6. CONCLUSIONS

Anisotropy of susceptibility and remanence indicate that magnetic fabrics of the Santa Marta batholith record the dextral shear deformation related to the oblique convergence of the Caribbean plate against the South American continental plate. The magmatism extended for approximately 10 Ma with the crystallization of tonalites, quartzdiorites and granodiorites in at least two main igneous pulses. The older one, between 58 and 54 Ma, corresponds to the main event of batholith construction. A SHRIMP analysis of the zircon U-rich cores and zoned rims from a tonalite provided a mean age 54.7 ± 0.9 Ma that support an Early Eocene age for main event of magmatism. The shear deformation divides the batholith nearly in a half by East-trending magnetic structures attributed to a synthetic extensional shear band related to a NE-trending arc-parallel shear plane. Such extensional structures would have been reactivated to assist the emplacement of the younger magmatic pulses at c. 50 Ma. The shear deformation combined with arc-normal shortening imparted a dominant oblate AMS ellipsoid and magmatic to solid-state fabrics foliations parallel to the wall-rock contacts and oblique fabrics close to the principal flattening plane of the strain ellipsoid. Investigations in the magnetic subfabrics using partial anisotropy of anhysteretic remanence showed that the coarse and fine magnetite grains are coaxial to the AMS principal directions. Magnetic fabrics, therefore, record the finite strain imposed by the long-lived shear deformation in the plate margin. Such a deformation recorded in Late Cretaceous forearc sequences that accommodated the Santa Marta batholith was localized in the continental suture that southward juxtaposed the Central and Western Cordilleras.

Capítulo 6

Discussão

O estudo do registro magmático, o detalhamento das idades de cristalização e as fontes dos magmas, além do reconhecimento das relações de campo com as unidades adjacentes, tem uma importância fundamental no estudo do magmatismo de arco. Isto porque os eventos tectônicos ao longo de um intervalo de tempo numa margem convergente são registrados através de variações geoquímicas das rochas plutônicas, o que permite traçar com relativa precisão a evolução tectônica de uma região.

A área de investigação deste projeto abrangeu um intervalo de tempo onde importantes eventos tectono-magmáticos moldaram a Cordilheira Central da Colômbia, como discutido nos capítulos 2, 3, 4 e 5. Foi abordada a formação do embasamento cristalino Permo-Triássico afetado pela intrusão de rochas plutônicas no Mesozóico associado a um metamorfismo regional no Jurássico, finalizando com a intrusão de rochas graníticas de afinidade adakítica no Eoceno. Assim, é possível traçar na Cordilheira Central dos Andes Colombianos uma linha de eventos tectono-magmáticos entre o Permiano e o Eoceno que registram diferentes cenários de extensão e compressão na margem continental relacionados com os processos de subducção acresção.

Os vestígios da separação do Pangea têm sido reconhecidos com precisão na margem oeste dos Andes do Norte (Martens *et al.*, 2014; Spikings *et al.*, 2015). Na Colômbia, esses vestígios foram tradicionalmente identificados a oeste da Falha Otú-Pericos, agrupados no denominado Terreno Tahamí, que é separado de um embasamento de idade Grenvilliana a leste e que constitui o denominado Terreno Chibcha (Restrepo *et al.*, 2011; Martens *et al.*, 2014 Vinasco *et al.*, 2006). Nossos dados permitiram identificar rochas de idade permiana e triássica também a leste da falha Otú-Pericos (Cochrane *et al.*, 2104a; Spikings *et al.*, 2015) que redefinem parte do embasamento anteriormente atribuído ao Grenvilliano como de idade Permo-Triássica (Capítulo 2). Isto sugere uma extensão maior do embasamento Permo-Triássico na Cordilheira Central, e uma redefinição do cinturão Grenvilliano na Colômbia, além de questionar o papel da Falha Otú-Pericos como limite de terrenos tectono-estratigráficos. O significado do evento de colisão que reune os Terrenos Tahamí e Chibcha seriam para-autóctones em relação à margem W da América do Sul. O registro da separação

do Pangea é constituído por ortognaisses e anfibolitos com idades entre ca. 268-239 Ma, e que têm uma assinatura de Σ_{Hf} inicial entre -0,1 e -2,5 sugerindo uma crosta continental como fonte do protólito. Para os anfibolitos triássicos, o Σ_{Hf} inicial é de +9,2 até +10,9 indicando uma fonte mantélica juvenil. Esses dados, quando comparados com rochas da mesma natureza em outras localidades de ambos os lados da Falha Otú Pericos e dos Andes Equatorianos, são isotopicamente similares às reportadas por Cochrane *et al.* (2014a) e Spikings *et al.* (2015). Este conjunto de rochas constitui um magmatismo bimodal de rifte numa margem em subducção no Permo-Triássico, e seguido pelo começo da subducção do proto-Pacífico na margem oeste da América do Sul (Cardona *et al.*, 2010; Villagómez *et al.*, 2011; Cochrane *et al.*, 2014a).

O começo de subducção no Jurássico Inferior, a aproximadamente 200 Ma marca o início de uma intensa e contínua atividade magmática (Aspden *et al.*, 1987; Bustamante *et al.*, 2010; Leal-Mejía, 2011; Cochrane *et al.*, 2014) que se estende até o Cretáceo Inferior (Capítulo 3). O magmatismo é distribuído ao longo da margem leste da Cordilheira Central, incluído a Sierra Nevada de Santa Marta no Caribe Colombiano, formando batólitos de composição variando entre granito até diorito, e com um vulcanismo presente pelo menos nas primeiras etapas da atividade plutônica (Zapata *et al.*, 2016). As características geoquímicas deste magmatismo são típicas de um arco magmático continental, tais como as anomalias negativas de Nb e Ti, e uma alta relação LREE/HREE, detalhadas no Capítulo 3.

No intervalo entre aproximadamente 170 e 129 Ma, vários eventos sugerem que o regime de subducção mudou de um ambiente extensivo para compressivo, possivelmente associado com mudanças no mergulho da placa em subducção, além da progressiva obliquidade da convergência. A compilação de idades de cristalização U-Pb (Capítulo 3) mostra que as primeiras fases de magmatismo de arco são as mais volumosas, mas a partir de ~170 Ma, o volume de magma começa a decrescer. Isto está registrado também na distribuição de idades U-Pb em zircões detriticos do Leste Colombiano (Fig. 3.11: Capítulo 3), e pela evidente diminuição da área de exposição dos plútuns mais jovens. Uma característica geoquímica importante do magmatismo neste período é que os isótopos de Hf e Nd mostram uma tendência mais juvenil nas rochas mais jovens, o que foi interpretado como produto de um *slab roll-back* (Cochrane *et al.*, 2014). No presente trabalho, entretanto, é associado com um balanceamento da fusão de basalto e sedimentos ao longo do tempo, no qual se tem uma diminuição progressiva do segundo componente associado a crescente obliquidade da convergência. O regime de convergência extremadamente obliqua poderia ter

sido a causa da interrupção do magmatismo em ca. 130 Ma (Capítulo 3), similar ao descrito na América Central por Rooney *et al.*(2015).

No final do magmatismo, em torno de 165 Ma, um importante evento de metamorfismo regional foi registrado na Cordilheira Central (Blanco-Quintero et al., 2014). Este evento é uma indicação adicional da compressão que caracterizou o final do magmatismo mesozóico da Colômbia. O evento metamórfico é caracterizado em rochas de composição pelítica e máfica que atingiram da fácie xisto verde até anfibolito (550-580 °C e 8 kbar: Blanco-Quintero *et al.*, 2014). Idades U-Pb obtidas em zircões detriticos nas rochas metapelíticas são indicativas de uma bacia deposicional jurássica tendo como embasamento rochas permo-triássico situadas a oeste do cinturão magmático jurássico. A fonte dos zircões detriticos dos metapelitos, embora as idades jurássicas sejam comuns nos Andes do Norte (Colômbia e Equador), são similares as composições isotópicas de Hf de rochas intrusivas aflorantes no Peru (Boekhout *et al.*, 2012). O zircão detritico mais jovem apresentou uma idade de 162 Ma, enquanto a idade do metamorfismo determinado em micas através do sistema Ar-Ar é de 158-147 Ma. (Blanco-Quintero *et al.*, 2014).

Uma etapa de convergência oblíqua, sem magmatismo granítico, é registrada no intervalo entre ~129 e 90 Ma, que marca a idade de cristalização do último pluton (*stock* de Mariquita), e a intrusão do primeiro granitóide depois do hiato no magmatismo, respectivamente. Os acontecimentos durante o mencionado hiato magmático, além das primeiras manifestações de magmatismo relacionado com o proto-Caribe, não fizeram parte deste estudo. Contudo, para contextualizar os eventos eocênicos, é possível mencionar que este intervalo caracterizou-se pela reaparição do magmatismo de arco na margem W da Colômbia entre ~90 - 70 Ma (Leal-Mejía *et al.*, 2011; Villagómez *et al.*, 2011), e a colisão de um arco oceânico com a margem continental (Cardona *et al.*, 2011; Villagómez *et al.*, 2011; Bayona *et al.*, 2012; Spikings *et al.*, 2015), o que teve como consequência o espessamento da crosta continental. Depois da colisão, a reativação da subducção deu início a um magmatismo de arco cujo aspecto marcante é a intrusão de *stocks* com características geoquímicas e petrográficas de diferenciação a alta pressão, tais como alto Sr/Y e presença de epidoto magmático (Capítulo 4). A diferenciação em alta pressão é o resultado de um regime tectônico possivelmente herdado do espessamento crustal, o que permitiu a colocação na crosta inferior, dentro do campo de estabilidade de granada, de *melts* transferidos da zona de subducção como produto da fusão de sedimentos e crosta oceânica na forma de diápiros (Capítulo 4).

Adicionalmente, o registro do magmatismo paleogênico marcado nos zircões detriticos depositados em bacias na Cordilheira Oriental e a região dos *Llanos* da Colômbia, são aparentemente contemporâneo ao da Cordilheira Central. De acordo com Bayona *et al.*, (2012), os zircões detriticos foram associados a um evento magmatismo intraplaca. Isótopos de Hf apresentados no Capítulo 4, obtidos nos zircões dos *stocks* da Cordilheira Central e dos zircões detriticos das rochas sedimentares do leste Colombiano, sugerem que os plút ons da Cordilheira Central podem ser uma fonte potencial dos zircões detriticos. Os estudos sedimentológicos de Bayona *et al.* (2012), no entanto, não descartam a presença de atividade vulcânica eocênica no leste da Colômbia.

Um regime de *flat-slab* decorrente da subducção do *plateau* do Caribe sob a América do Sul estaria atuando durante o Paleógeno (Cardona *et al.*, 2011; Bayona *et al.*, 2012). Esse regime promove compresão generalizada no arco magnético associado a cisalhamento simples destral decorrente da migração para Norte-Nordeste da placa caribenha. A deformação transpresiva resultante foi capaz de promover a colocação de plút ons, como o batólito Santa Marta situado na borda ocidental da Sierra Nevada de Santa Marta. A trama magnética do batólito e suas relações com a tectônica regional foram investigadas através da anisotropia de suscetibilidade e remanência magnética (Capítulo 5).

As propriedades magnéticas do batólito Santa Marta são controladas por grãos de magnetita formados durante a cristalização do magma. A suscetibilidade magnética (SM) média no batólito, da ordem de $4,9 \times 10^{-3}$ SI (mSI), ou seja, típica de granitóides cuja suscetibilidade magnética é controlada por minerais ferromagnéticos (Bouchez, 1997). Contudo, 25% das amostras (total de 759) apresentaram valores de suscetibilidade muito baixos, entre 0,35 mSI e 0,024 mSI, indicando que nessas amostras a SM depende do teor dos minerais paramagnéticos, particularmente a biotita e a hornblenda (Rochette, 1987). O exame mais detalhado das propriedades magnéticas dessas amostras revelou, contudo, que a magnetita ainda está presente nas rochas com SM muito baixa. Elas ocorrem como finos cristais que geralmente aparecem no microscópio petrográfico na forma de pequenas inclusões de opacos nos silicatos, ou então como produto local de alteração hidrotermal tardia pós-magmática. O estudo da orientação preferencial da fração ferromagnética mais fina através da anisotropia de remanência anisotrópica, mostrou que a anisotropia de suscetibilidade e remanência magnética são coaxiais independentemente da magnitude da SM. Esses resultados indicam, portanto, (i) a ausência de grãos de magnetita muito finos que

poderiam conduzir a tramas magnéticas inversas e, (ii) a coerência direcional da trama magnética independentemente das populações de grãos com tamanhos diferentes.

A forma da trama magnética e orientação das direções principais de ASM permitiram separar o batólito em dois setores (Capítulo 5). O setor norte contém uma foliação magnética de direção aproximadamente N-S e oblíqua ao alongamento NE-SW do batólito. No setor sul a foliação magnética tende a se paralelizar com as margens da intrusão, sendo que na margem sudeste foi possível mapear uma foliação/acamamento gnáissico também paralelo ao contato da intrusão com a rocha encaixante (Tschanz *et al.*, 1969). Os setores norte e sul são separados por uma estreita faixa cuja foliação magnética possui direção E-W. O conjunto de foliações foi interpretado em termos de um cisalhamento simples destral sin-magmático que definem um sistema de planos conjugados do tipo S (direção de máximo achataamento) / C' (cisalhamento oblíquo extensional). A ASM do batólito foi adquirida quando o magma estava cristalizando sob ação de uma deformação cisalhante regional relacionada ao componente lateral da convergência da Placa do Caribe. Os dados geocronológicos indicam que a fase principal de construção e deformação do batólito ocorreu no intervalo entre 58 e 54 Ma. Pulsos magmáticos mais tardios, entre 52 e 50 Ma, foram associados a reativações do sistema de cisalhamento preferencialmente na direção E-W (eg. borda NE do setor norte do batólito e intrusão do plúton Buritaca).

Reconstruções palinspáticas sugerem que as placas da América do Sul e Caribe migraram lateralmente por pelo menos 1.000 km entre 84 e 46 Ma, e que desde o Cretáceo aproximadamente 1.500 km da litosfera caribenha foi consumida sob a Colômbia e Venezuela (Kennan & Pindell, 2009). Parte da deformação continental foi acomodada na sutura de Romeral que separa a Cordilheira Central da Ocidental e, na Sierra Nevada de Santa Marta, sequências oceânicas do prisma acrecionário de rochas permo-triássicas e jurássicas da paleomargem continental. O alojamento do batólito Santa Marta ocorre junto à sutura e sua trama magnética/magnética registra, portanto, a deformação transpressiva relacionada compressão e migração lateral da placa do Caribe.

Capítulo 7

Conclusões

A integração entre a petrografia, geocronologia U-Pb e isótopos de Hf em zircão, isótopos de Sr, Nd, Pb e Hf e geoquímica em rocha total de rochas plutônicas e do embasamento metamórfico da Cordilheira Central dos Andes Colombianos permitiu propor um modelo de evolução tectônica que em parte se diferencia dos modelos atualmente vigentes.

As idades U-Pb em zircão e isótopos de Hf em gnaisses e anfibolitos da Unidade Tierradentro, que tradicionalmente foram consideradas como partes da continuação do cinturão Grenvilliano nos Andes Colombianos, mostram que a unidade é permo-triássica. Esses gnaisses e anfibolitos estão limitados pela falha Otú-Pericos, que por sua vez constitui o limite oriental de uma sequência metasedimentar jurássica cuja idade do zircão detritico mais jovem é de 162 Ma. As rochas metasedimentares, consideradas de idade permo-triássica em trabalhos anteriores, pode ser correlacionada à sequências similares da Cordilheira Real do Equador. A composição isotópica de Hf nos zircões detriticos, no entanto, indica que a área fonte dos zircões é distinta das rochas jurássicas atualmente expostas nas cordilheiras Central (Colômbia) e Real (Equador).

A atividade plutônica na Cordilheira Central e no Vale Superior do Magdalena é consistente com a presença de um arco estacionário entre 165 e 129 Ma, o qual é caracterizado por um incremento com o tempo no $\Sigma_{Nd(i)}$ e no $\Sigma_{Hf(i)}$, o que indica uma evolução da fonte dos magmas. Os dados isotópicos e geocronológicos sugerem que a fusão mantélica incluiria um componente sedimentar e basáltico que, com o tempo, se tornaria mais juvenil com o esgotamento do componente sedimentar radiogênico. Esta diminuição do componente sedimentar na cunha mantélica ocorria com a crescente obliquidade da subducção, que favoreceria o transporte longitudinal de sedimentos ao longo da trincheira, e o que poderia explicar ainda o término do magmatismo entre 129 e 90 Ma.

No Eoceno o magmatismo registra uma diferenciação a alta pressão para fornecer uma assinatura adakítica às rochas plutônicas, conforme indicado na elevada razão Sr/Y. O espessamento crustal que permitiu a diferenciação de magmas sob elevada pressão está relacionado à colisão arco-continentale que experimentou a margem oeste da América do Sul

no final do Cretáceo. Os eventos colisionais, relacionados à migração da placa do Caribe, favoreceram a movimentação destral de falhas no arco continental, que por sua vez permitiram a acomodação de magmas tal como documentado na anisotropia de suscetibilidade magnética do batólito Santa Marta. Zircões detriticos eocênicos depositados nas bacias do leste da Colômbia apresentam composições isotópicas de Hf comparáveis aos zircões ígneos do arco paleocênico, sugerindo que o magmatismo eocênico estava em parte exposto à erosão quando da deposição dos sedimentos nas bacias.

Referências

- Aitcheson, S.J., Harmon, R.S., Moorbath, S., Schneider, A., Soler, P., Soria, E.E., Steele, G., Swainbank, I., Wörner, G., 1995. Pb isotopes define basement domains of the Altiplano, Central Andes. *Geology* 23: 555-558.
- Alonso-Perez, R., Müntener, O., Ulmer, P., 2009. Igneous garnet and amphibole fractionation in the roots of island arcs: experimental constraints on andesitic liquids. *Contributions to Mineralogy and Petrology* 157: 541–558.
- Altenberger, U., and Concha, A., 2005. Late lower to early Middle Jurassic arc magmatism in the northern Ibagué batholith (Colombia). *Geología Colombiana* 30: 87-97.
- Alvarán, M., Naranjo, E., and Zapata, E., 2011. Skarn de cobre en la mina Río Frío, Payandé-Tolima: Aspectos mineralógicos, metalográficos y microtermométricos. *Boletín de Ciencias de la Tierra* 29: 7-20.
- Álvarez-Galindez, M.J., 2013. Petrologia, geoquímica e metalogenia dos depósitos de ouro El Silencio e La Gran Colômbia, distrito mineiro Segovia-Remédios, Colômbia [M.Sc. thesis]: Brasilia, Universidade de Brasilia, 192 p.
- Annen, C., and Sparks, R.S.J., 2002. Effects of repetitive emplacement of basaltic intrusions on thermal evolution and melt generation in the crust. *Earth and Planetary Science Letters* 203: 937-955.
- Annen, C., Blundy, J.D., and Sparks, R.S.J., 2006. The genesis of intermediate and silicic magmas in deep crustal hot zones. *Journal of Petrology* 47: 505-539.
- Arbaret, L., Launeau, P., Diot, H., Sizaret, S., 2013. Magnetic and shape fabrics of magnetite in simple shear flows. *Journal of Volcanology and Geothermal Research* 249: 25-38.
- Archango, C.J., Bouchez, J.L., Corsini, M., Vauchez, A., 1994. The Pombal granite pluton: magnetic fabric, emplacement and relationships with the Brasiliano strike-slip setting of NE Brazil (Paraíba State). *Journal of Structural Geology* 16: 323-335.
- Archango, C.J., Launeau, P., Hollanda, M.H.B.M., Macedo, J.W.P., Liu, D., 2009. Scattering of magnetic fabrics in the epizonal Cambrian alkaline granite of Meruoca (Ceará State, northeast Brazil). *International Journal of Earth Sciences* 98: 1793-1807.
- Aspden, J.A., McCourt, W.J., Brook, M., 1987. Geometrical control of subduction related magmatism: the Mesozoic and Cenozoic plutonic history of western Colombia. *Journal of the Geological Society, London* 144: 893–905.
- Ayala-Calvo, C., Bayona, G., Ojeda-Marulanda, C., Cardona, A., Valencia, V., Padrón, C. E., Yoris, F., Mesa-Salamanca, J. and García, A., 2009. Stratigraphy and provenance of

Campanian-Paleogene units in Cesar sub-basin: contributions to the regional tectonic evolution. *Geología Colombiana* 34: 1–34.

Bachmann, O., Dungan, M.A., Bussy, F., 2005. Insights into shallow magmatic processes in large silicic magma bodies: the trace element record in the Fish Canyon magma body, Colorado. *Contributions to Mineralogy and Petrology* 149: 338–349.

Barrero, D., 1969. Petrografía del stock de Payandé y metamorfitas asociadas: Boletín Geológico, v. XVII, p. 113-144.

Barrero, D., and Vesga, C., 1976. Mapa geológico del Cuadrángulo K-9 Armero y mitad sur del Cuadrángulo J-9 La Dorada. Ingeominas, scale 1:100.000, 1 sheet.

Barth, A.P., Wooden, J.L., Jacobson, C.E., and Economos, R.C., 2013. Detrital zircon as a proxy for tracking the magmatic arc system: The California arc example. *Geology* 41: 223–226.

Bayona, G., Cardona, A., Jaramillo, C., Mora, A., Montes, C., Caballero, V., Mahecha, H., Lamus, F., Montenegro, O., Jimenez, G., Mesa, A., and Valencia, V., 2013, Onset of fault reactivation in the Eastern Cordillera of Colombia and proximal Llanos Basin; response to Caribbean-South American convergence in early Palaeogene time: *in:* Nemčok, M., Mora, A., and Cosgrove, J.W., eds., Thick-skin-dominated orogens: from initial inversion to full accretion: London, Geological Society [London], Special Publication 377: 285–314.

Bayona, G., Cardona, A., Jaramillo, C., Mora, A., Montes, C., Valencia, V., Ayala, C., Montenegro, O., Ibañez-Mejia, M., 2012. Early Paleogene magmatism in the northern Andes: Insights on the effects of oceanic plateau – continent convergence. *Earth and Planetary Science Letters* 331 – 332: 97 – 111.

Bayona, G., Cardona, A., Tellez, G., Garzón A., Pinzón, D., Mendes, J., Ramirez, C., Rueda, M., 2015. Magmatismo Paleoceno-Eoceno Temprano (?) en la Cuenca proximal de los Llanos. XV Congreso Colombiano de Geología, Bucaramanga, Agosto 31-Septiembre 5. CD con resúmenes.

Bayona, G., García, D., and Mora, G., 1994. La Formación Saldaña: producto de la actividad de estratovolcanes continentales en un dominio de retroarco, *in* Etayo-Serna, F., ed., Estudios Geológicos del Valle Superior del Magdalena: Bogotá, Universidad Nacional de Colombia, Chapter I, 21 p.

Bayona, G., Jiménez, G., Silva, C., Cardona, A., Montes, C., Roncancio, J., and Cordani, U., 2010. Paleomagnetic data and K–Ar ages from Mesozoic units of the Santa Marta massif: A preliminary interpretation for block rotation and translations. *Journal of South American Earth Sciences* 29: 817–831.

Bayona, G., Montes, C., Cardona, A., Jaramillo, C., Ojeda, G., Valencia, V., 2011. Intraplate subsidence and basin filling adjacent to an oceanic arc–continental collision; a case from the southern Caribbean–South America plate margin. *Basin Research* 23: 403–422.

- Bayona, G.; Rapalini, V.; and Constazo-Alvarez, V. 2006. Paleomagnetism in Mesozoic rocks of the northern Andes and its implications in Mesozoic tectonics of northwestern South America. *Earth Planets Space* 58: 1–18.
- Behn, M.B., Keleman, P.B., Hirth, G., Hacker, B.R., and Massone, H.J., 2011. Diapirs as the source of the sediment arc signature in arc lavas. *Nature Geoscience* 4: 641-646.
- Bellos, L.I., Castro, A., Díaz-Alvarado, J., and Toselli, A., 2015. Multi-pulse cotectic evolution and in-situ fractionation of calc-alkaline tonalite–granodiorite rocks, Sierra de Velasco batholith, Famatinian belt, Argentina: *Gondwana Research* 27: 258-280.
- Benn, K., Paterson, S. R., Lund, S. P., Pignotta, G. S. & Kruse, S., 2001. Magmatic fabrics in batholiths as markers of regional strains and plate kinematics: example of the Cretaceous Mt. Stuart batholith. *Physics and Chemistry of the Earth* 26: 343–54.
- Best, M., 2003, Igneous and Metamorphic Petrology: Blackwell Publishing. 758 p.
- Black, L.P.; Kamo, S.L.; Allen, C.M.; Aleinikoff, J.N.; Davis, D.W.; Korsch, R.J.; Foudolis, C. 2003. TEMORA 1: a new zircon standard for Phanerozoic U-Pb geochronology. *Chemical Geology* 200: 155-170.
- Blanco-Quintero, I.F.; García-Casco, A.; Toro, L.M.; Moreno, M.; Ruiz, E.C.; Vinasco, C.J.; Cardona, A.; Lázaro, C.; and Morata, D. 2014. Late Jurassic terrane collision in the northwestern margin of Gondwana (Cajamarca Complex, eastern flank of the Central Cordillera, Colombia). *International Geology Review* 56: 1852-1872.
- Boekhout, F.; Spikings, R.; Sempere, T.; Chiaradia, M.; Ulianov, A.; and Schaltegger, U. 2012. Mesozoic arc magmatism along the southern Peruvian margin during Gondwana breakup and dispersal. *Lithos* 146–147: 48–64.
- Borradaile, G.J., Henry, B., 1997. Tectonic applications of magnetic susceptibility and its anisotropy. *Earth Science Reviews* 42: 49-93.
- Borradaile, G.J., Werner, T., 1994. Magnetic anisotropy of some phyllosilicates. *Tectonophysics* 235: 223-248.
- Boschman, L., van Hinsbergen, D.J.J., Torsvik, T.H., Spakman, W., Pindell, J., 2014. Kinematic reconstruction of the Caribbean region since Early Jurassic. *Earth-Science Reviews* 138: 102-136.
- Bouchez, J.L., 1997. Granite is never isotropic: an introduction to AMS studies in granitic rocks. In: Bouchez, J.L., Hutton, D.H.W., Stephens, W.E., (Eds.), *Granite: from segregation of melt to emplacement fabrics*. Kluwer Academis Publishers, 95 – 112.
- Bouvier, A., Vervoort, J.D., and Patchett, P. J., 2008. The Lu-Hf and Sm-Nd isotopic composition of CHUR: Constraints from unequilibrated chondrites and implications for the bulk composition of terrestrial planets. *Earth and Planetary Science Letters* 273: 48-57.

- Brook, M., 1984. New radiometric age data from S. W. Colombia. Ingeominas-Misión Británica (British Geological Survey), Cali, Colombia. Report 10.
- Bustamante, A., Juliani, C., Essene, E.J., Hall, C.M., Hyppolito, T., 2012. Geochemical constraints on blueschist- and amphibolite-facies rocks of the Central Cordillera of Colombia: The Andean Barragán Region. International Geology Review 54: 1013-1030.
- Bustamante, C., Archanjo, C., Cardona, A., Valencia, V., Vervoort, J., 2016. Geochronology and geochemistry of late Jurassic to early Cretaceous plutonism in the Central Cordillera and Upper Magdalena valley of the Colombian Andes: a record of long-term arc maturity and oblique subduction. Geological Society of America Bulletin (in press).
- Bustamante, C., Cardona, A., Bayona, G., Mora, A., Valencia, V., Gehrels, G., Vervoort, J., 2010. U-Pb LA-ICP-MS Geochronology and tectonic correlation of Middle Jurassic intrusive rocks from the Garzón Massif and the Central Cordillera, Southern Colombia. Boletín de Geología 32: 93-109.
- Caballero, V., Parra, M., Mora, A., López, C., Rojas, L.E., and Quintero, I., 2013. Factors controlling selective abandonment and reactivation in thick-skin orogens: a case study in the Magdalena Valley, Colombia: *in: Nemčok, M., Mora, A., and Cosgrove, J.W., eds., Thick-skin-dominated orogens: from initial inversion to full accretion: London, Geological Society [London], Special Publication 377: 343–367.*
- Calais, E., Symithe, S., de Lépinay, B., Prépetit, C., 2016. Plate Boundary Segmentation in the Northeastern Caribbean from Geodetic Measurements and Neogene Geological Observations. Comptes Rendus Geosciences 348: 42-51.
- Cardona, A., Valencia, V., Bayona, G., Duque, J., Ducea, M., Gerhels, G., Jaramillo, C., Montes, C., Ojeda, G., and Ruiz, J., 2011a. Early subduction orogeny in the Northern Andes: Turonian to Eocene magmatic and provenance record in the Santa Marta massif and Ranchería Basin, Northern Colombia. Terra Nova 23: 26-34.
- Cardona, A., Valencia, V., Weber, M., Duque, J., Montes, C., Reiners, P., Domanik, K., Nicolescu, S., Villagomez, D., 2011b. Transient Cenozoic tectonic stages in the southern margin of the Caribbean plate: U-Th/He thermochronological constraints from Eocene plutonic rocks in the Santa Marta Massif and Serranía de Jarara, northern Colombia. Geologica Acta 9: 445 – 466.
- Cardona, A., Weber, M., Valencia, V., Bustamante, C., Montes, C., Cordani, U., Muñoz, C.M., 2014. Geochronology and geochemistry of the Parashi granitoid, NE Colombia: Tectonic implications of short-lived Early Eocene plutonism along the SE Caribbean margin. Journal of South American Earth Sciences 50: 75-92.
- Cardona, A.; Valencia, V.; Garzón, A.; Montes, C.; Ojeda, C.; Ruiz, J.; and Weber, M. 2010. Permian to Triasic I to S-type magmatic switch in the northeast Sierra Nevada de Santa Marta and adjacent regions, Colombian Caribbean: tectonic setting and implications with Pangea paleogeography. Journal of South American Earth Sciences 29: 772-783.

- Cardona-Molina, A.; Cordani, U.G.; and Macdonald, W. 2006. Tectonic correlations of pre-Mesozoic crust from the northern termination of the Colombian Andes, Caribbean region. *Journal of South American Earth Sciences* 21: 337–354.
- Castillo, P.R., 2012. Adakite petrogenesis. *Lithos* 134-135: 304-316.
- Castro, A., 2014. The off-crust generation of granite batholiths. *Geosciences Frontiers* 5: 63-75.
- Castro, A., Gerya, T., García-Casco, A., Fernández, C., Díaz-Alvarado, J., Moreno-Ventas, I., and Löw, I., 2010. Melting relations of MORB-Sediment mélange in underplated mantle wedge plumes; implications for the origin of Cordilleran-type batholiths. *Journal of Petrology* 51: 1267-1295.
- Castro, A., Vogt, K., and Gerya, T., 2013. Generation of new continental crust by sublithospheric silicic-magma relamination in arcs: A test of Taylor's andesite model. *Gondwana Research* 23: 1554-1566.
- Cawood, P.A., Hawkesworth, C.J., and Dhuime, B., 2012. Detrital zircon record and tectonic setting. *Geology* 40: 875-878.
- Cediel, F., and C. Cáceres, 2000. Geological Map of Colombia, Third Edition: Geotec Ltd., Bogotá, digital format with legend and tectonostratigraphic chart.
- Cediel, F., R. P. Shaw, and C. Cáceres, 2003. Tectonic assembly of the Northern Andean Block, in C. Bartolini, R. T. Buffler, and J. Blickwede, eds., *The Circum-Gulf of Mexico and the Caribbean: Hydrocarbon habitats, basin formation, and plate tectonics*. AAPG Memoir 79: 815–848.
- Chang, Z., Vervoort, J.D. McClelland, W.C., and Knaack C., 2006. U-Pb dating of zircon by LA-ICP-MS. *Geochemistry, Geophysics, Geosystems* 7: 1-14.
- Chapman, J.B., Ducea, M.N., DeCelles, P.G., Profeta, L., 2015. Tracking changes in crustal thickness during orogenic evolution with Sr/Y; an example from the North American Cordillera. *Geology* 43: 919-922.
- Chiaradia, M., 2009. Adakite-like magmas from fractional crystallization and melting-assimilation of mafic lower crust (Eocene Macuchi arc, Western Cordillera, Ecuador). *Chemical Geology* 265: 468 – 487.
- Chiaradia, M., 2015. Crustal thickness control on Sr/Y signatures of recent arc magmas: an Earth scale perspective. *Science* 5: 8115.
- Chiaradia, M., Vallance, J., Fontboté, Ll., Stein, H., Schaltegger, U., Coder, J., Richards, J., Villeneuve, M., and Gendall, I., 2009. U-Pb, Re-Os and 40Ar/39Ar geochronology of the Nambija Au-skarn and Pangui porphyry Cu deposits, Ecuador: implications for the Jurassic metallogenic belt of the Northern Andes. *Mineralium Deposita* 44: 371–387.

- Cochrane, R., Spikings, R., Gerdes, A., Ulianov, A., Mora, A., Villagómez, D., Putlitz, B., and Chiaradia, M. 2014a. Permo-Triassic anatexis: continental rifting and the disassembly of western Pangaea. *Lithos* 190-191: 383-402.
- Cochrane, R., Spikings, R., Gerdes, A., Winkler, W., Ulianov, A., Mora, A., and Chiaradia, M. 2014b. Distinguishing between in-situ and accretionary growth of continents along active margins. *Lithos* 202-203: 382-394.
- Coldwell, B., Clemens, J., Petford, N., 2011. Deep crustal melting in the Peruvian Andes: Felsic magma generation during delamination and uplift. *Lithos* 125: 272-286.
- Coleman, D., Gray, W., Glazner, A.F., 2004. Rethinking the emplacement and evolution of zoned plutons: Geochronological evidence for incremental assembly of the Tuolumne intrusive suite, California. *Geology* 32: 433-436.
- Conrad, C. P., Wi, B., Smith, E. I., Bianco, T. A., Tibbetts, A., 2010. Shear-driven upwelling induced by lateral viscosity variations and asthenospheric shear: A mechanism for intraplate volcanism. *Physics of the Earth and Planetary Interiors* 178: 162-175
- Conrad, C.P., Bianco, T. A., Smith, E. I., Wessel, P., 2011. Patterns of intraplate volcanism controlled by asthenospheric shear. *Nature Geoscience* 4: 317-321.
- Cordani, U.; Cardona, A.; Jimenez, D.M.; Liu, D.; and Nutman, A. 2005. Geochronology of Proterozoic basement inliers in the Colombian Andes: tectonic history of remnants of a fragmented Grenville belt. *Geological Society of London: Special Publication* 246: 329-346.
- Cox, K.G., Bell, J.D., and Pankhurst, R.J., 1979. *The Interpretation of Igneous Rocks*: George Allen & Unwin, 450 p.
- Cuadros, F.A.; Botelho, N.F.; Ordóñez-Carmona, O.; and Matteini, M. 2014. Mesoproterozoic crust in the San Lucas Range (Colombia): An insight into the crustal evolution of the northern Andes. *Precambrian Research* 245: 186-206.
- Defant, M.J., Drummond, M.S., 1990. Derivation of some modern arc magmas by melting of young subducted lithosphere. *Nature* 347: 662–665.
- DeGraaff-Surpless, K., Wooden, J.L., and McWilliams, M.O., 2002. Detrital zircon provenance analysis of the Great Valley Group, California, Evolution of an arc–forearc system. *Geological Society of America Bulletin* 114: 1564–1580.
- DePaolo, D.J., 1988. Age dependence of the composition of continental crust: evidence from Nd isotopic variations in granitic rocks. *Earth and Planetary Science Letters* 90 (3): 263-271.
- Dickin, A.P., 2005. *Radiogenic isotope geology*. Cambridge University Press, 2 ed. 509 p.
- Dickinson, W.R.; and Lawton, T.F. 2001. Carboniferous to Cretaceous assembly and fragmentation of México. *Geological Society of America Bulletin* 113: 1142–1160.

- Ducea, M., 2001. The California arc: thick granitic batholiths, eclogitic residues, lithospheric-scale thrusting, and magmatic flare-ups. *Geological Society of America Today* 11: 4-10
- DuFrane, S.A., Vervoort, J.D., Hart, G.L., 2007. Uncertainty of Hf isotope analysis in zircon using LA-MC-ICPMS techniques: full disclosure: *Geochimica et Cosmochimica Acta*, V.M. Goldschmidt Conference, 17th, Cologne, Abstracts, v. 71, p. A241.
- Duncan, R.A., Hargraves, R.B., 1984. Plate tectonic evolution of the Caribbean region in the mantle reference frame. in Bonini, W. et al., eds., *The Caribbean-South American plate boundary and regional tectonics*. Geological Society of America Memoir 162, p. 81-93.
- Duque, F., 2009. Geocronología (U-Pb y Ar-Ar) y geoquímica de los intrusivos paleógenos de la Sierra Nevada de Santa Marta y sus relaciones con la tectónica del Caribe y el arco magmático circun-Caribeño. Tesis de Maestría en Ciencias de la Tierra, Universidad Nacional Autónoma de Mexico. 176 pp.
- Echeverri, S., Cardona, A., Pardo, A., Monsalve, G., Valencia, V.A., Borrero, C., Rosero, S., López, S., 2015. Regional provenance from southwestern Colombia fore-arc and intra-arc basins: implications for Middle to Late Miocene orogeny in the Northern Andes. *Terra Nova* 27: 356-363.
- Eggins, S.M., Kinsley, L.P.J., and Shelly, J.M.G., 1998. Deposition and elemental fractionation processes during atmospheric pressure laser ablation sampling for analysis by ICP-MS. *Applied Surface Science* 127: 278–286.
- Escalona, A., Mann, P., 2011. Tectonics, basin subsidence mechanisms and paleogeography of the Caribbean-South American plate boundary zone. *Marine and Petroleum Geology* 28: 8-39.
- Evans, B.W., Vance, J.A., 1987. Epidote phenocrysts in dacitic dikes, Boulder County, Colorado. *Contributions to Mineralogy and Petrology* 96: 178–185.
- Faure, G., Mensing, T.M., 2005. Isotopes: Principles and applications. John Wiley & Sons, Inc. 3 ed. 897 p.
- Fawcett, T.C., Burmester, R.F., Housen, B.A., Iriondo, A., 2003. Tectonic implications of magnetic fabrics and remanence in the Cooper Mountain pluton, North Cascade Mountains, Washington. *Canadian Journal of Earth Sciences* 40: 1335-1356.
- Feininger, T., Botero, G., 1982. The Antioquian batholith. Publicación Geológica Espacial INGEOMINAS 12, 50 pp.
- Ferré, E.C., Michelsen, K.J., Ernest, W.G., Boyd, J.D., Canon-Tapia, E., 2012. Vertical zonation of the Barcroft granodiorite, White Mountains, California: Implications for magmatic processes. *American Mineralogist* 97: 1049-1059.
- Galer, S.J.G., and Abouchami, W., 1998. Practical application of lead triple spiking for correction of instrumental mass discrimination: *Mineralogical Magazine* 62A: 491-492.

- Gehrels, G., Valencia, V.A., Ruiz, J., 2008. Enhanced precision, accuracy, efficiency, and spatial resolution of U-Pb ages by laser ablation-multicollector-inductively coupled plasma-mass spectrometry. *Geochemistry, Geophysics and Geosystems* 9 (3).
- Gendall, I.R., Quevedo, L.A., Sillitoe, R.H., Spencer, R.M., Puente, C.O., Leon, J.P., and Povedo, R.R., 2000. Discovery of a Jurassic porphyry copper belt, Pangui área, southern Ecuador: SEG Newsletter 43: 8–15.
- Gerya, T.V., Yuen, D.A., 2003. Characteristicsbased marker-in-cell method with conservative fitedifferences schemes for modeling geological flows with strongly variable transport properties. *Phys. Earth Planet. In.* 140: 293–318.
- Glazner, A. F., 1991. Plutonism, oblique subduction, and continental growth: An example from the Mesozoic of California. *Geology* 19: 784–786.
- Gómez-Tapias, J.; Montes-Ramírez, N.E.; Nivia-Guevara, A.; and Diedrix, H., 2015. Mapa Geológico de Colombia Escala 1:1.000.000 Servicio Geológico Colombiano.
- González, H., Londoño, A.C., 2002. Catálogo de las unidades Litoestratigráficas de Colombia: Granodiorita de Manizales. Ingeominas, Bogotá 19 p.
- Goodge, J.W., Vervoort, J.D., 2006. Origin of Mesoproterozoic A-type granites in Laurentia: Hf isotope evidence. *Earth and Planetary Science Letters* 243: 711-731.
- Gorczyk, W., Willner, A.P., Gerya, T.V., Connolly, J.A.D., and Burg, J.P., 2007. Physical controls of magmatic productivity at Pacific-type convergent margins: Numerical modeling. *Physics of the Earth and Planetary Interiors* 163: 209-232.
- Grocott, J., Taylor, G.K., 2002. Magmatic arc fault systems, deformation partitioning and emplacement of granitic complexes in the Coastal Cordillera, north Chilean Andes (25°30'S to 27°00'S). *Journal of the Geological Society, London* 159: 425-442.
- Gurnis, M., Hall, C., Lavier, L., Evolving force balance during incipient subduction. *Geochemistry. Geosystems*, 5, Q07001.
- Hacker, B.R., Kelemen, P.B., and Behn, M.D., 2011. Differentiation of the continental crust by relamination: *Earth and Planetary Science Letters* 307: 501-516.
- Harris, N.W., Pearce, J.A., and Tindle, A.G., 1986. Geochemical characteristics of collision-zone magmatism. *Geological Society [London], Special Publication* 19: 67-81.
- Henry, B., Légeois, J.P., Nouar, O., Derder, M.E.M., Bayou, B., Bruguier, O., Oubadi, A., Belhai, D., Amenna, M., Hemmi, A., Ayache, M., 2009. Repeated granitoid intrusions during the Neoproterozoic along the western boundary of the Saharan metacraton, Eastern Hoggar, Tuared shield, Algeria: An AMS and U-Pb zircon age study. *Tectonophysics* 474: 417-434.

- Hervé, F., Pankhurst, R.J., Fanning, C.M., Calderón, M., and Yaxley, G.M., 2007. The South Patagonian batholith: 150 my of granite magmatism on a plate margin. *Lithos* 97: 373-394.
- Hoernle, K., Abt, D.L., Fischer, K.M., Nichols, H., Hauff, F., Abers, G.A., van den Bogaard, P., Heydolph, K., Alvarado, G., Protti, M., and Strauch, W., 2008. Arc-parallel flow in the mantle wedge beneath Costa Rica and Nicaragua. *Nature Letters* 451: 1094-1098.
- Horton, B.K., Saylor, J.E., Nie, J., Mora, A., Parra, M., Reyes-Harker, A., and Stocki, D.F., 2010. Linking sedimentation in the northern Andes to basement configuration, Mesozoic extension, and Cenozoic shortening: evidence from detrital zircon U-Pb ages, Eastern Cordillera, Colombia. *Geological Society of America Bulletin* 122: 1423-1442.
- Howell, D.G. 1995. Principles of terrane analysis: new applications for global tectonics, 2nd edn. Chapman & Hall, London.
- Howell, D.G.; Schermer, E.R.; Jones, D.L.; Ben-Avraham, Z.; and Scheibner, E. 1983. Tectonostratigraphic terrane map of the circum-Pacific region. United States Department of the Interior Geological Survey. Open file report 83-716, 23 pp.
- Hrouda, F., 1982. Magnetic anisotropy of rocks and its application in geology and geophysics. *Geophysical Surveys*: 37-82.
- Ibañez-Mejía, M., Tassinari, C.C.G., and Jaramillo-Mejía, J.M., 2007, U-Pb ages of the Antioquian Batholith – Geochronological constraints of late Cretaceous magmatism in the Central Andes of Colombia: Congreso Colombiano de Geología, 11th, Bucaramanga, Abstracts, p. 11.
- Ibáñez-Mejía, M.; Ruiz, J.; Valencia, V.; Cardona, A.; Gehrels, G.; and Mora, A. 2011. The Putumayo Orogen of Amazonia and its implications for Rodinia reconstructions: New U-Pb geochronological insights into the Proterozoic tectonic evolution of northwestern South America. *Precambrian Research* 191: 58-77.
- Ishihara, S., 1977. The magnetite-series and ilmenite-series granitic rocks. *Mining Geology* 27: 293-305.
- Jackson, M., 1991. Anisotropy of magnetic remanence: a brief review of mineralogical sources, physical origins and geological applications, and comparison with susceptibility anisotropy. *Pageoph.*, 136: 1-28.
- Jackson, M., Gruber, W., Marvin, J., Benerjee, S.K., 1988. Partial anhysteretic remanence and its anisotropy: Applications and grain-size dependence. *Geophysical Research Letters* 15: 440-443.
- Jaillard, E., Hérail, G., Monfret, T., Diaz-Martinez, E., Baby, P., Lavenu, A., Dumon, J. F., 2000. Tectonic evolution of the Andes of Ecuador, Peru, Bolivia and northernmost Chile. In: Cordani, U. G., Milani, E. J., Thomaz-Filho, A., Campos, D. A., Tectonic evolution of South America. Rio de Janeiro 31st International Geological Congress. 481-559.

- Jaillard, E., Soler, P., Carlier, G., and Mourier, T., 1990. Geodynamic evolution of the northern and central Andes during early to middle Mesozoic times: a Tethyan model: Journal of the Geological Society [London] 147: 1009-1022.
- Jarrard, R.D., 1986. Relations among subduction parameters: Reviews of Geophysics, v. 24, no. 2, p. 217-284.
- Johnson, D.M., Hooper, P.R., and Conrey, R.M., 1999. XRF analysis of rocks and minerals for major and trace elements on a single low dilution Li-tetraborate fused bead: JCPDS-International Centre for Diffraction Data: 843-867.
- Just, J., Kontny, A., Wall, H., Hirt, A.M., Martin-Hernandez, F., 2004. Development of magmatic fabrics during hydrothermal alteration in the Soultz-sous-Forêts granite from the EPS-1 borehole, Upper Rhine Graben. in: Magnetic Fabric: Methods and Applications, F. Martin-Hernandez, C.M. Luneburg, C. Aubourg and M. Jackson (eds). Geological Society, London, Special Publications 238: 509-526.
- Kay, R.W., Kay, S.M., 1993. Delamination and delamination magmatism. Tectonophysics 219: 177-189.
- Kay, S., Mpodozis, C., 2001. Central Andean Ore Deposits Linked to Evolving Shallow Subduction Systems and Thickening Crust. GSA Today 3: 4-9.
- Kemp, A.I.S., Hawkesworth, C.J., Collins, W.J., Gray, C.M., Blevin, P.L., and EIMF, 2009. Isotopic evidence for rapid continental growth in an extensional accretionary orogen: The Tasmanides, eastern Australia. Earth and Planetary Science Letters 284: 455-466.
- Kennan, L., Pindell, J.L., 2009. Dextral shear, terrane accretion and basin formation in the Northern Andes. Best explained by interaction with a Pacific-derived Caribbean Plate? From: James, K.H., Lorente, M.A., Pindell, J.L. (eds) *The Origin and Evolution of the Caribbean Plate*. Geological Society, London, Special Publications 328: 487-531.
- Kerr, A.C., 2014. Oceanic Plateaus. Treatise on Geochemistry, 2nd Edition, Elsevier, p. 631-667.
- Kerr, A.C., Marriner, G.F., Tarney, J., Nivia, A., Saunders, A.D., Thirlwall, M.F., Sinton, C.W., 1997. Cretaceous basaltic terranes in Western Colombia: elemental, chronological and Sr-Nd Isotopic Constraints on petrogenesis. Journal of Petrology 38: 677-702.
- Kerr, A.C., Tarney, J., 2005. Tectonic evolution of the Caribbean and northwestern South America: the case for accretion on two Late Cretaceous oceanic plateaus. Geology, 23: 269-272.
- Kinny, P.D., Maas, R., 2003. Lu-Hf and Sm-Nd isotope systems in zircon. In: Hanchar, J.M., Hapskin, P.W.O., (Eds.), Zircon. Reviews in Mineralogy and Geochemistry 53: 327-339.
- Kosler, J., and Sylvester, P., 2003. Present trends and the future of zircon in geochronology: laser ablation ICPMS. Reviews in Mineralogy and Geochemistry 53: 243-275.

- Kroonenberg, S. 1982. A grenvillian granulite belt in the Colombian Andes and its relations to the Guiana Shield. *Geologie en Mijnbouw* 61: 325-333.
- Leal-Mejía, H. 2011. Phanerozoic gold metallogeny in the Colombian Andes: A tectono-magmatic approach. [PhD Thesis]: Barcelona, Universitat de Barcelona, 1000 p.
- Leal-Mejía, H., Shaw, R.P., Padilla, R., Valencia, V., 2010. Magmatism vs. Mineralization in the Segovia–Remedios and Central Antioquia Au Districts, Colombia [poster]: SEG2010 Conference.
- Lee, C.-T.A., Morton, D.M., Kistler, R.W., and Baird, A.K., 2007. Petrology and tectonics of Phanerozoic continent formation: From island arcs to accretion and continental arc magmatism. *Earth and Planetary Science Letters* 263: 370-387.
- Li, S., Wilde, S.A., Wang, T., Xiao, W., and Guo, Q., 2016. Latest Early Permian granitic magmatism in southern Inner Mongolia, China: Implications for the tectonic evolution of the southeastern Central Asian Orogenic Belt. *Gondwana Research* 29: 168-180.
- Litherland, M. 1994. The metamorphic belts of Ecuador. British Geological Survey. Overseas Memoir 11, 147 p.
- Ludwig, K.R., 2000. SQUID 1.00. A user manual. Berkeley Geochronology Center Spec. Publ., vol. 2. Berkeley, CA, 17p.
- Ludwig, K.R., 2003. Isoplot 3.00: a geochronological toolkit for Microsoft Excel® (revised version). Berkeley Geochronological Center, Special Publ. 4, Berkeley, California, 70pp.
- Luzieux, L.D.A., Heller, F., Spikings, R., Vallejo, C.F., Winkler, W., 2006. Origin and Cretaceous tectonic history of the coastal Ecuadorian forearc between 1°S-4°S: paleomagnetic, radiometric and fossil evidence. *Earth and Planetary Science Letters* 249: 400–414.
- Macpherson, C.G., Dreher, S.T., Thirlwall, M.F., 2006. Adakites without slab melting: high pressure differentiation of island arc magma, Mindanao, the Philippines. *Earth and Planetary Science Letters* 243: 581–593.
- Malatesta, C., Gerya, T., Crispini, L., Federico, L., and Capponi, G., 2013. Oblique subduction modeling indicates along-trench tectonic transport of sediments: *Nature Communications* 4: 2456.
- Maloney, K.T., Clarke, G.L., Klepeis, K.A., and Quevedo, L., 2013. The Late Jurassic to present evolution of the Andean margin: Drivers and the geological record. *Tectonics* 32: 1049–1065.
- Mantilla-Figueroa, L.C., Bissig, T., Valencia, V., and Hart, C., 2013. The magmatic history of the Vetas-California mining district, Santander Massif, Eastern Cordillera, Colombia. *Journal of South American Earth Sciences* 45: 235-249.

- Marquinez, G.; and Núñez, A. 1998. Catálogo de las unidades litoestratigráficas de Colombia: Neises y anfibolitas de Tierradentro. Ingeominas: 22 p. Bogotá.
- Martens, U.; Restrepo, J.J.; Ordóñez-Carmona, O.; and Correa-Martinez, A.M.. 2014. The Tahamí and Anacona terranes of the Colombian Andes: Missing links between the South American and Mexican Gondwana margins. *The Journal of Geology* 122: 507-530.
- Martin, H., Smithies, R.H., Rapp, R., Moyen, J.F., Champion, D., 2005. An overview of adakite, tonalite–trondhjemite–granodiorite (TTG), and sanukitoid: relationships and some implications for crustal evolution. *Lithos* 79: 1-24.
- Martín-Hernández, F. and Hirt, A.M., 2003. The anisotropy of magnetic susceptibility in biotite, muscovite and chlorite single crystals. *Tectonophysics* 367: 13-28.
- Massone, H.J.; and Toulkeridis, T. 2010. Widespread relics of high-pressure metamorphism confirm major terrane accretion in Ecuador: a new example from the Northern Andes. *International Geology Review* 54: 67-80.
- Matsumoto, Y., Enami, M., Tsuboi, M., Hong, M., 2014. Magmatic zoisite and epidote in tonalite of the Ryoke belt, central Japan. *European Journal of Mineralogy* 26: 279-291.
- Matzel, J.E.P., Bowring, S.A., Miller, R., 2006. Time scales of pluton construction at different crustal levels: Examples from the Mount Stuart and Tenpeak intrusions, North Cascades, Washington. *Geological Society of American Bulletin* 118: 1412-1430.
- Maya, M.; and González, H. 1995. Unidades litodémicas en la Cordillera Central de Colombia. *Boletín Geología* 35: 43-57.
- McCabe, C., Jackson, M., Ellwood, B.B., 1985. Magnetic anisotropy in the Trenton limestone: results of a new technique, anisotropy of anhysteretic susceptibility. *Geophysical Research Letters* 12: 333-336.
- McDougall, I., and Harrison, T.M., 1999. *Geochronology and thermochronology by the ⁴⁰Ar/³⁹Ar method*: Oxford University Press, 2nd ed. 261 p.
- Montes, C., Bayona, G., Cardona, A., Busch, D.M., Silva, C.A., Morón, S.A., Hoyos, N., Ramírez, D.A., Jaramillo, C., Valencia, V., 2012. Arc-Continent Collision and Orocline Formation: Closing of the Central America Seaway. *Journal of Geophysical Research* 117 B04125: 25 pp.
- Montes, C., Cardona, A., Jaramillo, C., Pardo, A., Silva, J.C., Valencia, V., Ayala, C., Pérez-Angel, L.C., Rodríguez-Parra, L.A., Ramírez, V., Niño, H., 2015. Middle Miocene closure of the Central American Seaway. *Science* 348: 226-229.
- Montes, C., Guzmán, G., Bayona, G., Cardona, A., Valencia, V., 2010. Clockwise rotation of the Santa Marta massif and simultaneous Paleogene to Neogene deformation of the Plato-San Jorge and Cesar-Ranchería basins. *Journal of South American Earth Sciences* 29: 832-848.

- Mora, A., Gaona, T., Kley, J., Montoya, D., Parra, M., Quiroz, L.I., Reyes, G., and Strecker, M.R., 2009. The role of inherited extensional fault segmentation and linkage in contractional orogenesis: A reconstruction of Lower Cretaceous inverted rift basin in the Eastern Cordillera of Colombia. *Basin Research* 21: 111–137
- Moyen, J.F., 2009. High Sr/Y and La/Yb ratios: The meaning of the “adakitic signature”. *Lithos* 112: 556-574.
- Moyen, J.F., Nédélec, A., Martin, H., Jayananda, M., 2003. Syntectonic granite emplacement at different structural levels: the Closepet granite, South India. *Journal of Structural Geology* 25: 611-631.
- Münker, C., Weyer, S., Scherer, E., Mezger, K., 2001. Separation of high field strength elements (Nb, Ta, Zr, Hf) and Lu from rock samples for MC-ICPMS measurements: *Geochemistry, Geophysics, Geosystems* 2 (12): 1064.
- Müntener, O., Kelemen, P.B., Grove, T.L., 2001. The role of H₂O during crystallization of primitive arc magmas under uppermost mantle conditions and genesis of igneous pyroxenites: an experimental study. *Contributins to Mineralogy and Petrology* 141: 643–658.
- Muxworthy, A.R., McClelland, E., 2000. Review of the low-temperature magnetic properties of magnetite from a rock magnetic perspective. *Geophysical Journal International* 140: 101-114.
- Nakamura, N., 1974. Determination of REE, Ba, Fe, Mg, Na and K in carbonaceous and ordinary chondrites. *Geochimica et Cosmochimica Acta* 38: 757-775.
- Nédélec, A., Trindade, R., Peschler, A., Archanjo, C.J., Macouin, M., Poitrasson, F., Bouchez, J.L., 2015. Hydrothermally-induced changes in mineralogy and magnetic properties of oxidized A-type granites. *Lithos* 212: 145-157.
- Neves, S.P., Vauchez, A., Archanjo, C.J., 1996. Shear zone-controlled magma emplacement or magma-assisted nucleation of shear zones? Insights from northeast Brazil. *Tectonophysics* 262: 349-364.
- Nie, J., Horton, B.K., Mora, A., Saylor, J.E., Housh, T.B., Rubiano, J., and Naranjo, J., 2010, Tracking exhumation of Andean ranges bounding the Middle Magdalena Valley Basin, Colombia. *Geological Society of America Bulletin* 38: 451-454.
- Nivia, A., 1996. The Bolívar mafic–ultramafic complex, SW Colombia: the base of an oceanic plateau. *Journal of South American Earth Sciences* 9: 59–68.
- Noble, S.R., Aspden, J.A., Jemelita, R., 1997, Northern Andean crustal evolution: New U-Pb geochronological constraints from Ecuador. *Geological Society of America Bulletin* 109: 789-798.

- Núñez, A. 2001. Mapa Geológico del Departamento del Tolima escala 1: 250.000. Memoria explicativa. Ingeominas: 101 p. Bogotá.
- Ordoñez, O., Pimentel, M., 2001a. Consideraciones geocronológicas e isotópicas del Batolito Antioqueño. Revista de la Academia de Ciencias Exactas, Fisicas y Naturales 25: 27 – 35.
- Ordoñez, O., Pimentel, M.M., Armstrong, R.A., Gioia, S.M.C.L., Junges, S., 2001b, U-Pb SHRIMP and Rb-Sr ages of the Sonsón Batholith: III South-American Symposium on Isotope Geology (SASIG 2001, Pucon, Chile), Extended Abstracts.
- Ordóñez-Carmona, O., Pimentel, M., and Laux, J.H., 2007, Edades U-Pb del Batolito Antioqueño. Boletín de Ciencias de la Tierra 22: 129–130.
- Ordóñez-Carmona, O.; Pimentel, M.M.; 2002. Rb–Sr and Sm–Nd isotopic study of the Puquí complex: Colombian Andes. Journal of South American Earth Sciences 15: 173-182.
- Ordóñez-Carmona, O.; Restrepo, J.J.; and Pimentel, M.M. 2006. Geochronological and isotopical review of pre-Devonian crustal basement of the Colombian Andes. Journal of South American Earth Sciences 21: 372-382.
- Ozdemir, O., Dunlop, D.J., Moskowitz, B.M. 1993. The effect of oxidation on the Verwey transition in magnetite. Geophysical Research Letters 20: 1671-1674.
- Pankhurst, R.J., Weaver, S.D., Hervé, F., and Larrondo, P., 1999, Mesozoic-Cenozoic evolution of the North Patagonian Batholith in Aysen, southern Chile: Journal of the Geological Society [London] 156: 673-694.
- Parada, M.A., Roperch, P., Guiresse, C., Ramirez, E., 2005. Magnetic fabrics and compositional evidence for the construction of the Caleu pluton by multiple injections, Coastal Range of Central Chile. Tectonophysics 399: 399-420.
- Parra, M., Mora, A., Lopez, C., Rojas, L.E., Horton, B.K., 2012. Detecting earliest shortening and deformation advance in thrust-belt hinterlands: example from the Colombian Andes. Geology 40: 175–178.
- Peacock, S.M., Rushmer, T., Thompson, A.B., 1994. Partial melting of subducting oceanic crust. Earth and Planetary Science Letters 121 (1–2): 227–244.
- Peccerillo, A., and Taylor, T.S., 1976. Geochemistry of Eocene calc-alkaline volcanic rocks from Kastamonu area, Northern Turkey. Contributions to Mineralogy and Petrology 58: 63-81.
- Pereira, M.F., Castro, A., and Fernández, C., 2015, The inception of a Paleotethyan magmatic arc in Iberia. Geosciences Frontiers 6: 297-306.
- Pindell, J. and Kennan, L., 2009. Tectonic evolution of the Gulf of Mexico, Caribbean and northern South America in the mantle reference frame: an update. In: The Origin and Evolution of the Caribbean Plate (K.H. James, M.A. Lorente and J. Pindell, eds.), Geological Society of London, Special Publication 328: 1–56.

- Pindell, J., Kennan, L., Maresch, W.V., Stanek, K.P., Draper, G., and Higgs, R., 2005. Plate kinematic and crustal dynamics of circum-Caribbean arc-Continent interactions: tectonics controls on basin development in the Proto-Caribbean margins. In: Avé Lallement, H. G., Sisson, V.B. (Eds.), Caribbean–South American Plate Interactions. Geological Society of America. Special Paper 394: 7–52.
- Plazas, J., Zuluaga, C., López, J., 2013. Condiciones de emplazamiento, mineralogía y geoquímica de la tonalita-granodiorita de Manizales, Caldas. XIV Congreso Colombiano de Geología, Bogotá. 354 pp.
- Poli, S., Schmidt, M.W., 2002. Petrology of subducted slabs. Annual Review of Earth and Planetary Science Letters 30: 207-235.
- Profeta, L., Ducea,M.N., Chapman, J.B., Paterson, S.R., Henríquez-González, S.M., Kirsch, M., Petrescu, L., DeCelles, P.G., 2015. Quantifying crustal thickness over time in magmatic arcs. Scientific Reports 5: 17786.
- Ramos, V. 2009 Anatomy and global context of the Andes: Main geologic features and the Andean orogenic cycle. *in* Kay, S.M., Ramos, V.A., Dickinson, W.D., eds., Backbone of the Americas: Shallow Subduction, Plateau Uplift, and Ridge and Terrane Collision. Geological Society of America Memoir 204: 31-66.
- Ramos, V., Aleman, A, 2000. Tectonic evolution of the Andes. In: Cordani, U.G., Milani, E.J., Thomaz-Filho, A, Campos, D.A, (Eds.), Tectonic evolution of South America. Rio de Janeiro 31st International Geological Congress. 635-685.
- Raposo, M.I.B., Gastal, M.C., 2009. Emplacement mechanism of the main granite pluton of the Lavras do Sul intrusive complex, South Brazil, determined by magnetic anisotropies. Tectonophysics 466: 18-31.
- Restrepo, J.J., Ordóñez-Carmona, O., Armstrong, R., and Pimentel, M.M., 2011. Triassic metamorphism in the northern part of the Tahamí Terrane of the central cordillera of Colombia. Journal of South American Earth Sciences 32: 497–507.
- Restrepo, J.J., Toussaint, J.F., 1988. Terranes and continental accretion in the Colombian Andes. Episodes 11: 189-193.
- Restrepo-Moreno, S., Foster, D., and Kamenov, G., 2007, Formation age and magma sources for the Antioqueño Batholith derived from LA-ICP-MS U-Pb and Hf isotope analysis of zircon grains: Geological Society of America Abstracts with programs 39: 493 pp.
- Restrepo-Moreno, S.A., Foster, D., Kamenov, G.D., 2009. Crystallization age and magma sources of the Antioqueño and Ovejas batholiths, Central Cordillera, Colombia: evidence from combined LA-ICP-MS U–Pb dating and Hf-isotope analysis of zircon grains and whole-rock geochemistry. Geological Society of America, Portland Annual Meeting, paper No. 79-3.

- Restrepo-Pace, P.A., Ruiz, J., Gehrels, G., Cosca, M., 1997. Geochronology and Nd isotopic data of Grenville-age rocks in the Colombian Andes: new constraints for Late Proterozoic–Early Paleozoic paleocontinental reconstructions of the Americas. *Earth and Planetary Science Letters* 150: 427–441.
- Richards, J.R., Kerrich, R., 2007. Special paper: Adakite-like rocks: their diverse origins and questionable role in metallogenesis. *Economic Geology* 102 (4): 537–576.
- Riel, N.; Guillot, S.; Jaillard, E.; Martelat, J.E.; Paquette, J.L.; Schwartz, S.; Goncalves, P.; Declaux, G.; Thebaud, N.; Lanari, P.; Janots, E.; and Yuquilema, J. 2013. Metamorphic and geochronological study of the Triassic El Oro metamorphic complex, Ecuador: Implications for high-temperature metamorphism in a forearc zone. *Lithos* 156-159: 41-68.
- Rochette, P., 1987. Magnetic susceptibility of the rock matrix related to magnetic fabric studies. *Journal of Structural Geology* 9(8): 1015-1020.
- Rollinson, H.R., 1993. *Using Geochemical Data: Evaluation, Presentation, Interpretation*. Prentice Hall, Singapore, 352 p.
- Rooney, T.O., Franceschi, P., Hall, C.M., 2011. Water-saturated magmas in the Panama Canal region: a precursor to adakite-like magma generation? *Geochemistry, Geophysics, Geosystems* 16: 4178–4208.
- Rooney, T.O., Morell, K.D., Hidalgo, P., and Fraceschi, P., 2015, Magmatic consequences of the transition from orthogonal to oblique subduction in Panama: *Geochemistry, Geophysics, Geosystems* 16: 4178–4208.
- Rosenberg, C.L., Handy, M.R., 2000. Syntectonic melt pathways during simple shearing of a partially molten rock analogue (Norcamphor-Bensamide). *Journal of Geophysical Research*, 105(B2), 3135-3149.
- Rubatto, D. 2002. Zircon trace element geochemistry: partitioning with garnet and the link between U-Pb ages and metamorphism. *Chemical Geology* 184: 123-138.
- Sagong, H., Kwon, S.T., and Ree, J.T., 2005, Mesozoic episodic magmatism in South Korea and its tectonic implication. *Tectonics* 24: 18, TC5002.
- Saint-Blanquat, M., Law, R.D., Bouchez, J.L., Morgan, S., 2001. Internal structure and emplacement of the Papoose Flat pluton: An integrated structural, petrographic and magnetic susceptibility study. *Geological Society of America Bulletin*, 113(8), 975-995.
- Salazar, C.A., Archanjo, C.J., Rodrigues, S.W., Hollanda, M.H.B.M., Liu, D., 2013. Age and magnetic fabric of the Três Córregos granite batholith: evidence for Ediacaran transtension in the Ribeira Belt (SE Brazil). *International Journal of Earth Sciences*, 102: 1563-1581.

- Sarmiento-Rojas, L.F., Van Wess, J.D., and Cloetingh, S., 2006, Mesozoic transtensional basin history of the Eastern Cordillera, Colombian Andes: Inferences from tectonic models. *Journal of South American Earth Sciences* 21: 383-411.
- Saylor, J.E., Horton, B., Nie, J., Corredor, J., and Mora, A., 2011. Evaluating foreland basin partitioning in the Northern Andes using Cenozoic fill of the Floresta Basin, Eastern Cordillera, Colombia. *Basin Research* 23: 377-402.
- Schaltegger, U., Brack, P., Ovtcharova, M., Peytcheva, I., Schoene, B., Stracke, A., Marocchi, M., Bargossi, G.M., 2009. Zircon and titanite recording 1.5 million years of magma accretion, crystallization and initial cooling in a composite pluton (southern Adamello batholith, northern Italy). *Earth and Planetary Science Letters* 286: 208-218.
- Schmidt, M.W. and Poli, S., 2004. Magmatic epidote. In “Epidotes”, Liebscher, A. & Franz, G. ed. Mineralogical Society of America and Geochemical Society, Washington, DC, 399–430.
- Schopha, A., Floess, D., Saint Blanquat, M., Annen, C., Launeau, P., 2015. The relation between magnetite and silicate fabric in granitoids of the Adamello Batholith. *Tectonophysics* 642: 1-15.
- Schwartz, J.J., Johnson, K., Miranda, E.A., Wooden, J.L., 2011. The generation of high Sr/Y plutons following Late Jurassic arc–arc collision, Blue Mountains province, NE Oregon. *Lithos* 126: 22-41.
- Seton, M., Müller, R. D., Zahirovic, S., Gaina, C., Torsvik, T., Shephard, G., Talsma, A., Gurnes, M., Turner, M., and Chandler, M., 2012. Global continental and ocean basin reconstructions since 200 Ma. *Earth Science Reviews* 113: 212-270
- Shand, S.J., 1943, Eruptive Rocks, their genesis, composition, classification, and their relation to ore-deposits with a chapter on meteorite: John Wiley & Sons., New York, 450 p.
- Sillitoe, R.H., Jaramillo, L., Damon, P.E., Shafiqullah, M., Escobar, R., 1982. Setting, characteristics and age of the Andean Porphyry Copper Belt in Colombia. *Economic Geology* 77: 1837-1850.
- Silva, A., Mora, A., Caballero, V., Rodríguez, G., Ruiz, G., Moreno, N., Parra, M., Ramírez-Arias, J.C., Ibáñez, M., and Quintero, I., 2013. Tectonic controls on sedimentation in an intermontane hinterland basin adjacent to inversion structures: the Nuevo Mundo syncline, Middle Magdalena Valley, Colombia: *in:* Nemčok, M., Mora, A., and Cosgrove, J.W., eds., Thick-skin-dominated orogens: from initial inversion to full accretion: London, Geological Society [London], Special Publication 377: 369–409.
- Sláma, J., Košler, J., Condon, D.J., Crowley, J.L., Gerdes, A., Hanchar, J.M., Horstwood, M.S.A., Morris, G.A., Nasdala, L., Norberg, N., Schaltegger, U., Schoene, B., Tubrett, M.N., and Whitehouse, M.J., 2008, Plešovice zircon – A new natural reference material for U-Pb and Hf isotopic microanalysis. *Chemical Geology* 249: 1–35.

- Spadea, P., Espinosa, A., 1996. Petrology and chemistry of late Cretaceous volcanic rocks from the southernmost segment of the Western Cordillera of Colombia (South America). *Journal of South American Earth Sciences* 9: 79-90.
- Spikings, R., Cochrane, R., Villagómez, D., Van der Lelij, R., Vallejo, C., Winkler, W., and Beate, B., 2015, The geological history of northwestern South America: from Pangaea to the early collision of the Caribbean Large Igneous Province (290–75 Ma). *Gondwana Research* 27: 95-139.
- Spikings, R.A., Winkler, W., Hughes, R.A., Handler, R., 2005. Thermochronology of Allochthonous Terranes in Ecuador: unraveling the accretionary and postaccretionary history of the Northern Andes. *Tectonophysics* 399: 195–220.
- Spikings, R.A., Winkler, W., Seward, D. Handler, R., 2001. Along-strike variations in the thermal and tectonic response of the continental Ecuadorian Andes to the collision with heterogeneous oceanic crust. *Earth and Planetary Science Letters* 186: 57–73.
- Stevenson, C.T.E., Owens, W.H., Hutton, D.H.W., 2007. Flow lobes in granite: The determination of magma flow direction in the Trawenagh Bay Granite, northwestern Ireland, using anisotropy of magnetic susceptibility. *Geological Society of America Bulletin* 119: 1368-1386.
- Sun, S.S., and McDonough, W.F., 1989, Chemical and isotopic systematics of oceanic basalts: implications for mantle composition and processes. *in* Sanders, A.D., Norry, M.J., eds., *Magmatism in oceanic basins*: London, Geological Society [London], Special Publication 42: 313–345.
- Tamura, Y., Tatsumi, Y., Zhao, D., Kido, Y., Shukuno, 2002. Hot fingers in the mantle wedge: new insights into magma genesis in subduction zones. *Earth and Planetary Science Letters* 197: 105-116
- Tarney, J., and Jones, C.E., 1994. Trace element geochemistry of orogenic igneous rocks and crustal growth models: *Journal of the Geological Society [London]* 151: 855–868.
- Tatsumi, Y. and Eggins, S., 1995. Subduction zone magmatism. Boston, Blackwell, Science, 211 p.
- Tikoff, B., Saint-Bланquat, M., 1997. Transpressional shearing and strike-slip partitioning in the Late Cretaceous Sierra Nevada magmatic arc, California. *Tectonics* 16(3): 442-459.
- Titus, S.J., Clark, R., Tikoff, B., 2005. Geologic and geophysical investigation of two fine-grained granites, Sierra Nevada Batholith, California: Evidence for structural controls on emplacement and volcanism. *Geological Society of America Bulletin* 117: 1255-1271.
- Toro-Toro, L.M., Moreno-Sánchez, M., Gómez, A., 2011, Geoquímica y petrografía de las rocas volcánicas de la formación Yaví. *Boletín de Geología* 33: 93-100.

- Torres, R.; Ruiz, J.; Patchett, P. J.; and Grajales, J. M. 1999. A Permo-Triassic continental arc in eastern Mexico: Tectonic implications for reconstructions of southern North America, in Bartolini, C., et al., eds., Mesozoic sedimentary and tectonic history of northcentral Mexico. Geological Society of America Special Paper 340: 191–196.
- Toussaint, J.F. 1995. Evolución Geológica de Colombia: Triásico–Jurásico: Editorial Universidad Nacional, Medellín, 277 p.
- Toussaint, J.F.; and Restrepo, J.J. 1989. Acreciones sucesivas en Colombia: un nuevo modelo de evolución geológica. In: Memorias V Congreso Colombiano de Geología, p. 127–146.
- Trindade, R.I.F., Raposo, M.I.B., Ernesto, M., Siqueira, R., 1999. Magnetic susceptibility and partial anhysteretic remanence anisotropies in the magnetite-bearing granite pluton of Tourão, NE Brazil. Tectonophysics 314: 443-468.
- Tschanz, C.M., Marvin, R.F., Cruz, J., Mehnert, H.H., Cebula, G.T, 1974. Geologic evolution of the Sierra Nevada de Santa Marta area, Colombia. Geological Society of America Bulletin 85: 273-284.
- Tschanz, C.M., Jimeno, A., Vesga, C., 1969. Geology of the Sierra Nevada de Santa Marta area (Colombia). Instituto de Investigaciones e Información Geocientífica, Minero – Ambiental y Nuclear. República de Colombia. 288 pp.
- Usui, Y., Nakamura, N., Yoshida, T., 2006. Magnetite microexsolution in silicate and magmatic flow fabric of the Goyozan granitoid (NE Japan): significance of partial remanence anisotropy. Journal of Geophysical Research, vol 111, B11101.
- Usui, Y., Shibuya, T., Sawaki, Y., Komiya, T., 2015. Rock magnetism of tiny exsolved magnetite in plagioclase from a Paleoarchean granitoid in the Pilbara craton. Geochemistry, Geophysics, Geosystems 16: 112-125.
- Vallejo, C., Spikings, R.A., Winkler, W., Luzieux, L., Chew, D., Page, L., 2006. The early interaction between the Caribbean Plateau and the NW South American plate. Terra Nova 18: 264–269.
- Van der Lelij, R., Spikings, R., Ulianov, A., Chiaradia, M., and Mora, A., 2016. Palaeozoic to Early Jurassic history of the northwestern corner of Gondwana, and implications for the evolution of the Iapetus, Rheic and Pacific Oceans. Gondwana Research 31: 271-294.
- van Hunen, J., ven de Berg, A.P., Vlaar, N.J., 2011. Various mechanisms to induce present-day shallow flat subduction and implications for the younger Earth: a numerical parameter study. Physics of the Earth and Planetary Interiors 146: 179-194.
- Vásquez, M., Altenberger; U., Romer, L.R., Sudo, M., and Moreno-Murillo, J.M., 2009. Magmatic evolution of the Andean Eastern Cordillera of Colombia during the Cretaceous: Influence of previous tectonic processes. Journal of South American Earth Sciences 29: 171-186.

- Vásquez, M., and Altenberger, U., 2005. Mid-Cretaceous extension-related magmatism in the eastern Colombian Andes. *Journal of South American Earth Sciences* 20: 193-210.
- Vervoort, J.D., Kemp, A.I.S., Fisher, C., Bauer, A., 2015. The rock record has it about right—no significant continental crust formation prior to 3.8 Ga. *American Geophysical Union, Fall Meeting, San Francisco, Abstracts*.
- Vervoort, J.D., and Blichert-Toft, J., 1999. Evolution of the depleted mantle: Hf isotope evidence from juvenile rocks through time. *Geochimica et Cosmochimica Acta* 63: 533–556.
- Vervoort, J.D., Patchett, P.J., 1996. Behavior of hafnium and neodymium isotopes in the crust: constraints from Precambrian crustally derived granites. *Geochimica et Cosmochimica Acta* 60: 3717–3733.
- Vervoort, J.D., Patchett, P.J., Albarede, F., Blichert-Toft, J., Rudnick, R., and Downes, H., 2000. Hf-Nd isotopic evolution of the lower crust. *Earth and Planetary Science Letters* 181: 115–129.
- Vervoort, J.D., Patchett, P.J., Söderlund, U., and Baker, M., 2004. Isotopic composition of Yb and the determination of Lu concentrations and Lu/Hf ratios by isotope dilution using MC-ICPMS: *Geochemistry, Geophysics, Geosystems* 5: 15.
- Vesga, C.J., and Barrero, D., 1978. Edades K/Ar en rocas ígneas y metamórficas de la Cordillera Central de Colombia y su implicación geológica. *Congreso Colombiano de Geología*, 2nd, Bogotá, Abstracts, p. 17.
- Villagomez, D., and Spikings, R., 2013. Thermochronology and tectonics of the Central and Western Cordilleras of Colombia: Early Cretaceous–Tertiary evolution of the Northern Andes. *Lithos* 160-161: 228-249.
- Villagomez, D., Spikings, R., Magna, T., Kammer, A., Winkler, W., and Beltrán, A., 2011. Geochronology, geochemistry and tectonic evolution of Western and Central cordilleras of Colombia. *Lithos* 125: 875–896.
- Villamil, T., 1999. Campanian-Miocene Tectonostratigraphy, Depocenter evolution and basin development of Colombia and Western Venezuela. *Palaeogeography, Palaeoclimatology, Palaeoecology* 153, 239-275.
- Vinasco, C.; Cordani, U.; González, H.; Weber, M.; and Peláez, C. 2006. Geochronological, isotopic, and geochemical data from Permo-Triassic granitic gneisses and granitoids of the Colombian Central Andes. *Journal of South American Earth Sciences* 21: 355-371.
- Vogt, K., Castro, A., and Gerya, T., 2013. Numerical modeling of geochemical variations caused by crustal relamination: *Geochemistry, Geophysics, Geosystems* 14: 470-487.
- Weber, M., Gómez-Tapias, J., Cardona, A., Duarte, E., Pardo-Trujillo, A., Valencia, V.A., 2015. Geochemistry of the Santa Fe Batholith and Buritica Tonalite in NW Colombia e Evidence of subduction initiation beneath the Colombian Caribbean Plateau. *Journal of South American Earth Sciences* 62: 257-274.

- Wei, W., Chen, Y., Faure, M., Shi, Y.H., Martelet, G., 2014. A multidisciplinary study on the emplacement mechanism of the Qingyang-Jiuhua Massif in Southeast China and its tectonic bearings. Part I: structural geology, AMS and paleomagnetism. *Journal of Southeast Asian Earth Sciences* 86: 76-93.
- White W.M., Albarède, F., and Télouk, P., 2000. High-precision analysis of Pb isotopic ratios using multi-collector ICP-MS. *Chemical Geology* 167: 227–257.
- Williams, I.S., 1998, U-Th-Pb geochronology by ion microprobe, in: McKibben, M.A., ShanksIII III, W.C., and Ridley, W.I., eds., Applications of Microanalytical Techniques to Understanding Mineralizing Processes. *Reviews in Economic Geology* 7: 1–35.
- Wilson, J., 1998. Magnetic susceptibility patterns in the Cordilleran granitoid: The Las Tazas Complex, northern Chile. *Journal of Geophysical Research* 103 (B3): 5257-5267.
- Wilson, J., Grocott, J., 1999. The emplacement of the granitic Las Tazas complex, northern Chile: the relationship between local and regional strain. *Journal of Structural Geology*. 21: 1513-1523.
- Zapata, S., Cardona, A., Jaramillo, C., Valencia, V., and Vervoort, J., 2016. U-Pb LA-ICP-MS geochronology and geochemistry of Jurassic volcanic and plutonic rocks from the Putumayo region (southern Colombia): tectonic setting and regional correlations. *Boletín de Geología* 38: 1-38.
- Zartman, R.E., and Doe, S.M., 1981, Plumbotectonics – the model. *Tectonophysics* 75: 135–162.
- Zuluaga, C., Stowell, H., 2012. Late Cretaceous-Paleocene metamorphic evolution of the Sierra Nevada de Santa Marta: Implications for Caribbean geodynamic evolution. *Journal of South American Earth Sciences* 14: 1-9.

ANEXOS

Table 2.1. U-Pb zircon ages from the Tierradentro unit.

Analysis	Th/U	$^{238}\text{U}/^{206}\text{Pb}$	% err	$^{207}\text{Pb}/^{206}\text{Pb}$	% err	Age $^{206}\text{Pb}/^{238}\text{U}$	abs error	Age $^{207}\text{Pb}/^{206}\text{Pb}$	abs error	Age (Ma)	abs error (Ma)
CAT1A											
40	0.15	27.0090	1.7	0.0513	0.9	234.4	4.0	254.9	19.6	234.4	4.0
39	0.05	25.6958	1.9	0.0521	1.2	246.1	4.7	288.3	26.3	246.1	4.7
38	0.10	28.8771	2.5	0.0484	2.1	219.5	5.3	116.6	49.2	219.5	5.3
37	0.12	27.6399	2.0	0.0516	1.7	229.1	4.6	265.9	39.7	229.1	4.6
36	0.22	27.6622	1.8	0.0513	1.1	228.9	4.0	254.2	24.6	228.9	4.0
35	0.12	28.1342	2.0	0.0505	1.8	225.2	4.5	215.9	40.9	225.2	4.5
34	0.22	27.4429	1.5	0.0526	1.5	230.7	3.4	310.8	33.6	230.7	3.4
28	0.18	26.4232	0.9	0.051	0.9	239.5	2.2	239.6	20.9	239.5	2.2
27	0.35	26.4917	1.3	0.0495	1.5	238.9	3.1	170.8	34.3	238.9	3.1
26	0.08	27.7288	1.6	0.0501	1.7	228.4	3.5	201.9	38.5	228.4	3.5
25	0.16	28.6917	0.9	0.0509	1.0	220.9	2.0	238.6	22.1	220.9	2.0
23	0.19	28.0222	1.9	0.0531	1.8	226.0	4.2	331.0	41.0	226.0	4.2
22	0.04	28.5203	3.3	0.0523	3.1	222.2	7.2	297.7	68.8	222.2	7.2
21	0.19	26.2227	1.0	0.0503	1.0	241.3	2.4	207.2	22.3	241.3	2.4
20	0.44	25.1953	2.1	0.052	1.7	250.9	5.2	284.1	39.5	250.9	5.2
19	0.03	26.4145	1.5	0.0509	1.4	239.5	3.6	237.4	31.5	239.5	3.6
18	0.15	26.0779	0.9	0.0506	0.8	242.6	2.2	224.2	17.3	242.6	2.2
17	0.14	26.9842	1.5	0.0503	2.2	234.6	3.6	207.4	51.0	234.6	3.6
16	0.17	28.8498	1.7	0.0514	1.8	219.7	3.6	258.6	40.0	219.7	3.6
15	0.16	31.4358	1.7	0.0505	2.0	201.9	3.4	219.6	46.5	201.9	3.4
14	0.15	26.1344	1.0	0.0506	1.2	242.1	2.4	224.5	27.5	242.1	2.4
13	0.14	27.4278	1.8	0.0498	2.1	230.8	4.0	185.4	47.5	230.8	4.0
11	0.04	25.7171	1.4	0.0555	1.6	245.9	3.3	430.5	34.6	245.9	3.3
10	0.18	28.0903	1.6	0.0506	1.9	225.5	3.5	224.4	43.9	225.5	3.5
9	0.25	26.3971	1.0	0.0511	1.1	239.7	2.3	243.4	25.3	239.7	2.3

8	0.07	31.0071	5.7	0.0588	3.1	204.6	11.4	559.7	65.8	204.6	11.4
5	0.20	26.6148	1.3	0.0505	1.3	237.8	3.0	217.7	30.1	237.8	3.0
4	0.15	28.4656	1.5	0.0505	1.9	222.6	3.3	216.8	42.9	222.6	3.3
3	0.12	26.4017	1.2	0.0507	1.3	239.7	2.8	228.8	29.9	239.7	2.8
2	0.95	19.0297	1.8	0.0514	2.5	330.2	5.9	256.9	57.3	330.2	5.9
1	0.87	19.2819	1.7	0.0537	2.3	325.9	5.3	356.6	50.8	325.9	5.3

GCC8											
25		26.9429	1.6	0.0515	0.8	234.9	3.8	265.1	17.4	234.9	3.8
24		25.9986	1.6	0.0516	0.6	243.3	3.7	266.7	13.1	243.3	3.7
23		26.4926	1.6	0.0512	0.6	238.8	3.7	248.6	13.3	238.8	3.7
22		26.699	1.6	0.0509	0.7	237.0	3.6	235.6	15.0	237.0	3.6
21		25.6548	1.6	0.0520	0.7	246.5	3.9	283.7	16.7	246.5	3.9
19		27.0936	1.7	0.0513	0.8	233.6	3.8	252.6	17.5	233.6	3.8
18		25.3305	1.6	0.0512	0.7	249.6	3.9	251.1	16.7	249.6	3.9
16		26.8629	1.7	0.0511	0.7	235.6	3.9	246.4	17.1	235.6	3.9
13		21.7673	2.4	0.0509	1.2	289.5	6.9	237.6	26.4	289.5	6.9
11		25.535	1.5	0.0514	0.9	247.6	3.6	261.0	21.3	247.6	3.6
10		24.7234	1.5	0.0512	0.8	255.6	3.6	248.7	18.8	255.6	3.6
8		26.0174	1.7	0.0513	1.1	243.1	4.0	255.9	25.0	243.1	4.0
7		26.3151	1.4	0.0517	1.0	240.4	3.3	271.7	22.5	240.4	3.3
6		28.6658	1.8	0.0511	1.0	221.0	4.0	245.1	22.6	221.0	4.0
5		25.3365	1.4	0.0514	0.9	249.5	3.4	260.8	20.2	249.5	3.4
4		25.8257	1.5	0.0511	1.0	244.9	3.6	243.8	22.9	244.9	3.6
3		27.5677	1.5	0.0514	0.8	229.7	3.4	259.3	19.0	229.7	3.4
2		26.1818	1.6	0.0520	1.2	241.6	3.9	285.7	26.5	241.6	3.9
1		24.4290	1.6	0.0518	0.8	258.6	4.1	277.5	18.7	258.6	4.1

CI12											
79	0.69	22.9375	0.9	0.0518	1.1	275.1	2.5	276.4	25.0	275.1	2.5
78	0.78	23.5812	0.9	0.0509	1.2	267.7	2.4	234.4	27.0	267.7	2.4

77	0.80	23.0767	0.9	0.0513	1.1	273.5	2.5	255.5	25.6	273.5	2.5
76	0.21	26.4683	0.9	0.0525	0.9	239.1	2.1	306.6	19.8	239.1	2.1
75	0.73	24.9916	0.9	0.0516	1.2	252.9	2.3	268.3	26.7	252.9	2.3
74	0.65	23.4321	0.9	0.0517	0.8	269.4	2.3	274.1	18.5	269.4	2.3
73	0.75	22.5919	0.9	0.0522	1.1	279.2	2.5	294.7	25.9	279.2	2.5
72	0.90	23.7758	1.0	0.0515	1.2	265.6	2.6	264.9	26.7	265.6	2.6
71	1.04	23.7701	0.9	0.0516	0.8	265.6	2.3	269	18.8	265.6	2.3
70	0.99	23.5769	0.9	0.0526	1.0	267.8	2.5	311.4	23.5	267.8	2.5
69	0.73	23.3647	0.9	0.0528	1.1	270.2	2.5	321.3	24.4	270.2	2.5
68	0.84	23.1179	0.9	0.0519	1.0	273.0	2.4	280.4	22.8	273.0	2.4
67	0.67	23.6224	1.0	0.0524	1.4	267.3	2.6	304.6	32.4	267.3	2.6
66	0.45	33.2901	1.2	0.0510	1.2	190.8	2.3	241.4	28.2	190.8	2.3
65	0.81	23.0809	0.9	0.0522	1.2	273.4	2.4	295.3	27.7	273.4	2.4
64	0.92	23.5361	0.9	0.0532	1.0	268.2	2.4	336.7	22.5	268.2	2.4
63	0.87	23.7377	0.9	0.0521	1.0	266.0	2.3	288.3	21.9	266.0	2.3
62	0.87	23.1599	0.9	0.0517	1.1	272.5	2.5	273.5	24.1	272.5	2.5
61	0.73	22.8918	0.9	0.0516	1.1	275.6	2.5	267.5	25.8	275.6	2.5
60	0.81	23.0818	0.9	0.0513	1.1	273.4	2.5	254.1	25.2	273.4	2.5
59	0.91	23.6421	0.9	0.0513	1.1	267.1	2.4	255.1	25.4	267.1	2.4
58	0.65	22.7024	0.8	0.0517	0.8	277.9	2.3	274.3	18.3	277.9	2.3
57	0.91	22.6733	0.9	0.0561	1.0	278.2	2.5	457.1	21.8	278.2	2.5
56	0.72	23.2912	0.9	0.0517	1.2	271.0	2.4	271.4	26.8	271.0	2.4
55	0.76	23.3666	0.9	0.0515	1.2	270.1	2.4	264.5	26.6	270.1	2.4
54	0.58	23.6053	1.0	0.0520	1.0	267.5	2.6	285.1	22.7	267.5	2.6
53	0.67	24.2324	1.0	0.0508	1.2	260.7	2.5	231.1	26.5	260.7	2.5
52	0.53	23.3557	0.8	0.0524	0.9	270.3	2.2	304.1	20.5	270.3	2.2
51	0.66	23.011	0.9	0.0526	1.2	274.2	2.5	312.1	26.5	274.2	2.5
50	0.77	23.4416	0.9	0.0516	0.9	269.3	2.3	267	20.9	269.3	2.3
49	0.98	23.7793	0.8	0.0514	1.0	265.5	2.2	259.8	22.9	265.5	2.2
48	0.59	23.8253	1.0	0.0506	1.2	265.0	2.6	221.4	27.0	265.0	2.6

47	0.90	23.6691	0.9	0.0557	1.1	266.8	2.4	442.4	24.5	266.8	2.4
46	0.73	23.5727	1.0	0.0525	1.1	267.8	2.6	308	24.1	267.8	2.6
45	0.98	23.2191	0.9	0.0523	1.1	271.8	2.5	297.4	25.7	271.8	2.5
44	0.72	22.8482	1.0	0.0520	1.3	276.1	2.7	284.6	29.7	276.1	2.7
43	0.77	22.786	1.0	0.0519	1.1	276.9	2.8	280.3	24.3	276.9	2.8
42	0.68	23.4715	1.0	0.0520	1.1	269.0	2.5	285.4	24.1	269.0	2.5
41	0.69	23.1648	0.9	0.0525	0.9	272.4	2.5	306.6	21.2	272.4	2.5
40	0.98	23.1571	0.9	0.0521	1.1	272.5	2.3	289.2	25.0	272.5	2.3
39	0.55	23.5479	1.0	0.0527	1.1	268.1	2.5	315.9	25.0	268.1	2.5
38	0.70	23.583	0.9	0.0513	1.0	267.7	2.4	252.6	23.3	267.7	2.4
37	0.95	23.2299	0.9	0.0512	1.0	271.7	2.5	247.6	22.3	271.7	2.5
36	0.50	22.7884	1.0	0.0539	1.1	276.9	2.6	367.2	23.7	276.9	2.6
35	0.73	22.6131	0.9	0.0520	0.8	279.0	2.4	287.4	19.1	279.0	2.4
34	0.75	23.066	1.0	0.0522	1.1	273.6	2.6	293.7	24.1	273.6	2.6
33	0.62	23.7828	0.9	0.0509	1.1	265.5	2.5	234.9	24.2	265.5	2.5
32	0.81	23.8198	0.9	0.0530	1.1	265.1	2.5	330.2	24.1	265.1	2.5
31	0.81	23.4793	1.0	0.0525	1.1	268.9	2.6	305.4	24.3	268.9	2.6
30	0.83	22.7142	0.9	0.0517	1.0	277.7	2.5	271.4	22.9	277.7	2.5
29	0.70	22.8694	1.1	0.0513	1.1	275.9	3.0	252.5	25.2	275.9	3.0
28	0.81	22.8839	1.2	0.0522	1.3	275.7	3.4	294	28.5	275.7	3.4
27	0.80	23.4882	1.1	0.0524	1.1	268.8	2.8	304	25.7	268.8	2.8
26	0.94	23.3323	1.1	0.0515	0.9	270.5	2.9	264.1	20.0	270.5	2.9
25	0.82	23.1315	1.1	0.0517	1.0	272.8	2.9	271.9	23.7	272.8	2.9
24	0.69	22.8195	1.1	0.0525	1.1	276.5	2.9	306.4	25.2	276.5	2.9
23	0.81	23.756	1.1	0.0516	1.1	265.8	2.9	269.1	25.2	265.8	2.9
22	0.82	23.1042	1.2	0.0516	1.1	273.1	3.1	268.7	25.6	273.1	3.1
21	0.86	23.5741	1.2	0.0519	1.0	267.8	3.0	282.3	22.3	267.8	3.0
20	0.93	24.0124	1.1	0.0511	1.1	263.0	2.9	245.3	24.2	263.0	2.9
19	0.64	24.7775	1.2	0.0504	1.0	255.1	3.0	214.4	23.4	255.1	3.0
18	0.79	23.6868	1.1	0.0529	0.9	266.6	2.9	322.5	20.1	266.6	2.9

17	0.89	23.9576	1.1	0.0531	1.0	263.6	2.8	333.9	23.4	263.6	2.8
16	0.47	28.1862	1.4	0.0647	1.5	224.7	3.1	763.8	30.5	224.7	3.1
15	0.80	23.5825	1.0	0.0512	1.0	267.7	2.7	249.4	22.7	267.7	2.7
14	0.73	23.5955	1.0	0.0517	0.8	267.6	2.6	270.9	17.8	267.6	2.6
13	0.87	23.3662	1.1	0.0518	1.1	270.1	2.9	276.3	24.9	270.1	2.9
12	0.71	22.754	1.2	0.0505	1.0	277.3	3.2	216.1	22.5	277.3	3.2
11	0.72	21.9351	1.2	0.0524	1.1	287.4	3.3	304.2	23.9	287.4	3.3
9	0.94	23.8755	1.2	0.0523	1.0	264.5	3.0	298.4	22.2	264.5	3.0
8	0.13	34.2273	1.2	0.0506	0.8	185.6	2.2	224.9	18.1	185.6	2.2
7	1.01	23.6109	1.2	0.0521	1.1	267.4	3.0	291.4	24.8	267.4	3.0
6	0.58	22.5223	1.2	0.0506	0.9	280.1	3.2	223.2	21.8	280.1	3.2
5	0.79	25.6777	1.1	0.0604	1.2	246.3	2.8	617.9	24.9	246.3	2.8
4	0.93	23.249	1.1	0.0518	1.1	271.5	3.0	277.5	25.3	271.5	3.0
3	0.47	25.3512	1.1	0.0509	0.9	249.4	2.8	236.4	19.7	249.4	2.8
2	0.90	22.8461	1.1	0.0515	1.0	276.2	3.0	263.5	23.7	276.2	3.0
1	0.61	23.5856	1.1	0.0512	0.8	267.7	2.9	251.3	19.3	267.7	2.9

Table 2.2. U-Pb detrital zircon ages from the Cajamarca Complex.

Analysis	Th/U	$^{238}\text{U}/^{206}\text{Pb}$	% err	$^{207}\text{Pb}/^{206}\text{Pb}$	% err	Age $^{206}\text{Pb}/^{238}\text{U}$	abs error	Age $^{207}\text{Pb}/^{206}\text{Pb}$	abs error	Age (Ma)	abs error (Ma)
98	1.53	12.25	0.86	0.06	1.0	505.84	4.20	622.88	20.78	505.8	4.2
97	1.63	36.08	0.92	0.05	1.6	176.26	1.59	251.35	36.11	176.3	1.6
96	0.83	24.15	1.14	0.05	0.8	261.53	2.92	310.06	17.11	261.5	2.9
94	0.84	4.20	1.36	0.09	0.9	1376.91	16.79	1473.30	16.74	1473.3	16.7
93	0.53	37.49	0.81	0.05	1.0	169.68	1.36	346.31	22.24	169.7	1.4
92	0.14	10.18	0.87	0.07	0.6	603.89	5.04	817.92	12.83	603.9	5.0
90	0.91	38.51	0.77	0.07	1.4	165.28	1.26	885.00	28.37	165.3	1.3
89	0.67	37.95	0.96	0.05	1.1	167.68	1.59	239.48	25.92	167.7	1.6
87	0.50	11.84	0.76	0.06	0.7	522.89	3.80	534.97	15.16	522.9	3.8
86	0.30	2.13	0.91	0.18	0.5	2482.86	18.79	2606.43	8.13	2606.4	8.1
85	0.04	9.19	1.43	0.06	1.5	666.14	9.04	655.53	31.86	666.1	9.0
84	0.63	10.98	0.88	0.06	0.7	561.80	4.73	555.47	16.00	561.8	4.7
83	0.69	9.59	0.72	0.06	0.7	639.30	4.39	686.62	14.45	639.3	4.4
82	0.53	5.95	1.23	0.08	0.8	1000.93	11.44	1173.72	16.00	1173.7	16.0
81	0.96	37.40	0.90	0.05	1.1	170.12	1.51	151.68	24.58	170.1	1.5
80	0.57	40.00	1.66	0.05	3.4	159.18	2.61	373.90	75.48	159.2	2.6
79	0.57	11.07	0.72	0.06	0.6	557.52	3.84	590.12	12.40	557.5	3.8
78	0.44	3.55	0.87	0.10	0.5	1600.73	12.27	1598.74	9.65	1598.7	9.7
77	0.47	3.58	0.74	0.11	0.5	1587.83	10.39	1730.00	8.75	1730.0	8.7
76	0.65	36.32	0.95	0.05	1.0	175.08	1.63	286.31	23.41	175.1	1.6
75	0.69	17.48	0.77	0.06	0.8	358.68	2.68	446.79	18.77	358.7	2.7
74	0.50	9.55	0.79	0.06	0.8	642.22	4.80	709.70	17.82	642.2	4.8
73	0.53	5.38	0.75	0.08	0.6	1098.32	7.59	1110.41	11.56	1110.4	11.6
72	0.76	3.93	0.97	0.10	0.6	1460.72	12.72	1639.91	11.38	1639.9	11.4
71	0.22	14.62	1.81	0.06	1.2	426.48	7.45	749.99	24.43	426.5	7.5
69	0.96	38.32	0.73	0.05	0.8	166.05	1.20	159.08	18.18	166.1	1.2
68	1.18	34.65	0.93	0.05	1.0	183.43	1.68	263.63	23.25	183.4	1.7

67	0.45	5.53	0.91	0.08	1.0	1070.96	8.94	1102.57	19.49	1102.6	19.5
66	0.20	9.60	0.67	0.06	0.6	639.04	4.05	631.41	11.91	639.0	4.0
65	0.76	5.63	0.77	0.07	0.7	1053.54	7.44	1048.84	13.80	1048.8	13.8
64	2.07	7.26	0.75	0.07	0.6	832.14	5.87	809.68	12.14	832.1	5.9
62	0.69	18.36	0.98	0.05	0.8	341.85	3.27	379.91	17.82	341.8	3.3
61	0.54	11.43	0.96	0.06	0.6	540.87	5.00	521.93	13.80	540.9	5.0
60	0.29	5.83	1.02	0.07	0.6	1020.22	9.58	1021.56	12.32	1021.6	12.3
59	0.66	12.89	1.04	0.06	0.9	481.64	4.82	468.23	20.74	481.6	4.8
58	1.09	3.49	0.88	0.10	0.6	1625.21	12.57	1709.18	10.41	1709.2	10.4
57	0.20	12.71	1.07	0.06	0.7	488.12	5.02	714.25	15.23	488.1	5.0
56	0.42	3.96	0.91	0.09	0.6	1451.15	11.87	1437.95	11.16	1438.0	11.2
55	0.57	23.42	1.06	0.05	1.2	269.48	2.78	313.58	26.73	269.5	2.8
54	1.58	33.48	1.11	0.05	1.4	189.75	2.08	127.73	31.80	189.8	2.1
53	0.34	20.13	0.79	0.06	0.6	312.47	2.40	446.32	13.29	312.5	2.4
52	0.77	3.94	0.94	0.11	0.5	1459.19	12.33	1725.11	9.91	1725.1	9.9
51	0.49	11.13	0.91	0.06	0.7	554.78	4.83	676.74	14.46	554.8	4.8
50	0.85	7.99	0.85	0.07	0.6	760.38	6.09	808.72	12.10	760.4	6.1
49	0.72	9.64	0.81	0.06	0.5	635.96	4.89	634.71	11.55	636.0	4.9
48	0.34	5.14	0.85	0.08	0.5	1145.86	8.88	1161.19	9.94	1161.2	9.9
47	0.43	6.29	0.86	0.07	0.6	950.48	7.61	1034.23	11.63	1034.2	11.6
46	1.32	9.65	0.84	0.06	0.5	635.77	5.10	630.78	11.23	635.8	5.1
45	0.75	39.12	1.06	0.05	1.2	162.71	1.70	212.19	26.72	162.7	1.7
44	0.66	38.96	1.08	0.06	1.1	163.37	1.75	485.68	24.33	163.4	1.7
43	1.48	35.41	1.29	0.05	1.8	179.53	2.28	238.23	40.02	179.5	2.3
42	1.32	12.89	1.15	0.06	1.2	481.73	5.34	452.51	27.07	481.7	5.3
41	0.76	5.49	1.32	0.08	0.7	1078.51	13.06	1211.55	13.39	1211.5	13.4
40	0.40	3.06	0.97	0.11	0.6	1821.58	15.30	1864.75	10.81	1864.7	10.8
39	0.36	4.91	0.98	0.08	0.6	1195.19	10.73	1196.51	12.53	1196.5	12.5
38	0.65	38.07	1.29	0.05	1.1	167.16	2.13	162.42	26.08	167.2	2.1
37	0.70	38.25	1.23	0.05	1.6	166.38	2.01	300.74	35.76	166.4	2.0

36	0.75	22.42	1.09	0.05	1.2	281.29	2.99	279.27	28.01	281.3	3.0
35	0.56	34.60	1.06	0.05	1.1	183.66	1.91	175.95	25.37	183.7	1.9
34	1.32	12.71	1.00	0.06	1.1	488.40	4.69	514.47	23.12	488.4	4.7
33	0.30	4.84	0.90	0.11	0.7	1211.01	9.95	1807.11	12.39	1807.1	12.4
32	0.71	5.62	0.97	0.07	0.9	1055.12	9.42	1025.12	18.00	1025.1	18.0
31	0.34	5.46	1.30	0.08	1.0	1084.88	12.97	1161.42	19.25	1161.4	19.2
30	1.62	33.14	0.84	0.05	0.8	191.63	1.59	256.40	19.20	191.6	1.6
29	0.52	4.20	1.21	0.16	0.7	1377.83	14.95	2415.38	12.41	2415.4	12.4
28	0.65	21.47	1.09	0.06	0.9	293.46	3.13	416.62	19.94	293.5	3.1
27	0.74	5.79	0.87	0.07	0.8	1026.74	8.30	1024.20	15.33	1024.2	15.3
26	0.43	5.78	0.86	0.07	0.8	1028.66	8.16	1028.18	15.30	1028.2	15.3
25	0.43	9.66	0.96	0.06	1.1	635.12	5.81	583.37	23.36	635.1	5.8
24	0.04	5.98	0.79	0.07	0.6	996.27	7.31	1029.89	12.88	1029.9	12.9
23	0.26	7.59	0.82	0.07	0.7	797.79	6.14	811.66	15.15	797.8	6.1
22	0.75	25.80	1.17	0.05	1.0	245.19	2.82	264.76	23.33	245.2	2.8
21	0.56	5.39	1.30	0.08	0.8	1097.49	13.13	1115.68	15.77	1115.7	15.8
20	0.58	13.97	1.15	0.06	1.0	445.68	4.97	568.26	20.77	445.7	5.0
19	0.45	37.91	1.09	0.05	0.8	167.85	1.80	207.93	19.56	167.8	1.8
17	0.45	38.50	1.10	0.05	0.8	165.31	1.79	175.66	18.79	165.3	1.8
15	0.74	13.51	1.11	0.06	0.7	460.40	4.94	477.32	16.06	460.4	4.9
14	1.13	15.02	1.27	0.06	0.7	415.61	5.13	496.98	16.30	415.6	5.1
13	0.61	38.80	1.21	0.05	1.4	164.03	1.96	145.94	33.16	164.0	2.0
12	0.39	39.25	1.29	0.05	1.9	162.18	2.06	355.31	41.50	162.2	2.1
8	0.76	3.69	1.06	0.10	0.6	1544.21	14.59	1528.39	11.30	1528.4	11.3
7	0.47	5.29	1.13	0.10	0.6	1116.69	11.58	1536.29	11.97	1536.3	12.0
5	0.48	37.69	1.28	0.05	1.4	168.79	2.13	204.76	31.49	168.8	2.1
4	0.41	5.61	1.13	0.08	0.7	1058.21	11.05	1151.63	14.17	1151.6	14.2
3	0.05	6.05	1.06	0.08	0.6	985.83	9.66	1094.61	12.03	1094.6	12.0
2	0.48	38.77	1.16	0.05	1.2	164.17	1.88	154.33	27.46	164.2	1.9
1	1.04	39.17	1.14	0.05	0.9	162.50	1.83	159.26	20.33	162.5	1.8

Table 2.3. Zircon Hf isotope data from the Tierradentro gneisses and amphibolites and micaschist from the Cajamarca Complex.

$^{176}\text{Hf}/^{177}\text{Hf}$	2SE	$^{176}\text{Lu}/^{177}\text{Hf}$	2SE	$^{176}\text{Yb}/^{177}\text{Hf}$	2SE	AGE	$^{176}\text{Hf}/^{177}\text{Hf}_{(i)}$	$\epsilon\text{Hf}_{(0)}$	2SE	$\epsilon\text{Hf}_{(i)}$
CH21C										
0.282604	0.000029	0.00180	0.00008	0.04890	0.00270	162.5	0.282599	-6.4	1.0	-3.0
0.282768	0.000043	0.00261	0.00003	0.07213	0.00099	166.1	0.282760	-0.6	1.5	2.8
0.282613	0.000026	0.00214	0.00009	0.05680	0.00240	168.8	0.282606	-6.1	0.9	-2.6
0.282733	0.000035	0.00168	0.00009	0.04580	0.00150	162.2	0.282728	-1.8	1.2	1.6
0.282703	0.000035	0.00220	0.00003	0.05870	0.00150	164.0	0.282696	-2.9	1.2	0.5
0.282677	0.000026	0.00164	0.00007	0.04340	0.00220	165.3	0.282672	-3.8	0.9	-0.3
0.282617	0.000039	0.00174	0.00010	0.04430	0.00160	167.8	0.282612	-5.9	1.4	-2.4
0.282664	0.000039	0.00117	0.00012	0.03640	0.00600	167.2	0.282660	-4.3	1.4	-0.7
0.282664	0.000040	0.00145	0.00006	0.03860	0.00150	166.4	0.282659	-4.3	1.4	-0.7
0.282415	0.000036	0.00113	0.00006	0.03160	0.00150	460.4	0.282405	-13.1	1.3	-3.2
0.282016	0.000080	0.00112	0.00006	0.02590	0.00140	488.4	0.282006	-27.2	2.8	-16.7
0.282265	0.000046	0.00111	0.00004	0.03350	0.00140	481.7	0.282255	-18.4	1.6	-8.0
0.281923	0.000028	0.00085	0.00003	0.02360	0.00120	488.1	0.281915	-30.5	1.0	-19.9
0.282253	0.000037	0.00085	0.00003	0.02282	0.00068	481.6	0.282245	-18.8	1.3	-8.4
0.281894	0.000022	0.00092	0.00003	0.02786	0.00078	1536.3	0.281867	-31.5	0.8	2.1
0.281814	0.000031	0.00073	0.00004	0.02150	0.00120	1528.4	0.281793	-34.3	1.1	-0.7
0.282713	0.000031	0.00190	0.00004	0.04694	0.00060	318.8	0.282702	-2.5	1.1	4.1
0.282444	0.000033	0.00166	0.00009	0.04630	0.00230	312.5	0.282434	-12.1	1.2	-5.5
0.282544	0.000048	0.00138	0.00006	0.04120	0.00170	341.8	0.282535	-8.5	1.7	-1.2
0.282461	0.000046	0.00129	0.00002	0.03522	0.00087	358.7	0.282452	-11.5	1.6	-3.8
0.282444	0.000044	0.00075	0.00009	0.01910	0.00210	635.1	0.282435	-12.1	1.6	1.8
0.282172	0.000040	0.00123	0.00004	0.03930	0.00150	635.8	0.282157	-21.7	1.4	-8.0
0.282410	0.000038	0.00081	0.00004	0.02470	0.00140	639.0	0.282400	-13.3	1.3	0.7
0.282181	0.000045	0.00082	0.00004	0.02169	0.00077	642.2	0.282171	-21.4	1.6	-7.4
0.282194	0.000025	0.00160	0.00005	0.04720	0.00110	1094.6	0.282161	-20.9	0.9	2.5
0.282141	0.000034	0.00057	0.00009	0.01500	0.00180	1029.9	0.282130	-22.8	1.2	-0.1

0.282033	0.000047	0.00089	0.00018	0.02520	0.00450	1025.1	0.282016	-26.6	1.7	-4.3
0.280926	0.000062	0.00096	0.00004	0.02130	0.00088	2606.4	0.280878	-65.7	2.2	-8.2

CAT1A										
0.282927	0.000028	0.00043	0.00002	0.00849	0.00034	201.9	0.282925	5.0	1.0	9.5
0.282928	0.000032	0.00037	0.00000	0.00774	0.00011	225.5	0.282926	5.1	1.1	10.0
0.282944	0.000030	0.00033	0.00003	0.00768	0.00065	230.7	0.282943	5.6	1.1	10.7
0.282954	0.000029	0.00039	0.00000	0.00934	0.00014	225.2	0.282952	6.0	1.0	10.9
0.282943	0.000027	0.00034	0.00001	0.00690	0.00037	228.9	0.282942	5.6	1.0	10.6
0.282938	0.000025	0.00043	0.00003	0.00882	0.00059	226.0	0.282936	5.4	0.9	10.4
0.282909	0.000029	0.00026	0.00001	0.00538	0.00026	219.7	0.282908	4.4	1.0	9.2
0.282944	0.000027	0.00043	0.00001	0.00973	0.00024	234.4	0.282942	5.6	1.0	10.8

CI12										
0.282604	0.000026	0.00050	0.00002	0.01412	0.00054	267.7	0.282601	-6.4	0.9	-0.5
0.282597	0.000029	0.00036	0.00002	0.00999	0.00052	246.3	0.282595	-6.6	1.0	-1.2
0.282578	0.000022	0.00055	0.00002	0.01571	0.00080	267.4	0.282575	-7.3	0.8	-1.5
0.282550	0.000021	0.00044	0.00002	0.01155	0.00069	266.6	0.282548	-8.3	0.7	-2.5
0.282569	0.000023	0.00066	0.00003	0.01816	0.00063	265.5	0.282566	-7.6	0.8	-1.9
0.282597	0.000025	0.00045	0.00001	0.01241	0.00014	267.5	0.282595	-6.6	0.9	-0.8
0.282616	0.000031	0.00045	0.00003	0.01230	0.00110	269.3	0.282614	-6.0	1.1	-0.1
0.282574	0.000022	0.00053	0.00001	0.01460	0.00020	275.1	0.282571	-7.5	0.8	-1.4

Table 3.1. U-Pb zircon ages from the Payandé, Ibagué and Mariquita plutons

Sample name	U (ppm)	Th/U	$^{238}\text{U}/^{206}\text{Pb}$	1σ % error	$^{207}\text{Pb}/^{206}\text{Pb}$	1σ % error	$^{206}\text{Pb}/^{238}\text{U}$ Age	1σ absolute error	$^{207}\text{Pb}/^{206}\text{Pb}$ Age	1σ absolute error	Best age (Ma)	1σ absolute error (Ma)
Payandé stock												
CSP 3												
CSP3_32	313.1	0.65	39.909	1.66	0.0495	1.49	159.5	2.6	172.3	34.5	159.5	2.6
CSP3_31	231.1	0.96	37.481	1.69	0.0491	1.69	169.7	2.8	151.8	39.1	169.7	2.8
CSP3_30	255.9	0.73	36.300	1.70	0.0486	1.55	175.2	2.9	129.0	36.0	175.2	2.9
CSP3_29	393.2	0.90	38.671	1.56	0.0491	1.37	164.6	2.5	150.4	31.8	164.6	2.5
CSP3_28	669.4	1.28	38.419	1.55	0.0492	1.15	165.6	2.5	157.7	26.6	165.6	2.5
CSP3_27	321.2	0.79	39.584	1.62	0.0503	1.60	160.8	2.6	208.4	36.6	160.8	2.6
CSP3_26	327.2	0.95	37.955	1.59	0.0491	1.47	167.6	2.6	152.3	34.1	167.6	2.6
CSP3_25	542.3	1.16	39.450	1.64	0.0554	1.71	161.4	2.6	428.9	37.7	161.4	2.6
CSP3_24	773.9	0.86	39.563	1.49	0.0474	2.93	160.9	2.4	71.8	68.3	160.9	2.4
CSP3_23	399.9	0.66	40.475	1.69	0.0487	3.30	157.3	2.6	132.1	75.9	157.3	2.6
CSP3_22	233.4	0.81	38.823	1.57	0.0481	3.12	163.9	2.5	105.6	72.0	163.9	2.5
CSP3_21	262.9	0.84	41.904	1.48	0.0487	3.11	152.0	2.2	135.4	71.6	152.0	2.2
CSP3_20	290.3	0.71	38.268	1.49	0.0492	3.07	166.3	2.5	159.5	70.2	166.3	2.5
CSP3_19	570.1	0.79	38.565	1.50	0.0470	3.01	165.0	2.4	49.5	70.4	165.0	2.4
CSP3_18	404.5	0.79	38.665	1.20	0.0485	1.51	164.6	1.9	125.9	35.2	164.6	1.9
CSP3_17	477.5	0.95	39.712	1.19	0.0493	1.54	160.3	1.9	160.4	35.6	160.3	1.9
CSP3_16	613.9	0.54	38.586	1.18	0.0499	1.31	164.9	1.9	189.2	30.2	164.9	1.9
CSP3_15	590.7	1.04	39.335	1.24	0.0508	1.45	161.8	2.0	230.6	33.1	161.8	2.0
CSP3_14	441.1	0.82	39.566	1.23	0.0478	1.43	160.9	2.0	87.5	33.7	160.9	2.0
CSP3_13	322.6	0.83	45.938	1.92	0.0492	1.93	138.8	2.6	158.4	44.4	138.8	2.6
CSP3_12	289.0	0.74	39.953	1.03	0.0489	1.64	159.4	1.6	143.0	38.0	159.4	1.6
CSP3_11	355.9	0.79	39.119	0.89	0.0487	1.46	162.7	1.4	132.1	33.9	162.7	1.4
CSP3_10	277.4	0.58	38.399	0.99	0.0496	1.61	165.7	1.6	176.3	37.1	165.7	1.6
CSP3_9	369.4	0.89	38.179	1.01	0.0519	1.48	166.7	1.7	281.5	33.5	166.7	1.7

CSP3_8	391.7	0.73	38.486	0.93	0.0476	1.49	165.4	1.5	80.7	34.9	165.4	1.5
CSP3_7	325.9	0.61	41.748	1.13	0.0505	1.53	152.6	1.7	219.1	35.0	152.6	1.7
CSP3_6	1538.3	0.74	36.413	1.04	0.0535	0.88	174.6	1.8	350.0	19.7	174.6	1.8
CSP3_5	388.3	0.67	38.749	1.33	0.0489	1.89	164.3	2.2	144.0	43.7	164.3	2.2
CSP3_4	439.1	0.88	40.325	1.19	0.0489	1.32	157.9	1.9	144.4	30.7	157.9	1.9
CSP3_3	329.1	0.86	36.458	1.23	0.0567	1.94	174.4	2.1	481.7	42.4	174.4	2.1
CSP3_2	454.3	0.74	37.566	1.57	0.0639	3.81	169.4	2.6	737.5	78.6	169.4	2.6

CSP 5

CSP5_33	505.8	0.76	38.907	2.06	0.0503	2.02	163.6	3.3	209.1	46.1	163.6	3.3
CSP5_32	469.5	0.66	37.985	2.07	0.0501	1.92	167.5	3.4	197.9	44.0	167.5	3.4
CSP5_31	659.1	0.68	37.657	1.88	0.0495	1.42	169.0	3.1	172.0	32.9	169.0	3.1
CSP5_30	406.6	0.64	37.315	1.91	0.0512	1.69	170.5	3.2	249.9	38.4	170.5	3.2
CSP5_29	806.6	0.56	39.070	1.92	0.0505	1.49	162.9	3.1	217.6	34.2	162.9	3.1
CSP5_27	332.4	0.51	40.220	2.08	0.0511	1.81	158.3	3.3	246.1	41.2	158.3	3.3
CSP5_26	464.8	0.44	39.332	2.46	0.0492	2.64	161.8	3.9	159.3	60.7	161.8	3.9
CSP5_24	261.6	0.73	39.041	2.17	0.0503	1.62	163.0	3.5	208.5	37.2	163.0	3.5
CSP5_23	427.0	0.55	39.264	2.23	0.0504	2.24	162.1	3.6	213.3	51.1	162.1	3.6
CSP5_22	710.9	0.58	38.715	2.10	0.0480	1.24	164.4	3.4	97.3	29.0	164.4	3.4
CSP5_21	1000.6	0.70	39.557	2.06	0.0498	1.19	160.9	3.3	184.0	27.4	160.9	3.3
CSP5_20	347.6	0.48	38.966	2.60	0.0535	1.87	163.4	4.2	350.8	41.8	163.4	4.2
CSP5_19	896.0	0.77	38.087	2.12	0.0490	2.14	167.1	3.5	147.5	49.5	167.1	3.5
CSP5_18	696.7	0.56	38.523	1.96	0.0493	1.91	165.2	3.2	160.5	44.1	165.2	3.2
CSP5_17	495.6	0.72	38.608	2.01	0.0500	2.06	164.8	3.3	196.7	47.2	164.8	3.3
CSP5_16	765.0	0.57	38.097	1.98	0.0497	1.87	167.0	3.3	180.1	42.9	167.0	3.3
CSP5_15	849.5	0.72	38.293	2.02	0.0488	1.92	166.2	3.3	136.2	44.5	166.2	3.3
CSP5_14	713.3	0.58	38.792	2.10	0.0491	2.05	164.1	3.4	151.2	47.2	164.1	3.4
CSP5_12	715.3	0.50	38.957	1.94	0.0487	2.38	163.4	3.1	131.8	55.0	163.4	3.1
CSP5_11	659.9	0.48	39.022	1.73	0.0496	2.01	163.1	2.8	178.3	46.2	163.1	2.8
CSP5_10	506.9	0.74	39.150	1.60	0.0489	2.00	162.6	2.6	141.5	46.2	162.6	2.6
CSP5_9	755.0	0.56	38.903	1.92	0.0483	2.04	163.6	3.1	112.5	47.5	163.6	3.1

CSP5_8	540.3	0.60	41.710	1.89	0.0499	2.94	152.7	2.9	192.5	67.1	152.7	2.9
CSP5_7	841.3	0.53	39.305	1.76	0.0504	2.23	162.0	2.8	212.5	50.8	162.0	2.8
CSP5_6	370.1	0.69	38.642	1.72	0.0481	1.65	164.7	2.8	105.5	38.4	164.7	2.8
CSP5_5	398.2	0.55	38.197	1.72	0.0498	1.62	166.6	2.8	185.4	37.2	166.6	2.8
CSP5_4	211.5	0.71	38.059	1.82	0.0495	2.06	167.2	3.0	169.4	47.3	167.2	3.0
CSP5_3	445.0	0.55	37.479	1.75	0.0489	1.61	169.7	2.9	143.5	37.5	169.7	2.9
CSP5_1	419.5	0.55	37.307	2.01	0.0523	1.79	170.5	3.4	296.9	40.3	170.5	3.4

Ibagué batholith

CI15

CI15_22	2137.0	0.54	42.434	1.73	0.0489	0.81	150.2	2.6	145.1	18.9	150.2	2.6
CI15_21	516.4	0.51	43.469	1.69	0.0482	1.28	146.6	2.4	107.4	29.9	146.6	2.4
CI15_20	148.0	0.75	44.041	2.10	0.0478	2.04	144.7	3.0	88.2	47.6	144.7	3.0
CI15_19	161.1	0.64	42.879	2.23	0.0467	2.19	148.6	3.3	35.0	51.4	148.6	3.3
CI15_18	155.1	0.63	44.831	1.95	0.0513	1.94	142.2	2.7	254.7	44.1	142.2	2.7
CI15_16	115.7	0.67	42.894	2.02	0.0502	2.28	148.6	3.0	205.4	52.0	148.6	3.0
CI15_15	302.0	0.52	43.544	1.80	0.0491	1.68	146.4	2.6	154.7	38.9	146.4	2.6
CI15_14	167.7	0.95	43.931	2.03	0.0486	1.85	145.1	2.9	126.4	43.0	145.1	2.9
CI15_12	166.0	0.70	44.583	2.01	0.0504	2.07	143.0	2.8	211.4	47.2	143.0	2.8
CI15_11	221.8	0.69	43.742	1.96	0.0504	1.64	145.7	2.8	213.3	37.6	145.7	2.8
CI15_10	188.7	0.55	43.524	2.25	0.0465	1.88	146.4	3.3	22.5	44.8	146.4	3.3
CI15_9	357.2	0.71	43.676	2.08	0.0471	1.32	145.9	3.0	52.1	31.3	145.9	3.0
CI15_8	153.4	0.87	43.408	2.16	0.0483	2.22	146.8	3.1	115.1	51.6	146.8	3.1
CI15_6	84.0	0.65	44.959	2.30	0.0436	2.97	141.8	3.2	0.0	0.0	141.8	3.2
CI15_5	301.9	0.60	44.393	1.92	0.0488	1.53	143.6	2.7	136.5	35.6	143.6	2.7
CI15_4	166.8	0.64	45.806	2.19	0.0487	2.11	139.2	3.0	132.0	48.9	139.2	3.0
CI15_3	164.5	0.99	43.540	2.93	0.0491	2.47	146.4	4.2	150.6	56.9	146.4	4.2
CI15_2	173.4	0.61	44.176	2.03	0.0502	1.85	144.3	2.9	204.7	42.4	144.3	2.9
CI15_1	190.4	0.72	44.029	2.22	0.0457	2.05	144.8	3.2	0.0	29.3	144.8	3.2

CI13

CI13_36	108.3	0.80	44.441	2.66	0.0502	2.43	143.4	3.8	204.8	55.3	143.4	3.8
---------	-------	------	--------	------	--------	------	-------	-----	-------	------	-------	-----

CI13_35	146.8	0.65	44.772	2.39	0.0504	2.02	142.4	3.4	212.2	46.2	142.4	3.4
CI13_34	509.4	0.30	45.159	2.36	0.0486	1.64	141.2	3.3	129.7	38.1	141.2	3.3
CI13_33	141.0	0.61	44.935	2.47	0.0500	2.81	141.9	3.5	193.4	64.0	141.9	3.5
CI13_31	217.2	0.98	45.343	2.43	0.0498	2.17	140.6	3.4	186.3	49.9	140.6	3.4
CI13_30	119.1	0.68	44.465	2.52	0.0508	2.13	143.4	3.6	230.0	48.5	143.4	3.6
CI13_29	122.2	0.67	44.365	2.39	0.0475	2.18	143.7	3.4	72.9	51.0	143.7	3.4
CI13_28	118.7	0.67	45.714	2.40	0.0451	2.62	139.5	3.3	0.0	6.7	139.5	3.3
CI13_27	147.6	0.75	44.810	2.57	0.0473	2.26	142.3	3.6	62.6	52.9	142.3	3.6
CI13_24	164.3	0.52	44.695	2.48	0.0491	2.16	142.6	3.5	154.6	49.7	142.6	3.5
CI13_22	164.6	0.50	43.831	2.57	0.0512	2.30	145.4	3.7	249.0	52.1	145.4	3.7
CI13_21	109.8	0.67	45.606	2.47	0.0524	2.27	139.8	3.4	301.7	50.9	139.8	3.4
CI13_20	123.8	0.66	43.379	2.48	0.0475	2.99	146.9	3.6	74.8	69.6	146.9	3.6
CI13_19	126.6	0.65	44.161	1.84	0.0465	2.38	144.3	2.6	23.2	56.1	144.3	2.6
CI13_18	241.7	0.69	45.458	2.85	0.0478	3.67	140.3	3.9	91.8	84.6	140.3	3.9
CI13_17	126.6	0.66	43.928	1.82	0.0468	2.33	145.1	2.6	41.1	54.9	145.1	2.6
CI13_14	117.8	0.63	44.705	1.83	0.0501	2.46	142.6	2.6	199.2	56.1	142.6	2.6
CI13_11	234.0	0.82	43.542	1.80	0.0480	1.75	146.4	2.6	99.5	40.8	146.4	2.6
CI13_9	167.9	0.61	44.794	1.54	0.0491	2.95	142.3	2.2	152.4	67.7	142.3	2.2
CI13_8	211.8	0.60	44.122	1.56	0.0480	2.75	144.5	2.2	101.0	63.8	144.5	2.2
CI13_7	216.0	0.96	43.849	1.35	0.0493	2.64	145.4	1.9	163.3	60.5	145.4	1.9
CI13_6	145.2	0.67	45.099	1.60	0.0485	2.94	141.4	2.2	124.6	67.8	141.4	2.2
CI13_5	166.2	0.68	43.263	1.43	0.0479	2.85	147.3	2.1	94.6	66.1	147.3	2.1
CI13_4	402.3	1.07	44.321	1.32	0.0490	2.45	143.8	1.9	145.6	56.6	143.8	1.9
CI13_3	119.0	0.76	45.023	1.62	0.0503	2.92	141.6	2.3	210.6	66.3	141.6	2.3
CI13_2	106.8	0.65	43.176	1.63	0.0464	3.07	147.6	2.4	17.5	71.4	147.6	2.4
CI13_1	186.3	0.77	43.782	1.55	0.0473	2.77	145.6	2.2	65.7	64.8	145.6	2.2

CI11

CI11_30	257.9	0.56	42.693	1.28	0.0485	2.48	149.3	1.9	123.1	57.4	149.3	1.9
CI11_29	269.6	0.82	41.304	1.25	0.0498	2.80	154.2	1.9	184.2	63.9	154.2	1.9
CI11_28	181.0	0.82	42.691	1.34	0.0482	2.62	149.3	2.0	109.3	60.8	149.3	2.0

CI11_27	141.9	0.78	41.246	1.36	0.0475	2.82	154.4	2.1	72.6	65.8	154.4	2.1	
CI11_26	197.3	0.95	42.669	1.24	0.0489	2.53	149.3	1.8	143.9	58.4	149.3	1.8	
CI11_25	180.0	0.89	42.708	1.37	0.0481	2.84	149.2	2.0	103.9	65.7	149.2	2.0	
CI11_24	197.3	1.04	41.611	1.19	0.0490	2.51	153.1	1.8	148.2	57.9	153.1	1.8	
CI11_23	268.6	0.82	43.961	1.15	0.0468	2.49	145.0	1.7	36.4	58.8	145.0	1.7	
CI11_22	506.3	0.55	41.979	1.02	0.0503	2.30	151.8	1.5	208.8	52.4	151.8	1.5	
CI11_21	216.8	1.00	40.669	1.25	0.0482	2.62	156.6	1.9	111.5	60.7	156.6	1.9	
CI11_20	219.1	0.55	42.004	1.18	0.0478	2.58	151.7	1.8	87.2	60.0	151.7	1.8	
CI11_19	312.6	0.87	41.905	1.08	0.0508	2.56	152.0	1.6	233.4	58.0	152.0	1.6	
CI11_18	237.7	0.97	41.937	1.14	0.0499	2.70	151.9	1.7	188.8	61.6	151.9	1.7	
CI11_17	156.8	0.89	41.463	1.34	0.0507	2.89	153.6	2.0	226.1	65.4	153.6	2.0	
CI11_16	209.0	1.02	41.948	1.25	0.0466	2.72	151.9	1.9	28.2	64.1	151.9	1.9	
CI11_15	116.1	0.65	42.220	1.46	0.0490	3.07	150.9	2.2	147.2	70.4	150.9	2.2	
CI11_14	233.6	1.01	42.236	1.24	0.0480	2.72	150.9	1.8	97.9	63.2	150.9	1.8	
CI11_13	202.7	0.67	41.808	1.24	0.0475	2.76	152.4	1.9	72.6	64.3	152.4	1.9	
CI11_12	256.8	0.92	41.743	1.84	0.0488	2.19	152.6	2.8	140.6	50.7	152.6	2.8	
CI11_11	182.1	0.80	42.683	1.90	0.0489	2.30	149.3	2.8	140.7	53.1	149.3	2.8	
CI11_10	296.3	0.94	40.677	1.81	0.0500	2.18	156.6	2.8	196.6	50.0	156.6	2.8	
CI11_9	215.0	1.00	41.893	1.94	0.0503	2.35	152.1	2.9	210.1	53.5	152.1	2.9	
CI11_8	278.8	0.82	41.241	1.90	0.0489	2.24	154.4	2.9	143.1	51.6	154.4	2.9	
CI11_7	464.9	0.73	39.369	1.78	0.0493	2.02	161.7	2.8	162.8	46.6	161.7	2.8	
CI11_6	213.2	0.69	41.360	2.40	0.0476	2.88	154.0	3.7	80.5	66.9	154.0	3.7	
CI11_5	294.0	0.88	41.244	2.37	0.0479	2.81	154.4	3.6	93.6	65.2	154.4	3.6	
CI11_4	189.6	0.92	40.897	2.34	0.0481	2.98	155.7	3.6	105.7	68.9	155.7	3.6	
CI11_3	319.8	0.86	41.163	2.42	0.0465	2.76	154.7	3.7	22.0	65.9	154.7	3.7	
CI11_2	491.0	0.52	41.160	2.26	0.0489	2.71	154.7	3.5	141.9	62.4	154.7	3.5	
CI11_1	307.1	0.70	40.833	2.20	0.0475	2.91	156.0	3.4	73.9	67.7	156.0	3.4	
CI12													
CI2_30	109.5	0.65	44.394	2.50	0.0489	3.20	143.6	3.5	143.3	73.4	143.6	3.5	
CI2_29	117.9	0.79	44.618	2.50	0.0493	3.19	142.9	3.5	162.9	73.0	142.9	3.5	

CI2_28	348.3	0.81	45.341	2.23	0.0489	2.73	140.6	3.1	145.3	62.8	140.6	3.1
CI2_27	1142.5	0.59	41.895	2.23	0.0476	2.48	152.1	3.3	80.3	57.7	152.1	3.3
CI2_26	379.2	0.54	43.879	2.25	0.0493	2.68	145.3	3.2	163.5	61.4	145.3	3.2
CI2_25	329.1	0.48	44.588	2.30	0.0484	2.65	143.0	3.3	120.7	61.3	143.0	3.3
CI2_24	461.8	0.74	44.450	2.19	0.0479	2.61	143.4	3.1	92.7	60.7	143.4	3.1
CI2_23	422.9	0.61	43.066	2.34	0.0481	2.63	148.0	3.4	102.8	61.1	148.0	3.4
CI2_22	434.8	0.71	46.142	2.39	0.0492	2.69	138.2	3.3	156.2	61.7	138.2	3.3
CI2_21	292.5	0.57	44.139	2.40	0.0563	2.90	144.4	3.4	464.1	63.0	144.4	3.4
CI2_20	384.8	0.52	43.990	1.92	0.0487	2.08	144.9	2.8	133.7	48.2	144.9	2.8
CI2_19	574.1	1.12	44.064	2.09	0.0480	1.97	144.7	3.0	97.5	46.0	144.7	3.0
CI2_18	293.5	0.92	45.918	2.07	0.0468	2.24	138.9	2.8	40.0	52.7	138.9	2.8
CI2_16	280.8	0.63	44.056	1.97	0.0495	2.22	144.7	2.8	171.1	51.0	144.7	2.8
CI2_15	667.6	1.08	43.708	1.92	0.0479	1.95	145.8	2.8	95.2	45.5	145.8	2.8
CI2_14	318.8	0.55	44.610	2.09	0.0480	2.10	142.9	3.0	99.9	49.0	142.9	3.0
CI2_12	161.1	0.67	45.691	2.05	0.0471	2.57	139.6	2.8	52.3	60.2	139.6	2.8
CI2_10	779.0	0.91	44.418	2.10	0.0476	1.87	143.5	3.0	79.3	43.7	143.5	3.0
CI2_9	401.7	0.63	45.620	1.46	0.0490	1.90	139.8	2.0	147.5	43.9	139.8	2.0
CI2_8	343.8	0.73	44.922	1.48	0.0490	1.93	141.9	2.1	148.3	44.6	141.9	2.1
CI2_6	130.2	0.48	43.001	1.80	0.0462	2.50	148.2	2.6	8.9	57.6	148.2	2.6
CI2_5	410.4	0.58	42.994	1.36	0.0484	1.87	148.2	2.0	119.3	43.6	148.2	2.0
CI2_4	345.5	0.63	44.576	1.38	0.0491	1.92	143.0	2.0	153.9	44.3	143.0	2.0

CI9B

CI9B_31	130.9	1.00	44.196	1.46	0.0472	1.70	144.2	2.1	58.7	40.1	144.2	2.1
CI9B_30	119.8	0.90	44.938	1.51	0.0475	1.92	141.9	2.1	74.9	45.1	141.9	2.1
CI9B_29	94.3	0.85	45.812	1.61	0.0487	2.01	139.2	2.2	135.6	46.5	139.2	2.2
CI9B_28	69.3	0.67	46.275	1.87	0.0535	2.51	137.8	2.6	351.9	55.7	137.8	2.6
CI9B_27	99.2	0.74	44.826	1.45	0.0498	2.05	142.2	2.0	185.7	47.0	142.2	2.0
CI9B_26	119.6	0.91	44.539	1.59	0.0497	1.77	143.1	2.3	179.9	40.6	143.1	2.3
CI9B_25	116.6	0.92	45.320	1.49	0.0502	2.00	140.7	2.1	204.1	45.7	140.7	2.1
CI9B_23	168.7	0.91	44.927	1.55	0.0487	1.57	141.9	2.2	135.2	36.4	141.9	2.2

CI9B_22	117.8	0.75	45.153	1.51	0.0509	1.83	141.2	2.1	238.3	41.8	141.2	2.1
CI9B_20	169.8	0.92	46.433	1.45	0.0485	1.52	137.4	2.0	122.9	35.4	137.4	2.0
CI9B_19	138.5	0.60	45.050	1.77	0.0494	1.95	141.5	2.5	164.7	45.0	141.5	2.5
CI9B_18	160.2	0.97	45.464	1.55	0.0488	1.69	140.3	2.1	136.1	39.3	140.3	2.1
CI9B_17	101.8	0.76	44.177	1.74	0.0489	1.90	144.3	2.5	145.3	44.0	144.3	2.5
CI9B_16	119.7	0.80	45.912	1.59	0.0498	1.80	138.9	2.2	183.5	41.5	138.9	2.2
CI9B_15	137.4	0.47	44.322	1.57	0.0486	1.79	143.8	2.2	129.8	41.5	143.8	2.2
CI9B_14	172.9	0.96	44.535	1.31	0.0488	1.63	143.1	1.9	136.2	37.8	143.1	1.9
CI9B_13	140.3	0.81	44.105	1.61	0.0475	1.67	144.5	2.3	75.1	39.2	144.5	2.3
CI9B_12	126.1	0.96	44.802	2.15	0.0486	1.73	142.3	3.0	126.8	40.2	142.3	3.0
CI9B_11	144.8	0.88	44.882	2.06	0.0500	1.63	142.1	2.9	197.2	37.4	142.1	2.9
CI9B_10	107.8	0.70	44.935	2.18	0.0504	1.79	141.9	3.1	211.7	41.0	141.9	3.1
CI9B_9	123.8	0.92	45.692	2.33	0.0506	2.33	139.6	3.2	224.7	52.9	139.6	3.2
CI9B_8	128.5	0.93	45.387	2.04	0.0478	1.67	140.5	2.8	90.9	39.1	140.5	2.8
CI9B_7	99.2	0.63	44.872	2.13	0.0497	2.02	142.1	3.0	182.8	46.5	142.1	3.0
CI9B_6	126.6	0.97	44.445	1.92	0.0484	1.71	143.4	2.7	118.3	39.8	143.4	2.7
CI9B_5	123.2	0.91	44.030	1.90	0.0513	1.83	144.8	2.7	255.6	41.5	144.8	2.7
CI9B_4	92.6	0.71	44.206	2.14	0.0498	2.31	144.2	3.0	186.3	52.9	144.2	3.0
CI9B_3	100.7	0.71	44.355	2.10	0.0496	2.06	143.7	3.0	177.2	47.3	143.7	3.0
CI9B_2	103.9	0.63	45.824	2.21	0.0478	2.21	139.2	3.0	87.9	51.5	139.2	3.0
CI9B_1	119.0	0.63	44.860	2.06	0.0461	2.19	142.1	2.9	1.8	50.6	142.1	2.9

GCC6

GCC6-1	192.9	0.57	40.433	0.02	0.0476	0.05	157.5	3.0	77.9	113.2	157.5	3.0
GCC6-2	166.5	0.60	39.691	0.01	0.0474	0.09	160.4	1.1	69.1	202.6	160.4	1.1
GCC6-3	131.1	0.43	40.184	0.01	0.0488	0.09	158.5	0.8	138.7	200.8	158.5	0.8
GCC6-4	132.6	0.45	39.480	0.01	0.0490	0.06	161.2	1.8	147.5	133.9	161.2	1.8
GCC6-5	282.1	1.22	40.299	0.01	0.0492	0.06	158.0	1.4	158.9	130.0	158.0	1.4
GCC6-6	234.7	0.38	40.319	0.02	0.0484	0.03	157.9	2.4	117.8	69.3	157.9	2.4
GCC6-7	468.8	0.69	40.264	0.02	0.0506	0.01	158.1	3.2	222.6	33.5	158.1	3.2
GCC6-8	219.6	0.48	40.349	0.01	0.0483	0.03	157.8	0.8	116.4	64.8	157.8	0.8

GCC6-9	165.4	0.44	40.946	0.03	0.0486	0.04	155.5	5.2	128.6	102.9	155.5	5.2
GCC6-10	119.6	0.43	39.957	0.02	0.0449	0.10	159.3	3.0	-59.9	232.4	159.3	3.0
GCC6-11	187.4	0.54	40.094	0.03	0.0466	0.06	158.8	4.4	26.6	139.8	158.8	4.4
GCC6-12	214.3	0.62	40.406	0.01	0.0463	0.06	157.6	2.2	12.3	148.7	157.6	2.2
GCC6-13	242.5	0.40	39.716	0.01	0.0477	0.03	160.3	1.1	82.9	82.6	160.3	1.1
GCC6-14	198.1	0.53	39.134	0.01	0.0490	0.05	162.7	2.0	146.8	117.8	162.7	2.0
GCC6-15	289.3	1.08	40.375	0.01	0.0495	0.07	157.7	1.2	169.9	162.2	157.7	1.2
GCC6-16	266.5	0.38	40.382	0.01	0.0477	0.04	157.7	0.8	84.1	99.1	157.7	0.8
GCC6-17	807.9	0.47	40.096	0.01	0.0535	0.03	158.8	1.6	351.4	61.0	158.8	1.6
GCC6-18	184.2	0.45	40.647	0.02	0.0500	0.17	156.7	2.5	194.4	408.6	156.7	2.5
GCC6-19	276.3	0.44	40.648	0.01	0.0486	0.03	156.7	0.8	128.4	80.5	156.7	0.8
GCC6-20	210.3	0.54	39.596	0.01	0.0478	0.04	160.8	0.8	88.2	99.2	160.8	0.8
GCC6-21	195.2	0.46	41.219	0.03	0.0586	0.11	154.5	3.9	553.3	249.1	154.5	3.9
GCC6-22	798.1	0.53	40.436	0.02	0.0531	0.17	157.5	2.6	334.7	376.4	157.5	2.6
GCC6-23	226.6	0.49	39.664	0.01	0.0473	0.04	160.5	0.8	63.4	106.2	160.5	0.8
GCC6-24	228.9	0.72	40.348	0.02	0.0480	0.06	157.8	2.6	97.0	135.0	157.8	2.6
GCC6-25	137.8	0.45	40.581	0.02	0.0474	0.05	156.9	3.1	69.8	117.7	156.9	3.1
GCC6-26	148.3	0.50	39.446	0.01	0.0471	0.07	161.4	2.1	55.5	161.0	161.4	2.1
GCC6-27	376.1	0.44	40.262	0.02	0.0489	0.02	158.2	3.5	143.9	43.0	158.2	3.5
GCC6-28	394.0	0.45	40.253	0.01	0.0481	0.03	158.2	0.9	101.9	68.3	158.2	0.9
GCC6-29	220.0	0.54	39.807	0.01	0.0476	0.04	159.9	1.3	81.6	95.3	159.9	1.3
GCC6-30	149.5	0.55	39.599	0.01	0.0457	0.09	160.8	1.6	-15.9	206.3	160.8	1.6
GCC6-31	204.4	0.63	40.452	0.02	0.0473	0.05	157.4	2.8	64.1	111.4	157.4	2.8
GCC6-32	282.4	0.48	40.207	0.01	0.0492	0.04	158.4	1.7	157.6	83.8	158.4	1.7
GCC6-33	230.9	0.50	39.843	0.01	0.0492	0.02	159.8	0.8	156.9	54.5	159.8	0.8
GCC6-35	217.5	0.46	39.952	0.01	0.0519	0.08	159.4	1.2	283.0	187.7	159.4	1.2
GCC6-36	239.3	0.58	39.428	0.01	0.0610	0.15	161.5	0.8	639.0	333.6	161.5	0.8
GCC6-37	330.2	0.56	39.010	0.01	0.0476	0.04	163.2	0.9	77.8	105.0	163.2	0.9
GCC6-38	278.3	0.52	40.593	0.01	0.0484	0.04	156.9	1.1	121.1	82.7	156.9	1.1
GCC6-39	262.4	0.46	39.521	0.02	0.0481	0.05	161.1	3.7	103.4	107.8	161.1	3.7

GCC6-40	202.4	0.53	39.927	0.02	0.0486	0.03	159.5	3.0	129.4	66.0	159.5	3.0
GCC6-41	124.5	0.43	39.700	0.01	0.0481	0.18	160.4	1.9	105.8	427.2	160.4	1.9
GCC6-42	109.5	0.38	40.423	0.01	0.0573	0.30	157.5	1.7	503.2	681.4	157.5	1.7
GCC6-43	277.8	0.57	40.690	0.01	0.0486	0.03	156.5	1.4	129.9	75.4	156.5	1.4
GCC6-44	126.1	0.44	40.264	0.01	0.0543	0.07	158.1	1.8	383.6	168.0	158.1	1.8
GCC6-45	744.1	0.27	39.918	0.04	0.0500	0.01	159.5	5.9	195.1	33.6	159.5	5.9
GCC6-46	255.7	0.57	40.105	0.01	0.0512	0.04	158.8	0.8	248.1	98.1	158.8	0.8
GCC6-47	225.2	0.51	40.253	0.01	0.0481	0.04	158.2	1.3	103.7	92.8	158.2	1.3
GCC6-48	173.3	0.53	40.718	0.02	0.0457	0.08	156.4	2.9	-17.7	190.0	156.4	2.9

Mariquita stock

CM7

CM7_39	1957.9	0.37	48.706	1.13	0.0494	0.50	131.0	1.5	166.9	11.6	131.0	1.5
CM7_38	2484.4	0.42	49.231	1.06	0.0496	0.52	129.6	1.4	177.0	12.1	129.6	1.4
CM7_37	782.7	0.28	50.058	1.27	0.0496	0.92	127.5	1.6	178.0	21.3	127.5	1.6
CM7_36	775.9	0.33	49.316	1.21	0.0534	0.73	129.4	1.5	347.7	16.4	129.4	1.5
CM7_35	1686.0	0.37	49.751	1.27	0.0510	0.96	128.3	1.6	239.1	21.9	128.3	1.6
CM7_33	1346.3	0.51	46.985	1.02	0.0492	0.56	135.8	1.4	157.7	13.1	135.8	1.4
CM7_31	4194.0	0.48	48.222	1.01	0.0490	0.41	132.3	1.3	145.5	9.6	132.3	1.3
CM7_30	756.1	0.23	48.763	1.54	0.0491	0.84	130.9	2.0	154.9	19.5	130.9	2.0
CM7_27	442.2	0.38	49.371	1.71	0.0528	1.59	129.3	2.2	320.9	35.6	129.3	2.2
CM7_26	1751.1	0.40	49.997	2.21	0.0484	0.99	127.7	2.8	118.7	23.2	127.7	2.8
CM7_25	348.0	0.24	50.290	1.65	0.0498	1.17	126.9	2.1	184.7	27.1	126.9	2.1
CM7_24	4792.7	0.39	47.272	1.49	0.0506	0.60	134.9	2.0	221.1	13.8	134.9	2.0
CM7_21	600.8	0.34	49.267	1.60	0.0688	1.52	129.5	2.1	891.5	31.1	129.5	2.1
CM7_20	1440.7	0.46	49.163	1.42	0.0513	0.87	129.8	1.8	256.2	19.9	129.8	1.8
CM7_18	2040.7	0.40	48.678	1.49	0.0490	0.77	131.1	1.9	146.9	18.0	131.1	1.9
CM7_17	1761.8	0.36	49.091	1.63	0.0498	0.77	130.0	2.1	186.7	17.9	130.0	2.1
CM7_16	1729.2	0.32	49.069	1.50	0.0566	0.83	130.1	1.9	477.0	18.3	130.1	1.9
CM7_15	444.5	0.29	48.859	1.65	0.0476	1.15	130.6	2.1	81.4	27.1	130.6	2.1
CM7_14	1929.7	0.47	48.057	1.52	0.0505	0.80	132.8	2.0	217.0	18.5	132.8	2.0

CM7_13	1290.5	0.42	47.646	1.46	0.0494	0.87	133.9	1.9	167.0	20.2	133.9	1.9	
CM7_12	1128.2	0.40	47.266	1.48	0.0489	0.86	135.0	2.0	142.3	19.9	135.0	2.0	
CM7_11	404.5	0.26	48.386	1.38	0.0520	1.11	131.9	1.8	287.5	25.3	131.9	1.8	
CM7_10	746.9	0.27	48.442	1.16	0.0509	0.93	131.7	1.5	237.2	21.3	131.7	1.5	
CM7_9	595.7	0.28	49.424	1.26	0.0518	1.04	129.1	1.6	274.5	23.7	129.1	1.6	
CM7_7	779.8	0.40	50.149	1.46	0.0501	1.29	127.3	1.8	200.1	29.7	127.3	1.8	
CM7_6	1483.7	0.45	48.266	1.17	0.0492	0.80	132.2	1.5	158.9	18.6	132.2	1.5	
CM7_4	702.0	0.25	49.817	1.29	0.0483	0.98	128.1	1.6	112.5	22.9	128.1	1.6	
CM7_3	972.0	0.37	48.166	1.25	0.0492	0.87	132.5	1.6	157.1	20.1	132.5	1.6	
CM7_2	828.8	0.33	48.621	1.27	0.0485	0.91	131.2	1.7	125.7	21.3	131.2	1.7	
CM7_1	1127.2	0.33	49.361	1.08	0.0481	0.96	129.3	1.4	104.8	22.5	129.3	1.4	
CM19													
CM19_39	2190.2	0.43	49.542	1.07	0.0502	0.78	128.8	1.4	205.3	17.9	128.8	1.4	
CM19_38	985.5	0.40	48.167	1.10	0.0840	0.86	132.5	1.4	1293.1	16.7	132.5	1.4	
CM19_37	299.8	0.36	49.735	1.35	0.0489	1.29	128.3	1.7	143.2	30.0	128.3	1.7	
CM19_36	758.9	0.26	49.201	1.18	0.0493	1.14	129.7	1.5	162.9	26.5	129.7	1.5	
CM19_35	1131.7	0.50	50.354	1.26	0.0496	0.97	126.8	1.6	175.1	22.4	126.8	1.6	
CM19_34	800.4	0.46	49.010	1.01	0.0485	0.91	130.2	1.3	124.8	21.3	130.2	1.3	
CM19_33	502.5	0.33	49.256	1.28	0.0512	1.22	129.6	1.6	251.3	27.9	129.6	1.6	
CM19_31	1903.4	0.48	48.596	1.05	0.0500	0.74	131.3	1.4	196.6	17.1	131.3	1.4	
CM19_30	937.9	0.33	47.994	1.18	0.0492	0.84	132.9	1.6	159.0	19.6	132.9	1.6	
CM19_29	123.4	0.24	50.737	1.87	0.0540	2.15	125.8	2.3	370.5	47.6	125.8	2.3	
CM19_28	498.0	0.33	49.100	1.45	0.0512	1.27	130.0	1.9	250.4	29.0	130.0	1.9	
CM19_27	117.8	0.22	50.378	1.62	0.0492	1.98	126.7	2.0	155.5	45.7	126.7	2.0	
CM19_26	728.4	0.32	49.472	1.17	0.0484	1.16	129.0	1.5	120.2	27.1	129.0	1.5	
CM19_25	614.4	0.33	50.380	1.34	0.0478	1.10	126.7	1.7	86.9	25.8	126.7	1.7	
CM19_24	836.8	0.26	49.519	1.09	0.0492	0.95	128.9	1.4	159.4	22.1	128.9	1.4	
CM19_23	1462.4	0.27	47.177	1.02	0.0513	0.87	135.2	1.4	253.0	19.9	135.2	1.4	
CM19_22	3281.3	0.30	47.503	0.99	0.0526	0.59	134.3	1.3	312.8	13.4	134.3	1.3	
CM19_21	253.4	0.33	48.345	1.34	0.0502	1.33	132.0	1.8	203.6	30.7	132.0	1.8	

CM19_20	359.8	0.30	47.053	1.25	0.0496	1.00	135.6	1.7	174.1	23.2	135.6	1.7
CM19_19	929.6	0.36	46.574	0.91	0.0558	0.87	136.9	1.2	443.8	19.2	136.9	1.2
CM19_18	513.1	0.31	47.931	1.12	0.0485	1.14	133.1	1.5	122.3	26.6	133.1	1.5
CM19_16	1148.9	0.57	49.880	0.95	0.0568	0.78	128.0	1.2	483.1	17.1	128.0	1.2
CM19_15	2620.9	0.42	46.990	1.04	0.0522	0.65	135.7	1.4	295.5	14.7	135.7	1.4
CM19_14	703.7	0.27	49.021	1.45	0.0504	0.95	130.2	1.9	215.6	21.8	130.2	1.9
CM19_13	387.1	0.33	48.143	1.22	0.0492	1.02	132.5	1.6	155.9	23.6	132.5	1.6
CM19_10	816.5	0.38	47.830	1.22	0.0507	1.00	133.4	1.6	228.0	23.0	133.4	1.6
CM19_8	335.7	0.38	47.874	1.25	0.0534	1.59	133.3	1.6	347.6	35.6	133.3	1.6
CM19_7	2727.6	0.58	49.545	1.15	0.0489	0.66	128.8	1.5	140.8	15.4	128.8	1.5
CM19_6	286.0	0.33	51.473	1.41	0.0490	1.35	124.0	1.7	148.3	31.4	124.0	1.7
CM19_5	1042.1	0.31	49.068	1.12	0.0487	0.89	130.1	1.4	134.4	20.9	130.1	1.4
CM19_4	647.0	0.47	51.303	1.25	0.0502	1.17	124.4	1.5	202.5	26.9	124.4	1.5
CM19_3	1105.9	0.68	47.247	1.14	0.0477	0.77	135.0	1.5	85.8	18.2	135.0	1.5
CM19_1	1991.0	0.40	47.825	1.12	0.0483	0.61	133.4	1.5	115.5	14.4	133.4	1.5

CM17B

CM17B_37	2171.3	0.25	47.021	1.75	0.0490	0.44	135.7	2.4	148.2	10.3	135.7	2.4
CM17B_36	1232.7	0.34	49.800	1.88	0.0505	0.70	128.2	2.4	219.0	16.0	128.2	2.4
CM17B_33	919.7	0.50	50.074	1.80	0.0475	0.73	127.5	2.3	73.2	17.2	127.5	2.3
CM17B_32	330.1	0.24	49.106	2.18	0.0485	1.66	130.0	2.8	126.0	38.6	130.0	2.8
CM17B_30	252.9	0.27	47.745	1.83	0.0470	1.30	133.6	2.4	46.7	30.9	133.6	2.4
CM17B_29	786.3	0.25	47.482	1.89	0.0510	0.94	134.4	2.5	240.4	21.5	134.4	2.5
CM17B_28	188.0	0.25	47.538	1.90	0.0486	1.54	134.2	2.5	129.0	35.8	134.2	2.5
CM17B_27	296.0	0.34	47.746	1.73	0.0478	1.19	133.6	2.3	87.7	27.9	133.6	2.3
CM17B_26	269.0	0.26	48.660	1.78	0.0496	1.35	131.1	2.3	176.1	31.3	131.1	2.3
CM17B_25	1911.0	0.33	48.737	1.60	0.0488	0.57	130.9	2.1	137.1	13.2	130.9	2.1
CM17B_23	2630.5	0.32	47.279	1.49	0.0491	0.50	134.9	2.0	151.7	11.6	134.9	2.0
CM17B_22	667.0	0.44	48.802	1.58	0.0493	0.86	130.8	2.0	164.1	19.9	130.8	2.0
CM17B_21	2493.3	0.47	48.848	1.62	0.0494	0.70	130.6	2.1	167.6	16.2	130.6	2.1
CM17B_20	1127.0	0.30	47.835	1.53	0.0498	0.65	133.4	2.0	183.3	15.1	133.4	2.0

CM17B_19	1068.1	0.36	48.196	1.52	0.0491	0.70	132.4	2.0	151.1	16.4	132.4	2.0
CM17B_18	649.1	0.33	45.884	1.60	0.0506	0.80	139.0	2.2	221.8	18.3	139.0	2.2
CM17B_16	1208.6	0.33	49.818	1.56	0.0485	0.59	128.1	2.0	122.7	13.9	128.1	2.0
CM17B_15	955.7	0.26	47.895	1.54	0.0514	0.73	133.2	2.0	257.8	16.7	133.2	2.0
CM17B_14	1537.4	0.36	48.057	1.42	0.0490	0.60	132.8	1.9	149.8	14.1	132.8	1.9
CM17B_13	1508.5	0.25	48.763	1.46	0.0491	0.71	130.9	1.9	152.1	16.7	130.9	1.9
CM17B_12	2165.8	0.28	49.745	1.53	0.0488	0.64	128.3	1.9	139.4	14.9	128.3	1.9
CM17B_11	1484.7	0.27	49.204	1.46	0.0495	0.72	129.7	1.9	170.4	16.7	129.7	1.9
CM17B_10	2301.3	0.33	48.544	1.44	0.0524	0.62	131.4	1.9	303.8	14.1	131.4	1.9
CM17B_9	227.1	0.26	46.722	1.71	0.0682	1.23	136.5	2.3	875.6	25.3	136.5	2.3
CM17B_8	742.4	0.38	47.988	1.58	0.0536	1.14	133.0	2.1	354.5	25.6	133.0	2.1
CM17B_7	224.0	0.23	47.839	1.75	0.0486	1.40	133.4	2.3	129.8	32.6	133.4	2.3
CM17B_6	700.3	0.32	47.141	1.59	0.0506	0.88	135.3	2.1	224.5	20.2	135.3	2.1
CM17B_5	359.1	0.30	47.887	1.62	0.0492	1.08	133.2	2.1	156.2	25.1	133.2	2.1
CM17B_4	903.0	0.54	47.151	1.75	0.0592	1.27	135.3	2.3	573.6	27.3	135.3	2.3
CM17B_3	2482.3	0.22	46.728	1.43	0.0492	0.54	136.5	1.9	157.2	12.5	136.5	1.9

CM4

CM4_44	301.0	0.56	47.486	1.64	0.1001	1.75	134.3	2.2	1626.6	32.2	1626.6	2.2
CM4_43	1559.3	0.54	47.694	1.46	0.0486	1.05	133.8	1.9	130.6	24.6	133.8	1.9
CM4_42	731.2	0.42	50.227	1.34	0.0522	1.51	127.1	1.7	292.4	34.1	127.1	1.7
CM4_41	925.2	0.46	46.435	1.30	0.0496	1.24	137.4	1.8	175.0	28.7	137.4	1.8
CM4_40	458.7	0.39	47.763	1.41	0.0523	1.44	133.6	1.9	297.0	32.4	133.6	1.9
CM4_39	604.6	0.38	47.933	1.37	0.0490	1.54	133.1	1.8	150.2	35.7	133.1	1.8
CM4_38	898.0	0.40	48.263	1.58	0.0510	1.88	132.2	2.1	242.2	42.6	132.2	2.1
CM4_37	424.5	0.44	50.159	1.50	0.0482	1.51	127.3	1.9	108.7	35.3	127.3	1.9
CM4_36	1467.3	0.37	49.170	1.38	0.0583	1.22	129.8	1.8	541.2	26.6	129.8	1.8
CM4_35	1605.3	0.30	48.414	1.35	0.0495	1.10	131.8	1.8	173.4	25.4	131.8	1.8
CM4_34	707.3	0.46	47.334	1.39	0.0522	1.38	134.8	1.9	296.2	31.3	134.8	1.9
CM4_33	775.4	0.55	48.620	1.34	0.0726	1.88	131.2	1.7	1002.1	37.6	131.2	1.7
CM4_32	702.1	0.45	51.395	1.71	0.0528	2.11	124.2	2.1	321.6	47.2	124.2	2.1

CM4_31	1065.9	0.40	49.132	1.32	0.0504	1.15	129.9	1.7	212.3	26.4	129.9	1.7
CM4_30	1491.3	0.26	46.663	1.30	0.0493	1.08	136.7	1.8	160.9	25.2	136.7	1.8
CM4_29	1281.9	0.47	46.613	1.32	0.0493	1.14	136.8	1.8	161.1	26.4	136.8	1.8
CM4_28	2533.4	0.68	48.005	1.58	0.0503	1.60	132.9	2.1	209.9	36.6	132.9	2.1
CM4_27	579.5	0.31	50.215	1.28	0.0577	2.36	127.1	1.6	517.4	51.0	127.1	1.6
CM4_26	1035.9	0.44	50.544	1.16	0.0483	1.26	126.3	1.5	111.7	29.5	126.3	1.5
CM4_25	587.8	0.30	49.246	1.19	0.0505	1.62	129.6	1.5	219.4	37.2	129.6	1.5
CM4_23	2532.9	0.34	50.230	1.05	0.0488	1.01	127.1	1.3	138.9	23.5	127.1	1.3
CM4_21	393.9	0.36	46.668	1.32	0.0486	1.81	136.7	1.8	130.8	42.0	136.7	1.8
CM4_20	282.3	0.40	49.455	1.24	0.0491	1.57	129.0	1.6	153.3	36.5	129.0	1.6
CM4_19	409.1	0.40	45.611	1.21	0.0516	1.43	139.8	1.7	266.0	32.5	139.8	1.7
CM4_18	947.5	0.37	48.640	1.10	0.0487	1.17	131.2	1.4	131.2	27.3	131.2	1.4
CM4_16	775.5	0.45	45.635	1.47	0.0510	1.16	139.7	2.0	240.2	26.4	139.7	2.0
CM4_14	2235.0	0.58	47.593	1.45	0.0493	0.82	134.0	1.9	160.1	19.2	134.0	1.9
CM4_13	1035.1	0.55	47.958	1.48	0.0559	0.91	133.0	1.9	450.4	20.0	133.0	1.9
CM4_12	620.1	0.34	47.511	1.52	0.0522	1.19	134.3	2.0	292.9	26.9	134.3	2.0
CM4_11	677.1	0.45	48.422	1.81	0.0532	2.25	131.8	2.4	338.3	50.1	131.8	2.4
CM4_10	265.5	0.28	46.947	1.67	0.0495	1.61	135.9	2.2	172.8	37.1	135.9	2.2
CM4_9	311.9	0.47	48.859	1.58	0.0497	1.65	130.6	2.0	183.0	38.0	130.6	2.0
CM4_7	946.6	0.42	46.224	1.47	0.0545	1.00	138.0	2.0	391.1	22.2	138.0	2.0
CM4_6	1770.8	0.40	44.671	1.45	0.0537	0.88	142.7	2.0	356.6	19.7	142.7	2.0
CM4_5	1277.0	0.31	48.105	1.46	0.0499	0.92	132.6	1.9	190.5	21.3	132.6	1.9
CM4_4	440.1	0.33	45.532	1.56	0.0514	1.43	140.0	2.2	256.6	32.5	140.0	2.2
CM4_3	631.5	0.31	46.601	1.94	0.0518	2.39	136.9	2.6	275.3	53.9	136.9	2.6
CM4_2	485.0	0.37	46.073	1.50	0.0486	1.29	138.4	2.1	130.2	30.0	138.4	2.1
CM4_1	325.6	0.25	46.456	2.03	0.0525	2.10	137.3	2.8	308.1	47.2	137.3	2.8

CM10

CM10_49	2005.0	0.45	47.762	1.04	0.0493	0.83	133.6	1.4	161.0	19.4	133.6	1.4
CM10_48	805.8	0.32	47.122	1.21	0.0673	1.26	135.4	1.6	848.2	25.9	135.4	1.6
CM10_47	1394.0	0.30	47.747	1.15	0.0500	0.98	133.6	1.5	195.7	22.7	133.6	1.5

CM10_45	1839.6	0.36	48.194	1.17	0.0490	1.14	132.4	1.5	146.6	26.5	132.4	1.5
CM10_44	1108.4	0.32	47.649	1.10	0.0507	0.99	133.9	1.5	228.9	22.7	133.9	1.5
CM10_43	587.1	0.36	47.797	1.13	0.0489	1.21	133.5	1.5	140.7	28.1	133.5	1.5
CM10_42	752.2	0.28	46.721	1.12	0.0483	1.05	136.5	1.5	112.5	24.6	136.5	1.5
CM10_41	3690.4	0.22	48.025	1.05	0.0515	0.76	132.9	1.4	262.6	17.4	132.9	1.4
CM10_38	784.0	0.22	46.131	1.12	0.0489	1.16	138.2	1.5	144.2	26.9	138.2	1.5
CM10_36	950.7	0.21	48.781	1.14	0.0505	1.01	130.8	1.5	218.7	23.2	130.8	1.5
CM10_35	827.3	0.26	48.568	1.18	0.0534	1.11	131.4	1.5	344.3	24.9	131.4	1.5
CM10_34	1320.7	0.27	48.266	1.11	0.0520	0.89	132.2	1.5	283.8	20.2	132.2	1.5
CM10_33	1474.6	0.20	47.441	1.11	0.0501	0.96	134.5	1.5	200.8	22.1	134.5	1.5
CM10_32	2336.7	0.23	48.508	1.16	0.0492	1.06	131.5	1.5	159.6	24.5	131.5	1.5
CM10_31	262.3	0.22	48.411	1.29	0.0488	1.74	131.8	1.7	136.1	40.4	131.8	1.7
CM10_30	1744.3	0.27	47.692	1.20	0.0547	0.98	133.8	1.6	399.7	21.7	133.8	1.6
CM10_28	2941.2	0.37	47.208	1.07	0.0492	0.77	135.1	1.4	158.5	17.9	135.1	1.4
CM10_27	1166.5	0.33	47.119	1.14	0.0493	0.91	135.4	1.5	160.4	21.1	135.4	1.5
CM10_26	987.2	0.25	48.001	1.22	0.0489	1.29	132.9	1.6	142.1	30.0	132.9	1.6
CM10_24	217.1	0.24	46.332	1.30	0.0501	2.05	137.7	1.8	199.2	47.0	137.7	1.8
CM10_23	1130.8	0.22	47.673	1.10	0.0528	1.04	133.8	1.5	318.2	23.5	133.8	1.5
CM10_22	2103.4	0.62	48.552	1.10	0.0493	0.83	131.4	1.4	161.2	19.2	131.4	1.4
CM10_21	302.5	0.40	46.768	1.26	0.0493	1.47	136.4	1.7	161.1	34.0	136.4	1.7
CM10_20	1057.6	0.30	47.169	1.22	0.0519	1.03	135.2	1.6	281.1	23.4	135.2	1.6
CM10_18	641.3	0.24	47.045	1.00	0.0500	1.37	135.6	1.3	196.2	31.6	135.6	1.3
CM10_17	477.5	0.23	47.865	0.94	0.0524	1.18	133.3	1.2	300.8	26.6	133.3	1.2
CM10_16	2153.4	0.31	47.146	0.88	0.0645	1.80	135.3	1.2	757.8	37.5	135.3	1.2
CM10_15	675.8	0.20	47.163	0.94	0.0514	1.09	135.3	1.3	256.9	24.9	135.3	1.3
CM10_14	282.2	0.34	48.297	1.06	0.0504	1.67	132.1	1.4	212.8	38.1	132.1	1.4
CM10_13	2363.0	0.32	47.911	0.88	0.0512	0.71	133.2	1.2	248.5	16.3	133.2	1.2
CM10_12	740.8	0.38	47.593	0.91	0.0493	0.98	134.0	1.2	162.4	22.9	134.0	1.2
CM10_11	1934.0	0.46	47.391	0.85	0.0503	0.69	134.6	1.1	208.1	15.9	134.6	1.1
CM10_10	2641.8	0.34	48.161	0.88	0.0489	0.63	132.5	1.1	143.9	14.8	132.5	1.1

CM10_9	1509.2	0.34	48.535	0.88	0.0502	0.72	131.5	1.1	202.0	16.6	131.5	1.1
CM10_8	342.5	0.26	48.918	1.45	0.0503	1.50	130.5	1.9	207.1	34.3	130.5	1.9
CM10_7	1202.5	0.21	46.916	1.35	0.0488	0.76	136.0	1.8	137.6	17.8	136.0	1.8
CM10_6	1290.1	0.39	48.620	1.31	0.0487	0.88	131.2	1.7	134.3	20.5	131.2	1.7
CM10_5	1434.8	0.39	49.231	1.28	0.0495	0.78	129.6	1.6	172.1	18.1	129.6	1.6
CM10_4	2475.0	0.37	47.781	1.31	0.0491	0.95	133.5	1.7	153.9	22.0	133.5	1.7
CM10_3	1654.8	0.34	49.127	1.36	0.0500	0.81	129.9	1.7	193.1	18.8	129.9	1.7
CM10_2	670.9	0.21	48.386	1.58	0.0473	1.77	131.9	2.1	63.9	41.8	131.9	2.1
CM10_1	3894.3	0.21	50.812	1.39	0.0501	0.70	125.6	1.7	200.3	16.2	125.6	1.7
GCC1												
GCC1-1	1108.4	0.19	47.262	0.01	0.0493	0.01	135.0	1.8	161.8	22.8	135.0	1.8
GCC1-2	394.9	0.22	47.491	0.01	0.0485	0.03	134.3	1.1	125.6	71.1	134.3	1.1
GCC1-3	1074.9	0.15	47.434	0.02	0.0496	0.02	134.5	2.1	178.3	46.6	134.5	2.1
GCC1-4	1425.2	0.11	47.779	0.03	0.0479	0.05	133.5	3.8	94.1	127.4	133.5	3.8
GCC1-5	1879.2	0.48	47.738	0.01	0.0608	0.09	133.6	0.9	632.2	192.9	133.6	0.9
GCC1-6	1251.0	0.29	47.839	0.01	0.0542	0.10	133.4	1.6	380.2	226.6	133.4	1.6
GCC1-7	1424.9	0.18	46.290	0.01	0.0491	0.01	137.8	0.7	150.6	34.5	137.8	0.7
GCC1-8	1203.8	0.38	47.381	0.01	0.0493	0.02	134.6	0.8	162.7	42.2	134.6	0.8
GCC1-9	419.7	0.16	45.544	0.01	0.0485	0.03	140.0	0.7	121.9	65.0	140.0	0.7
GCC1-10	751.6	0.22	47.301	0.01	0.0504	0.03	134.9	1.4	214.2	72.3	134.9	1.4
GCC1-13	914.8	0.22	47.048	0.01	0.0489	0.02	135.6	0.7	145.3	44.4	135.6	0.7
GCC1-14	1055.3	0.18	47.943	0.01	0.0538	0.14	133.1	1.6	361.7	317.9	133.1	1.6
GCC1-15	1104.5	0.36	46.715	0.02	0.0552	0.06	136.5	3.3	420.5	138.3	136.5	3.3
GCC1-16	1133.5	0.13	47.988	0.01	0.0511	0.18	133.0	1.0	246.4	425.3	133.0	1.0
GCC1-18	585.0	0.26	46.533	0.01	0.0497	0.02	137.1	1.0	180.9	58.0	137.1	1.0
GCC1-19	1311.4	0.14	47.175	0.01	0.0488	0.01	135.2	1.1	140.2	18.8	135.2	1.1
GCC1-20	651.3	0.28	47.354	0.01	0.0480	0.02	134.7	0.7	98.1	53.1	134.7	0.7
GCC1-22	1762.0	0.21	47.477	0.01	0.0493	0.01	134.4	1.8	163.3	23.3	134.4	1.8
GCC1-25	912.3	0.18	47.038	0.02	0.0498	0.01	135.6	2.2	186.9	19.4	135.6	2.2
GCC1-26	3171.2	0.25	47.174	0.01	0.0516	0.02	135.2	2.0	266.2	39.1	135.2	2.0

GCC1-27	881.0	0.21	46.678	0.01	0.0588	0.20	136.6	1.2	559.9	449.5	136.6	1.2	
GCC1-28	2266.8	0.22	47.720	0.01	0.0503	0.01	133.7	1.4	210.2	30.7	133.7	1.4	
GCC1-29	1092.6	0.33	47.457	0.01	0.0547	0.16	134.4	1.2	400.0	352.4	134.4	1.2	
GCC1-30	1951.8	0.41	47.284	0.01	0.0492	0.03	134.9	1.1	156.7	71.8	134.9	1.1	
GCC1-31	3091.1	0.41	47.016	0.01	0.0503	0.02	135.7	0.9	208.3	37.7	135.7	0.9	
GCC1-32	1040.2	0.25	47.504	0.01	0.0503	0.02	134.3	0.7	208.0	48.1	134.3	0.7	
GCC1-33	64.0	6.15	47.581	0.01	0.0546	0.05	134.1	1.2	395.0	103.8	134.1	1.2	
GCC1-35	1631.8	0.29	47.127	0.01	0.0516	0.01	135.4	1.2	266.3	23.8	135.4	1.2	
GCC1-36	876.0	0.29	47.535	0.02	0.0490	0.02	134.2	2.2	147.0	36.6	134.2	2.2	
GCC1-37	1639.7	0.19	47.537	0.01	0.0491	0.01	134.2	0.8	151.1	26.9	134.2	0.8	
GCC1-38	312.0	0.16	47.541	0.01	0.0491	0.05	134.2	1.6	154.2	108.4	134.2	1.6	
GCC1-39	566.6	0.25	47.196	0.01	0.0500	0.03	135.2	1.0	192.8	74.5	135.2	1.0	
GCC1-40	2017.4	0.26	47.014	0.01	0.0495	0.01	135.7	1.1	171.6	18.2	135.7	1.1	
GCC1-41	850.0	0.35	47.284	0.01	0.0520	0.03	134.9	0.7	285.0	64.6	134.9	0.7	
GCC1-43	453.5	0.17	47.126	0.02	0.0487	0.02	135.4	2.9	133.4	47.9	135.4	2.9	
GCC1-45	602.6	0.08	47.677	0.01	0.0517	0.05	133.8	1.6	273.4	103.6	133.8	1.6	
GCC7A													
GCC7A-1	213.9	0.28	44.464	0.01	0.0481	0.06	143.4	1.0	105.5	141.2	143.4	1.0	
GCC7A-2	1126.1	0.34	44.126	0.01	0.0503	0.02	144.5	1.8	210.4	38.6	144.5	1.8	
GCC7A-3	545.3	0.29	44.994	0.02	0.0592	0.14	141.7	2.2	573.7	301.5	141.7	2.2	
GCC7A-4	1258.3	0.17	44.982	0.01	0.0488	0.03	141.7	1.9	138.5	59.6	141.7	1.9	
GCC7A-5	784.2	0.38	44.303	0.01	0.0484	0.14	143.9	1.5	119.3	323.3	143.9	1.5	
GCC7A-6	1460.0	0.18	44.734	0.01	0.0504	0.02	142.5	0.7	214.4	45.7	142.5	0.7	
GCC7A-8	1051.5	0.13	44.314	0.01	0.0498	0.01	143.9	0.7	185.0	30.9	143.9	0.7	
GCC7A-10	613.2	0.21	44.345	0.01	0.0482	0.01	143.8	0.7	111.2	35.2	143.8	0.7	
GCC7A-11	367.4	0.20	44.844	0.01	0.0476	0.05	142.2	1.2	78.7	116.9	142.2	1.2	
GCC7A-12	405.7	0.22	44.548	0.02	0.0483	0.04	143.1	2.7	112.7	92.6	143.1	2.7	
GCC7A-13	478.9	0.20	44.722	0.01	0.0473	0.14	142.6	1.8	62.2	328.5	142.6	1.8	
GCC7A-14	339.0	0.18	44.668	0.01	0.0483	0.03	142.7	0.7	111.7	72.9	142.7	0.7	
GCC7A-15	253.8	0.19	45.051	0.01	0.0469	0.04	141.5	1.7	44.8	103.7	141.5	1.7	

GCC7A-17	274.8	0.22	44.853	0.01	0.0477	0.09	142.1	1.7	85.1	209.5	142.1	1.7
GCC7A-18	884.9	0.20	44.203	0.01	0.0478	0.03	144.2	0.8	87.8	71.4	144.2	0.8
GCC7A-19	661.5	0.19	44.488	0.01	0.0479	0.02	143.3	0.8	96.2	53.7	143.3	0.8
GCC7A-20	542.2	0.27	44.168	0.01	0.0487	0.04	144.3	1.0	135.5	91.0	144.3	1.0
GCC7A-21	730.0	0.17	44.285	0.01	0.0483	0.01	143.9	0.9	113.5	35.3	143.9	0.9
GCC7A-22	437.3	0.21	44.260	0.01	0.0483	0.02	144.0	0.7	116.2	43.2	144.0	0.7
GCC7A-25	422.9	0.39	44.461	0.01	0.0498	0.13	143.4	1.4	183.3	299.4	143.4	1.4
GCC7A-26	513.4	0.31	44.198	0.01	0.0500	0.06	144.2	1.2	196.2	139.5	144.2	1.2
GCC7A-27	1143.1	0.25	44.203	0.01	0.0493	0.02	144.2	0.8	160.6	45.2	144.2	0.8
GCC7A-28	583.8	0.31	44.544	0.01	0.0480	0.03	143.1	1.1	97.0	77.4	143.1	1.1

Table 3.2. Hf isotopic data from the Payandé, Ibagué and Mariquita plutons.

Sample	$^{176}\text{Hf}/^{177}\text{Hf}$	2 σ error (x10 $^{-6}$)	$^{176}\text{Lu}/^{177}\text{Hf}$	2 σ error (x10 $^{-5}$)	$^{176}\text{Yb}/^{177}\text{Hf}$	2 σ error (x10 $^{-5}$)	$^{178}\text{Hf}/^{177}\text{Hf}$	2 σ error (x10 $^{-6}$)	$^{180}\text{Hf}/^{177}\text{Hf}$	2 σ error (x10 $^{-6}$)	$^{238}\text{U}/^{206}\text{Pb}$ Age	$^{176}\text{Hf}/^{177}\text{Hf}_i$	ϵHf_0	2 σ error	ϵHf_i
Payandé stock															
CSP3															
CSP3	0.282783	28	0.00118	2.5	0.02933	36	1.467141	36	1.886965	71	169.4	0.282779	-0.1	1.0	3.6
CSP3	0.282789	27	0.00103	6.8	0.02550	180	1.467188	31	1.887024	97	162.7	0.282786	0.1	1.0	3.6
CSP3	0.282765	29	0.00123	4.4	0.03212	91	1.467178	31	1.886971	90	165.7	0.282761	-0.7	1.0	2.8
CSP3	0.282753	26	0.00121	12.0	0.03110	330	1.467161	34	1.886979	99	161.4	0.282749	-1.1	0.9	2.3
CSP3	0.282769	28	0.00108	3.7	0.02686	96	1.467143	26	1.886930	110	152.6	0.282766	-0.6	1.0	2.7
CSP3	0.282775	26	0.00068	5.2	0.01550	110	1.467139	30	1.886958	83	164.6	0.282773	-0.4	0.9	3.2
CSP3	0.282790	26	0.00139	19.0	0.03640	560	1.467139	34	1.886868	82	165.6	0.282786	0.2	0.9	3.7
CSP3	0.282776	24	0.00099	4.9	0.02540	130	1.467147	26	1.886883	80	152.0	0.282773	-0.3	0.8	3.0
CSP 5															
CSP5	0.282786	29	0.00093	11.0	0.02120	250	1.467166	26	1.887005	85	155.6	0.282783	0.0	1.0	3.4
CSP5	0.282773	22	0.00065	3.5	0.01539	79	1.467152	36	1.886890	95	162.0	0.282771	-0.4	0.8	3.1
CSP5	0.282767	27	0.00073	2.2	0.01819	60	1.467138	38	1.886833	91	164.7	0.282765	-0.6	1.0	2.9
CSP5	0.282761	28	0.00073	2.7	0.01707	62	1.467145	25	1.886903	91	166.6	0.282759	-0.8	1.0	2.8
CSP5	0.282773	29	0.00104	1.7	0.02425	42	1.467155	33	1.886869	89	164.1	0.282770	-0.4	1.0	3.1
CSP5	0.282754	25	0.00077	3.3	0.01752	75	1.467176	25	1.886980	100	166.2	0.282752	-1.1	0.9	2.5
CSP5	0.282752	28	0.00088	2.0	0.01999	52	1.467128	36	1.887011	79	167.0	0.282749	-1.2	1.0	2.4
CSP5	0.282801	30	0.00121	20.0	0.03060	510	1.467131	39	1.886918	93	163.6	0.282797	0.6	1.1	4.1
Ibagué batholith															
CI2															
CI2	0.282848	24	0.00051	2.6	0.01321	64	1.467138	32	1.886933	83	142.9	0.282847	2.2	0.8	5.4
CI2	0.282860	30	0.00121	4.4	0.03078	97	1.467145	38	1.886986	96	145.3	0.282857	2.7	1.1	5.8
CI2	0.282886	33	0.00119	2.7	0.03196	60	1.467149	29	1.886800	110	143.0	0.282883	3.6	1.2	6.6
CI2	0.282922	38	0.00227	8.1	0.05990	250	1.467178	34	1.886801	93	148.2	0.282916	4.8	1.3	7.9
CI2	0.282867	24	0.00081	4.4	0.02130	100	1.467124	31	1.886793	99	148.2	0.282865	2.9	0.8	6.1
CI2	0.282857	20	0.00095	1.2	0.02512	33	1.467142	34	1.886930	91	139.6	0.282855	2.5	0.7	5.6
CI2	0.282856	23	0.00131	9.9	0.03370	260	1.467162	32	1.886920	110	148.0	0.282852	2.5	0.8	5.7
CI9B															
CI9B	0.282867	23	0.00072	2.8	0.01916	81	1.467153	31	1.886876	87	142.1	0.282865	2.9	0.8	6.0
CI9B	0.282860	23	0.00085	3.3	0.02263	92	1.467151	30	1.886931	77	141.9	0.282858	2.7	0.8	5.7
CI9B	0.282860	29	0.00101	2.4	0.02689	49	1.467164	31	1.886925	91	141.5	0.282857	2.7	1.0	5.7
CI9B	0.282856	26	0.00094	0.5	0.02513	11	1.467142	32	1.886968	98	140.7	0.282854	2.5	0.9	5.6
CI9B	0.282836	29	0.00086	1.3	0.02347	34	1.467133	36	1.886960	110	142.1	0.282834	1.8	1.0	4.9
CI9B	0.282832	29	0.00066	1.9	0.01751	60	1.467130	30	1.886970	100	144.3	0.282830	1.7	1.0	4.8
CI9B	0.282872	26	0.00096	1.3	0.02599	22	1.467157	36	1.886968	88	142.1	0.282869	3.1	0.9	6.1
CI9B	0.282850	23	0.00086	3.7	0.02260	110	1.467147	24	1.886966	97	141.2	0.282848	2.3	0.8	5.4
CI11															
CI11	0.282877	27	0.00055	1.9	0.01446	58	1.467143	37	1.886730	110	151.7	0.282875	3.3	1.0	6.6

CI11	0.282869	22	0.00073	3.4	0.01941	89	1.467165	33	1.886773	90	152.4	0.282867	3.0	0.8	6.3
CI11	0.282860	28	0.00074	1.7	0.02011	65	1.467137	30	1.886830	100	150.9	0.282858	2.7	1.0	5.9
CI11	0.282910	32	0.00065	1.2	0.01763	28	1.467133	36	1.886760	120	151.9	0.282908	4.4	1.1	7.7
CI11	0.282861	38	0.00081	2.8	0.02167	63	1.467188	29	1.886891	91	153.6	0.282859	2.7	1.3	6.0
CI11	0.282872	27	0.00056	1.9	0.01415	53	1.467141	20	1.886808	92	156.0	0.282870	3.1	1.0	6.5
CI11	0.282853	25	0.00031	1.0	0.00789	26	1.467150	33	1.886964	88	154.7	0.282852	2.4	0.9	5.8
CI11	0.282854	27	0.00076	0.5	0.02103	33	1.467179	33	1.886940	93	149.3	0.282852	2.4	1.0	5.7
CI13															
CI13	0.282882	24	0.00049	2.3	0.01331	65	1.467167	27	1.886910	79	147.6	0.282881	3.4	0.8	6.7
CI13	0.282871	46	0.00074	4.5	0.02070	120	1.467148	43	1.886860	170	141.6	0.282869	3.0	1.6	6.1
CI13	0.282864	28	0.00191	7.6	0.05490	240	1.467164	33	1.886910	79	147.3	0.282859	2.8	1.0	5.9
CI13	0.282865	30	0.00083	2.4	0.02274	70	1.467171	32	1.886956	93	142.3	0.282863	2.8	1.1	5.9
CI13	0.282818	37	0.00108	3.0	0.02937	66	1.467119	33	1.887130	140	145.1	0.282815	1.2	1.3	4.3
CI13	0.282812	42	0.00068	9.9	0.01800	280	1.467098	37	1.887060	140	140.3	0.282810	1.0	1.5	4.0
CI13	0.282853	41	0.00072	2.7	0.01902	72	1.467164	39	1.886950	130	144.3	0.282851	2.4	1.4	5.5
CI13	0.282865	21	0.00072	1.5	0.01941	49	1.467131	31	1.886884	94	142.6	0.282863	2.8	0.7	5.9
CI15															
CI15	0.282854	37	0.00067	2.6	0.01870	92	1.467165	33	1.886950	110	144.8	0.282852	2.4	1.3	5.6
CI15	0.282900	40	0.00087	1.0	0.02466	63	1.467185	36	1.886860	140	146.4	0.282898	4.1	1.4	7.2
CI15	0.282892	31	0.00087	1.4	0.02406	23	1.467158	35	1.886779	95	139.2	0.282890	3.8	1.1	6.8
CI15	0.282838	36	0.00064	1.6	0.01676	55	1.467155	29	1.886980	120	143.6	0.282836	1.9	1.3	5.0
CI15	0.282896	30	0.00082	2.2	0.02312	48	1.467175	36	1.886860	100	146.8	0.282894	3.9	1.1	7.1
CI15	0.282880	30	0.00073	2.8	0.01973	88	1.467181	26	1.886870	100	145.9	0.282878	3.4	1.1	6.5
CI15	0.282855	28	0.00046	0.8	0.01216	11	1.467186	32	1.886911	93	146.4	0.282854	2.5	1.0	5.7
CI15	0.282862	28	0.00030	1.1	0.00765	28	1.467159	33	1.886890	100	142.2	0.282861	2.7	1.0	5.9
CI15	0.282858	26	0.00063	0.6	0.01714	19	1.467145	27	1.886860	100	142.0	0.282856	2.6	0.9	5.7
CI15	0.282888	29	0.00052	0.2	0.01386	2	1.467172	30	1.886870	100	146.4	0.282887	3.6	1.0	6.8
Mariquita stock															
CM4															
CM4	0.282918	32	0.00150	3.8	0.03919	68	1.467151	37	1.886969	97	131.2	0.282914	4.7	1.1	7.5
CM4	0.282991	34	0.00215	21.0	0.05740	640	1.467155	37	1.886923	90	139.8	0.282985	7.3	1.2	10.2
CM4	0.282951	50	0.00234	17.0	0.06300	550	1.467120	40	1.886990	140	129.0	0.282945	5.9	1.8	8.5
CM4	0.282990	30	0.00149	2.4	0.03673	51	1.467167	40	1.886950	120	136.7	0.282986	7.2	1.1	10.2
CM4	0.282927	24	0.00152	1.7	0.04105	36	1.467150	36	1.887016	76	127.1	0.282923	5.0	0.8	7.7
CM4	0.282936	24	0.00161	7.5	0.04240	230	1.467145	38	1.887028	80	129.6	0.282932	5.3	0.8	8.1
CM4	0.282972	35	0.00176	7.9	0.04610	240	1.467140	46	1.886910	130	131.8	0.282968	6.6	1.2	9.4
CM4	0.282938	42	0.00298	9.3	0.07920	250	1.467067	35	1.886960	130	124.2	0.282931	5.4	1.5	7.9
CM7															
CM7	0.282972	27	0.00166	3.1	0.04460	100	1.467168	34	1.886872	96	131.2	0.282968	6.6	1.0	9.4
CM7	0.282975	35	0.00223	19.0	0.05870	520	1.467151	37	1.886890	97	127.3	0.282970	6.7	1.2	9.4
CM7	0.282926	45	0.00178	5.0	0.04610	130	1.467117	34	1.887070	150	130.9	0.282922	5.0	1.6	7.7
CM7	0.282933	28	0.00208	6.8	0.05440	180	1.467145	38	1.886909	87	133.9	0.282928	5.2	1.0	8.0
CM7	0.282947	69	0.00207	4.6	0.05900	160	1.467141	60	1.886950	230	129.5	0.282942	5.7	2.4	8.4

CM7	0.282885	38	0.00197	8.6	0.05230	230	1.467149	49	1.887030	130	128.3	0.282880	3.5	1.3	6.2
CM7	0.282938	33	0.00302	3.8	0.07850	120	1.467125	30	1.886990	110	131.1	0.282931	5.4	1.2	8.1
CM7	0.282886	46	0.00306	32.0	0.08570	930	1.467111	51	1.887140	150	129.4	0.282879	3.6	1.6	6.2
CM10															
CM10	0.282921	35	0.00135	6.6	0.03520	160	1.467120	39	1.886820	120	136.0	0.282918	4.8	1.2	7.7
CM10	0.283014	24	0.00203	5.2	0.04980	150	1.467174	30	1.886830	84	131.9	0.283009	8.1	0.8	10.9
CM10	0.282955	31	0.00170	2.3	0.04337	55	1.467125	35	1.886880	96	133.2	0.282951	6.0	1.1	8.8
CM10	0.282931	26	0.00211	6.8	0.05570	200	1.467175	30	1.886883	80	131.5	0.282926	5.2	0.9	7.9
CM10	0.283049	78	0.00111	5.8	0.02810	160	1.467181	82	1.886440	220	131.8	0.283046	9.3	2.8	12.2
CM10	0.282896	48	0.00159	6.3	0.04050	140	1.467124	37	1.886900	150	132.9	0.282892	3.9	1.7	6.7
CM10	0.282982	31	0.00138	4.2	0.03382	85	1.467134	32	1.886768	90	135.2	0.282979	7.0	1.1	9.8
CM10	0.283010	31	0.00175	5.4	0.04110	130	1.467152	32	1.886800	110	136.4	0.283006	8.0	1.1	10.8
CM17B															
CM17B	0.282911	26	0.00155	5.1	0.04230	140	1.467165	32	1.886889	84	133.2	0.282907	4.5	0.9	7.3
CM17B	0.282948	22	0.00154	2.1	0.04072	57	1.467140	20	1.886911	80	128.1	0.282944	5.8	0.8	8.5
CM17B	0.282961	35	0.00173	18.0	0.04770	580	1.467164	38	1.886880	100	132.4	0.282957	6.2	1.2	9.0
CM17B	0.282902	28	0.00194	1.2	0.05319	66	1.467138	36	1.886828	82	130.9	0.282897	4.1	1.0	6.9
CM17B	0.282954	32	0.00186	5.2	0.05240	170	1.467132	30	1.886906	99	134.4	0.282949	6.0	1.1	8.8
CM17B	0.282937	32	0.00225	11.0	0.06210	410	1.467111	50	1.886960	120	133.0	0.282931	5.4	1.1	8.1
CM17B	0.282910	37	0.00176	4.7	0.04380	150	1.467114	37	1.887030	100	130.0	0.282906	4.4	1.3	7.2
CM17B	0.282907	30	0.00162	3.2	0.04451	75	1.467142	38	1.886960	110	135.3	0.282903	4.3	1.1	7.2
CM19															
CM19	0.283039	49	0.00236	12.0	0.06290	350	1.467159	48	1.886730	170	125.5	0.283033	9.0	1.7	11.6
CM19	0.282920	75	0.00134	6.3	0.03480	150	1.467116	64	1.887000	250	135.0	0.282917	4.8	2.7	7.7
CM19	0.282879	60	0.00311	16.0	0.09010	610	1.467119	43	1.887170	190	130.1	0.282871	3.3	2.1	5.9
CM19	0.282982	65	0.00248	25.0	0.06580	750	1.467178	41	1.886870	190	133.3	0.282976	7.0	2.3	9.7
CM19	0.282998	43	0.00192	5.2	0.05020	170	1.467157	39	1.886760	120	130.2	0.282993	7.5	1.5	10.3
CM19	0.282969	40	0.00244	15.0	0.07160	480	1.467163	38	1.886900	120	126.7	0.282963	6.5	1.4	9.1
CM19	0.282945	30	0.00131	3.3	0.03575	84	1.467165	33	1.886826	95	135.2	0.282942	5.7	1.1	8.5
CM19	0.282995	60	0.00191	10.0	0.05180	300	1.467139	43	1.886810	180	130.0	0.282990	7.4	2.1	10.2

Table 3.3. Geochemistry of major, trace and rare earth elements of the Payandé, Ibagué and Mariquita plutons.

Sample	CSP3	CSP5	CI2	CI5B	CI7	CI9B	CI10	CI11A	CI13	CI15	CM2	CM4	CM6	CM7	CM8	CM10	CM11	CM13	CM14	CM17C	CM19	CM21B	CM22A
SiO ₂	67.70	67.90	67.84	64.32	63.66	57.80	57.19	61.20	61.70	58.91	71.13	71.00	70.99	75.07	73.20	73.35	73.14	72.27	71.74	70.40	73.60	68.00	68.87
Al ₂ O ₃	15.19	14.85	15.59	15.78	17.91	17.88	17.18	16.06	16.35	16.79	14.50	14.74	14.46	13.57	13.22	14.28	13.70	14.32	14.87	14.97	13.94	15.16	15.20
Fe ₂ O ₃	3.54	3.51	3.56	4.75	4.63	6.86	6.67	6.25	5.45	6.00	2.69	2.85	2.59	1.68	1.98	2.13	1.93	2.45	2.20	3.02	2.12	3.54	3.22
MgO	2.05	2.19	1.37	2.06	1.82	3.93	4.19	3.61	3.02	3.70	1.09	0.95	1.14	0.38	0.72	0.78	0.67	0.87	0.92	1.13	0.69	1.78	1.32
MnO	0.07	0.07	0.04	0.10	0.09	0.12	0.13	0.11	0.10	0.12	0.06	0.06	0.07	0.04	0.05	0.05	0.04	0.05	0.05	0.06	0.06	0.07	0.06
CaO	3.73	3.78	3.35	3.97	5.93	7.15	5.35	6.05	5.43	6.66	3.26	3.09	3.25	1.75	2.18	2.69	2.34	2.94	3.01	3.36	2.38	4.25	3.73
K ₂ O	2.37	2.69	2.31	1.93	1.32	0.84	1.08	1.97	1.83	1.38	2.19	2.19	2.07	2.87	2.97	2.26	3.02	2.25	2.41	2.12	2.22	1.77	1.87
Na ₂ O	3.85	3.63	4.14	4.68	3.68	4.04	4.31	3.92	3.81	3.60	3.82	4.34	4.00	4.28	3.59	3.94	3.67	3.98	4.10	4.11	4.14	4.15	3.83
P ₂ O ₅	0.10	0.10	0.12	0.14	0.14	0.17	0.17	0.22	0.13	0.16	0.11	0.12	0.10	0.05	0.08	0.10	0.08	0.11	0.08	0.12	0.07	0.11	0.17
TiO ₂	0.42	0.43	0.48	0.61	0.50	0.82	0.86	0.72	0.67	0.75	0.43	0.49	0.41	0.23	0.31	0.32	0.32	0.39	0.34	0.48	0.31	0.51	0.53
LOI	1.23	0.90	1.48	2.23	0.61	0.79	2.16	0.55	1.25	0.78	0.46	0.72	0.60	0.46	0.57	0.59	0.47	0.38	0.33	0.35	0.61	1.12	0.73
SUM	100.3	100.1	98.8	98.3	99.7	100.4	97.1	100.7	99.8	98.1	99.3	100.6	99.1	99.9	98.3	99.9	98.9	99.6	99.7	100.1	100.1	100.5	98.8
Ba	636.0	608.0	488.5	525.8	674.2	318.0	285.5	804.0	475.0	292.2	446.7	389.0	328.8	372.8	476.5	406.8	543.9	410.7	515.2	405.0	358.0	252.0	382.5
Ce	30.0	44.8	47.3	36.1	25.2	27.4	39.2	49.8	44.9	33.6	49.3	40.8	32.0	37.1	41.9	27.7	48.7	30.1	29.5	56.2	36.5	28.7	36.3
Ga	14.7	14.0	17.4	16.8	18.8	17.9	17.7	17.8	16.6	18.9	16.7	14.9	15.1	14.9	14.9	15.4	15.6	16.5	16.1	14.4	13.6	14.8	17.3
La	16.2	26.6	24.4	19.0	12.7	12.8	16.0	23.5	18.8	13.4	23.0	20.1	17.7	18.6	25.1	13.1	25.6	13.7	15.6	28.6	19.1	14.0	15.4
Nb	5.8	5.8	7.6	8.6	4.9	6.0	7.6	5.9	8.0	7.3	7.0	6.4	6.0	6.3	6.4	6.0	6.4	5.9	6.2	4.5	4.0	7.3	
Nd	12.5	14.5	21.9	19.6	9.9	13.8	21.9	21.7	26.1	16.7	21.8	19.0	15.9	18.9	20.3	12.4	21.5	13.3	14.4	24.9	14.5	13.1	16.1
Rb	66.4	63.0	45.3	43.6	52.3	12.2	21.7	43.7	41.0	36.0	91.0	80.2	92.0	121.5	125.6	97.1	119.9	91.3	101.5	80.5	85.2	57.5	81.9
Sr	366.3	351.5	305.6	514.4	420.5	503.6	438.8	704.0	458.0	402.4	127.4	139.7	119.2	86.7	83.5	118.2	99.0	127.9	149.8	154.1	112.3	144.7	153.5
Th	10.1	14.5	6.5	8.8	4.5	1.3	3.2	3.3	8.3	5.1	6.4	7.6	6.4	8.9	8.9	4.9	7.3	9.5	5.8	7.7	6.2	4.3	3.0
U	2.2	3.8	3.0	2.7	0.0	0.3	0.0	0.9	5.0	1.4	3.0	3.6	2.8	2.8	3.7	3.8	4.2	3.7	3.0	2.8	2.6	2.3	2.4
V	63.0	65.0	75.7	101.4	63.6	172.0	178.3	172.0	138.0	166.5	41.4	39.0	42.5	15.5	26.6	33.7	29.9	33.7	34.0	38.0	25.0	64.0	49.3
Y	13.0	11.1	18.8	23.5	12.2	17.3	29.5	18.6	31.3	24.2	30.7	31.3	26.8	32.7	30.4	24.3	22.8	26.9	23.1	24.5	22.4	24.3	25.5
Zr	114.7	108.7	166.9	202.0	134.0	112.5	182.0	182.1	151.0	130.6	178.2	225.1	190.9	151.4	143.4	163.7	146.6	183.8	134.9	189.7	154.2	144.7	231.9
Cu	2.4	1.8	5.9	3.3	6.6	23.9	36.6	63.9	52.6	27.3	7.8	8.9	8.1	1.2	4.4	7.0	7.3	3.5	3.6	8.7	2.4	8.8	4.8
Ni	14.9	13.7	2.2	7.1	4.3	10.1	11.5	10.3	7.3	13.5	3.8	2.6	8.4	1.6	3.5	2.7	4.2	4.4	3.8	3.7	1.9	4.8	5.4
Pb	2.0	2.1	4.2	2.5	5.9	0.4	4.6	1.3	2.3	6.7	10.4	3.5	8.8	10.7	13.8	12.5	13.5	11.6	11.9	1.7	2.7	2.3	8.9
Zn	23.0	26.0	17.2	37.0	71.3	22.0	79.4	37.0	32.0	72.6	61.3	46.0	53.4	32.6	48.6	51.0	46.9	51.7	51.5	47.0	38.0	35.0	66.8

Table 3.4. Whole rock Nd, Pb and Hf isotopic analyses of the Payandé, Ibagué and Mariquita plutons.

Sample	U-Pb Age (Ma)	$^{143}\text{Nd}/^{144}\text{Nd}$ (pd)	2SE	$^{143}\text{Nd}/^{144}\text{Nd}$ (i)	ϵ_{Nd} (pd)	2SE	ϵ_{Nd} (i)								
CM19	130	0.512864	0.000006	0.512750	4.6	0.12	5.6								
CM4	132	0.512800	0.000006	0.512670	3.3	0.12	4.1								
CM8	130	0.512755	0.000006	0.512641	2.4	0.11	3.5								
CI7	140	0.512600	0.000006	0.512490	-0.6	0.12	0.8								
CI9B	142	0.512795	0.000006	0.512664	3.2	0.12	4.2								
CI11A	152	0.512747	0.000006	0.512626	2.3	0.12	3.7								
CSP5	165	0.512649	0.000008	0.512532	0.4	0.15	2.2								
Sample	U-Pb Age (Ma)	$^{206}\text{Pb}/^{204}\text{Pb}$	$^{207}\text{Pb}/^{204}\text{Pb}$	$^{208}\text{Pb}/^{204}\text{Pb}$	$^{207}\text{Pb}/^{206}\text{Pb}$	$^{208}\text{Pb}/^{206}\text{Pb}$									
CM19	130	18.84	± 0.0106	15.61	± 0.0231	38.37	± 0.0360	0.828362	0.000838	2.03672	± 0.00082				
CM4	132	18.72	± 0.0106	15.61	± 0.0231	38.52	± 0.0361	0.833981	0.000837	2.05774	± 0.00082				
CM8	130	18.70	± 0.0106	15.61	± 0.0231	38.56	± 0.0361	0.834626	0.000837	2.06171	± 0.00082				
CI7	140	18.60	± 0.0106	15.62	± 0.0231	39.10	± 0.0360	0.839596	0.000838	2.10197	± 0.00082				
CI9B	142	18.50	± 0.0106	15.59	± 0.0231	38.28	± 0.0362	0.842394	0.000837	2.06895	± 0.00082				
CI11A	152	18.71	± 0.0106	15.60	± 0.0231	38.53	± 0.0361	0.833419	0.000837	2.05900	± 0.00082				
CSP5	165	18.80	± 0.0106	15.62	± 0.0231	38.55	± 0.0361	0.830961	0.000837	2.05082	± 0.00082				
Sample	U-Pb Age (Ma)	Lu (ppm)	Hf (ppm)	^{175}Lu	^{176}Hf	$^{176}\text{Lu}/^{175}\text{Lu}$	$^{176}\text{Lu}/^{177}\text{Hf}$	$^{176}\text{Yb}/^{177}\text{Hf}$	$^{176}\text{Lu}/^{177}\text{Hf}$	$^{176}\text{Hf}/^{177}\text{Hf}$	err	$\epsilon_{\text{Hf(pd)}}$	2SE	$\epsilon_{\text{Hf(i)}}$	2SE
CM19	130	0.367	4.334	1.45	1.32	0.416365	0.000001	0.000001	0.012003	0.283032	0.000004	8.75	0.14	10.61	0.14
CM4	132	0.489	5.677	1.88	1.33	0.337066	0.000002	0.000001	0.012210	0.283001	0.000004	7.65	0.15	9.52	0.15
CM8	130	0.455	4.094	3.06	1.24	0.312949	0.000058	0.000017	0.015769	0.282948	0.000005	5.76	0.16	7.29	0.16
CI7	140	0.164	2.835	0.96	1.27	0.595604	0.000005	0.000004	0.008186	0.282843	0.000004	2.07	0.16	4.42	0.16
CI9B	142	0.266	2.070	1.06	1.31	0.345096	0.000001	0.000002	0.018217	0.282968	0.000004	6.47	0.15	7.92	0.15
CI11A	152	0.256	2.074	1.84	1.20	0.272092	0.000023	0.000020	0.017500	0.282955	0.000004	6.01	0.16	7.63	0.16
CSP5	165	0.195	2.997	0.80	1.39	0.586801	0.000071	0.000011	0.009248	0.282820	0.000004	1.24	0.13	3.90	0.13

Table 4.1. Whole rock geochemistry and Sr, Nd and Pb isotopes from the Hatillo and El Bosque plutons.

	CH2	CH6A	CH9	CH12	CH14	CH15	CH10	CH8	CH19	CH20	CH21B	CH5	CB1	CB2
SiO ₂	66.39	65.85	66.28	65.83	65.85	65.94	65.80	65.31	67.20	67.20	67.20	65.30	68.50	67.96
TiO ₂	0.54	0.54	0.54	0.54	0.52	0.50	0.50	0.580	0.52	0.49	0.44	0.57	0.42	0.44
Al ₂ O ₃	16.63	17.10	16.75	16.92	16.77	16.69	16.61	17.29	16.80	16.63	15.93	16.86	16.48	16.47
FeOt	3.47	3.50	3.53	3.47	3.47	3.26	3.42	3.66	3.10	3.06	2.90	3.54	2.41	2.49
MnO	0.07	0.07	0.07	0.07	0.07	0.06	0.07	0.077	0.06	0.06	0.06	0.07	0.05	0.05
MgO	1.95	2.01	2.02	1.93	1.93	1.81	2.09	2.09	1.76	2.01	1.94	2.21	1.10	0.99
CaO	4.48	4.72	4.60	4.88	4.68	4.52	4.89	4.87	4.34	4.46	3.99	4.98	3.52	2.98
Na ₂ O	4.01	4.17	3.88	4.05	3.98	4.09	4.01	4.18	4.20	4.28	4.23	4.05	3.38	3.32
K ₂ O	1.54	1.39	1.67	1.48	1.53	1.56	1.46	1.77	1.74	1.60	1.72	1.52	2.53	2.20
P ₂ O ₅	0.18	0.17	0.17	0.19	0.18	0.17	0.16	0.181	0.18	0.15	0.14	0.19	0.14	0.14
Sum	99.2	99.5	99.5	99.4	99.0	98.6	99.0	100.0	100.9	101.0	100.0	100.4	100.2	97.0
LOI	1.38	0.77	0.65	0.56	0.72	0.68	0.38	0.53	0.62	0.66	1.05	0.61	1.30	1.98
La	27.55	19.40	19.17	21.95	20.24	24.27	22.59	16.95	25.30	16.90	22.40	19.50	40.80	25.62
Ce	52.07	38.30	38.40	43.25	40.25	47.25	43.22	34.23	50.40	32.60	45.20	38.50	71.60	46.40
Pr	6.52	4.85	4.76	5.43	5.11	5.72	5.20	4.46	5.70	4.08	5.23	4.83	8.67	5.82
Nd	25.00	18.96	18.74	21.01	20.32	22.03	19.37	18.48	21.70	19.60	20.20	16.40	31.40	21.36
Sm	4.86	3.83	4.04	4.19	4.29	4.09	3.66	4.18	4.12	3.35	4.07	3.55	5.46	4.19
Eu	1.38	1.16	1.16	1.22	1.27	1.19	1.08	1.25	1.07	0.93	0.98	1.08	1.22	1.16
Gd	4.00	3.18	3.36	3.59	3.53	3.25	2.96	3.56	3.31	2.72	3.39	3.06	4.45	3.24
Tb	0.60	0.46	0.50	0.52	0.54	0.49	0.43	0.53	0.40	0.37	0.50	0.44	0.61	0.45
Dy	3.38	2.59	2.80	2.86	3.11	2.71	2.38	3.02	2.27	2.05	2.69	2.87	2.52	2.10
Ho	0.64	0.49	0.52	0.54	0.60	0.51	0.45	0.57	0.40	0.39	0.57	0.48	0.44	0.34
Er	1.61	1.27	1.39	1.41	1.54	1.37	1.14	1.50	1.00	1.01	1.49	1.27	1.13	0.81
Tm	0.23	0.18	0.20	0.20	0.22	0.20	0.17	0.22	0.13	0.16	0.21	0.18	0.12	0.10
Yb	1.44	1.16	1.23	1.25	1.39	1.27	1.05	1.35	0.86	0.88	1.47	1.22	0.97	0.65
Lu	0.22	0.18	0.19	0.20	0.21	0.20	0.17	0.21	0.14	0.14	0.20	0.19	0.14	0.10
Ba	710.82	631.62	745.41	682.92	813.50	766.04	683.10	758	833.00	720.00	696.00	768.00	1004.00	893.95
Th	6.12	4.25	4.83	5.20	5.24	7.17	4.56	4.87	5.40	3.60	7.50	4.20	11.20	7.51
Nb	5.31	4.80	5.24	5.12	5.12	5.01	4.41	6.97	4.90	4.10	5.80	4.20	7.60	6.48
Y	16.62	12.89	14.00	14.40	14.75	13.45	11.47	15.40	11.70	10.70	14.70	13.20	13.30	9.03
Hf	3.65	3.44	3.13	3.39	3.72	3.71	3.30	3.71	3.00	3.20	2.80	3.40	3.90	3.67
Ta	0.51	0.34	0.41	0.40	0.53	0.49	0.42	0.56	0.30	0.30	0.40	0.30	0.70	0.56
U	1.98	1.51	2.36	2.75	2.65	2.26	1.45	2.10	2.50	1.60	2.00	1.80	1.60	2.66
Pb	8.93	8.38	8.85	9.32	9.63	8.13	7.26	9.47	25.20	0.60	0.60	0.60	1.80	14.64
Rb	44.24	38.46	59.84	42.89	46.85	43.08	38.13	49.2	48.60	47.00	43.40	38.00	86.60	92.77
Cs	2.10	1.89	2.68	1.81	2.57	1.84	1.77	2.30	2.30	1.60	3.10	2.00	5.00	9.13

Sr	570.9	576.1	551.4	600.2	566.5	558.0	551.1	579.3	647.9	589.9	568.8	625.6	377.3	304.6
Sc	9.50	9.77	9.86	9.93	9.42	9.24	9.94	10.3						5.26
Zr	134.54	130.81	115.89	126.89	134.22	131.86	119.64	137	130.30	116.70	102.20	138.30	131.70	134.37
Sm (ppm)			3.64				3.02				3.61	3.66	5.06	
Nd (ppm)			18.36				15.74				17.41	18.34	27.74	
$^{147}\text{Sm}/^{144}\text{Nd}$			0.1199				0.1161				0.1254	0.1205	0.1104	
$^{143}\text{Nd}/^{144}\text{Nd}$ (pd)			0.512657				0.512653				0.512694	0.512646	0.512497	
2SE			0.000006				0.000006				0.000010	0.000006	0.000007	
$^{143}\text{Nd}/^{144}\text{Nd}$ (i)			0.512614				0.512612				0.512648	0.512604	0.512455	
$\epsilon_{\text{Nd(pd)}}$			0.52				0.46				1.25	0.32	-2.60	
2SE			0.13				0.11				0.19	0.11	0.13	
$\epsilon_{\text{Nd(i)}}$			1.06				1.01				1.76	0.84	-1.98	
$^{206}\text{Pb}/^{204}\text{Pb}$			18.9776				18.8140				18.8441	18.8588	18.7637	
			0.0107				0.0106				0.0106	0.0107	0.0106	
$^{207}\text{Pb}/^{204}\text{Pb}$			15.6330				15.6278				15.6305	15.6255	15.5753	
			0.0233				0.0231				0.0232	0.0231	0.0231	
$^{208}\text{Pb}/^{204}\text{Pb}$			38.8149				38.7343				38.7646	38.7616	38.6555	
			0.0362				0.0363				0.0361	0.0362	0.0361	
$^{207}\text{Pb}/^{206}\text{Pb}$			0.8238				0.8307				0.8295	0.8286	0.8301	
			0.0008				0.0008				0.0008	0.0008	0.0008	
$^{208}\text{Pb}/^{206}\text{Pb}$			2.0453				2.0588				2.0571	2.0554	2.0601	
			0.0008				0.0008				0.0008	0.0008	0.0008	
$^{87}\text{Sr}/^{86}\text{Sr}$			0.7047				0.7047				0.7031	0.7048	0.7062	

Table 4.2. Zircon U-Pb geochronology results.

Ssample name	U ppm	Th U	$^{238}\text{U}/^{206}\text{Pb}$	1 sigma % error	$^{207}\text{Pb}/^{206}\text{Pb}$	1 sigma % error	$^{206}\text{Pb}/^{238}\text{U}$ age	1 sigma abs err	$^{207}\text{Pb}/^{206}\text{Pb}$ age	1 sigma abs err	Best age	1 sigma abs err Ma
Hatillo Stock												
CH8_53	639	0.52	116.7887	1.16	0.0476	1.79	55.0	0.6	78.0	41.9	55.0	0.6
CH8_52	284	0.30	117.3998	1.50	0.0522	2.53	54.7	0.8	293.4	56.8	54.7	0.8
CH8_51	593	0.43	116.4599	1.21	0.0482	1.87	55.1	0.7	110.1	43.6	55.1	0.7
CH8_50	618	0.34	122.8578	1.91	0.0515	2.44	52.3	1.0	262.0	55.1	52.3	1.0
CH8_49	375	0.32	117.6800	1.27	0.0482	2.31	54.5	0.7	107.1	53.8	54.5	0.7
CH8_48	330	0.54	117.0847	1.38	0.0504	2.34	54.8	0.8	212.1	53.3	54.8	0.8
CH8_47	282	0.46	115.1027	1.56	0.0445	2.99	55.8	0.9	0.0	0.0	55.8	0.9
CH8_46	533	0.27	122.6024	1.57	0.0519	1.72	52.4	0.8	279.6	38.9	52.4	0.8
CH8_45	279	0.35	117.2890	1.55	0.0471	3.21	54.7	0.8	52.5	74.9	54.7	0.8
CH8_44	629	0.36	116.0551	1.21	0.0482	1.65	55.3	0.7	110.7	38.4	55.3	0.7
CH8_43	255	0.33	111.7879	2.21	0.0513	4.47	57.4	1.3	255.5	99.6	57.4	1.3
CH8_42	768	0.44	118.6470	1.26	0.0479	1.60	54.1	0.7	93.5	37.4	54.1	0.7
CH8_41	440	0.36	114.0809	1.51	0.0474	2.30	56.3	0.8	69.2	53.8	56.3	0.8
CH8_40	383	0.51	114.1143	3.03	0.0538	4.77	56.2	1.7	363.4	104.1	56.2	1.7
CH8_39	481	0.52	118.7859	1.63	0.0473	2.14	54.0	0.9	66.6	50.2	54.0	0.9
CH8_38	600	0.28	117.6285	1.75	0.0456	2.66	54.6	1.0	0.0	41.6	54.6	1.0
CH8_37	595	0.44	120.7981	1.51	0.0463	1.60	53.1	0.8	15.1	37.9	53.1	0.8
CH8_36	282	0.34	119.5697	1.67	0.0482	2.65	53.7	0.9	108.6	61.4	53.7	0.9
CH8_35	279	0.33	115.7864	2.45	0.0630	3.24	55.4	1.4	708.2	67.4	55.4	1.4
CH8_34	383	0.64	109.8967	1.75	0.0575	2.41	58.4	1.0	509.0	52.2	58.4	1.0
CH8_33	277	0.61	111.1176	1.61	0.0471	2.77	57.8	0.9	53.3	64.7	57.8	0.9
CH8_32	565	0.15	88.9423	1.98	0.0499	1.33	72.1	1.4	190.1	30.6	72.1	1.4
CH8_31	317	0.31	118.8815	1.81	0.0499	3.73	54.0	1.0	188.3	84.6	54.0	1.0
CH8_30	434	0.49	117.2787	1.50	0.0456	2.00	54.7	0.8	0.0	24.4	54.7	0.8
CH8_29	218	0.26	113.2228	1.79	0.0526	2.86	56.7	1.0	312.9	63.9	56.7	1.0
CH8_28	348	0.32	117.0160	1.57	0.0480	2.23	54.9	0.9	97.6	51.9	54.9	0.9
CH8_27	553	0.35	120.4603	1.58	0.0478	1.80	53.3	0.8	91.2	42.2	53.3	0.8

CH8_26	197	0.21	117.0872	2.02	0.0452	3.13	54.8	1.1	0.0	28.1	54.8	1.1
CH8_25	419	0.94	43.6835	3.34	0.0591	1.75	145.9	4.8	569.5	37.6	145.9	4.8
CH8_24	404	0.43	119.1525	1.61	0.0490	2.39	53.9	0.9	146.7	55.0	53.9	0.9
CH8_23	260	0.47	123.7672	1.74	0.0461	2.83	51.9	0.9	3.4	66.4	51.9	0.9
CH8_22	578	0.30	108.1112	1.42	0.0490	1.80	59.4	0.8	146.4	41.7	59.4	0.8
CH8_21	342	0.55	113.5549	1.43	0.0576	2.37	56.5	0.8	515.3	51.2	56.5	0.8
CH8_20	813	0.26	82.5385	1.53	0.0502	1.49	77.6	1.2	205.9	34.2	77.6	1.2
CH8_19	178	0.33	117.0288	1.95	0.0493	3.16	54.8	1.1	161.0	72.4	54.8	1.1
CH8_18	241	0.33	117.2350	1.77	0.0444	2.93	54.8	1.0	0.0	0.0	54.8	1.0
CH8_17	505	0.33	120.0569	1.48	0.0470	2.14	53.5	0.8	48.9	50.4	53.5	0.8
CH8_16	226	0.42	129.2107	1.93	0.1453	4.01	49.7	1.0	2291.8	67.3	2291.8	67.3
CH8_15	570	0.37	114.4461	1.56	0.0607	1.92	56.1	0.9	627.0	40.8	56.1	0.9
CH8_14	511	0.38	122.3922	1.67	0.0461	1.97	52.5	0.9	0.0	48.8	52.5	0.9
CH8_13	282	0.36	116.6422	1.84	0.0509	2.53	55.0	1.0	234.8	57.4	55.0	1.0
CH8_12	688	0.47	117.4675	1.52	0.0482	1.86	54.6	0.8	108.7	43.4	54.6	0.8
CH8_11	295	0.19	117.2547	1.56	0.0471	2.89	54.7	0.9	52.4	67.6	54.7	0.9
CH8_10	380	0.44	117.0869	1.56	0.0475	2.40	54.8	0.8	75.8	56.0	54.8	0.8
CH8_9	554	0.34	119.7902	1.48	0.0480	1.98	53.6	0.8	101.0	46.2	53.6	0.8
CH8_8	366	0.34	118.0387	1.50	0.0474	2.48	54.4	0.8	71.5	58.0	54.4	0.8
CH8_7	624	0.46	117.9444	1.38	0.0499	2.02	54.4	0.7	192.4	46.4	54.4	0.7
CH8_6	651	0.80	121.8317	1.43	0.0462	1.97	52.7	0.8	1.1	53.4	52.7	0.8
CH8_5	479	0.31	117.0096	1.44	0.0452	2.21	54.9	0.8	0.0	5.4	54.9	0.8
CH8_4	384	0.35	116.5082	1.56	0.0483	2.27	55.1	0.9	112.7	52.6	55.1	0.9
CH8_3	486	0.45	115.8109	1.55	0.0480	2.20	55.4	0.9	99.3	51.2	55.4	0.9
CH8_2	249	0.31	119.1978	1.76	0.0459	2.90	53.9	0.9	0.0	63.2	53.9	0.9
CH8_1	329	0.41	121.0468	1.70	0.0451	2.69	53.0	0.9	0.0	15.4	53.0	0.9
CH19_35	404	0.49	123.5497	1.87	0.0471	1.95	52.0	1.0	54.8	45.9	52.0	1.0
CH19_34	336	0.37	111.0124	2.11	0.0687	2.39	57.8	1.2	890.6	48.6	57.8	1.2
CH19_33	641	0.53	118.7256	1.61	0.0479	1.63	54.1	0.9	94.3	38.1	54.1	0.9
CH19_32	903	0.32	118.1972	2.80	0.0473	2.65	54.3	1.5	62.4	62.0	54.3	1.5
CH19_31	643	0.58	124.4643	1.65	0.0488	1.77	51.6	0.8	137.9	41.1	51.6	0.8

CH19_30	208	0.27	90.9240	3.76	0.1521	4.83	70.5	2.6	2369.4	80.1	2369.4	80.1
CH19_29	434	0.49	120.2912	2.40	0.0511	2.70	53.4	1.3	244.1	61.0	53.4	1.3
CH19_28	488	0.37	125.2725	1.98	0.0446	2.01	51.3	1.0	0.0	0.0	51.3	1.0
CH19_27	650	0.46	114.5198	2.14	0.0472	1.59	56.0	1.2	61.8	37.4	56.0	1.2
CH19_26	817	0.53	112.7937	2.12	0.0472	1.49	56.9	1.2	61.3	35.2	56.9	1.2
CH19_25	314	0.41	109.0934	2.53	0.0452	4.18	58.8	1.5	0.0	53.7	58.8	1.5
CH19_23	641	0.43	114.9741	2.14	0.0480	1.86	55.8	1.2	98.4	43.4	55.8	1.2
CH19_22	607	0.31	128.1354	2.79	0.0449	2.34	50.1	1.4	0.0	0.0	50.1	1.4
CH19_21	560	0.44	106.8251	1.99	0.1000	2.58	60.1	1.2	1624.5	47.1	60.1	1.2
CH19_20	966	0.46	115.8011	1.59	0.0466	1.36	55.4	0.9	27.8	32.3	55.4	0.9
CH19_19	408	0.39	102.0586	1.78	0.0999	2.95	62.9	1.1	1621.4	54.0	62.9	1.1
CH19_18	638	0.38	117.0428	1.61	0.0451	1.66	54.8	0.9	0.0	0.0	54.8	0.9
CH19_17	596	0.42	115.4847	1.60	0.0471	1.67	55.6	0.9	54.8	39.3	55.6	0.9
CH19_16	548	0.40	111.5450	1.61	0.0461	1.75	57.5	0.9	0.0	45.2	57.5	0.9
CH19_15	531	0.47	115.6318	1.63	0.0486	1.91	55.5	0.9	127.0	44.3	55.5	0.9
CH19_14	1334	1.43	117.4698	1.53	0.0473	1.16	54.6	0.8	65.4	27.3	54.6	0.8
CH19_13	555	0.42	118.1211	2.51	0.0433	4.63	54.3	1.4	0.0	0.0	54.3	1.4
CH19_12	762	0.56	111.7852	1.27	0.0499	1.62	57.4	0.7	192.2	37.2	57.4	0.7
CH19_10	803	0.29	128.3049	1.98	0.0555	1.22	50.0	1.0	431.8	26.9	50.0	1.0
CH19_9	515	0.54	114.3863	1.48	0.0475	1.90	56.1	0.8	75.6	44.6	56.1	0.8
CH19_8	641	0.37	117.1635	1.46	0.0468	1.67	54.8	0.8	36.8	39.5	54.8	0.8
CH19_7	398	0.50	118.1455	1.67	0.0483	2.28	54.3	0.9	114.8	53.0	54.3	0.9
CH19_6	589	0.42	112.5541	2.08	0.0472	1.80	57.0	1.2	60.7	42.3	57.0	1.2
CH19_4	539	0.34	116.0968	2.60	0.0467	3.44	55.3	1.4	32.8	80.3	55.3	1.4
CH19_3	688	0.41	114.4027	2.04	0.0474	1.66	56.1	1.1	68.9	39.0	56.1	1.1
CH19_2	1002	0.50	117.5739	2.02	0.0480	1.54	54.6	1.1	97.9	36.1	54.6	1.1
CH19_1	543	0.37	116.6847	2.04	0.0469	1.99	55.0	1.1	46.1	46.8	55.0	1.1
CH5_26	429	0.28	118.5998	2.34	0.0479	2.11	54.1	1.3	94.8	49.2	54.1	1.3
CH5_25	710	0.39	119.1388	2.40	0.0458	1.60	53.9	1.3	0.0	24.3	53.9	1.3
CH5_24	543	0.44	123.6454	2.62	0.0468	1.92	51.9	1.4	37.6	45.2	51.9	1.4
CH5_23	673	0.35	119.3373	2.42	0.0490	1.71	53.8	1.3	149.9	39.5	53.8	1.3

CH5_22	420	0.33	118.2779	2.32	0.0467	2.11	54.3	1.3	32.0	49.9	54.3	1.3
CH5_21	546	0.41	117.7984	2.26	0.0450	1.78	54.5	1.2	0.0	0.0	54.5	1.2
CH5_20	970	0.42	120.1819	1.48	0.0454	1.32	53.4	0.8	0.0	0.5	53.4	0.8
CH5_19	830	0.46	120.7208	1.49	0.0472	1.45	53.2	0.8	58.6	34.2	53.2	0.8
CH5_18	559	0.40	119.4792	1.52	0.0477	2.52	53.7	0.8	83.4	58.8	53.7	0.8
CH5_17	367	0.35	121.3569	1.31	0.0478	2.36	52.9	0.7	90.8	54.9	52.9	0.7
CH5_16	426	0.28	119.3378	1.78	0.0448	2.18	53.8	1.0	0.0	0.0	53.8	1.0
CH5_15	757	0.19	120.5872	2.23	0.0497	1.64	53.2	1.2	181.5	37.7	53.2	1.2
CH5_14	453	0.31	119.8515	1.53	0.0474	2.02	53.6	0.8	68.4	47.5	53.6	0.8
CH5_13	332	0.33	121.4643	1.53	0.0452	2.32	52.9	0.8	0.0	7.8	52.9	0.8
CH5_12	453	0.29	123.1242	1.63	0.0451	2.03	52.1	0.8	0.0	0.0	52.1	0.8
CH5_11	635	0.35	118.1343	1.29	0.0478	1.85	54.3	0.7	89.6	43.2	54.3	0.7
CH5_10	689	0.43	117.7050	1.59	0.0465	1.69	54.5	0.9	24.8	40.2	54.5	0.9
CH5_9	638	0.37	118.4383	1.26	0.0479	1.75	54.2	0.7	93.7	40.9	54.2	0.7
CH5_8	487	0.33	119.6996	1.88	0.0603	2.33	53.6	1.0	615.2	49.5	53.6	1.0
CH5_7	362	0.36	121.9317	1.45	0.0460	2.34	52.7	0.8	0.0	53.9	52.7	0.8
CH5_6	397	0.41	122.7623	2.14	0.0445	2.95	52.3	1.1	0.0	0.0	52.3	1.1
CH5_5	611	0.39	116.9712	1.17	0.0464	1.85	54.9	0.6	20.3	43.7	54.9	0.6
CH5_4	522	0.42	117.6472	1.15	0.0478	1.89	54.6	0.6	89.7	44.1	54.6	0.6
CH5_3	519	0.29	117.8210	1.22	0.0485	1.85	54.5	0.7	124.0	43.0	54.5	0.7
CH5_2	633	0.29	119.2765	1.20	0.0477	1.78	53.8	0.6	86.0	41.7	53.8	0.6
CH5_1	419	0.35	118.2616	1.37	0.0457	2.43	54.3	0.7	0.0	37.9	54.3	0.7
CH20_59	470	0.46	121.7720	1.07	0.0472	2.53	52.7	0.6	59.6	59.2	52.7	0.6
CH20_58	440	0.31	117.9028	1.11	0.0481	2.55	54.4	0.6	105.1	59.3	54.4	0.6
CH20_57	683	0.32	117.2195	0.95	0.0458	2.21	54.8	0.5	1.7	39.2	54.8	0.5
CH20_56	707	0.12	116.2659	0.96	0.0484	2.12	55.2	0.5	119.3	49.3	55.2	0.5
CH20_55	503	0.39	115.7745	1.12	0.0443	2.36	55.4	0.6	0.0	0.0	55.4	0.6
CH20_54	454	0.32	119.5344	1.06	0.0484	2.59	53.7	0.6	118.0	59.9	53.7	0.6
CH20_53	442	0.37	117.4617	1.23	0.0471	2.67	54.6	0.7	52.0	62.3	54.6	0.7
CH20_52	630	0.30	120.2849	0.99	0.0448	2.40	53.4	0.5	0.0	0.0	53.4	0.5
CH20_51	358	0.41	115.9385	1.16	0.0752	3.11	55.4	0.6	1074.8	61.3	55.4	0.6

CH20_50	1686	0.02	112.6869	0.89	0.0468	1.86	57.0	0.5	39.3	43.3	57.0	0.5
CH20_49	568	0.29	120.5321	1.03	0.0462	2.26	53.3	0.5	12.3	49.1	53.3	0.5
CH20_48	840	0.27	112.9796	0.91	0.0460	2.10	56.8	0.5	6.5	42.1	56.8	0.5
CH20_47	969	0.66	119.2160	1.01	0.0485	2.42	53.8	0.5	123.9	56.1	53.8	0.5
CH20_46	895	0.52	114.5063	0.88	0.0474	1.27	56.1	0.5	70.6	30.0	56.1	0.5
CH20_45	356	0.38	113.0473	1.22	0.0472	2.19	56.8	0.7	57.6	51.4	56.8	0.7
CH20_44	634	0.40	117.0914	1.09	0.0477	1.58	54.8	0.6	85.3	37.1	54.8	0.6
CH20_43	524	0.39	116.1139	0.95	0.0485	1.76	55.3	0.5	124.1	40.9	55.3	0.5
CH20_42	605	0.35	112.3550	1.03	0.0492	1.56	57.1	0.6	158.8	36.0	57.1	0.6
CH20_41	631	0.38	109.2411	1.51	0.0518	2.15	58.7	0.9	276.2	48.4	58.7	0.9
CH20_40	656	0.35	121.1067	1.05	0.0470	1.52	53.0	0.6	47.8	35.8	53.0	0.6
CH20_39	663	0.52	116.6390	0.86	0.0463	1.71	55.0	0.5	17.6	38.8	55.0	0.5
CH20_38	1055	0.78	116.5167	0.77	0.0456	1.34	55.1	0.4	0.0	10.2	55.1	0.4
CH20_37	746	0.37	117.7309	0.97	0.0478	1.58	54.5	0.5	89.0	36.9	54.5	0.5
CH20_36	472	0.40	114.4093	1.09	0.0491	1.75	56.1	0.6	151.7	40.4	56.1	0.6
CH20_35	907	0.56	116.5040	0.85	0.0465	1.28	55.1	0.5	23.3	29.5	55.1	0.5
CH20_34	543	0.40	113.5858	1.05	0.0514	1.73	56.5	0.6	258.9	39.3	56.5	0.6
CH20_33	1014	0.53	115.6806	0.84	0.0465	1.29	55.5	0.5	25.9	29.9	55.5	0.5
CH20_32	517	0.34	115.6263	1.38	0.0472	2.59	55.5	0.8	58.7	60.7	55.5	0.8
CH20_31	384	0.44	119.9059	1.32	0.0508	2.13	53.5	0.7	233.9	48.4	53.5	0.7
CH20_30	906	0.58	117.8432	1.02	0.0468	1.46	54.5	0.6	37.3	35.1	54.5	0.6
CH20_29	761	0.46	117.4885	1.03	0.0480	1.68	54.6	0.6	97.7	39.3	54.6	0.6
CH20_28	504	0.40	114.1921	1.17	0.0470	2.04	56.2	0.7	50.7	48.0	56.2	0.7
CH20_27	593	0.41	122.4846	1.27	0.0477	1.67	52.4	0.7	84.4	39.1	52.4	0.7
CH20_26	376	0.30	117.3802	1.19	0.0467	2.26	54.7	0.6	31.6	53.9	54.7	0.6
CH20_25	419	0.50	111.7609	1.24	0.0507	2.29	57.4	0.7	226.7	52.0	57.4	0.7
CH20_24	516	0.39	123.1354	1.54	0.0481	2.96	52.1	0.8	103.6	68.5	52.1	0.8
CH20_23	758	0.39	112.5658	1.07	0.0471	1.43	57.0	0.6	56.7	33.8	57.0	0.6
CH20_22	725	0.47	119.9760	1.10	0.0473	1.45	53.5	0.6	64.3	34.3	53.5	0.6
CH20_21	870	0.47	118.4597	1.27	0.0495	1.79	54.2	0.7	171.9	41.3	54.2	0.7
CH20_20	704	0.32	119.3396	2.01	0.0523	3.21	53.8	1.1	298.7	71.7	53.8	1.1
CH20_19	970	0.20	106.3910	1.64	0.0495	2.68	60.3	1.0	170.4	61.4	60.3	1.0

CH20_18	851	0.41	116.5628	1.11	0.0460	1.45	55.1	0.6	0.0	28.9	55.1	0.6
CH20_17	703	0.40	118.2311	1.06	0.0462	1.65	54.3	0.6	0.0	45.5	54.3	0.6
CH20_16	547	0.38	118.5687	1.07	0.0475	1.74	54.1	0.6	74.8	41.0	54.1	0.6
CH20_15	514	0.31	114.8243	1.13	0.0467	1.98	55.9	0.6	28.0	52.4	55.9	0.6
CH20_14	432	0.37	118.0405	1.23	0.0444	2.09	54.4	0.7	0.0	0.0	54.4	0.7
CH20_13	856	0.38	110.3357	1.01	0.0539	1.62	58.2	0.6	367.9	36.1	58.2	0.6
CH20_12	568	0.39	118.9510	1.42	0.0476	2.44	54.0	0.8	80.8	56.9	54.0	0.8
CH20_11	585	0.45	110.5514	1.27	0.0540	2.23	58.0	0.7	370.0	49.5	58.0	0.7
CH20_10	522	0.35	119.7113	1.22	0.0575	2.59	53.6	0.6	509.8	56.0	53.6	0.6
CH20_9	399	0.47	120.4389	1.45	0.0448	2.27	53.3	0.8	0.0	0.0	53.3	0.8
CH20_8	254	0.43	118.4004	1.45	0.0663	2.99	54.2	0.8	814.6	61.3	54.2	0.8
CH20_7	353	0.34	114.9395	1.28	0.0469	2.48	55.8	0.7	42.2	58.2	55.8	0.7
CH20_6	361	0.37	114.4565	1.24	0.0470	2.19	56.1	0.7	50.8	51.5	56.1	0.7
CH20_5	886	0.43	122.7491	1.05	0.0491	1.53	52.3	0.5	152.2	35.5	52.3	0.5
CH20_4	605	0.54	119.2683	1.17	0.0512	1.65	53.8	0.6	252.0	37.6	53.8	0.6
CH20_3	519	0.50	118.2828	1.18	0.0512	1.73	54.3	0.6	249.5	39.4	54.3	0.6
CH20_2	732	0.65	118.8927	1.14	0.0458	1.58	54.0	0.6	0.0	27.5	54.0	0.6
CH20_1	565	0.45	114.7077	1.20	0.0464	1.89	56.0	0.7	17.7	43.4	56.0	0.7
CH21B_58	569	0.35	110.5036	1.59	0.0512	2.90	58.1	0.9	250.7	65.4	58.1	0.9
CH21B_57	611	0.30	118.5465	1.10	0.0466	2.00	54.2	0.6	30.4	46.6	54.2	0.6
CH21B_56	450	0.37	110.0967	1.16	0.0668	2.00	58.3	0.7	832.1	41.2	58.3	0.7
CH21B_55	738	0.57	107.9856	0.93	0.0595	1.56	59.4	0.6	583.7	33.4	59.4	0.6
CH21B_54	890	0.77	117.2460	0.99	0.0470	1.52	54.7	0.5	47.9	35.7	54.7	0.5
CH21B_53	456	0.58	112.7132	1.04	0.0494	1.97	56.9	0.6	166.7	45.4	56.9	0.6
CH21B_52	867	0.67	112.3715	1.00	0.0495	1.55	57.1	0.6	169.7	35.8	57.1	0.6
CH21B_51	709	0.40	101.7259	1.02	0.0464	1.65	63.1	0.6	20.5	37.7	63.1	0.6
CH21B_50	1050	1.23	114.8644	1.12	0.0560	1.88	55.9	0.6	452.3	41.3	55.9	0.6
CH21B_49	572	0.39	118.5879	1.71	0.0612	3.49	54.1	0.9	647.3	73.3	54.1	0.9
CH21B_48	701	0.55	116.9080	1.08	0.0476	1.60	54.9	0.6	80.8	37.5	54.9	0.6
CH21B_47	518	0.41	116.2740	1.18	0.0455	1.85	55.2	0.6	0.0	17.2	55.2	0.6
CH21B_46	630	0.32	117.7114	1.01	0.0469	1.79	54.5	0.5	46.6	42.0	54.5	0.5

CH21B_45	598	0.45	116.8899	1.09	0.0467	1.81	54.9	0.6	34.1	42.2	54.9	0.6
CH21B_44	762	0.38	127.5047	1.73	0.0484	2.63	50.4	0.9	119.9	60.8	50.4	0.9
CH21B_43	476	0.46	116.2572	1.24	0.0483	2.07	55.2	0.7	112.4	48.1	55.2	0.7
CH21B_42	1285	0.40	128.0855	1.02	0.0481	1.32	50.1	0.5	103.9	30.9	50.1	0.5
CH21B_41	508	0.38	115.0152	1.17	0.0489	1.79	55.8	0.6	141.9	41.5	55.8	0.6
CH21B_40	483	0.77	121.3087	1.29	0.0455	2.32	52.9	0.7	0.0	29.0	52.9	0.7
CH21B_39	468	0.39	112.2577	1.18	0.0473	2.01	57.2	0.7	64.7	47.2	57.2	0.7
CH21B_38	519	0.53	121.6586	1.19	0.0486	2.07	52.8	0.6	128.0	48.0	52.8	0.6
CH21B_37	878	0.43	118.2187	1.08	0.0465	1.64	54.3	0.6	26.2	38.1	54.3	0.6
CH21B_36	645	0.34	116.3561	1.09	0.0479	1.66	55.2	0.6	94.4	38.7	55.2	0.6
CH21B_35	348	0.44	120.1570	1.61	0.0531	2.87	53.4	0.9	334.4	63.8	53.4	0.9
CH21B_34	634	0.54	115.0497	1.00	0.0505	1.95	55.8	0.6	218.6	44.5	55.8	0.6
CH21B_33	284	0.38	127.6559	2.29	0.0967	4.69	50.3	1.1	1560.8	85.5	50.3	1.1
CH21B_32	586	0.93	114.9558	1.31	0.0500	1.68	55.8	0.7	194.6	38.7	55.8	0.7
CH21B_31	609	0.43	112.7245	1.22	0.0469	1.76	56.9	0.7	42.1	41.4	56.9	0.7
CH21B_30	658	0.49	116.1230	1.19	0.0481	1.55	55.3	0.7	105.3	36.2	55.3	0.7
CH21B_29	2098	0.40	113.9008	1.29	0.0475	1.39	56.3	0.7	72.1	32.7	56.3	0.7
CH21B_28	279	0.28	121.8820	1.52	0.0507	3.41	52.7	0.8	228.7	76.8	52.7	0.8
CH21B_27	521	0.34	117.0228	1.25	0.0675	2.06	54.9	0.7	852.3	42.3	54.9	0.7
CH21B_26	542	0.45	111.9209	1.23	0.0478	1.93	57.3	0.7	87.8	45.0	57.3	0.7
CH21B_25	839	0.51	116.4525	1.15	0.0471	1.61	55.1	0.6	52.7	37.9	55.1	0.6
CH21B_24	318	0.38	124.3521	2.00	0.0508	3.52	51.6	1.0	232.1	79.2	51.6	1.0
CH21B_23	1498	0.38	115.0808	1.45	0.0480	1.56	55.8	0.8	99.1	36.5	55.8	0.8
CH21B_22	463	0.51	119.4276	1.76	0.0452	2.01	53.8	0.9	0.0	2.7	53.8	0.9
CH21B_21	526	0.42	112.9143	1.42	0.0475	1.87	56.8	0.8	75.2	43.8	56.8	0.8
CH21B_20	1864	0.24	82.4515	1.34	0.0485	1.13	77.7	1.0	123.5	26.4	77.7	1.0
CH21B_19	527	0.36	120.6280	1.43	0.0473	1.87	53.2	0.8	62.6	43.9	53.2	0.8
CH21B_18	1330	0.40	101.6564	1.42	0.0470	1.33	63.1	0.9	51.4	31.5	63.1	0.9
CH21B_17	521	0.39	118.9768	1.52	0.0470	2.00	54.0	0.8	48.4	47.2	54.0	0.8
CH21B_16	514	0.47	116.5607	1.40	0.0491	1.93	55.1	0.8	154.0	44.6	55.1	0.8
CH21B_15	662	0.47	122.5278	1.35	0.0460	1.80	52.4	0.7	0.0	42.0	52.4	0.7
CH21B_14	577	0.43	109.1142	1.39	0.0483	1.78	58.8	0.8	114.9	41.4	58.8	0.8

CH21B_13	513	0.48	117.5736	1.46	0.0484	1.91	54.6	0.8	117.5	44.5	54.6	0.8
CH21B_12	821	0.38	123.6892	1.34	0.0479	1.59	51.9	0.7	94.5	37.2	51.9	0.7
CH21B_11	868	0.61	114.2735	1.49	0.0517	1.58	56.2	0.8	274.1	35.8	56.2	0.8
CH21B_10	544	0.34	111.9777	1.11	0.0492	1.96	57.3	0.6	155.8	45.2	57.3	0.6
CH21B_9	302	0.43	118.0706	1.31	0.0456	2.30	54.4	0.7	0.0	31.5	54.4	0.7
CH21B_8	842	0.47	123.3954	1.08	0.0474	1.45	52.0	0.6	68.3	34.1	52.0	0.6
CH21B_7	667	0.56	122.8859	1.11	0.0513	1.81	52.2	0.6	254.7	41.1	52.2	0.6
CH21B_6	589	0.42	115.5410	1.18	0.0480	1.87	55.6	0.7	99.6	43.6	55.6	0.7
CH21B_5	693	0.50	120.5734	1.04	0.0498	1.82	53.2	0.5	187.9	41.9	53.2	0.5
CH21B_4	932	0.30	120.0275	0.92	0.0481	1.56	53.5	0.5	104.2	36.4	53.5	0.5
CH21B_3	407	0.54	121.3948	1.22	0.0564	2.28	52.9	0.6	469.5	49.7	52.9	0.6
CH21B_2	347	0.38	122.9232	1.28	0.0457	2.49	52.2	0.7	0.0	39.8	52.2	0.7
CH21B_1	1224	0.37	115.9095	0.97	0.0443	1.55	55.4	0.5	0.0	0.0	55.4	0.5
Bosque batholith												
CB1_33	3991	0.19	118.0425	1.67	0.0517	1.10	54.4	0.9	271.4	25.1	54.4	0.9
CB1_32	13720	0.07	109.1547	1.97	0.0466	0.97	58.8	1.2	30.9	23.0	58.8	1.2
CB1_31	587	0.38	112.9761	1.98	0.0458	2.11	56.8	1.1	0.0	35.8	56.8	1.1
CB1_30	3206	0.26	116.4683	1.66	0.0468	1.21	55.1	0.9	40.0	28.8	55.1	0.9
CB1_29	2185	0.28	112.7510	2.04	0.0469	1.57	56.9	1.2	43.2	37.1	56.9	1.2
CB1_28	824	0.26	16.2261	2.01	0.0668	1.13	385.5	7.5	832.7	23.4	385.5	7.5
CB1_27	2123	0.25	113.0986	1.76	0.0464	1.66	56.7	1.0	16.7	39.3	56.7	1.0
CB1_26	1502	0.34	26.5206	1.54	0.0702	0.88	238.6	3.6	935.4	18.0	238.6	3.6
CB1_25	940	0.09	119.0885	1.59	0.0477	1.59	53.9	0.9	86.4	37.4	53.9	0.9
CB1_24	2402	0.28	120.0046	1.79	0.0466	1.41	53.5	1.0	28.7	33.5	53.5	1.0
CB1_23	6537	0.11	117.6860	1.43	0.0490	0.87	54.5	0.8	148.7	20.2	54.5	0.8
CB1_22	252	0.62	118.4373	3.49	0.0507	5.98	54.2	1.9	227.5	132.5	54.2	1.9
CB1_21	2646	0.24	112.0430	1.47	0.0471	1.09	57.3	0.8	54.7	25.9	57.3	0.8
CB1_20	1062	0.45	26.8682	1.61	0.0525	1.24	235.6	3.7	308.3	28.0	235.6	3.7
CB1_19	865	0.12	119.9749	1.60	0.0485	1.64	53.5	0.9	121.5	38.3	53.5	0.9
CB1_18	621	1.32	9.8090	1.40	0.0606	0.79	625.8	8.3	624.7	16.9	625.8	8.3
CB1_17	2663	0.46	81.5246	1.97	0.0531	1.65	78.6	1.5	331.1	36.9	78.6	1.5
CB1_16	4508	0.15	108.2290	1.46	0.0465	0.87	59.3	0.9	22.8	20.6	59.3	0.9

CB1_15	1055	0.42	111.8473	1.50	0.0486	1.44	57.4	0.9	128.3	33.6	57.4	0.9
CB1_14	1344	0.20	76.0193	1.96	0.0561	0.82	84.2	1.6	458.3	18.1	84.2	1.6
CB1_13	2244	0.24	109.8940	1.48	0.0469	1.00	58.4	0.9	43.5	23.7	58.4	0.9
CB1_12	3135	0.24	115.4386	1.53	0.0472	1.19	55.6	0.8	60.9	28.0	55.6	0.8
CB1_11	1935	0.24	112.7442	1.78	0.0474	1.53	56.9	1.0	69.7	35.9	56.9	1.0
CB1_10	668	0.45	115.7464	1.25	0.0461	1.63	55.5	0.7	0.0	39.7	55.5	0.7
CB1_9	2508	0.21	114.3365	1.18	0.0471	1.04	56.1	0.7	54.1	24.5	56.1	0.7
CB1_8	4726	0.21	113.0889	1.11	0.0471	0.72	56.8	0.6	54.7	17.0	56.8	0.6
CB1_7	743	0.32	112.3122	1.42	0.0475	1.61	57.1	0.8	73.3	37.7	57.1	0.8
CB1_6	1757	0.18	113.4217	1.84	0.0463	1.03	56.6	1.0	12.0	23.7	56.6	1.0
CB1_5	2030	0.15	111.0487	1.86	0.0475	1.26	57.8	1.1	76.9	29.6	57.8	1.1
CB1_4	1465	0.24	112.3340	1.84	0.0461	1.27	57.1	1.0	5.8	28.0	57.1	1.0
CB1_3	1270	0.28	118.9109	2.03	0.0482	1.52	54.0	1.1	108.7	35.5	54.0	1.1
CB1_2	2435	0.18	110.1076	1.81	0.0473	0.98	58.3	1.0	63.4	23.3	58.3	1.0
CB1_1	1554	1.13	113.8881	2.08	0.0465	1.14	56.4	1.2	21.7	27.0	56.4	1.2

Table 4.3. Zircon Hf isotope results.

Sample	$^{176}\text{Hf}/^{177}\text{Hf}$	2SE	$^{176}\text{Lu}/^{177}\text{Hf}$	2SE	$^{176}\text{Yb}/^{177}\text{Hf}$	2SE	AGE	$^{176}\text{Hf}/^{177}\text{Hf}_{(i)}$	$\epsilon\text{Hf}_{(0)}$	2SE	$\epsilon\text{Hf}_{(i)}$
Bosque Batholith											
CB1	0.282789	0.000027	0.00221	0.00005	0.05470	0.00150	56.4	0.282789	0.1	1.0	1.3
CB1	0.282700	0.000026	0.00115	0.00002	0.03233	0.00054	58.3	0.282700	-3.0	0.9	-1.8
CB1	0.282638	0.000021	0.00012	0.00000	0.00329	0.00002	57.1	0.282638	-5.2	0.7	-3.9
CB1	0.282661	0.000030	0.00031	0.00001	0.00909	0.00019	57.8	0.282661	-4.4	1.1	-3.1
CB1	0.282624	0.000029	0.00085	0.00002	0.02235	0.00090	56.6	0.282624	-5.7	1.0	-4.5
CB1	0.282654	0.000024	0.00016	0.00002	0.00460	0.00042	56.8	0.282654	-4.6	0.8	-3.4
CB1	0.282694	0.000028	0.00035	0.00001	0.00967	0.00014	58.8	0.282694	-3.2	1.0	-1.9
CB1	0.282694	0.000029	0.00059	0.00001	0.01698	0.00025	56.9	0.282694	-3.2	1.0	-2.0
Hatillo Stock											
CH5	0.282801	0.000026	0.00102	0.00001	0.02445	0.00018	54.3	0.282801	0.6	0.9	1.7
CH5	0.282796	0.000020	0.00134	0.00002	0.03101	0.00066	54.9	0.282796	0.4	0.7	1.6
CH5	0.282796	0.000026	0.00118	0.00004	0.02813	0.00094	52.3	0.282796	0.4	0.9	1.5
CH5	0.282635	0.000037	0.00105	0.00004	0.02610	0.00120	53.6	0.282635	-5.3	1.3	-4.2
CH5	0.282813	0.000024	0.00066	0.00001	0.01505	0.00032	54.2	0.282813	1.0	0.8	2.2
CH5	0.282430	0.000120	0.00070	0.00004	0.01656	0.00092	52.1	0.282430	-12.6	4.2	-11.4
CH5	0.282803	0.000028	0.00106	0.00002	0.02445	0.00051	53.9	0.282803	0.6	1.0	1.8
CH5	0.282791	0.000030	0.00087	0.00007	0.02040	0.00160	54.5	0.282791	0.2	1.1	1.4
CH8	0.282744	0.000032	0.00261	0.00029	0.06810	0.00790	52.7	0.282744	-1.4	1.1	-0.4
CH8	0.282815	0.000028	0.00111	0.00005	0.02691	0.00095	53.0	0.282815	1.1	1.0	2.2
CH8	0.282732	0.000030	0.00099	0.00010	0.02540	0.00270	53.9	0.282732	-1.9	1.1	-0.7
CH8	0.282751	0.000034	0.00083	0.00005	0.02070	0.00120	54.4	0.282751	-1.2	1.2	0.0
CH8	0.282752	0.000027	0.00079	0.00002	0.01874	0.00047	53.6	0.282752	-1.2	1.0	0.0
CH8	0.282808	0.000033	0.00078	0.00003	0.01921	0.00080	52.3	0.282808	0.8	1.2	1.9
CH8	0.282806	0.000026	0.00061	0.00006	0.01430	0.00140	51.9	0.282806	0.7	0.9	1.9
CH8	0.282819	0.000027	0.00071	0.00002	0.01681	0.00062	54.7	0.282819	1.2	1.0	2.4
CH10	0.282420	0.000160	0.00061	0.00004	0.01470	0.00110	52.4	0.282420	-12.9	5.7	-11.8

CH10	0.282835	0.000026	0.00086	0.00003	0.02029	0.00074	54.1	0.282835	1.8	0.9	2.9
CH10	0.282820	0.000027	0.00195	0.00023	0.04920	0.00590	55.1	0.282820	1.2	1.0	2.4
CH10	0.282793	0.000021	0.00101	0.00010	0.02500	0.00270	55.1	0.282793	0.3	0.7	1.5
CH10	0.282820	0.000023	0.00085	0.00003	0.02085	0.00078	53.6	0.282820	1.2	0.8	2.4
CH10	0.282823	0.000024	0.00095	0.00002	0.02275	0.00059	54.1	0.282823	1.3	0.8	2.5
CH10	0.282740	0.000048	0.00094	0.00013	0.02280	0.00340	51.8	0.282740	-1.6	1.7	-0.5
CH10	0.282815	0.000029	0.00068	0.00002	0.01571	0.00027	55.9	0.282815	1.1	1.0	2.3
CH10	0.282774	0.000028	0.00102	0.00012	0.03200	0.00450	52.2	0.282774	-0.4	1.0	0.7
CH19	0.282863	0.000028	0.00090	0.00003	0.02167	0.00058	55.0	0.282863	2.8	1.0	3.9
CH19	0.282784	0.000048	0.00089	0.00005	0.02180	0.00100	54.6	0.282784	0.0	1.7	1.1
CH19	0.282856	0.000027	0.00077	0.00003	0.01959	0.00099	55.3	0.282856	2.5	1.0	3.7
CH19	0.282877	0.000042	0.00188	0.00008	0.04930	0.00230	54.6	0.282877	3.3	1.5	4.4
CH19	0.282877	0.000031	0.00069	0.00004	0.01685	0.00087	55.6	0.282877	3.3	1.1	4.5
CH19	0.282790	0.000078	0.00089	0.00006	0.02130	0.00120	51.6	0.282790	0.2	2.8	1.3
CH19	0.282819	0.000038	0.00091	0.00004	0.02198	0.00087	54.3	0.282819	1.2	1.3	2.4
CH19	0.282908	0.000042	0.00083	0.00005	0.02050	0.00120	57.8	0.282908	4.3	1.5	5.6
CH21B	0.282835	0.000029	0.00098	0.00004	0.02380	0.00077	52.2	0.282835	1.8	1.0	2.9
CH21B	0.282855	0.000032	0.00088	0.00003	0.02158	0.00069	51.9	0.282855	2.5	1.1	3.6
CH21B	0.282812	0.000034	0.00167	0.00015	0.04270	0.00380	58.8	0.282812	1.0	1.2	2.2
CH21B	0.282817	0.000032	0.00085	0.00001	0.02116	0.00023	52.4	0.282817	1.1	1.1	2.3
CH21B	0.282852	0.000026	0.00077	0.00003	0.02004	0.00083	54.9	0.282852	2.4	0.9	3.6
CH21B	0.282814	0.000032	0.00221	0.00040	0.06200	0.01200	52.9	0.282814	1.0	1.1	2.1
CH21B	0.282852	0.000026	0.00112	0.00004	0.02942	0.00092	52.8	0.282852	2.4	0.9	3.5
CH21B	0.282861	0.000032	0.00122	0.00014	0.03090	0.00350	56.9	0.282861	2.7	1.1	3.9
MLH1_10	0.282852	0.000023	0.0006	0.000037	0.01568	0.00096	50.7	0.282851	2.4	0.8	3.5
MLH1_9	0.282839	0.000022	0.00062	0.000016	0.01567	0.00042	53.0	0.282838	1.9	0.8	3.1
MLH1_8	0.282796	0.000025	0.00065	0.000025	0.01752	0.00079	53.0	0.282795	0.4	0.9	1.5
MLH1_7	0.282807	0.000030	0.00087	0.00003	0.02414	0.00077	53.2	0.282806	0.8	1.1	1.9
MLH1_6	0.282807	0.000026	0.00065	0.000027	0.01734	0.00074	53.5	0.282806	0.8	0.9	1.9
MLH1_5	0.282850	0.000022	0.00069	0.000027	0.01762	0.00068	53.8	0.282849	2.3	0.8	3.5

MLH1_4	0.282821	0.000027	0.00063	0.000032	0.01611	0.00082	54.2	0.282820	1.3	1.0	2.5
MLH1_3	0.282815	0.000048	0.00187	0.00042	0.05100	0.012	57.5	0.282813	1.1	1.7	2.3
MLH1_2	0.282791	0.000026	0.00305	0.00037	0.09600	0.012	63.5	0.282787	0.2	0.9	1.5
MLH1_1	0.282295	0.000077	0.00095	0.000027	0.02700	0.0012	1000.0	0.282277	-17.3	2.7	4.4

D928 - Bogotá Fm. (Tuff)

D928_19	0.282950	0.000024	0.00058	0.000047	0.01680	0.0015	50.0	0.282949	5.8	0.9	6.9
D928_18	0.282916	0.000026	0.00087	0.000052	0.02450	0.0015	50.0	0.282915	4.6	0.9	5.7
D928_17	0.282574	0.000022	0.00163	0.000018	0.05118	0.00045	50.0	0.282572	-7.5	0.8	-6.4
D928_16	0.282347	0.000025	0.0014	0.000034	0.04520	0.0012	50.0	0.282346	-15.5	0.9	-14.4
D928_15	0.282593	0.000036	0.00106	0.000089	0.02700	0.0017	54.0	0.282592	-6.8	1.3	-5.6
D928_14	0.282641	0.000027	0.00123	0.000044	0.03440	0.0012	54.7	0.282640	-5.1	1.0	-3.9
D928_13	0.282877	0.000030	0.00059	0.000043	0.01680	0.0012	56.2	0.282876	3.3	1.1	4.5
D928_12	0.282944	0.000028	0.00067	0.00003	0.01809	0.00095	56.4	0.282943	5.6	1.0	6.9
D928_11	0.282910	0.000031	0.00066	0.000018	0.01741	0.00073	57.6	0.282909	4.4	1.1	5.7
D928_10	0.282895	0.000027	0.00099	0.000065	0.02770	0.002	57.9	0.282894	3.9	1.0	5.1
D928_9	0.282949	0.000032	0.00095	0.000045	0.02830	0.0013	58.4	0.282948	5.8	1.1	7.1
D928_8	0.282910	0.000027	0.00087	0.000049	0.02380	0.0012	58.4	0.282909	4.4	1.0	5.7
D928_7	0.282939	0.000024	0.00069	0.000044	0.02030	0.0015	58.8	0.282938	5.4	0.9	6.7
D928_6	0.282931	0.000027	0.00121	0.000091	0.03340	0.0022	59.0	0.282930	5.2	1.0	6.4
D928_5	0.282651	0.000027	0.00106	0.000035	0.03010	0.001	60.0	0.282650	-4.7	1.0	-3.4
D928_4	0.282617	0.000038	0.00129	0.000073	0.03660	0.0021	60.8	0.282616	-5.9	1.3	-4.6
D928_3	0.282730	0.000024	0.00105	0.000066	0.03270	0.002	61.0	0.282729	-1.9	0.9	-0.6
D928_2	0.282506	0.000056	0.00097	0.000057	0.02820	0.0022	100.1	0.282504	-9.9	2.0	-7.7
D928_1	0.282684	0.000038	0.00148	0.00013	0.04210	0.0038	141.0	0.282680	-3.6	1.3	-0.6

D937 - Bogotá Fm. (Sandstone)

D937_1	0.282653	0.000027	0.00096	0.000038	0.02600	0.0011	55.0	0.282652	-4.7	1.0	-3.5
D937_2	0.282918	0.000025	0.00094	0.00002	0.02545	0.00069	55.0	0.282917	4.7	0.9	5.9
D937_3	0.282684	0.000022	0.00105	0.000025	0.02843	0.00096	56.0	0.282683	-3.6	0.8	-2.4
D937_4	0.282952	0.000034	0.00104	0.00008	0.03000	0.0026	56.0	0.282951	5.9	1.2	7.1
D937_5	0.282701	0.000024	0.00095	0.000011	0.02612	0.00027	57.4	0.282700	-3.0	0.9	-1.7

D937_6	0.282663	0.000027	0.00094	0.000036	0.02590	0.0011	57.7	0.282662	-4.3	1.0	-3.1
D937_7	0.282910	0.000030	0.00095	0.000034	0.02630	0.0011	58.5	0.282909	4.4	1.1	5.7
D937_8	0.282677	0.000059	0.00114	0.000048	0.02990	0.00044	58.9	0.282676	-3.8	2.1	-2.6
D937_9	0.282921	0.000019	0.00081	0.000033	0.02273	0.00093	59.2	0.282920	4.8	0.7	6.1
D937_10	0.282654	0.000034	0.00283	0.00018	0.07720	0.0053	60.0	0.282651	-4.6	1.2	-3.4
D937_11	0.282978	0.000043	0.00134	0.000092	0.03910	0.0029	60.1	0.282976	6.8	1.5	8.1
D937_12	0.282705	0.000025	0.00116	0.000017	0.03228	0.00046	60.5	0.282704	-2.8	0.9	-1.5
D937_13	0.282918	0.000027	0.0007	0.000056	0.01820	0.0015	60.7	0.282917	4.7	1.0	6.0
D937_14	0.282893	0.000024	0.00047	0.00002	0.01356	0.00062	61.8	0.282892	3.8	0.9	5.2
D937_15	0.282677	0.000032	0.0011	0.000021	0.02960	0.00049	62.8	0.282676	-3.8	1.1	-2.5
D937_16	0.282634	0.000031	0.00162	0.00014	0.05020	0.0047	62.9	0.282632	-5.3	1.1	-4.0
D937_17	0.282660	0.000031	0.00152	0.000045	0.04150	0.0011	63.0	0.282658	-4.4	1.1	-3.1
D937_18	0.282677	0.000023	0.00127	0.000024	0.03405	0.00078	63.2	0.282675	-3.8	0.8	-2.5
D937_19	0.282681	0.000040	0.00115	0.000081	0.03340	0.0026	63.4	0.282680	-3.7	1.4	-2.3
D937_20	0.282675	0.000021	0.00088	0.000027	0.02431	0.0008	63.5	0.282674	-3.9	0.7	-2.5
D937_21	0.282666	0.000029	0.00138	0.000037	0.03810	0.0011	64.3	0.282664	-4.2	1.0	-2.8
D937_22	0.282689	0.000024	0.0011	0.000055	0.03020	0.0014	64.5	0.282688	-3.4	0.9	-2.0
D937_23	0.282931	0.000031	0.00092	0.000052	0.02620	0.0012	65.0	0.282930	5.2	1.1	6.6
D937_24	0.282669	0.000028	0.0011	0.000036	0.02922	0.00081	65.4	0.282668	-4.1	1.0	-2.7
D937_25	0.282939	0.000021	0.00108	0.000032	0.03120	0.00071	66.6	0.282938	5.4	0.7	6.9
D937_26	0.282914	0.000025	0.00079	0.00004	0.02130	0.001	66.7	0.282913	4.6	0.9	6.0
D937_27	0.282646	0.000030	0.00126	0.000081	0.03570	0.0023	67.5	0.282644	-4.9	1.1	-3.5
D937_28	0.282964	0.000023	0.00094	0.00003	0.02464	0.00088	67.6	0.282963	6.3	0.8	7.8
D937_29	0.282780	0.000047	0.00221	0.00017	0.07010	0.0056	68.1	0.282777	-0.2	1.7	1.2
D937_30	0.282555	0.000041	0.00167	0.00015	0.04550	0.0041	69.6	0.282553	-8.1	1.5	-6.7
D937_31	0.282633	0.000033	0.00141	0.000045	0.03900	0.0012	70.1	0.282631	-5.4	1.2	-3.9
D937_32	0.282938	0.000043	0.00121	0.000083	0.03340	0.0021	70.6	0.282936	5.4	1.5	6.9
D937_33	0.282900	0.000021	0.00054	0.000016	0.01447	0.00044	70.8	0.282899	4.1	0.7	5.6
D937_34	0.282901	0.000026	0.00097	0.000021	0.03029	0.00085	70.9	0.282900	4.1	0.9	5.6
D937_35	0.282911	0.000026	0.00092	0.000092	0.02570	0.0026	72.1	0.282910	4.5	0.9	6.0

D937_36	0.282895	0.000024	0.00065	0.000066	0.01880	0.0018	73.6	0.282894	3.9	0.9	5.5
D937_37	0.282649	0.000026	0.00101	0.00003	0.02607	0.00092	75.2	0.282648	-4.8	0.9	-3.2
D937_38	0.282859	0.000025	0.00057	0.000012	0.01706	0.00026	76.4	0.282858	2.6	0.9	4.3
D937_39	0.282679	0.000024	0.00105	0.000056	0.02930	0.0016	76.5	0.282678	-3.7	0.9	-2.1
D937_40	0.282670	0.000030	0.00118	0.000043	0.03301	0.00098	77.8	0.282668	-4.1	1.1	-2.4
D937_41	0.282562	0.000038	0.00114	0.000031	0.03262	0.00098	81.8	0.282560	-7.9	1.3	-6.1
D937_42	0.282789	0.000026	0.00108	0.000036	0.03220	0.0014	83.9	0.282787	0.1	0.9	1.9
D937_43	0.282684	0.000027	0.00116	0.000049	0.03140	0.0013	89.0	0.282682	-3.6	1.0	-1.7
D937_44	0.282643	0.000028	0.00126	0.000031	0.03442	0.00081	89.0	0.282641	-5.0	1.0	-3.1
D937_45	0.282915	0.000024	0.00061	0.000009	0.01806	0.00017	89.6	0.282914	4.6	0.9	6.6
D937_46	0.282687	0.000032	0.00133	0.000041	0.03730	0.0016	91.9	0.282685	-3.5	1.1	-1.5
D937_47	0.282792	0.000028	0.00139	0.000056	0.04130	0.0017	93.2	0.282790	0.2	1.0	2.2
D937_48	0.282794	0.000036	0.0014	0.00002	0.04106	0.00074	98.2	0.282791	0.3	1.3	2.4
D937_49	0.282680	0.000029	0.00116	0.000069	0.03350	0.0023	99.2	0.282678	-3.7	1.0	-1.6
D937_50	0.282638	0.000025	0.00104	0.000033	0.02928	0.00097	107.3	0.282636	-5.2	0.9	-2.9
D937_51	0.282859	0.000030	0.00075	0.00012	0.02180	0.0034	109.3	0.282857	2.6	1.1	5.0
D937_52	0.282853	0.000027	0.001	0.000026	0.03041	0.00089	125.2	0.282851	2.4	1.0	5.1
D937_53	0.282879	0.000030	0.00058	0.000049	0.01600	0.0013	130.3	0.282878	3.3	1.1	6.2
D937_54	0.282873	0.000025	0.00099	0.000016	0.03192	0.00041	142.1	0.282870	3.1	0.9	6.2
D937_55	0.282788	0.000037	0.00119	0.000056	0.03090	0.0013	144.4	0.282785	0.1	1.3	3.2
D937_56	0.282647	0.000031	0.00088	0.00001	0.02482	0.00061	146.4	0.282645	-4.9	1.1	-1.7
D937_57	0.282897	0.000030	0.00086	0.000072	0.02300	0.0019	152.1	0.282895	4.0	1.1	7.3
D937_58	0.282714	0.000025	0.00091	0.000024	0.02507	0.00081	156.0	0.282711	-2.5	0.9	0.9
D937_59	0.282837	0.000026	0.00104	0.000022	0.02665	0.00062	161.3	0.282834	1.8	0.9	5.3
D937_60	0.282830	0.000030	0.00095	0.000064	0.02540	0.0018	176.6	0.282827	1.6	1.1	5.4
D937_61	0.282773	0.000024	0.00123	0.000054	0.03580	0.0018	177.9	0.282769	-0.4	0.9	3.4
D937_62	0.282946	0.000033	0.00068	0.000026	0.01898	0.00071	180.5	0.282944	5.7	1.2	9.6
D937_63	0.282765	0.000022	0.00065	0.00002	0.01871	0.00048	186.3	0.282763	-0.7	0.8	3.4
D937_64	0.282376	0.000027	0.0003	0.000063	0.00980	0.0017	193.5	0.282375	-14.5	1.0	-10.2
D937_65	0.282702	0.000030	0.00111	0.000023	0.03098	0.00074	194.9	0.282698	-2.9	1.1	1.3

D937_66	0.282905	0.000030	0.00098	0.000062	0.02790	0.0016	210.3	0.282901	4.2	1.1	8.8
D937_67	0.282559	0.000032	0.00178	0.000077	0.05970	0.003	215.0	0.282552	-8.0	1.1	-3.5
D937_68	0.282561	0.000028	0.00101	0.000065	0.02860	0.0019	242.7	0.282556	-7.9	1.0	-2.7
D937_69	0.282559	0.000036	0.00123	0.000062	0.03870	0.0021	244.4	0.282553	-8.0	1.3	-2.8
D937_70	0.282570	0.000025	0.00068	0.000008	0.01923	0.00041	264.4	0.282567	-7.6	0.9	-1.8
D937_71	0.282469	0.000024	0.00069	0.00018	0.02040	0.0051	264.8	0.282466	-11.2	0.9	-5.4
D937_72	0.282569	0.000026	0.00133	0.000025	0.03969	0.00094	311.9	0.282561	-7.6	0.9	-1.0
D937_73	0.282270	0.000036	0.00041	0.000008	0.01276	0.00038	313.6	0.282268	-18.2	1.3	-11.3
D937_74	0.282374	0.000027	0.0013	0.000077	0.04330	0.0028	430.4	0.282364	-14.5	1.0	-5.3
D937_75	0.282276	0.000025	0.00085	0.000014	0.02638	0.00036	449.1	0.282269	-18.0	0.9	-8.3
D937_76	0.282345	0.000029	0.00014	0.000002	0.00512	0.00007	525.0	0.282344	-15.6	1.0	-3.9
D937_77	0.282253	0.000031	0.00169	0.00025	0.05750	0.0085	777.5	0.282228	-18.8	1.1	-2.3
D937_78	0.281925	0.000034	0.00092	0.000031	0.02792	0.00096	1000.0	0.281908	-30.4	1.2	-8.7
D937_79	0.281901	0.000033	0.00042	0.000037	0.01097	0.00083	1044.2	0.281893	-31.3	1.2	-8.2
D937_80	0.281925	0.000028	0.00064	0.000023	0.01904	0.00071	1137.7	0.281911	-30.4	1.0	-5.4
D937_81	0.282090	0.000031	0.00038	0.000009	0.01168	0.00025	1141.1	0.282082	-24.6	1.1	0.7
D937_82	0.282130	0.000029	0.00041	0.000007	0.01342	0.00018	1200.0	0.282121	-23.2	1.0	3.4
D937_83	0.282051	0.000027	0.00053	0.000033	0.01740	0.0013	1200.3	0.282039	-26.0	1.0	0.5
D937_84	0.282105	0.000024	0.00052	0.000005	0.01638	0.00013	1222.6	0.282093	-24.0	0.9	3.0
D937_85	0.281996	0.000059	0.00069	0.000045	0.02170	0.0016	1600.0	0.281975	-27.9	2.1	7.4
D937_86	0.281619	0.000027	0.00096	0.000062	0.02930	0.0024	1701.8	0.281588	-41.2	1.0	-4.0

Table 5.1. SHRIMP U-Pb zircon data of a tonalite from the Santa Marta batholith.

Spot	%	ppm U	ppm Th	^{232}Th $/^{238}\text{U}$	ppm $^{206}\text{Pb}^*$	(1) ^{206}Pb $/^{238}\text{U}$	(2) ^{206}Pb $/^{238}\text{U}$	(3) ^{206}Pb $/^{238}\text{U}$	(1) ^{207}Pb $/^{206}\text{Pb}$	(1) ^{208}Pb $/^{232}\text{Th}$	% Dis- cor- dant	Total ^{238}U $/^{206}\text{Pb}$	% $\pm\%$
	$^{206}\text{Pb}_c$					Age	Age	Age	^{206}Pb Age	^{207}Pb Age	^{208}Pb Age		
SM54-1.1	6.11	189	71	0.39	1.47	54.2 \pm 1.8	53.5 \pm 1.0	54.5 \pm 1.2	485 \pm 880	50 \pm 26	89	110.7	1.8
SM54-2.1	11.38	113	50	0.46	0.930	55.4 \pm 3.7	53.9 \pm 1.6	54.4 \pm 2.0	860 \pm 1500	69 \pm 50	94	104.7	2.5
SM54-3.1	10.40	126	57	0.47	1.04	55.3 \pm 2.8	53.0 \pm 1.3	55.1 \pm 1.7	1,177 \pm 910	57 \pm 37	95	104.3	2.1
SM54-4.1	8.58	177	67	0.39	1.39	55.4 \pm 1.9	53.3 \pm 1.2	53.6 \pm 1.4	1,122 \pm 630	83 \pm 28	95	109.4	1.8
SM54-5.1	13.96	123	53	0.45	1.06	57.7 \pm 3.0	55.6 \pm 1.3	55.5 \pm 2.0	1,114 \pm 980	88 \pm 42	95	99.6	2.1
SM54-6.1	13.97	105	50	0.49	0.843	55.4 \pm 2.9	53.4 \pm 1.5	51.7 \pm 1.9	1,090 \pm 1000	100 \pm 36	95	106.9	2.3
SM54-7.1	11.78	125	56	0.46	1.02	58.7 \pm 2.0	54.2 \pm 1.5	53.5 \pm 1.7	1,759 \pm 390	127 \pm 23	97	105.9	2.1
SM54-8.1	8.92	142	66	0.48	1.15	58.3 \pm 1.6	55.2 \pm 1.4	55.4 \pm 1.8	1,418 \pm 380	95 \pm 18	96	105.5	2.0
SM54-8.2	8.87	191	104	0.56	1.57	56.9 \pm 2.0	55.3 \pm 1.5	55.9 \pm 1.7	896 \pm 840	67 \pm 21	94	104.6	1.8
SM54-9.1	13.42	125	58	0.48	1.15	62.0 \pm 3.2	58.7 \pm 2.0	59.9 \pm 2.3	1,412 \pm 870	88 \pm 42	96	92.8	2.0
SM54-10.1	14.93	114	51	0.46	0.971	54.9 \pm 3.8	55.8 \pm 2.2	54.2 \pm 2.0		65 \pm 52		100.8	2.2
SM54-11.1	7.88	177	85	0.50	1.41	54.9 \pm 1.8	54.9 \pm 1.1	54.9 \pm 1.4	-20 \pm 1200	54 \pm 20	442	107.7	1.8
SM54-12.1	11.36	135	51	0.39	1.12	53.5 \pm 3.9	53.0 \pm 2.6	54.7 \pm 3.3	420 \pm 1800		87	104.1	4.8
SM54-13.1	11.02	108	43	0.41	0.838	54.9 \pm 1.9	52.7 \pm 1.4	51.7 \pm 1.8	1,197 \pm 540	102 \pm 25	95	110.4	2.2
SM54-14.1	11.47	96	52	0.56	0.834	61.6 \pm 1.5	56.5 \pm 1.4	57.2 \pm 2.0	1,861 \pm 170	109 \pm 11	97	99.3	2.3
SM54-14.2	13.56	185	74	0.41	1.50	57.5 \pm 1.7	53.5 \pm 1.0	52.4 \pm 1.8	1,678 \pm 330	134 \pm 25	97	106.0	1.8
SM54-15.1	13.70	128	52	0.42	1.07	53.7 \pm 3.1	53.6 \pm 1.8	54.1 \pm 2.1	100 \pm 2300	47 \pm 47	48	102.3	2.1
SM54-16.1	9.84	142	59	0.43	1.14	54.8 \pm 2.5	52.6 \pm 1.6	54.0 \pm 1.5	1,199 \pm 880	67 \pm 35	95	107.3	2.0
SM54-16.2	10.33	133	75	0.58	1.11	57.1 \pm 2.4	55.0 \pm 1.3	55.5 \pm 2.2	1,099 \pm 780	74 \pm 26	95	103.8	2.0

Table 5.1. Continuation.

Total ^{207}Pb $/^{206}\text{Pb}$	$\pm\%$	(1) $^{238}\text{U}/$ $^{206}\text{Pb}^*$	$\pm\%$	(1) $^{207}\text{Pb}^*$ $/^{206}\text{Pb}^*$	$\pm\%$	(1) $^{207}\text{Pb}^*$ $/^{235}\text{U}$	$\pm\%$	(1) $^{206}\text{Pb}^*$ $/^{238}\text{U}$	$\pm\%$	err corr	(3) $^{238}\text{U}/$ $^{206}\text{Pb}^*$	$\pm\%$	(3) $^{207}\text{Pb}^*$ $/^{206}\text{Pb}^*$	$\pm\%$	(3) $^{207}\text{Pb}^*$ $/^{235}\text{U}$	$\pm\%$	(3) $^{206}\text{Pb}^*$ $/^{238}\text{U}$	$\pm\%$	err corr
0.1080	4.9	118.4	3.3	0.057	40	0.066	40	0.00844	3.3	.083	117.9	1.8	0.0588	9.6	0.0688	9.8	0.00848	1.8	.182
0.143	7.6	115.9	6.7	0.068	72	0.081	73	0.00863	6.7	.091	118.1	2.5	0.050	24	0.059	25	0.00847	2.5	.100
0.1568	5.0	116.2	5.1	0.079	46	0.094	46	0.00861	5.1	.110	116.4	2.1	0.0747	12	0.088	12	0.00859	2.1	.174
0.1194	6.9	115.9	3.5	0.077	31	0.092	32	0.00863	3.5	.110	119.7	1.8	0.0495	18	0.057	19	0.00835	1.8	.099
0.1564	4.9	111.2	5.2	0.077	49	0.095	49	0.00899	5.2	.106	115.7	2.1	0.0416	22	0.050	22	0.00864	2.1	.096
0.135	8.8	116.0	5.3	0.076	51	0.090	51	0.00862	5.3	.103	124.3	2.3	0.017	83	0.019	83	0.00805	2.3	.028
0.131	9.2	109.4	3.3	0.108	21	0.136	21	0.00914	3.3	.157	120.0	2.1	0.033	42	0.038	42	0.00833	2.1	.051
0.120	8.7	110.0	2.8	0.090	20	0.112	20	0.00909	2.8	.137	115.8	2.0	0.048	24	0.057	24	0.00864	2.0	.083
0.125	12	112.9	3.5	0.069	41	0.084	41	0.00886	3.5	.085	114.8	1.8	0.054	30	0.064	30	0.00871	1.8	.058
0.167	11	103.5	5.2	0.089	46	0.119	46	0.00966	5.2	.113	107.1	2.0	0.059	35	0.076	35	0.00933	2.0	.059
0.145	15	116.8	7.0					0.00856	7.0		118.5	2.2					0.00844	2.2	
0.1092	4.8	117.0	3.2	0.046	48	0.054	48	0.00854	3.2	.067	116.9	1.8	0.0446	13	0.0526	13	0.00856	1.8	.138
0.1589	4.8	119.9	7.3	0.055	79	0.063	79	0.00834	7.3	.091	117.4	4.8	0.0685	13	0.080	14	0.00852	4.8	.356
0.1218	7.6	116.8	3.4	0.080	27	0.094	27	0.00856	3.4	.124	124.1	2.2	0.030	35	0.033	35	0.00806	2.2	.064
0.1472	5.5	104.1	2.4	0.114	9.2	0.151	9.5	0.00961	2.4	.256	112.2	2.3	0.0543	17	0.067	17	0.00892	2.3	.134
0.1396	4.2	111.5	2.9	0.103	18	0.127	18	0.00897	2.9	.162	122.6	1.8	0.0259	27	0.0292	27	0.00816	1.8	.066
0.162	11	119.5	5.8	0.048	99	0.055	99	0.00837	5.8	.058	118.6	2.1	0.051	41	0.059	41	0.00843	2.1	.051
0.144	11	117.1	4.6	0.080	45	0.094	45	0.00854	4.6	.102	119.0	2.0	0.065	27	0.075	27	0.00841	2.0	.073
0.1344	5.7	112.3	4.2	0.076	39	0.093	39	0.00890	4.2	.108	115.7	2.0	0.0504	17	0.060	17	0.00864	2.0	.117

Table 5.2. AMS parameters of the Santa Marta batholith. N, number of specimens; K, mean-site susceptibility (10^{-3} SI); P, anisotropy degree; T, shape parameter; K_1 , K_2 and K_3 are the orientation (in azimuth and dip) of the AMS principal directions. $\alpha_{1,2,3}$ are the angular dispersion (measured in degree) of the confidence ellipses around the principal directions.

Site	UTM	N	K (mSI)	P	T	K_1			K_2			K_3			
						dec	inc	α_1	dec	inc	α_2	dec	inc	α_3	
SM1	595420	1231860	11	0.08	1.07	0.29	33	4	7.1	187	86	7.6	303	2	8.1
SM2	584904	1236044	11	0.04	1.04	0.10	95	77	12.6	228	9	28.7	28	3	2.7
SM3	610742	1247622	10	0.06	1.11	0.17	275	80	6.7	37	5	8.9	128	8	9.1
SM4	614284	1247143	9	0.05	1.12	0.49	323	62	5.6	190	19	14.6	93	19	14.1
SM5	597291	1239609	11	10.40	1.32	0.03	209	28	10.7	96	37	12.3	325	40	10.9
SM6	598354	1239671	10	6.95	1.31	-0.03	341	39	13.1	178	50	18.9	78	9	17.5
SM7	599879	1240850	9	5.84	1.23	-0.33	63	19	18.6	245	71	26.5	153	1	25.0
SM8	601448	1242326	12	5.95	1.25	0.35	92	47	15.8	293	41	15.9	194	10	12.3
SM9	601942	1243181	10	13.10	1.15	0.10	236	69	26.5	340	6	28.4	72	20	16.0
SM10	597150	1241586	9	7.79	1.24	0.48	293	43	34.6	89	44	34.6	191	12	8.1
SM11	606092	1247514	9	8.69	1.28	0.52	33	84	22.5	174	5	22.7	264	4	7.6
SM12	605804	1249331	9	0.22	1.04	0.37	46	38	13.8	304	17	20.4	194	47	20.3
SM13	605545	1248396	9	0.48	1.09	0.17	188	18	16.6	285	21	17.6	61	61	18.9
SM14	604940	1246576	10	8.19	1.20	0.40	175	3	37.5	78	68	37.5	266	21	11.1
SM15	601354	1245856	10	11.80	1.13	0.20	25	49	14.6	219	40	13.2	123	7	11.2
SM16	602768	1242329	17	15.50	1.22	-0.19	240	4	10.5	350	78	13.1	149	11	11.9
SM17	604055	1242246	9	15.00	1.18	0.54	154	41	8.9	310	46	8.9	53	12	10.3
SM18	606590	1241100	12	11.50	1.26	0.48	320	63	30.0	109	23	29.9	205	12	12.2
SM19	606699	1241801	8	7.74	1.27	0.34	211	28	25.6	18	62	26.1	118	5	16.4
SM20	607207	1242959	12	7.48	1.43	0.54	163	0	21.1	253	57	21.2	72	33	6.0
SM21	592612	1240447	13	0.70	1.06	0.00	57	11	24.4	324	17	29.6	177	69	28.5
SM22	593735	1241763	9	0.80	1.03	0.00	192	30	18.4	98	6	20.8	358	60	13.2
SM23	594427	1239925	10	5.06	1.29	0.60	224	34	21.3	102	38	21.2	341	33	5.7
SM24	584366	1235366	10	0.16	1.07	0.65	310	40	14.7	51	12	14.2	154	48	7.8
SM25	615951	1250722	6	0.02	1.08	0.04	328	16	20.0	92	63	20.2	231	21	5.6
SM26	606673	1242317	9	0.09	1.07	-0.06	131	29	10.3	28	22	22.4	266	52	23.0
SM27	596357	1242193	10	8.58	1.20	0.52	182	63	12.8	72	10	15.3	338	25	10.8
SM28	599758	1242489	9	6.04	1.38	0.42	200	60	19.7	44	27	19.9	309	10	5.8
SM29	624506	1245924	11	6.27	1.10	0.07	245	13	27.7	149	22	27.6	2	64	12.4
SM30	622239	1246458	11	4.06	1.28	0.03	90	29	9.8	354	10	15.1	247	59	14.2
SM31	620463	1244937	13	4.57	1.29	0.12	246	48	15.2	345	16	16.3	97	38	9.5
SM32	620447	1247919	12	4.67	1.21	0.25	241	14	19.0	147	16	13.3	10	69	21.3
SM33	609225	1248711	15	8.58	1.41	0.26	24	2	24.2	118	60	27.8	293	30	17.6

SM34	609682	1249957	9	0.46	1.07	0.11	188	21	27.3	96	7	32.5	348	68	32.4
SM35	610558	1251223	12	6.31	1.30	0.18	179	4	12.7	88	2	12.8	334	85	10.1
SM36	611511	1252129	10	0.23	1.07	0.58	69	21	11.6	162	8	11.6	271	67	5.6
SM37	612435	1252738	11	7.55	1.51	0.52	54	9	11.5	158	57	11.4	318	32	8.9
SM38	613221	1252644	17	1.63	1.24	0.43	232	18	13.3	122	47	13.4	336	37	5.0
SM39	614501	1251296	13	4.18	1.16	-0.06	203	61	12.0	316	12	11.3	52	26	11.6
SM40	617350	1250217	8	2.79	1.20	0.36	11	8	25.7	279	13	25.1	132	75	15.0
SM41	616476	1250712	11	10.80	1.45	0.02	179	35	8.2	295	31	10.3	54	39	9.2
SM42	618562	1247768	13	6.30	1.18	0.00	89	44	18.7	267	46	18.7	358	1	9.7
SM43	613524	1246921	10	13.30	1.38	0.29	208	12	21.7	303	25	21.5	95	62	8.7
SM44	611302	1247652	19	7.67	1.27	-0.01	192	2	9.8	92	81	12.4	282	8	10.4
SM45	603274	1245857	8	11.80	1.17	0.23	19	44	34.9	199	46	35.6	289	1	12.5
SM46	585930	1224522	12	0.05	1.12	0.22	151	54	15.9	46	11	16.6	308	34	11.1
SM47	588299	1235795	14	0.38	1.04	0.27	118	1	21.6	209	20	21.5	27	69	13.9
SM48	590518	1234530	9	0.28	1.05	-0.26	141	36	21.6	21	35	33.5	261	35	32.9
SM49	589950	1235418	9	0.43	1.04	-0.07	72	23	13.3	183	39	22.7	320	42	21.9
SM50	591892	1237930	13	11.90	1.23	0.32	17	37	14.0	123	20	14.2	236	46	6.4
SM51	592797	1236730	8	11.50	1.20	0.28	208	45	26.2	42	44	26.4	306	7	10.0
SM52	593424	1235046	10	13.80	1.21	0.25	112	55	15.7	251	28	26.8	352	19	26.8
SM53	594688	1234200	7	12.40	1.18	0.15	89	31	16.7	193	21	18.6	311	51	17.2
SM54	595477	1233814	15	15.70	1.23	0.18	87	11	27.4	348	38	25.4	190	50	16.1
SM55	596298	1231703	8	1.01	1.14	-0.04	234	68	15.5	21	18.9	27.6	115	11	26.7
SM56	597866	1231161	12	0.16	1.07	0.37	165	46	11.8	272	16	10.3	16	39	12.1
SM57	598159	1230251	10	0.25	1.11	0.61	13	42	9.8	126	24	7.2	237	39	9.9
SM58	596385	1230241	10	0.40	1.07	0.02	341	14	67.2	175	76	67.1	72	3	19.5
SM59	596249	1229377	12	0.69	1.06	-0.35	214	7	10.9	305	2	21.1	53	82	19.5
SM60	595856	1228812	11	0.50	1.06	-0.28	5	59	13.5	100	3	18.6	192	31	18.8
SM61	595582	1228075	10	0.72	1.07	-0.18	109	42	5.3	353	25	8.1	242	37	8.0
SM62	593702	1233100	12	0.30	1.09	0.72	174	12	32.1	273	35	32.0	67	52	4.8
SM63	584898	1228839	9	0.22	1.04	0.42	106	63	23.3	291	27	23.3	200	2	9.6
SM64	586868	1227619	18	0.20	1.06	0.47	42	31	22.9	134	4	22.8	230	58	6.7
SM65	588238	1227768	15	0.93	1.09	-0.13	124	15	12.2	32	6	14.9	289	74	15.0
SM66	586236	1227343	14	0.47	1.08	-0.11	69	22	7.3	331	20	8.7	202	59	8.8
SM67	588538	1221387	10	2.34	1.14	-0.09	244	29	12.8	339	9	27.0	85	60	27.0
SM68	587275	1218411	15	1.55	1.09	0.31	272	18	53.9	149	60	54.0	10	24	16.7
SM69	584570	1234156	10	0.18	1.06	0.16	50	3	6.5	142	40	13.4	316	49	14.1